REGIONAL SURFACE WAVE MAGNITUDE AND MOMENT DETERMINATION METHODS APPLIED TO NUCLEAR EXPLOSIONS AT THE NEVADA TEST SITE: IMPLICATIONS FOR YIELD ESTIMATION AND SEISMIC DISCRIMINATION

Thesis by

Bradley B. Woods

In Partial Fulfillment of the Requirements

for the Degree of

Doctor of Philosophy

California Institute of Technology

Pasadena, California

1994

(Submitted August 19, 1993)

Acknowledgements

I was very fortunate to have the opportunity to study here at the Seismological Laboratory and to make use of the rich resources available for research here–including the accessible ear of any professor. I have also had the pleasure of having gotten to know a lot of good people here. Many of these persons have also been very helpful to me, and I would like to especially thank them. David Harkrider and Don Helmberger have been very supportive and knowlegable thesis advisors, who (for the most part) have been very easy to work with. Janet Fernandez, their secretary, has been of great help to me in clerical matters and has always been very understanding of my egregiously late travel reports. I would also like to thank Hiroo Kanamori for the instructive conversations I have had with him, his commitment to the improvement of the Seismolab and his and Tom Heaton's ability to keep the coffee conversation topics from being dominated by convection. Paul Roberts has been very helpful in retreiving seismograms from Kresge for me and Riley Geary has given a lot of useful information concerning NTS blasts. Special thanks go to Cindy Arveson for the digitizing that she did for me and for the condition in which she left the film-chip room for future generations of seismologists. To Doug Neuhauser, I and the entire Seismolab owe immense gratitude for giving us a dependable, excellently

maintained computer system. And then there are a whole lot of graduate students that I would like to thank in near-chronological order: John Vidale for his help and advice when I was a new student here; Richard Stead for the immense amount of help, knowledge and advice he bestowed upon me, and for being an anomalous office mate; Ed Garnero, Shawn Larsen and Lian-she Zhao for being most suppportive and helpful classmates and buddies; and Dave Scott and Oli Gudmundsson for their sage advise and ability to always put up with my sense of humor. I would also like to extend a most hearty thanks to Katherine Wolff for nothing at all whatsoever.

This research was supported by the Defense Advanced Research Projects Agency (DOD), Nuclear Monitoring Research Office and was monitored by Air Force Geophysics Laboratory under Contracts F29601-91-K-DB14 and F19628-89-K-0028, and by Phillips Laboratory (formerly Geophysics Laboratory) of the Air Force Systems Command under Contract F19628-90-K-0049. Contribution No. 5187 and 5200 Division of Geological and Planetary Sciences, California Institute of Technology, Pasadena, California.

Abstract

Bradley B. Woods, Ph.D.

California Institute of Technology 1994

This thesis examines the use of regional surface-wave data to measure the long-period source spectrum of underground nuclear explosions for the purposes of yield determination and seismic discrimination. It is demonstrated that regional ($D < 2500$ km) fundamental-mode Rayleigh and Love waveforms can be modeled with considerable accuracy. The procedure for modeling regional earth structure for such seismograms by inverting surface-wave dispersion data is described. This technique is a hybrid of preexisting surface-wave analysis and inversion methods. Theoretical path corrections are determined from the Green's function for a given modeled path. A method is described to obtain consistent, stable, time-domain surface-wave magnitude (M_S) or seismic moment (M_0) measurements from poorly dispersed regional Rayleigh waves. Source parameters for 190 Nevada Test Site explosions are determined using these methods. Observations demonstrate that the measurement/detection threshold for regional surface-waves is $m_b \geq 4.0$ (Yield = 1 kt)–a significant improvement over classical teleseismic M_S measurements. The results indicate that the M_S (or log M_0) - yield scaling relationship is near unity and constant for explosions of all measurable

sizes. Site effects are also investigated to determine the portability of such surface-wave measurements. Spectral-domain moment estimates also were performed on the digital portion of the data set. Besides obtaining an average scalar moment from Rayleigh wave amplitudes, the isotropic (explosive source) and deviatoric moment (double-couple source generated by tectonic release) components were determined by a joint inversion of Rayleigh and Love wave amplitude and phase data. Although in the most general case the inversion solution is non-unique, constraining the depth of the deviatoric source to be equal to that of the explosion and assuming a vertical strike-slip orientation yields a unique linear inversion solution. The spectral moment estimates are similar to the time-domain values, although the spectral-domain moment variances are appreciably smaller than the time-domain ones. A regional short-period vs. long-period seismic discriminant is developed using the ratio of the seismic moment to local magnitude (M_L). This discriminant successfully separates the explosion and earthquake populations at all measurable source sizes, so that for a given seismic moment source level, an explosion has an M_L 0.5 magnitude units larger than a comparable-sized earthquake.

Table of Contents

1 Introduction to the Study of Long-Period Explosion Seismology 1
1.1 General Introduction 1
1.2 Yield Estimation and Discrimination Methods of the Past and Present 3
1.3 Outline 5

2 Determining Surface Wave Magnitudes from Regional NTS Data 8
2.1 Summary 8
2.2 Introduction 10
2.3 Data 13
2.4 Magnitude Calculation Technique 16
2.5 Data Analysis and Results 36
2.6 Conclusion 64

3 Long-Period Explosion Source Spectra of Regional Surface Waves 68
3.1 Summary 68
3.2 Introduction 69
3.3 Data Processing and Analysis 74
3.4 Path Modeling 90
3.5 Synthetic Seismogram Generation and Moment Inversion Technique . 127
3.6 Results 133
3.7 Conclusion 171

4 M_L:M_0 as a Regional Seismic Discriminant 177
4.1 Summary 177
4.2 Introduction 178
4.3 Data Analysis and Results 186
4.4 Discussion and Conclusions 197

Bibliography 204

List of Tables

2.1 Network Path Corrections 26
2.2 M_S Results 52

3.1 Event Source Information 75
3.2 NTS to JAS Path Model 120
3.3 NTS to PAS Path Model 121
3.4 NTS to RSSD Path Model 122
3.5 NTS to RSON Path Model 123
3.6 NTS to RSCP Path Model 124
3.7 NTS to RSNT Path Model 125
3.8 NTS to RSNY Path Model 126
3.9 Inverted Explosion and Tectonic Release Source Parameters 134
3.10 Explosion Log Moments and Associated Errors 145
3.11 Theoretical Source Inversion Results 150
3.12 Offsets in M_0:m_b Regression Curves for NTS Subsites 164
3.13 Offsets in M_0:Yield Regression Curves for NTS Subsites 172
3.14 Offsets in M_0:Yield Regression Curves for NTS Subsites 173

4.1 List of Earthquake M_L's and M_0's 188
4.2 List of Explosion M_L's and M_0's 190

List of Figures

1.1 Example of small explosions recorded broadband at ALQ 6

2.1 Map of regional super-network 14
2.2 Vertical Component Rayleigh Wave Waveform Comparisons 17
2.3 Schematic of M_S calculation method 23
2.4 $M_S : M_0(PPA)$ regression curve 30
2.5 Time-domain vs. spectral domain moments 34
2.6 m_b vs. yield curve 38
2.7 Comparison of M_S:m_b for various M_S path corrections 41
2.8 Generic path attenuation curves 44
2.9 Comparisons with other M_S studies 47
2.10 M_S variation with distance and azimuthal 50
2.11 M_S vs. m_b regression curves for entire NTS data set 57
2.12 M_S vs. m_b regression curves for Yucca Flats 59
2.13 M_S vs. m_b regression curves for Pahute Mesa 60
2.14 M_s vs. m_b regression curves for combined Pahute+Ranier data set . 62
2.15 M_s vs. log-yield regression curves for aggregate NTS and Yucca Flats data sets 63
2.16 M_s vs. log-yield regression curves for aggregate Pahute Mesa and Rainier Mesa data sets 65
2.17 Floydada regional long-period waveforms 66

3.1 Representative NTS Surface Waves observed at Albequerque, N.M. (ALQ) 79
3.2 Representative NTS Surface Waves observed at Longmire, WA (LON) 86
3.3 Fundamental-Mode Rayleigh Wave Dispersion Curves for JAS 103
3.4 Fundamental-Mode Rayleigh Wave Dispersion Curves for PAS 104
3.5 Fundamental-Mode Rayleigh Wave Dispersion Curves for RSSD . . . 105
3.6 Fundamental-Mode Rayleigh Wave Dispersion Curves for RSON . . 106
3.7 Fundamental-Mode Rayleigh Wave Dispersion Curves for RSCP . . . 107
3.8 Fundamental-Mode Rayleigh Wave Dispersion Curves for RSNT . . . 108
3.9 Fundamental-Mode Rayleigh Wave Dispersion Curves for RSNY . . . 109

3.10 Waveform Comparisons of Love Waves 111
3.11 Waveform Comparisons of Paths Modeled in this Study 112
3.12 NTS to JAS Path Model 113
3.13 NTS to PAS Path Model 114
3.14 NTS to RSSD Path Model 115
3.15 NTS to RSON Path Model 116
3.16 NTS to RSCP Path Model 117
3.17 NTS to RSNT Path Model 118
3.18 NTS to RSNY Path Model 119
3.19 Fault Plane Geometry and Vertical Strike-slip Radiation Patterns . . 128
3.20 Tectonic Release Moment vs. Isotropic Moment 143
3.21 M_0 vs. m_b for all NTS Events 156
3.22 M_0 vs. m_b for Yucca and Pahute Events 159
3.23 M_0 vs. m_b for Pahute and Rainier Events 160
3.24 M_0 vs. m_b for expanded NTS data set 161
3.25 M_0 vs. m_b for expanded Yucca and Pahute data sets 162
3.26 M_0 vs. Log-Yield for NTS events 165
3.27 M_0 vs. Log-Yield for Yucca and Pahute Data Sets 167
3.28 M_0 vs. Log-Yield for Combined Yucca and Pahute Data Sets 168
3.29 M_0 vs. Log-Yield for Expanded NTS Data Sets 170

4.1 Map of Study Area 181
4.2 Examples of Regional Seismic Waveforms 183
4.3 M_L:M_0 plots 194
4.4 Regional Recordings of a Small NTS Explosion 199

Chapter 1

Introduction to the Study of Long-Period Explosion Seismology

1.1 General Introduction

This thesis examines the use of regional surface wave data as a measure of the long-period source spectrum of underground nuclear explosions for the purposes of yield determination and seismic discrimination. Just as seismology is the primary method to remotely sense the Earth's innards, it is also the primary means to monitor underground nuclear explosions, since the successful implementation of any limited or comprehensive test ban treaty would require the ability to monitor potentially uncooperative, unfriendly states from outside of said country. As such the politics of test ban treaties are, in part, inter-related to the capabilities of seismic monitoring technology. The task of nuclear seismology is three-fold: (1) to detect that a seismic event has taken place, (2) to discriminate the event, *i.e.*, to identify a seismic event as being either a nuclear test or an earthquake, and (3) if it is a nuclear test, to determine yield of the explosion. This study focuses on the latter two points, that is yield determination and discrimination.

Before introducing the technical aspects of this research, some background information is provided on the history of nuclear testing and seismic monitoring in the context of motivation for this work. Further background information can be found in Bolt (1976), Dahlman & Israelson (1977), Sykes & Evernden (1982), Hannon (1985), U.S. Congress (1988) and Richards & Zavales (1990).

Due to in-country health concerns, as well as international political pressure, nuclear testing by the U.S. and the Soviet Union developed into underground testing programs. The first underground test was RAINIER, detonated at the Nevada Test Site (NTS) in 1957. After several years of antagonism between the two super-powers over nuclear testing issues, culminating with the Cuban Missle Crisis, the Limited Test Ban Treaty (LTBT) was agreed upon limiting the signatories solely to underground nuclear tests.

Since then negotiations between the two countries centered on affecting a Comprehensive Test Ban Treaty (CTBT) in which tests with yields greater than a certain threshold would be proscribed. Besides political obstacles, the primary issue barring the ratification of a CTBT or Limited Yield Test Ban Treaty (LYTBT) is the yield threshold that could realistically be seismically monitored. The sticking point being that to verify a low-yield threshold (yields less than 10 kilotons (kt)) in-country seismic data would be necessary. For larger yield explosions teleseismic body waves and surface wave measurements are adequate, but for smaller events regional seismic data is necessary. Schlittenhardt (1988) estimates the P-wave detection/measurement threshold for explosions at the various test sites to be between 4.2 and 4.8, corresponding to (approximately) a 10 kt device. The threshold for measuring teleseismic explosion-generated surface waves is even higher. During this time period nuclear proliferation was not a major concern; rather efforts concentrated on the issue of yield estimation in order to infer the composition of the other superpower's nuclear arsenal. As such, discriminating small explosions from earthquakes

was not a critical issue, since for teleseismic monitoring, the m_b:M_s ratio worked well as a discriminant criterion (Marshall *et al.*, 1971) for larger nuclear tests (Y> 20kt).

In 1974 the U.S. and the Soviet Union agreed upon the Threshold Test Ban Treaty (TTBT) limiting explosion yields to 150 kt or less. However, controversy ensued when it was found that the largest Soviet tests in East Kazakhstan had measured body wave magnitudes m_b 0.3 to 0.5 units larger than U.S. explosions. Until this effect was later explained by differential upper-mantle attenuation between the two sites (shield structure for the Soviet site and a tectonic upper-mantle for NTS) giving rise to a m_b bias of 0.38 magnitude units, it helped give rise to the notion that the Soviets were cheating on the TTBT and precluded further progress in nuclear test ban treaties.

With the break-up of the Soviet Union and the end of the Cold War in the period from 1988 to the the present, nuclear proliferation has become the primary concern of most interested parties, so that the focus of nuclear monitoring has changed to global monitoring and discrimination as well. The verification of a world-wide CTBT, as well as military intelligence concerning burgeoning nuclear powers requires lower detection and discrimination thresholds than is possible with teleseismic data, hence attention focused towards regional seismic data for such purposes. The opening-up of the ex-Soviet States has made it possible to deploy a world-wide regional broadband seismic network.

1.2 Yield Estimation and Discrimination Methods of the Past and Present

In the past, the primary means to quantify teleseismic events were with P-wave (m_b) and surface wave (M_s) magnitudes and the ratio of the two made for an effective discriminant. As discussed above, both have measurement thresholds in the $m_b \approx$

4.75 range. Part of the problem with M_s is that it is based on the peak amplitude of the 20 second surface wave. However, at regional distances (less than 1500 km) the predominant pulse is the Airy Phase, which has a period between 8 and 14 seconds and was thought to be unstable because of lateral variability of the crustal waveguide.

Although some attempts were made to incorporate regional surface wave data into M_s measuring schemes, magnitude and discrimination methods using short-period regional phases such as P_n and L_g (see Pomeroy *et al.* (1982) and Bache (1982) for reviews of these methods) were seen as the primary means to monitor low-yield explosions. As short-period seismic monitoring techniques became relied upon, the thrust of advances in instrumentation throughout the 1970's and early 1980's were also in the high frequency band, so regional surface wave studies also suffered because they relied mostly on older analog instruments with low dynamic ranges, making it difficult to uniformly study explosions of all sizes with surface wave data.

The introduction of digital long-period networks in the early 1980's and a new generation of broadband seismometers and high-dynamic-range digital recording systems in the late 1980's came as a boon to regional seismology as well as seismology as a whole. Evernden *et al.* (1971) concluded that with optimal long-period instrumentation, that is an improvement in signal detection by a factor of three over existing long-period World Wide Seismic Network stations in low noise conditions, surface waves from a $m_b = 4$ earthquake could be detected at teleseismic distances. The detection threshold for regional surface waves should decrease significantly as well. Figure 1.1 shows three explosions observed at ALQ, the site of a broadband, high-dynamic range seismometer. The observed displacements have been convolved with a Press-Ewing, 30-90 (long-period) instrument. The lower trace in each case has been butterworth-filtered between 6 and 20 seconds to improve the signal to noise ratio. KEARSARGE ($m_b = 5.5$) is the top-most event. The middle event is Bristol ($m_b = 4.6$). The smallest event, HUNTER'S TROPHY ($m_b = 4.2$), cannot be read-

ily identified on the trace, but after optimal filtering the Airy phase, and possibly later portions of the wavetrain, are observed. ALQ is approximately 900 km away from NTS, yet small surface waves are still detectable and measurable. Note that the peak amplitude for the small event, 0.03 mm would be impossible to detect on older analog instruments. Hence surface wave are, in fact measurable from relatively small (Y< 10 kt) exploosions.

1.3 Outline

This study makes use of this modern long-period data to determine the present day detection/measuring threshold capabilities of long-period surface wave observations of underground nuclear explosions. In an effort to further reduce this operational threshold, methods are developed to measure the long-period explosion source spectrum from regional ($\Delta < 15^o$) surface wave data in a uniform fashion with more distant data. From these results will be derived scaling relationships between yield, magnitude, and seismic moment for explosions.

Chapter 2 investigates time-domain surface wave magnitude and moment measurements. An advantage to such methods is that historical analog events can be easily analyzed and the required signal to noise ratio is minimal, being near unity. Chapter 3 is a study of spectral moment estimate techniques and the effect of tectonic strain release on such measurements. Great effort went into making the explosion data sets for these two studies as extensive as possible in order to achieve reliable statistical results. Previous published surface wave studies have suffered from too few data and/or too narrow a range of magnitude/yield events. Chapter 4 is an investigation of a regional short-period:long-period discriminant using seismic moment

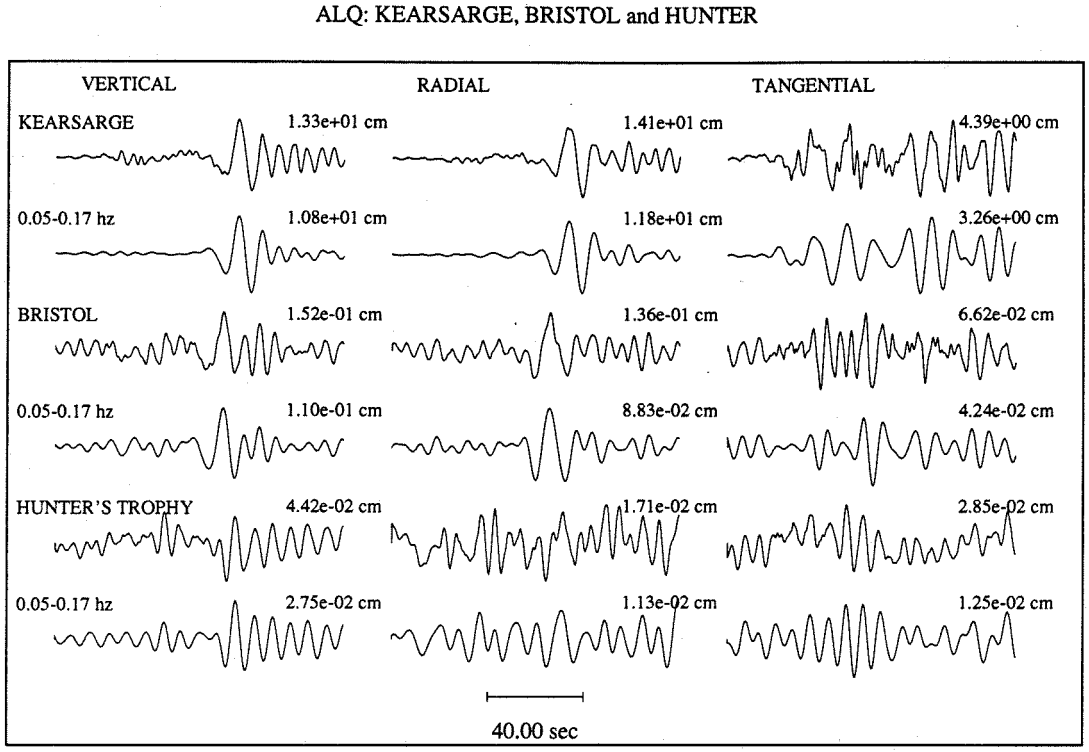

Figure 1.1: Broadband displacement recordings (convolved with a long-period instrument) of a suite of NTS explosions observed at ALQ, over 900 km away. (top) KEARSARGE (m_b = 5.5), (middle) BRISTOL (m_b = 4.6) and (bottom) HUNTER'S TROPHY (m_b = 4.2). The lower trace in each pair has been band-passed-filtered between 6 and 20 seconds.

as the long-period portion of the criterion.

Long-period observations of explosions show less variability between test sites than do short-period observations which are more susceptible to small scale heterogeneities, including near-source effects. With improvements in the detection and measurement of surface waves (and a reduction in the error in such measurements), long-period source spectrum observations can play a significant role in the future of nuclear monitoring, by complementing established short-period seismic methods.

Chapter 2

Determining Surface Wave Magnitudes from Regional NTS Data

2.1 Summary

We re-examine the use of surface wave magnitudes to determine the yield of underground nuclear explosions and the associated magnitude-yield scaling relationship. We have calculated surface wave magnitudes for 190 Nevada Test Site (NTS) shots using regional long-period seismograms from a combined super-network of 55 North American stations. Great effort went towards making the data set comprehensive and diverse in terms of yield, source location and shot medium in order to determine the portability of surface wave magnitude scales. In particular, we examine Pahute Mesa, Rainier Mesa and Yucca Flat explosions detonated above and below the water table, and which range over three orders of magnitude in yield. By observation we find a low-yield measure threshold of approximately one kiloton (kt) for (assumed) moderately well-coupled explosions recorded at near regional (< 500 km), stations which have little microseismic noise. In order to utilize regional surface wave ($\Delta < 15°$) for quantifying sources and for discrimination purposes, we have de-

veloped related methods for determining time-domain surface wave magnitudes and scalar moments from regional Rayleigh waves. Employing regional surface wave data lowers the effective magnitude threshold. One technique employs synthetic seismograms to establish a relationship between the amplitude of the regional Airy phase, or Rayleigh pulse of the Rayleigh wave-train and an associated surface wave magnitude, based on conventional M_S determinations, calculated from a synthetic seismogram propagated to 40°. The other method uses synthetic seismograms in a similar fashion, but the relationship used is a more straightforward one between scalar moment and peak Rayleigh wave amplitude. Path corrections are readily implemented to both methods. The inclusion of path corrections decreases the M_S variance by a factor of two and affects the absolute scaling relationship by up to a factor of 0.1 magnitude units. This latter effect is attributed to the particular station network used and the Green's function used to obtain the 40° M_S values. Using a generic structure for the distance traveled past the actual source receiver path minimizes the difference between magnitudes determined with and without path corrections. The method gives stable M_S values that correlate well with other magnitude scale values over a range of three orders of magnitude in source yield. Our M_S values scale very similarly to more standard teleseismic M_S values from other studies, although the absolute M_S values vary by $\pm$ 0.5 magnitude units. Such differences are due in part to the choice of M_S formula used. Our most refined M_S values give the relationship $M_S = 1.0 \times log_{10}(\text{yield}) + B$, where B is dependent upon source region and shot medium. This yield exponent of unity holds for events of all sizes and is in line with M_S-yield scaling relations found by other studies. When events are grouped with respect to source region, significantly better fits to these individual site linear regression curves are obtained compared to the fits obtained using a single, all inclusive model. This observation implies that shot site parameters and source structure can significantly affect surface wave magnitude measurements.

2.2 Introduction

We re-examine the use of surface waves for determining underground nuclear explosion magnitudes, particularly for smaller yield (Y < 20 kt) events. The surface wave magnitude-yield scaling relationship for such low-yield events is not well defined. Even for larger-yield explosions there is some debate as to the scaling relation between yield and the long-period energy radiation, as well as the relationship between M_S and m_b. Evernden and Filson (1971) found that $M_S = 1.4 + 1.3 \times log_{10}(\text{yield})$ for hard rock sites in North America. Marshall *et al.* (1971) found that M_S scales with yield to the first power, with consolidated rock (tuff, salt, granite, andesite and sandstone) coupling ten times more efficiently than detonations in alluvium. More recently Marshall *et al.* (1979) found that for events detonated in hard rock (salt or granite) or water saturated material (below the water table) that $M_S = 2.16 + 0.97 \times$ log(Y) and that $M_S = 1.88 + 1.06 \times$ log(Y) for explosions above the water table. Taken together these two populations yield the relationship $M_S = 2.05 +$ log(Y) (Bache, 1982). Basham and Horner (1973) found the scaling relationship for explosions in consolidated rock at sites throughout the world (a majority of the events being from NTS) to be $M_S = 1.56 + 1.24 \times$ log(Y). Sykes and Cifuentes (1984) found a world-wide empirical relationship of $M_S = 2.16 + 0.95 \times$ log(Y) for explosions. Murphy (1977) found that the scaling law varied between events larger than 100 kt ($M_S = 1.2 + 1.33 \times$ log(Y)) and smaller events ($M_S = 2.14 + 0.84 \times$ log(Y)).

The above studies utilized data from a suite of sites to determine magnitude-yield relationships. Doing so is likely to add scatter to the results, for the shot medium, the source region, and regional propagation effects may all affect surface wave amplitudes. We sub-grouped our data set into specific source region data subsets in order to ascertain whether or not the separated explosion populations have different magnitude scaling relationships.

The data for this study are long-period vertical component surface wave records

for 190 Nevada Test Site (NTS) events. The stations used are from several North American networks. Their respective instruments all have pass bands that lie within the 6 to 60 second range. Surface waves are very useful for yield estimation purposes, for M_S is determined from relatively long-period seismic waves which are insensitive to high frequency near-source effects, which may be caused by asymmetries in the shot cavity (Zhao and Harkrider, 1991), spall (Taylor and Randall, 1989; Day and McLaughlin, 1991) or other possible mechanisms. These high frequency source effects may cause appreciable bias in magnitudes that are based on higher frequency waves, such as the m_b and L_g scales. There are advantages to using body wave measurements. Teleseismic body waves traverse mantle paths that are relatively homogeneous, whereas surface wave travel in crustal and upper-mantle waveguides which are are known to have strong lateral inhomogeneities.

Evernden and Filson (1971) suggest, based on their observations of body wave and surface wave magnitudes of U.S. underground explosions detonated both within and outside of NTS, that the change in $M_S - m_b$ relationship from site to site is due to abnormal m_b values, rather than abnormal M_S values, and that regional crustal and upper mantle attenuation variations near the source (Δt^*) are responsible for the larger scatter in m_b-yield correlations. M_S measurements are also less sensitive to source depth effects than are body wave measured magnitudes (Marshall and Basham, 1972). If it weren't for contamination due to tectonic release, which has a more pronounced effect on long period surface waves than body waves, and lateral inhomogeneity along the surface wave propagation path near the earth's surface, the long-period energy measured from surface waves might be a more stable measure of seismic yield than teleseismic body wave measurements. It is the purpose of this paper to develop and apply a technique for reducing the contaminating effect of lateral propagation on M_S measurements.

Another advantage of using seismic moment or M_S is that empirical evidence and

theoretical studies show that the scaling relationship between M_S (or log moment) and yield has an approximate slope of unity, *i.e.*, M_S = Log(yield)+B, whereas the m_b-yield and $m_b(L_g)$-yield relationships have slopes between 0.65 and 0.90. As Evernden and Filson (1971) point out, a 0.3 error in m_b corresponds to a 3-fold error in yield determination, while an equivalent error in M_S results in only a 2-fold error in the yield estimate. Thus the error in yield estimation is inherently larger when obtained from higher frequency magnitude measurements.

For lower yield events it becomes necessary to include the data from regional stations ($\Delta < 25°$), for teleseismic surface wave recordings have too low a signal to noise ratio (SNR), which makes them unusable. At regional distances surface waves are not well dispersed, having a prominent Airy phase pulse with a period between 6 and 20 seconds (Alewine, 1972), so that it is not possible to measure M_S conventionally (that is measuring the amplitude of a stable, prominent 20 second surface wave). For North America in general, there is minimum in the group velocity curve near 12 seconds for the fundamental Rayleigh wave (Marshall *et al.*, 1979). To make accurate surface wave magnitude measurements, this energy bandwidth ought to be modeled as well as possible, for it is the predominant signal of the wave-train.

To measure M_S we first model regional Rayleigh waves with theoretical seismograms. These synthetic wavefields are then propagated out to 40°, at which distance, stable 20 second surface wave magnitudes can be measured. In using this procedure several propagation path models were tested to determine the effect of attenuation and seismic velocity structure upon the M_S values. These calculated M_S values remain stable, have reasonably small errors and correlate well with associated m_b magnitudes and log yield for the event data set. The $M_S - m_b$ relationships are determined by a weighted least-squares linear regression; both free and fixed slope curves were fit to the data.

We also determine time-domain moment measurements from the same data. The

moment is determined from the ratio of the maximum peak to peak amplitude of the surface wave train to that of a synthetic, with a given input step moment, propagated to the same distance as the data. These two time domain magnitude measurements (M_S and $\log(M_0)$ give very consistent scaling results.

Besides comparing the M_S results with several different independent magnitude scales, the data have also been separated with respect to source region and shot material. No corrections were made in magnitude for shot medium coupling effects, although such affects can be considerable, even for long-period energy (Werth and Herbst, 1963), because such shot-site information would not necessarily be available for events detonated in other countries. This study is meant to test the effectiveness and portability of a surface wave magnitude scale in the most general case.

We do not account for tectonic release effects upon the magnitude measurements. Such effects are best accounted for with moment tensor inversions of sources which involves more sophisticated data analysis. Standard M_S measurement techniques ignore this factor as well. The effects of tectonic release are considered in the next chapter.

2.3 Data

The data are long-period vertical seismograms recorded at North America stations for 190 explosions at NTS and consist of digitized World Wide Standard Seismographic Network (WWSSN) and Canadian Seismographic Network (CSN) records, Digital World Wide Seismographic Network (DWWSN), Lawrence Livermore Regional Seismic Network (LLNL) and Regional Seismic Test Network (RSTN) digital data. The analog WWSSN and CSN data were digitized by ENSCO Inc. Figure 2.1 shows a map of this 58 station super-network. Epicentral distances range from 220 km for NTS to GSC (Goldstone, California), to 4350 km for NTS to MBC (Mould

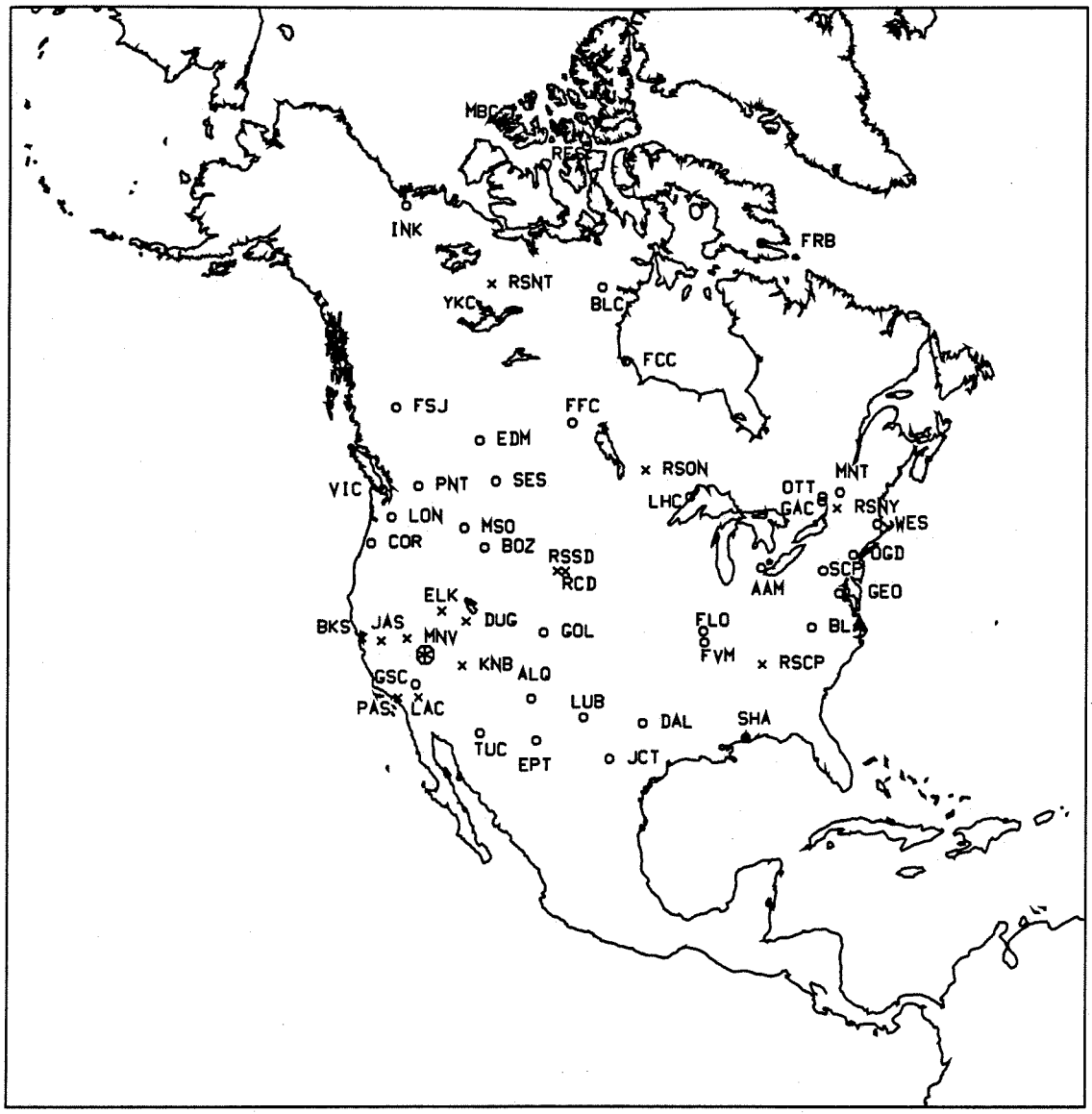

Figure 2.1: Map of North American station network used in this study. The "spoked wheel" is the Nevada Test Site.

Bay, Northwest Territories). For the smaller events, particularly Rainer Mesa explosions, only the nearer stations (distance $<$ 1000 km) had usable data. Station coverage varies widely between events. Twenty-two of the smaller events (or very early events) only had one usable station seismogram each, while some events had over 30. The average number of stations reporting per event is approximately ten. For current and future geographical areas of monitoring interest, it is reasonable to assume that only sparse networks will be able to record any given event, particularly smaller explosions (below 10 kt) or intentionally "muffled" explosions, so it is important to see how well an explosion magnitude can be estimated with only a few observations.

Because our methods for determining magnitudes are done by means of time domain measurements, analog records can be readily used as well. We took advantage of this fact to add considerably more events (72 of the 190) to the sample population. These events were chosen with a mind to filling-out the data set with respect to yield, depth to water table and geographic location.

We chose to confine our study to surface waves traveling solely along continental paths, *i.e.*, within North America. Surface waves that propagate across oceanic-continental margins undergo significant modification in their waveforms because of the great lateral variation in crustal and upper mantle structure at such boundaries. These propagation effects are not straightforward to model, hence meaningful Green's functions, or transfer functions, are difficult to obtain. Without robust Green's functions it is hard to infer accurate source information from the data. Smaller events also are not likely to be observed at the distant stations, which often include oceanic structure along their propagation path, and make these longer paths even less attractive to include in the monitoring network.

Of the 190 events, 48 are from Pahute Mesa, 30 are from Rainer Mesa, 105 are from Yucca Flat and 7 others are from other sites in or around NTS, but outside of the

three major test sites. Of these seven events, PILEDRIVER (detonated at Climax stock) was the only one for which digital data was available. For some specific stations, waveforms varied somewhat between events, depending upon source location. The PILEDRIVER data from a given station look appreciably different from that of any other events recorded at that same station. This was true for every station recording PILEDRIVER and probably is caused by differences in the source region for this explosion. PILEDRIVER was detonated in a granitic source region, north of the other sites. The source to receiver geometries for this event are approximately the same as those as the other NTS events, so the difference in waveforms appears to be a source effect rather than a propagation effect. Because PILEDRIVER was the only Climax Stock event with readily available data, no further examination of this site was carried out.

Figure 2.2 compares representative NTS vertical component long-period data with synthetic Rayleigh waves for each source-receiver path. More than one event was used since no one event was observed at every station. The darker traces are the observations and the lighter trace below each is a synthetic seismogram made with the fundamental mode Rayleigh wave only. The seismograms were band-passed filtered between 6 and 60 seconds to suppress the long period and short period noise which would otherwise affect the peak to peak measurement of the Rayleigh pulse.

2.4 Magnitude Calculation Technique

We have developed a method to measure surface wave magnitudes indirectly. Because a large portion of the data for low yield events is from stations recording at regional distances ($\Delta < 25°$), it is not possible to calculate M_S conventionally, for the Rayleigh wave is pulse-like which precludes measuring a well dispersed 20 second phase (Alewine, 1972). We address this problem with the use of synthetic

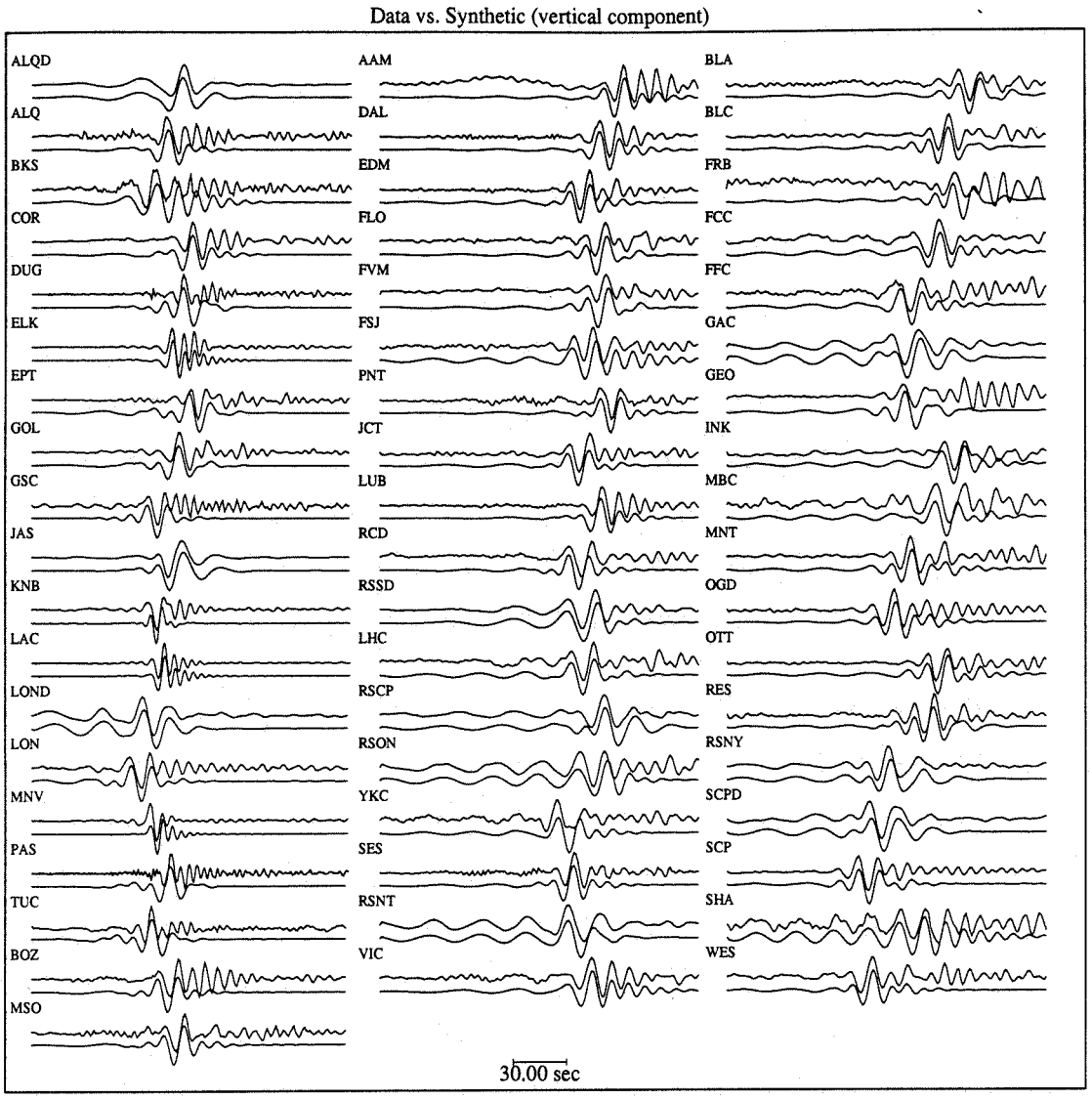

Figure 2.2: Comparison of vertical component fundamental Rayleigh wave waveforms. The data time series are the upper, thicker traces; the lower trace in each case is the fundamental mode synthetic. All time series band-passed between 60 and 6 seconds.

seismograms of the fundamental-mode Rayleigh wave using an asymptotic relation for mixed-path surface waves.

For our mixed-path expressions, we follow Levshin (1985) and write the spectral Rayleigh wave vertical displacement for approximate propagation in a slowly varying laterally inhomogeneous media (*e.g.*, Burridge and Weinberg, 1977; Babich *et al.*, 1976; Woodhouse, 1974, and Yomogida, 1985) as

$$w_0 = \frac{\exp(-i3\pi/4)}{\sqrt{8\pi\omega}} \frac{\exp\left[-i\omega \int_{P_0}^{P} ds/c\right]}{\sqrt{[J]_P}} \exp\left[-\int_{P_0}^{P} \gamma ds\right] \left[\frac{1}{\sqrt{UI}}\right]_P \left[\frac{W}{\sqrt{UIc}}\right]_{P_0} \quad (2.1)$$

where the energy integral is

$$I = \int_0^\infty \rho(z)[y_1^2 + y_3^2]dz, \quad (2.2)$$

$\rho(z)$ is the local density distribution in the medium and we have used Saito's (1967) Rayleigh wave eigenfunction notation, $y_i(z)$. The eigenfunctions are normalized in such a way that the vertical displacement eigenfunction, $y_1(z)$ is equal to 1 at the free surface, $z = 0$. This results in the horizontal displacement eigenfunction, $y_3(z)$, being equal to the Rayleigh mode surface ellipticity at this boundary. U and c are respectively the local group and phase velocities. By local we mean the eigenvalues and eigenfunctions that one would obtain for a laterally homogeneous half-space consisting of the vertical elastic and density distribution at that location. P is the receiver location and P_0 is the point source location and quantities within the P or P_0 subscripted square brackets are evaluated at these locations. The integrals are taken along the ray path between the two surface locations. J describes the geometrical spreading of the surface wave energy. γ is the frequency-dependent distance attenuation coefficient due to the anelastic structure of the path. The above expression is applicable in the absence of foci or shadow zones in the vicinity of the receiver. If there are foci along the path, an additional phase factor of $\exp(i\pi/2)$

should be included for each foci. For an explosion, W is

$$W = M(\omega)\left[\frac{dy_1}{dz} - \frac{\omega}{c}y_3\right] \tag{2.3}$$

where $M(\omega)$ is the isotropic or explosion spectral seismic moment. We also assume a step for our explosion history, *i.e.*, $M(\omega) = M_0/(i\omega)$.

Since we will assume that the directions of the horizontal gradients of the material properties are approximately aligned in the direction of the source to receiver, the ray path is a straight line and $J = r$, which is the distance between the two locations. We further assume that the lateral inhomogeneity can be considered to be made up of n homogeneous segments of radius r_i, *i.e.*, $\sum r_j = r$. For comparison with Stevens (1986), who used a similar expression to estimate seismic moments for explosions, and earlier works on which his expressions were based (*e.g.*, Bache *et al.*, 1978, and Harkrider, 1981), we write W in terms of K where

$$K = y_3(z) - \frac{c}{2\mu\omega}y_2(z) \tag{2.4}$$

and y_2 is the normalized vertical normal stress eigenfunction. The relation between K and W is obtained by substituting

$$\frac{dy_1}{dz} = \frac{1}{(\lambda + 2\mu)}\left[y_2 + \frac{\omega}{c}\lambda y_3\right] \tag{2.5}$$

into the previous W expression.

Now we can write the multipath dispacement as

$$w_0 = -\frac{\exp(-i3\pi/4)}{\sqrt{2\pi\omega}}\frac{\beta_1^2}{\alpha_1^2}\frac{M_0}{c_1}\frac{\exp\left[-i\omega(r_j/c_j)\right]}{\sqrt{r}}\exp(-\gamma_j r_j)\left[\frac{1}{\sqrt{UI}}\right]_n\left[\frac{K}{\sqrt{UIc}}\right]_1 \tag{2.6}$$

where the summation convention of repeated subscripts is used. The 1 subscript denotes the local quantities for the source medium, and the n subscript, the local quantities at the receiver. The shear velocity is denoted by β, and the compressional velocity, by α. For a given moment, M_0, the ratio of the square of these two quantities plays a key role in determining the amplitude effect of various shot media. To

this order of approximation the spectral amplitude neglecting attenuation is only dependent on the local properties at the source and receiver. The attenuation and phase are dependent on the local properties along the whole path.

With the substitution

$$\mathbf{A} = \frac{1}{2cUI} \tag{2.7}$$

(Harkrider and Anderson, 1966 and Harkrider, 1981) and multiplying by $-\sqrt{c_n/c_1}$, we obtain the same expression as used by Stevens (1986) to obtain his path corrections from NTS to 24 WWSSN station in United States and Canada and to 12 SRO stations. For his models $n = 2$. The negative sign results from the differences in our sign criteria for vertical displacement. In Stevens (1986) vertical displacement is positive up while in this article it is positive down. The phase velocity factor is due to the use of wavenumber spreading by Bache *et al.* (1978), Harkrider (1981), and Stevens (1986) compared to geometric spreading by the others. Bache *et al.* (1978) based their expressions on the conservation of lateral energy flux while these expressions are from the main term in an asymptotic expansion.

Glover and Harkrider (1986) performed numerical tests in order to estimate the frequency range for which these approximations were valid for Rayleigh waves generated at NTS where the source region may be limited by sharp boundaries such as in the low velocity basin at Yucca Flat. Rayleigh wave seismograms were calculated for explosive sources at depth in a finite vertical cylinder with contrasting elastic properties representative of the various test areas at NTS embedded in a vertically stratified propagation media. The technique couples laterally inhomogeneous finite-element calculations of the source region with Green's functions for teleseismic Rayleigh waves using the elastodynamic representation theorem. The details of the technique can be found in Harkrider (1981) and Bache *et al.* (1982). The spectra for these Rayleigh waves were then compared with those, which used the two approximations to cross the sharp boundary. It is surprising that both approximations worked

as well as they did since they are based on gradual transitions. It was found that both approximations worked equally well for periods greater than four seconds and that for shorter periods the asymptotic approximation used in this paper is better. The period range is dependent on the material contrast and the vertical extent of the contrast, but this mixed-path approximation is certainly adequate for the determination of long period moments and surface wave magnitudes from NTS Rayleigh wave observations at continental stations.

It is interesting to note that for this geometry, *i.e.*, $n = 2$ the Rayleigh wave transmission coefficient, $T(\omega)$, of Bache *et al.* (1978),

$$T(\omega) = \left(\frac{c_2 \mathbf{A}_2}{c_1 \mathbf{A}_1}\right)^{1/2} = \left(\frac{U_1 I_1}{U_2 I_2}\right)^{1/2} \tag{2.8}$$

is identical to the factor R of Levshin (1985) and was used in both articles to illustrate the effect of mixed-paths on the amplitude of Rayleigh waves.

For each source to receiver path, a theoretical Rayleigh wave is generated. The Earth model used to create this synthetic is meant to reflect the average Earth structure between NTS and the given station. The Earth models used in this study were determined from inversions of dispersion and attenuation data as well as forward modeling of the waveform to fine tune the models. The criteria for determining the goodness of fit of the synthetic to the data are dispersion, absolute travel time and waveform fit (relative amplitude of different dispersed phases). Hence the synthetic seismogram displays the same spectral and time domain waveform characteristics as the data which it simulates (see Figure 2.2). This was done for all paths. The paths to WWSSN and Canadian stations were taken from the explosion moment study by Stevens (1986). We determined the RSTN, LLNL and DWWSN path structures.

To determine M_S for a particular source-receiver geometry, two synthetics are generated: one which is propagated the actual path distance that is meant to simulate the data and one which is propagated to 40°. At 40° the surface wave train is well dispersed and stable, so that a conventional M_S value can be calculated. Figure 2.3

illustrates this method. The upper set of seismograms are a comparison of data to its corresponding synthetic seismogram. For this particular example the station COR (Corvallis, Oregon) and the event LOWBALL are used. The data is the solid line and the dashed line is the synthetic time series. Note that the waveform fit (dispersion and relative amplitude) is exceptional. This feature is important in order to make maximum peak to peak amplitude comparisons. The middle figure schematically shows the propagation paths for the synthetic seismograms. The path of length R is the actual source to receiver distance. The longer path is of length 40°. The bottom figures are of the two synthetic seismograms. The left one is calculated for the distance R (10.4° in this case) and the right seismogram is the one propagated out to 40°. They are plotted to the same time scale. Note the much better dispersed wave train in the 40° case. The arrows in the right-hand figure mark the cycle or phase of the record which is used to obtain an M_S value.

To calculate M_S we use a modified version of the Von Seggern formula (Von Seggern, 1977):

$$M_S = \log_{10}(A/T) + 1.08 \times \log_{10}(\Delta) + 4.38, \tag{2.9}$$

where A is one-half the maximum peak to peak amplitude (in microns) for periods between 17 and 23 seconds of a well dispersed wave train measured from the vertical record, T is the period of the arrival measured in seconds, and Δ is the propagation distance in degrees. This formula was chosen because the distance coefficient (1.08) more closely approximates the effect of attenuation along continental paths (Basham, 1971, and Marshall and Basham, 1972). Evernden (1971) found the distance coefficient to be 0.92 for M_S measurements at less than 25° and 1.66 for measurements at greater distances. This latter attenuation coefficient is more characteristic of mixed continental-oceanic path 20 second surface waves. Basham (1971) also found that the surface wave magnitude distance coefficient for regional Rayleigh waves ($10 < T < 14$ seconds) is between 0.7 and 0.8. Marshall and Basham (1972) make similar

Figure 2.3: Schematic of the Ms Calculation Method: (a) The top figure is a comparison of observed to synthetic seismograms for the event Lowball recorded at the WWSN station COR ($\Delta = 10.4^o$). This record shows a prominent Airy phase with a dominant period that is considerably less than 20 seconds. The solid line is the observed time series, and the dashed line is that of the synthetic seismogram. Both time series have been band pass filtered between 60 and 6 seconds. (b) The middle figure shows the paths for which synthetic Rayleigh waves are calculated. There are two receiver distances. One, R, is the distance between the actual receiver and the source. The other distance is 40^o. A synthetic generated for the distance R is made with a structure which best models the regional seismogram. (c) The bottom two figures show synthetic seismograms calculated for the two receiver distances for the COR path model. The left-hand one is for the actual regional path distance R; it is flipped in polarity with respect to the same synthetic in the top figure. The right-hand one is a Rayleigh wave propagated to 40^o; the arrows denote the pulse that is used to calculate M_S. Notice that the dominant period for this case is 17.5 seconds. This pulse is considerably closer in period to 20 seconds than that of the regional seismogram which has a period near 12 seconds.

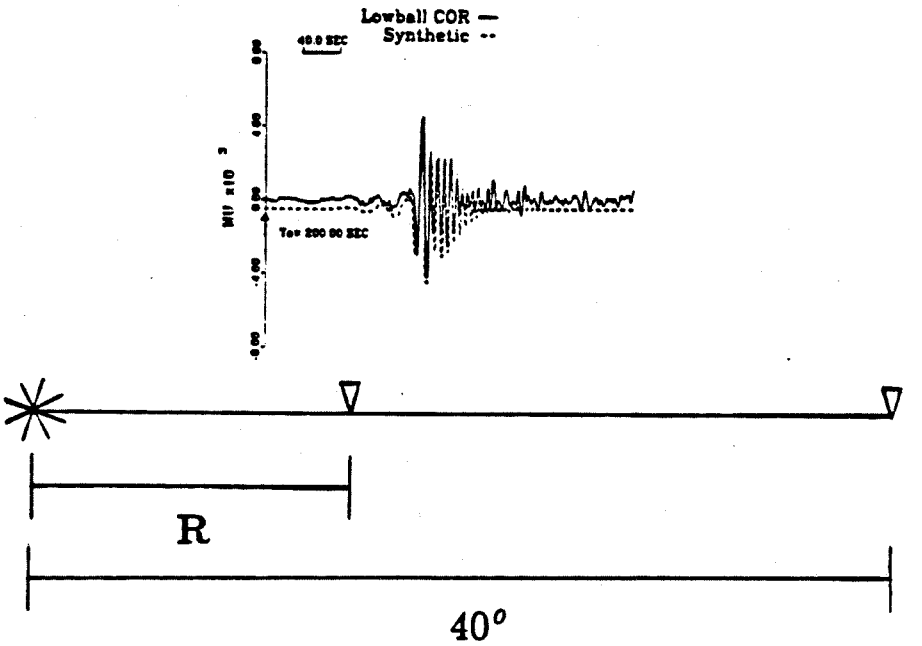
Lowball COR —
Synthetic --
R
40°

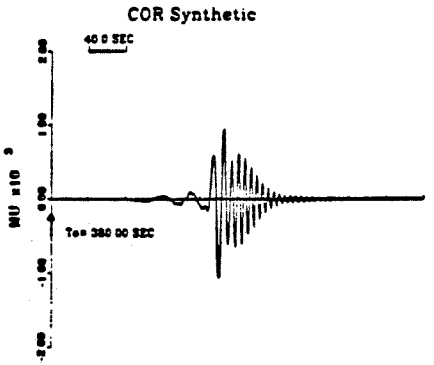
COR Synthetic

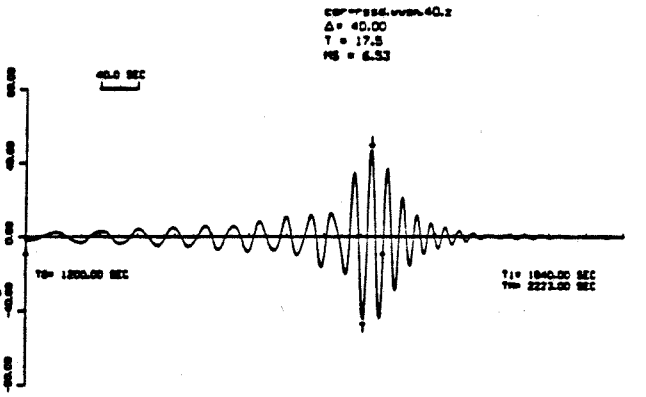

assertions, but employ a distance correction which is a function of period as well.

A vertical component measurement has two advantages over horizontal component measurements. The horizontal components usually have lower signal to noise ratios than the vertical component and generally are more likely to be contaminated by Love wave signals which may be generated by tectonic release, source effects, or scattering due to lateral variations in the Earth's structure. Both the regional and teleseismic (40°) synthetics are generated with the same site and source function, so that the peak to peak amplitude of the Rayleigh pulse of the regional synthetic can be directly related to the M_S value determined for a theoretical Rayleigh wave train propagated out to 40°. The relationship between the data peak to peak amplitude (PPA) and its indirectly determined M_S is:

$$M_S(data) = M_S(synth|_{40°}) + \log_{10}[(PPA|_{data})/(PPA|_{synth})], \qquad (2.10)$$

where PPA is the peak to peak amplitude of the Rayleigh pulse. A path correction may be included in this expression. This path correction is the difference between the individual path synthetic derived M_S and the average theoretical M_S for the entire network. It also differs from a classical station correction which comes from the data and not the synthetics. For each source-receiver pair, an M_S is calculated from a synthetic seismogram propagated to 40°. Each such synthetic has the same site and source size, so ideally one would want each M_S value so measured to be equal in value. Yet this is not so, for each path's dispersion and effective attenuation at the periods measured may be different. The difference between the mean network synthetic M_S and a particular receiver M_S is the path correction. A negative path correction value implies that the theoretical 40° station M_S is larger than the network average. Table 2.1 lists the network path corrections used.

The question arises, whether or not it is valid to use the average Earth structure for a particular path to propagate a surface wave to 40° when the Earth model is only meant to reflect the seismic properties of the Earth for a path that may

Table 1: Network Path Corrections

Dominant Period	Path Correction Dispersion	Path Correction Single Path	Path Correction Mixed Path 1	Path Correction Mixed Path 2	Station Name
11.5	-0.64	0.20	-0.07	-0.11	AAM
12.0	-0.61	0.18	-0.02	0.17	ALQ
13.5	-0.50	0.57	0.08	0.27	BKS
15.0	-0.38	-0.24	-0.28	-0.32	BLA
10.5	-0.71	0.18	0.00	-0.47	BLC
11.0	-0.67	-0.26	-0.02	0.16	BOZ
11.5	-0.64	-0.12	0.07	0.14	COR
11.0	-0.67	0.35	-0.12	0.09	DAL
12.0	-0.61	-0.03	-0.02	0.19	DUG
11.0	-0.67	-0.26	0.10	0.03	EDM
11.2	-0.66	0.26	-0.03	0.20	ELK
12.0	-0.61	-0.03	-0.03	0.12	EPT
12.0	-0.61	-0.22	0.06	0.01	FCC
12.5	-0.57	-0.22	-0.02	0.01	FFC
12.0	-0.61	-0.24	-0.12	-0.09	FLO
11.5	-0.64	0.18	0.18	-0.02	FRB
13.5	-0.50	0.45	0.20	0.25	FSJ
11.5	-0.64	-0.24	-0.12	-0.09	FVM
16.0	-0.30	0.18	0.40	-0.29	GAC
15.0	-0.38	-0.24	-0.15	-0.47	GEO
11.5	-0.64	-0.11	0.03	0.08	GOL
11.0	-0.67	0.26	-0.04	0.22	GSC
12.0	-0.61	-0.40	-0.11	-0.23	INK
11.0	-0.67	0.18	0.04	0.13	JCT
11.2	-0.66	1.06	0.02	0.26	KNB
11.2	-0.66	0.26	-0.05	0.20	LAC
12.5	-0.57	-0.13	-0.01	0.00	LHC
11.0	-0.67	0.20	0.01	0.17	LON
11.5	-0.64	-0.19	0.06	0.03	LUB

Table 2.1: Network M_S path corrections. The dominant period refers to that of the peak amplitude Airy Phase wave and the second column is the Marshall and Basham (1972) continental North American path correction for that period.

Table 1: Network Path Corrections (cont.)

Dominant Period	Path Correction Dispersion	Path Correction Single Path	Path Correction Mixed Path 1	Path Correction Mixed Path 2	Station Name
12.5	-0.57	-0.44	0.26	0.06	MBC
11.5	-0.64	0.18	0.37	-0.39	MNT
11.5	-0.64	0.26	-0.04	0.22	MNV
11.0	-0.67	-0.26	-0.03	0.14	MSO
10.5	-0.71	0.16	0.30	0.19	OGD
11.5	-0.64	0.18	0.40	-0.28	OTT
12.5	-0.57	1.12	0.03	0.27	PAS
11.0	-0.67	-0.26	-0.03	0.11	PNT
11.0	-0.67	-0.26	-0.04	0.10	RCD
11.5	-0.64	-0.39	-0.39	-0.59	RES
11.0	-0.67	-0.53	-0.17	-0.31	SCP
11.0	-0.67	-0.26	-0.05	0.07	SES
12.5	-0.57	0.03	0.04	0.09	SHA
11.5	-0.64	-0.03	-0.04	0.15	TUC
11.5	-0.64	0.45	0.16	0.27	VIC
11.5	-0.64	0.22	-0.30	-0.41	WES
12.5	-0.57	-0.40	-0.20	-0.23	YKC
19.5	-0.04	0.18	-0.02	0.17	ALQD
16.5	-0.27	0.20	0.01	0.17	LOND
16.5	-0.27	-0.53	-0.17	-0.31	SCPD
15.0	-0.38	-0.51	0.02	0.02	RSCP
16.0	-0.30	-0.09	-0.05	0.09	RSSD
15.5	-0.34	-0.19	-0.07	-0.05	RSON
16.0	-0.30	0.18	0.33	0.22	RSNY
15.5	-0.34	-0.40	-0.20	-0.23	RSNT
18.0	-0.16	1.21	0.01	0.19	JAS

only be a small fraction of this distance. This is particularly true of the shortest paths for which the seismic waves traverse only Western, North America, an area of relatively high attenuation compared to the continental craton and shield areas. A surface wave propagated 40° along a characteristic tectonic North American crust and mantle model (NTS to DUG, for example) for 40° will be much more attenuated than a wave propagated the same distance through an average structure from NTS to Eastern North America (NTS to SCP, for example). Hence the calculated M_S for the NTS to DUG structure would be smaller than the NTS to SCP M_S.

There are several methods to correct for this path dependent effect. As explained above one may implement path corrections which account for the theoretical difference in attenuation between paths. Another means is to make a mixed-path structure which has the appropriate path structure from the source to the actual station distance, with the rest of the path out to 40° being a generic seismic velocity and attenuation model. For the cases in this study where the structures which comprise the mixed-path are both continental structures (*i.e.*, not too dissimilar) the approximation is robust enough for the synthetic seismogram calculations.

We have implemented both procedures individually and in conjunction to see what their effects are. Another method would be to include empirical station corrections (Yacoub, 1983, Given and Mellman, 1986). Path correction effects are discussed in the results section.

Besides the M_S determination, we also calculated a time domain moment for the same data. This time domain, scalar moment is determined as follows:

$$M_0(data) = M_0(synth) \times [(PPA|_{data})/(PPA|_{synth})], \qquad (2.11)$$

where PPA is the peak to peak amplitude of the Rayleigh pulse or Airy phase. This method is simpler than the M_S method and has the added advantage that the synthetic involves only two structures: the source region and the propagation path to the station. Path corrections were not incorporated into the time domain

M_0 determinations since the propagation path synthetic takes the place of a path correction, and we are not correcting to a generic (RSSD) structure. Making a correction based on the difference between the average station value and some mean for a collection of events is a form of the classical empirical station correction and is most useful when there are only a few stations reporting since a zero sum of the corrections is the usual constraint (Given and Mellman, 1986). The mean moment can then be converted to an M_S using the moment-M_S relation for the generic structure (RSSD) propagated to 40°, *i.e.*,

$$M_S(PPA) = \log M_0(PPA) - 11.38. \tag{2.12}$$

Figure 2.4 plots M_S vs. $M_0(PPA)$ for the entire data set. The correlation between the two types of magnitude measurements is extremely good. The regression constant 11.42 is very close to the theoretical value 11.38 given above. Thus the difference between our best mixed-path M_S regression with moment, and the M_S - moment relation for a pure path of the generic RSSD model is only 0.04 magnitude units. On first glance it might appear that both techniques are identical. This would be true if we didn't make the additional correction to a mean of the theoretical values for all stations in the mixed-path evaluation. These observations imply that the RSSD model is a good average model for the network and that our M_S calculations are sound and result in robust measurements of surface wave magnitude, which are not too dependent on which of the two techniques we use. In our analysis of the data, we will use only M_S measurements. A table of the $\log M_0$ and their standard deviations will be given in chapter 3.

Source structure significantly affects absolute surface wave amplitudes, hence surface wave magnitudes or moments. For all of the synthetic seismograms generated, we used the Stevens (1986) and Given and Mellman (1986) NTS source elastic structure, which is basically a Pahute Mesa velocity structure. By numerical simulations using a variety of different NTS structures, we found that for the frequencies of inter-

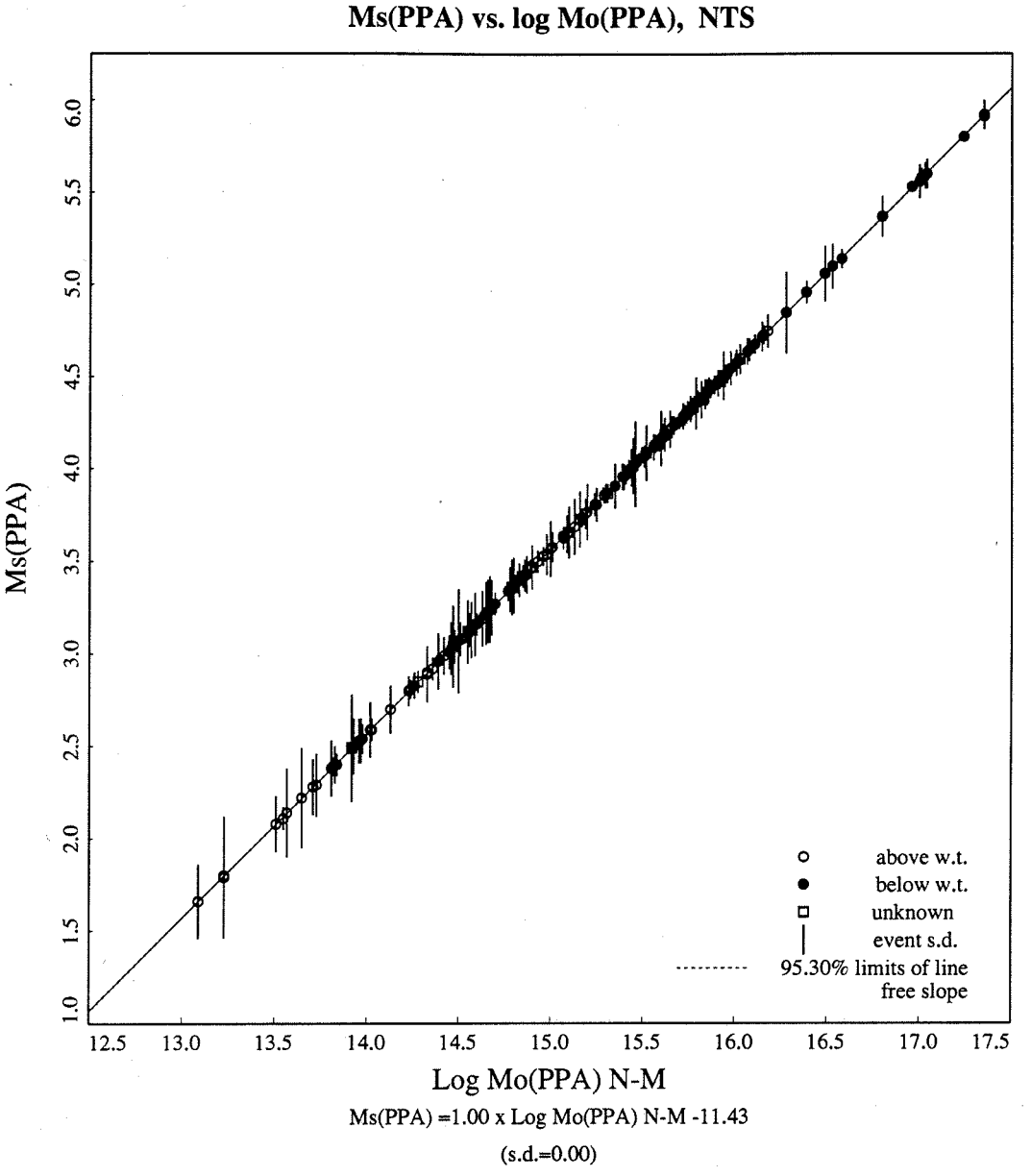

Figure 2.4: Time domain M_S values regressed vs. time domain moments for all the events in this study. Note the extremely good correlation between the two scales. Vertical error bars are the variance for the indivudal events.

est and sources in the upper 6 kilometers, the primary effect was due to the difference in shot point velocity ratios. The size of the effect can be predicted extremely well from their explicit presence in the mixed-path expression, equation 2.6. As an example, our Green's functions are computed for an explosive source at a depth of 600 meters. In the Stevens (1986) source structure, the second layer starts at a depth of 500 meters. There is a significant difference between the Poisson's ratio of the surface and second layer in the source earth structure. The log difference between the square of their compressional to shear velocities would predict from equation 2.6 an M_S difference of 0.17. The actual difference between the Ms of a surface explosion and our Green's function is 0.16 with the near surface explosion smaller as predicted. In order to reduce the effect of differing shot point velocity ratios, Stevens (1986) suggested a new explosion moment, M_0', defined by

$$M_0' = 3\frac{\beta^2}{\alpha^2}M_0 \tag{2.13}$$

For a shot point medium with Poisson's ratio of 0.25 (α^2/β^2=3), the value of the moment is unchanged.

In figure 2.2, we see that for the WWSSN stations, denoted by three letters, the period of the dominant phase is significantly lower than the recommended lower cutoff of 17 seconds for the standard M_S formula. This period was determined by taking twice the time difference between the arrival of the largest peak and trough. We also calculated the 'instantaneous period' of this arrival and found it to be essentially the same value. The dominant period at each station is given in Table 2.1. For the WWSSN stations, the periods are between 10 and 15 seconds. Most are near 11 seconds. For the digital stations, denoted by four letters, the dominant period is between 15 and 19.5 seconds, with the average being 16.5 seconds. An alternate approach for using the maximum amplitude of Rayleigh wave observations, where the dominant period is significantly different than 20 seconds, was developed by Marshall and Basham (1972). Using the stationary phase approximation, they determined a

path correction which corrected for the dispersive characteristics of the path. Using observed dispersion curves for North America, Eurasia, mixed ocean-continent, and pure ocean paths, they were able to determine an M_S correction based on the period of an observed Airy phase to the 20 second period arrival in North America or Eurasia. Their North American dispersion correction appropriate for the dominant period measured at each station in our network is also given in Table 2.1 (column 2). An advantage of our technique is that our path corrections are independent of recording instrument, whereas Marshall and Basham's correction depends on the dominant period, which depends not only on dispersion but also instrument response. As an example, the station ALQ has a dominant period of 12 seconds and ALQD has a dominant period of 19.5 seconds.

An advantage that time domain estimates of M_S or M_0 have over spectral estimates can be seen in figure 2.2. Except for the work of Patton (*e.g.*, Patton, 1991), the Green's functions used for spectral estimates of explosions have been fundamental Rayleigh and Love waves. As can be seen from the figure, it is very important to isolate the fundamental surface wave in the data before taking its spectra for moment estimates. The Rayleigh waves at almost every station show the additional presence of higher modes. The higher modes are primarily due to constructive interference of multiple reflected shear waves and are, therefore, very sensitive to lateral variations in crust and upper mantle structure. This is especially true for non-parallel layers with sharp contrasts. Therefore, in the presense of nearby signals or noise, it makes more sense to use the larger time domain amplitudes of the fundamental-mode Airy phases at regional distances. Because of the possibility of tectonic release, it is also necessary to determine the polarity of the surface wave. Again this is best done in the time domain, especially for Love waves.

If a spectral estimate is desired, comparing the Green's function with the data in the time domain should allow one to determine time windows and tapers so as reduce

the contamination of spectral amplitude estimates with higher modes and spurious scattered arrivals at intermediate ranges. And at close ranges where this may not be possible, it should help in deciding which time domain amplitude measurements best represent the spectral amplitudes of the fundamental-modes.

The question remains how well do either of these two measurements compare to spectral moment estimates. For the events for which digital data were available, spectral-domain moments were also determined. Spectral moments were calculated using the method of Stevens (1986), with the exception that station corrections were not included in our moment calculations. Spectral moments were calculated in the band-width between 6 and 60 seconds. These spectral moments will be referred to as M_0. Moments were also obtained by inverting for an isotropic (explosion source) component (M_I) and a deviatoric component (caused by tectonic release or an asymmetric source cavity) of moment ($M_\#$). Details of these moments are the subject of chapter 3.

The time-domain moments are compared with these two types of spectral-domain moments. Figure 2.5a compares $M_0(PPA)$ to $M_0(\omega)$ and figure 2.5b compares $M_0(PPA)$ to $M_I(\omega)$. $M_0(\omega)$ refers to the average spectral scalar moment, and $M_I(\omega)$ refers to the isotropic source component determined from a moment tensor inversion scheme (chapter 3). $M_0(PPA)$ correlates well with the two types of spectral moments. The advantage to time-domain moments is that analog data can be used directly and the SNR necessary for such measurements is lower than that for spectral moment methods, thus smaller events can be measured.

In the top figure there is some scatter in the moment correlation for several of the smaller events, with the time-domain moments being significantly larger than the spectral-domain moments. Most of these outlying events are Rainier shots; none are from Yucca, and only one, REX, is from Pahute. REX ($M_S(PPA)$=3.91) was detonated below the water table and had an anomalously large deviatoric moment

Figure 2.5: Time domain log moments regressed against spectral domain moments. In the top figure spectral moments were determined assuming an isotropic source only, while in the bottom figure the spectral moments were determined by inverting for an isotropic source + a double-couple source. The regressions were constrained to a slope of unity.

Mo(PPA) vs Mo(spectral)

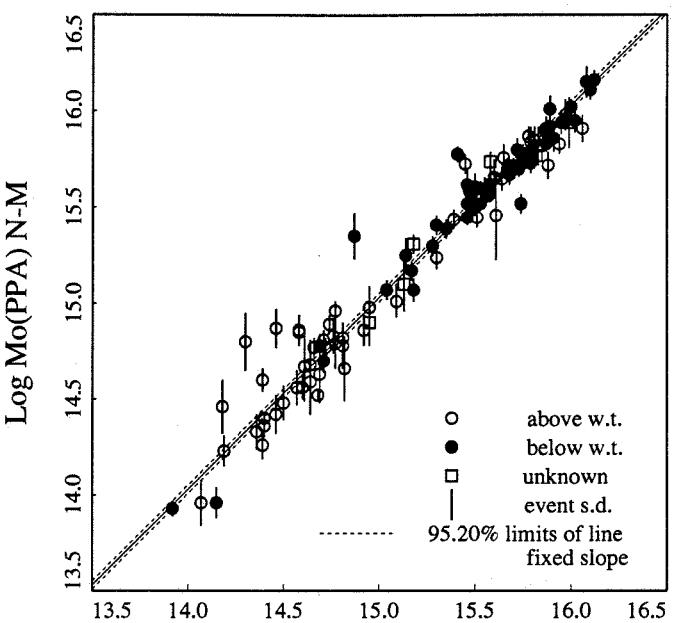

Log Mo(PPA) N-M =1.00 x Log Mo(spectral) N-M + 0.03

(s.d.=0.11)

Mo(PPA) vs Mi(spectral)

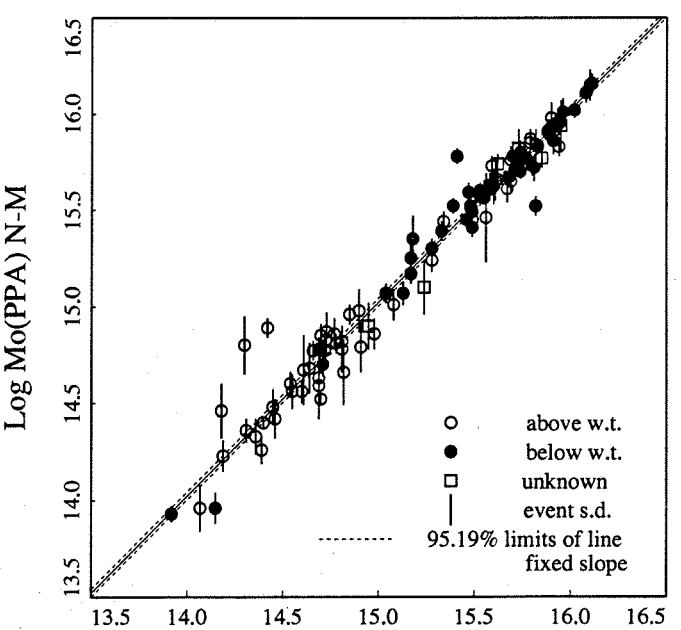

Log Mo(PPA) N-M =1.00 x Log Mi(spectral) N-M + 0.02

(s.d.=0.10)

component (chapter 3). It may be that the spectral moment is more sensitive to the secondary source than is the time-domain moment. The scatter is somewhat less in the $M_0(PPA)$:$M_I(\omega)$ curve (figure 2.5b). In particular, REX no longer stands out, although several of the Rainer events lie well off the scaling curve. These outlying Rainier events can be explained in two ways. First, these events are relatively small and are only measured at very few stations (sometimes only one to three stations), thus the scatter, or error, in the moment measurement is larger. One problem with this explanation is that there are other small events recorded at Pahute Mesa and Yucca Flat that lie right on the moment scaling curve (Figure 2.5a), and these events are no better recorded than the Rainier events. The other possibility is that these outlying events reflect differences in source spectra. As discussed previously the time-domain moments measure energy predominantly in the 10-14 second range, the period range of the continental Airy phase, whereas the spectral moment is an average of the spectral ratio between 6 and 60 seconds. So, it is possible that the Rainier test sites excite more high frequency energy than do either the Pahute or Yucca sites. This effect was seen in data at several of the closer stations, in particular.

2.5 Data Analysis and Results

The seismograms were band-passed filtered between 6 and 60 seconds to minimize contaminating noise as described previously. The vertical records were visually inspected to insure that the correct time window was used and that their signal to noise ratio was above 2.0 (approximately). M_S values were then calculated for the data as per the method described above (equation 9) with several variations. The synthetic seismograms were also band-passed filtered between 6 and 60 seconds for consistency. The M_S values are plotted against seismic magnitudes of several scales for the same set of events. It should be noted that no complete magnitude list was

available for all 190 events.

We chose to compare or plot our data primarily with body wave magnitudes determined by Lilwall and McNeary (1985). The Lilwall-McNeary (LM) data set contains 143 of the 190 events examined by us and is believed to be a well determined and self-consistent list of m_b values that have small errors due to, among other things, the inclusion of network station corrections. Figure 2.6 shows the m_b-yield relationship for events in this study for which m_b and yield information were available. It is important to notice that events above and below the water table separate into two distinct populations. For this data set this separation is only apparent near the cluster of events with m_b's around 5.4. Also notice the very small error bars for this data; for many events the error bars are smaller than the symbols demarking a data point. The solid line is the best-fitting, least squares curve, with the dashed curves being the two sigma confidence interval of the regression relationship. The correlation between m_b and yield is good, with the scatter mostly being due to the above water table shots. The slope of the regression curve is 0.67.

This scaling curve slope is slightly lower than that found in other studies of teleseismic m_b-yield scaling relationships. Marshall *et al.* (1979) found that m_b was proportional to $Y^{0.74}$ for well-coupled Yucca flat explosions, and proportional to $Y^{0.78}$ for explosions throughout NTS and Amchitka. Longer period teleseismic body wave magnitudes m_{LPP} introduced by Basham and Horner (1973) show that for events in tuff and rhyolite, the amplitude of the arrivals is proportional to $Y^{0.72}$. Murphy (1977) compared theoretical m_b-yield scaling relations for cube-root scaling models and the modified Mueller and Murphy (1971) source model. He found that the yield exponent varies between 0.6 and 1.0 for the cube-root model in the yield range of interest, whereas the exponent is a constant 0.85 for their modified source model. Schlittenhardt (1988) found m_b to be proportional to $Y^{0.82}$ for NTS explosions. The empirically derived curves have errors in their slopes on the order of 0.05 to 0.1 units

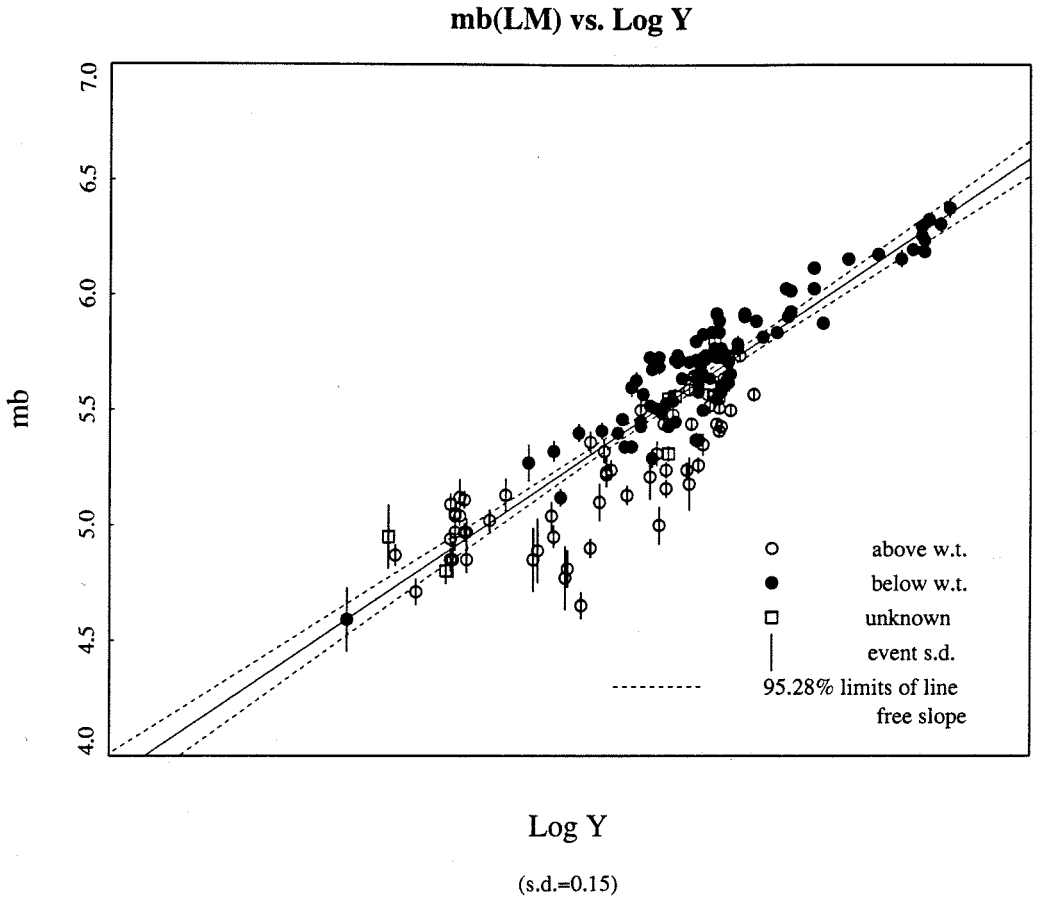

Figure 2.6: $m_{b(LM)}$ vs. log-Yield for events from this study. The solid line is the best-fitting regression line. The dashed lines show the 95 percent confidence interval of this line. Lines through the data points represent one standard deviation in a datum measurement. Blackened cirlces represent sources beneath the water table, open circles are events above the water table and open squares are events for which this information is not known. Events detonated below the water table have a larger m_b for a given yield. Besides this separation of data, there is little scatter to the data. The consistency of the m_b-yield relationship makes it reasonable to use these m_b values to plot our M_S measurements against.

and are based on small sampling populations. The LM m_b-yield scaling relationship is determined from a significantly larger data set, making it at least as reliable as any other empirical scaling curve.

The same scaling law slope ($\sim$ 0.67) holds for the LM data when they were separated with respect to test site and shot medium coupling (whether detonated above or below the water table). There is consensus in the literature that seismic coupling is a function of the percentage dry (or gaseous) porosity of a material. In a study of small scale, high explosive experiments with 15 rock-types, Larson (1981) found for a given size explosion that a porous material's (such as tuff) elastic radius increased with increasing water content. The dominant non-linear mechanism (within the plastic radius) working at low yields appears to be pore crushing of the surrounding material (Stevens *et al.*, 1991). Non-linear finite difference calculations (Bache, 1982) also indicate that porosity is the most important characteristic of NTS tuff for seismic coupling purposes. In the same study, source functions for Yucca Flat wet and dry tuff are significantly different, with the wet tuff's long-period amplitude being larger by 50 percent and its corner frequency being lower. Springer (1966) has observed this effect for teleseismic P-wave amplitudes. Patton (1988), Gupta *et al.* (1989), and Vergino and Mensing (1989) have observed this coupling effect in regional phases such as L_g, P_n and P_g.

Several sets of synthetic Rayleigh waves were generated at the 40° distance for calculating M_s. One set was propagated along the single structure model (hereafter referred to as the single-path case) which reflects the average Earth structure between NTS and a given station. We also generated mixed-path synthetics for which that part of the path beyond the actual source receiver distance, out to 40°, the surface wave is propagated along a generic earth structure. The NTS-RSSD Earth structure was chosen for this generic path section, as it is a relatively simple structure which generates stable surface waves and it is roughly an intermediate range station

(distance < 1900 km), so that its structure can be considered to be an "average" North American structure for the network.

Surface wave magnitudes were first calculated from the 40° synthetics generated with a single structure propagation path. Figure 2.7a and 2.7b display single-path M_S values, calculated as described above, versus m_b. These m_b 's are those of Lilwall and McNeary (1985). In the upper figure (2.7a) M_S is calculated without path corrections, whereas M_S is calculated with path corrections in the lower figure. The solid line is the best fitting weighted least-squares regression of the data, with the weighting factor being inversely proportional to individual event variances. The dashed lines represent the two standard deviation error (assuming a Student t distribution) of the fit of the line to the data. Since Student t statistics (Lapin, 1983) are functions of the population size, the confidence level will vary with data set size. Solid black circles are shots below the water table, open circles are shots above the water tables, and open squares are shots for which this information is not known. Note the error bars are approximately 50 percent larger for the uncorrected M_S's (figure 2.7a) than for the case of path-corrected M_S's (fig 2.7b). The scatter in the data is also significantly less for the path-corrected M_S's, so it appears that the path corrections do improve M_S measurements.

There are two significant effects of including path corrections. One is the reduction in variance of individual magnitudes. Without path corrections the individual station magnitudes have a bi-modal distribution reflecting the two generic earth models of North America: the tectonic western and stable cratonic eastern crust and upper mantle structures. The path corrections bring in the outlying station magnitude values towards the mean value. Including path corrections for the single-path derived M_S's increases the average value by 0.14 units (or 32 percent). This effect can be attributed to the smaller events which are brought more in line with the curve containing larger events. This in turn is due to the fact that the smaller events are

Figure 2.7: Here M_s is plotted vs. $m_{b(LM)}$'s. For the left figures M_s is calculated with single-path Green's functions, without path corrections (npc) and with path corrections (pc). The best-fitting regression model is the solid line running through the data points. The dashed lines are the two sigma confidence intervals of the line. The M_s-m_b relationship and the r.m.s. error of the data are at the bottom of each figure. The middle figure M_s values are determined using the mixed-path 1 synthetics and in the right two figures mixed-path 2 Green's functions were used.

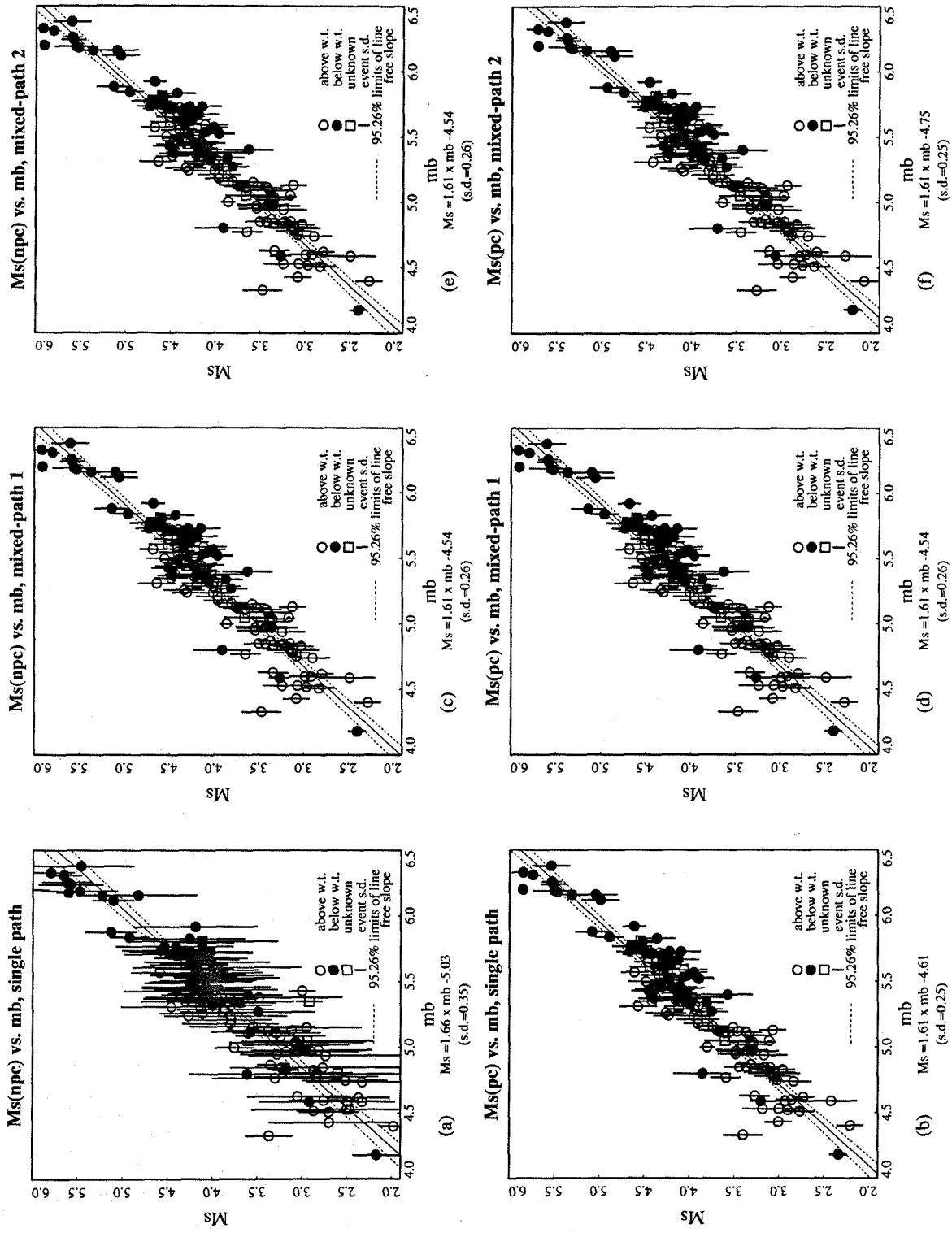
Ms(npc) vs. mb, single path
Ms(npc) vs. mb, mixed-path 1
Ms(npc) vs. mb, mixed-path 2
Ms(pc) vs. mb, single path
Ms(pc) vs. mb, mixed-path 1
Ms(pc) vs. mb, mixed-path 2
Ms
mb
above w.t.
below w.t.
unknown
event s.d.
95.26% limits of line
free slope
(a) Ms =1.66 x mb -5.03 (s.d.=0.35)
(b) Ms =1.61 x mb -4.61 (s.d.=0.25)
(c) Ms =1.61 x mb -4.54 (s.d.=0.26)
(d) Ms =1.61 x mb -4.54 (s.d.=0.26)
(e) Ms =1.61 x mb -4.54 (s.d.=0.26)
(f) Ms =1.61 x mb -4.75 (s.d.=0.25)

only observed at nearer stations in tectonic North America (TNA), for which path structures exhibit higher attenuation than do more cratonic or shield-like models, so that surface waves propagated along a TNA path for 40° will be significantly more attenuated than waves propagated along a craton or shield path for that same distance. Path corrections reduce this effect significantly for the single-path derived magnitudes. Table 2.1 lists these network path corrections. The third column lists the corrections for single-path synthetics. A positive value denotes that the M_S for a station is smaller than the network theoretical average.

We next explored the effect of mixed-path transfer functions upon the M_S calculations. As described above, we chose the path to RSSD as a generic structure for the second portion of the mixed-path synthetic seismogram calculations. We generated two sets of these synthetics. The difference between these two mixed-path earth structures is in their spectral attenuation coefficients, with $\gamma(\omega)$ (equation 2.1) being twice as large, at a given frequency, for the mixed-path 2 case as for the mixed-path 1 case. Figure 2.8 is a plot of the attenuation factor ($\gamma(\omega)$) as a function of period. The line labeled RSSDx2 is that of the increased attenuation model. It is referred to as "mixed-path 2" throughout this study. The lower, dashed curve is the attenuation curve for the RSSD structure. Synthetics made with this RSSD generic structure for the latter portion of the 40° travel path will be referred to as "mixed-path 1." Table 2.1 gives the path corrections for each station for these two cases, also.

In figures 2.7c and 2.7d the M_S magnitudes were calculated using synthetic seismograms using the mixed-path 1 model. In figure 2.7c the M_S's are calculated without path correction terms, while in figure 2.7d path corrections are included. The addition of the path correction terms cuts the data variance, but by no more than 25 percent, and then not in all cases. Assuming a fixed slope regression (m=1.50), there is no off-set in the intercept between the uncorrected and path-corrected M_S's. So using a generic structure for the remainder of the 40° path acts a path correction

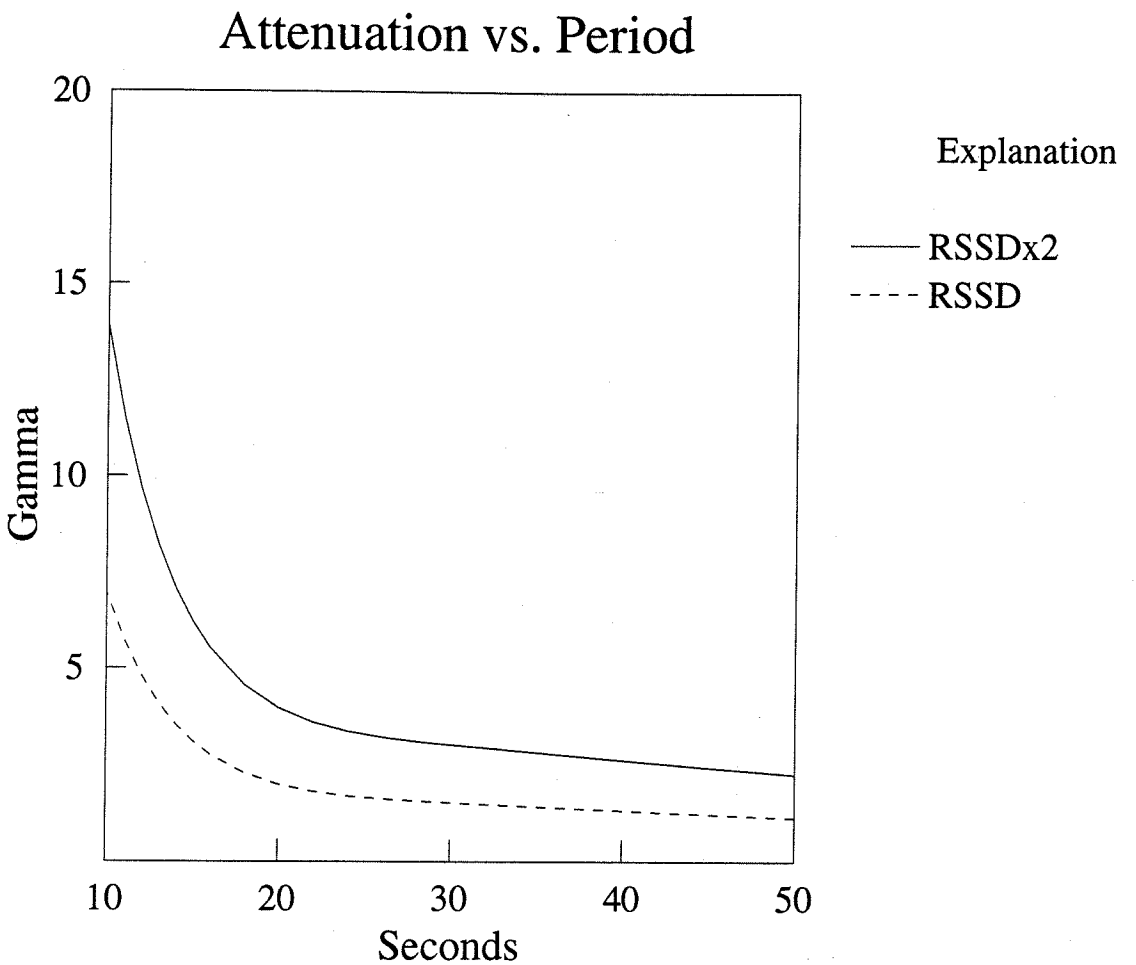

Figure 2.8: The two attenuation models for the generic portion of the hybrid propagation model are plotted versus period. Gamma is the distance attenuation coefficient (equation 2.1) at a given period. Model RSSDx2's attenuation is twice that of the RSSD model. M_S values calculated with synthetics using model RSSD are referred to as mixed-path 1, while values determined from synthetics created using attenuation model RSSDx2 are referred to as mixed-path 2.

as well.

Figures 2.7e and 2.7f are M_S vs. m_b plots for the mixed-path 2 case without and with path corrections, respectively. What is most striking is that the slope of the regression line is nearly the same (1.64) for all three path-corrected cases (figures 2.7b, 2.7d, and 2.7f). However, if explosions at only one site are plotted, the slope of the curve is closer to 1.5, so that we will take the M_S-m_b scaling relationship to be:

$$M_S = 1.50 \times m_b + B. \tag{2.14}$$

For this fixed-slope scaling relationship, the uncorrected and path-corrected mixed-path 1 M_S curves have the same intercept, whereas for the mixed-path 2 case the intercept is 0.10 units larger for the path-corrected curve than for the uncorrected curve. For path-corrected M_S's, the mixed-path 1 y-intercept is 0.21 log units greater than that of the mixed-path 2 curve. Because mixed-path synthetics are propagated to 40° along a more attenuative path, the M_S measured also will be smaller.

For the single-path case, path-corrected M_S values give the same relationship (slope=1.64), but the slope is significantly larger (1.71) for the uncorrected magnitudes, although the difference lies within the error bounds. It would seem that both path corrections and mixed-path Green's functions improve M_S determinations for the method used here. The most consistent, reliable magnitudes are obtained using mixed-path generated synthetics in conjunction with path corrections for the 40° M_S measurements. The variance among the mixed-path based M_S values for the network is smaller than that when M_S is derived from single-path synthetics, so that magnitude measurements will be more consistent when they are determined from mixed-path synthetics. This is particularly important for events with few reporting stations. All further plots of M_S in this study use values obtained from the mixed-path 1 case with path corrections, unless stated otherwise.

How well the final M_S values reflect the actual seismic magnitude of these events

necessitates having another measure of their size. In the event of anomalously high or low seismic source coupling, for example, both body waves and surface waves should be affected similarly by coupling effects. A magnitude parameter independent of seismic observations would be useful to plot the M_S against, so we have also fitted our results to estimated log yields. These relationships are shown and discussed later in the paper. Yield values are estimated to be within 10 percent of the actual yield (Springer and Kinnaman, 1971). Yield information was available for 174 of the events, thus yields make up the most comprehensive data set with which to compare our results. The yields for this data set range over three orders of magnitude in size. The greatest scatter, as in the case of m_b vs. log yield, is due to shots above the water table. It should also be be kept in mind that the scatter would be further reduced if the data were separated into populations based on their location at NTS, (*i.e.*, Pahute Mesa, Rainier Mesa and Yucca Flat).

Since our magnitude values are based on theoretical continental structures, as well as the particular network used, we wanted to compare our M_S values to those obtained from more standard M_S methods. Figure 2.9a-f shows our M_S values (x axis) versus those from six other studies (y axis) (Basham, 1969, Marshall and Basham, 1972, Marhsall, Springer and Rodean, 1979, Basham and Horner, 1973, Yacoub, 1983 and Von Seggern, 1973). The overlap in data sets varies between 8 and 16 events. We performed a fixed-slope (slope=1.0), linear regression of our M_S values to those of the six outside studies; in general the correlation is very good. It's important to note that with our method we are able to measure M_S for events one-tenth the size of the smallest events measured in the other studies (*i.e.*, M_S =1.75 to 2.0). This is after having corrected for differences in absolute M_S scales. We are able to measure M_S for these smaller events, because we are able to make use of near-regional (< 500 km) records with the method described in this paper.

The offset in M_S values between ours and the other scales varies considerably.

Figure 2.9: M_s of this study regressed against those determined by other studies.

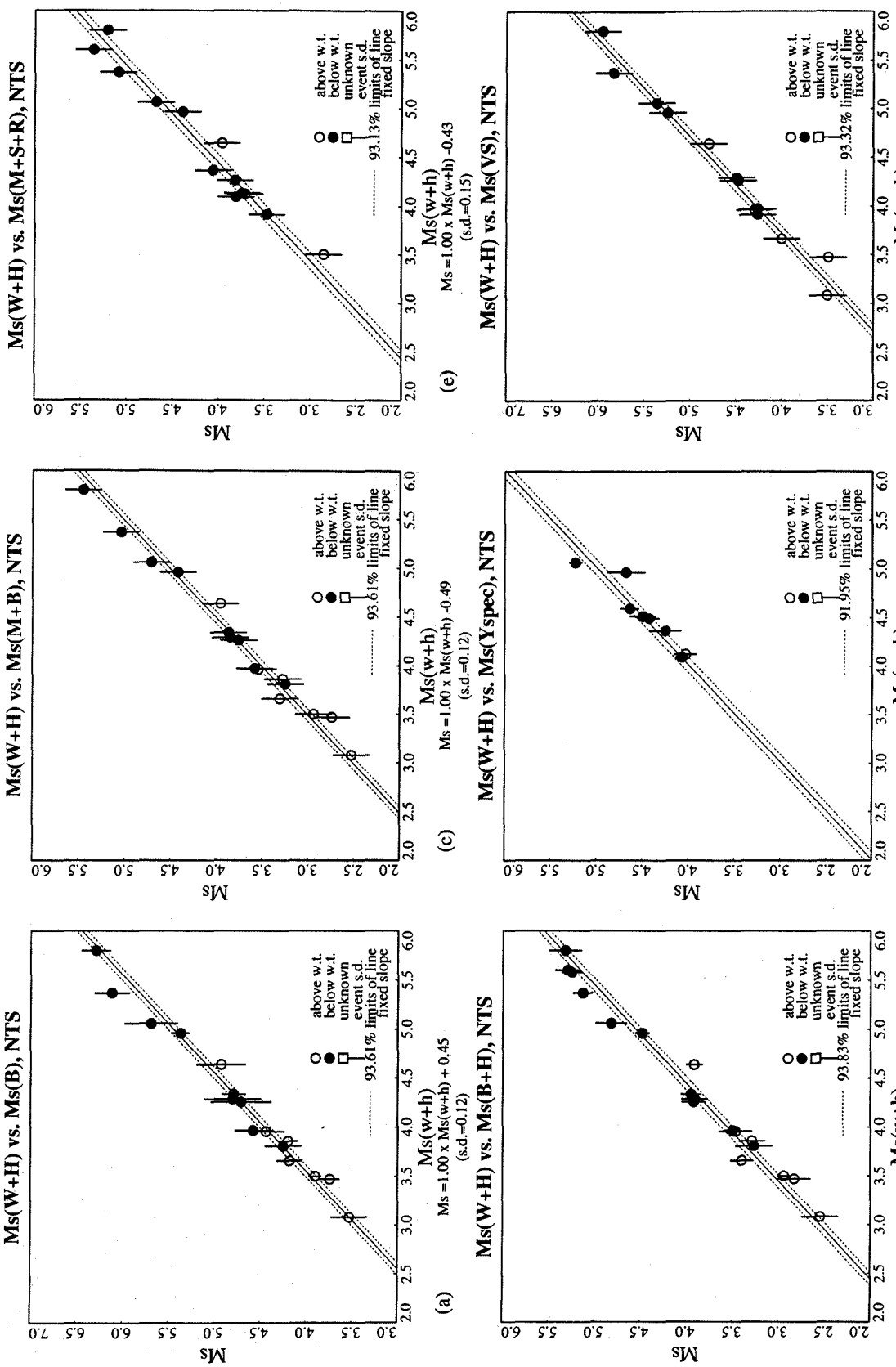
Ms(W+H) vs. Ms(B), NTS
Ms(W+H) vs. Ms(M+B), NTS
Ms(W+H) vs. Ms(M+S+R), NTS
Ms(W+H) vs. Ms(B+H), NTS
Ms(W+H) vs. Ms(Yspec), NTS
Ms(W+H) vs. Ms(VS), NTS
Ms
Ms(w+h)
above w.t.
below w.t.
unknown
event s.d.
93.61% limits of line
fixed slope
93.83% limits of line
91.95% limits of line
93.13% limits of line
93.32% limits of line
(a) Ms =1.00 x Ms(w+h) + 0.45 (s.d.=0.12)
(b) Ms =1.00 x Ms(w+h) -0.45 (s.d.=0.14)
(c) Ms =1.00 x Ms(w+h) -0.49 (s.d.=0.12)
(d) Ms =1.00 x Ms(w+h) -0.01 (s.d.=0.11)
(e) Ms =1.00 x Ms(w+h) -0.43 (s.d.=0.15)
(f) Ms =1.00 x Ms(w+h) + 0.28 (s.d.=0.13)

This offset is due in part to the difference in definition of M_S for each study, in particular the distance correction term. As discussed earlier, we chose the distance correction term ($1.08 \times \log_{10}(\Delta)$), whereas the other studies use a variety of ones. Yacoub (1983) and Basham (1972) use variations of the Prague formula: ($1.66 \times \log_{10}(\Delta)$) (Båth *et al.*, 1967). Von Seggern (1973) used a slightly smaller distance factor ($0.9 \times \log_{10}(\Delta)$) than that of his later study which we use. The other three studies use distance corrections developed by Marshall and Basham (1972) and all have offsets of approximately 0.45 magnitude units. The difference in distance correction factor is believed to be the primary cause of the offset in magnitude between their results and ours. Our distance correction is also dependent upon the generic path structure chosen to generate the 40° synthetics. These three studies, as well as that of Basham (1969) use mostly, if not all, data recorded at Canadian stations, thus their networks have strong azimuthal and distance biases as well, which may also affect magnitude measurements. It should be noted that the method described in this study to calculate M_S also is based upon a theoretical network average M_S, so it will have a bias attached to it which is dependent upon the network used. This network bias may be responsible for part of the offset, as well.

Our network does have considerably better azimuthal coverage than these other studies, so that tectonic release effects upon the long-period radiation, assuming strike-slip faulting, should be mitigated, thus giving more accurate M_S measurements.

A significant difference between our M_S calculations and those of the other studies is that we include data from close-in stations. Since the 40° synthetics used to calculate M_S travel further along an arbitrary path model for these nearer stations, it is important to consider whether or not our M_S values have some functional dependence upon distance. Figure 2.10a plots relative event M_S vs. distance for the entire data set. No apparent distance dependence is observed. We also examined this

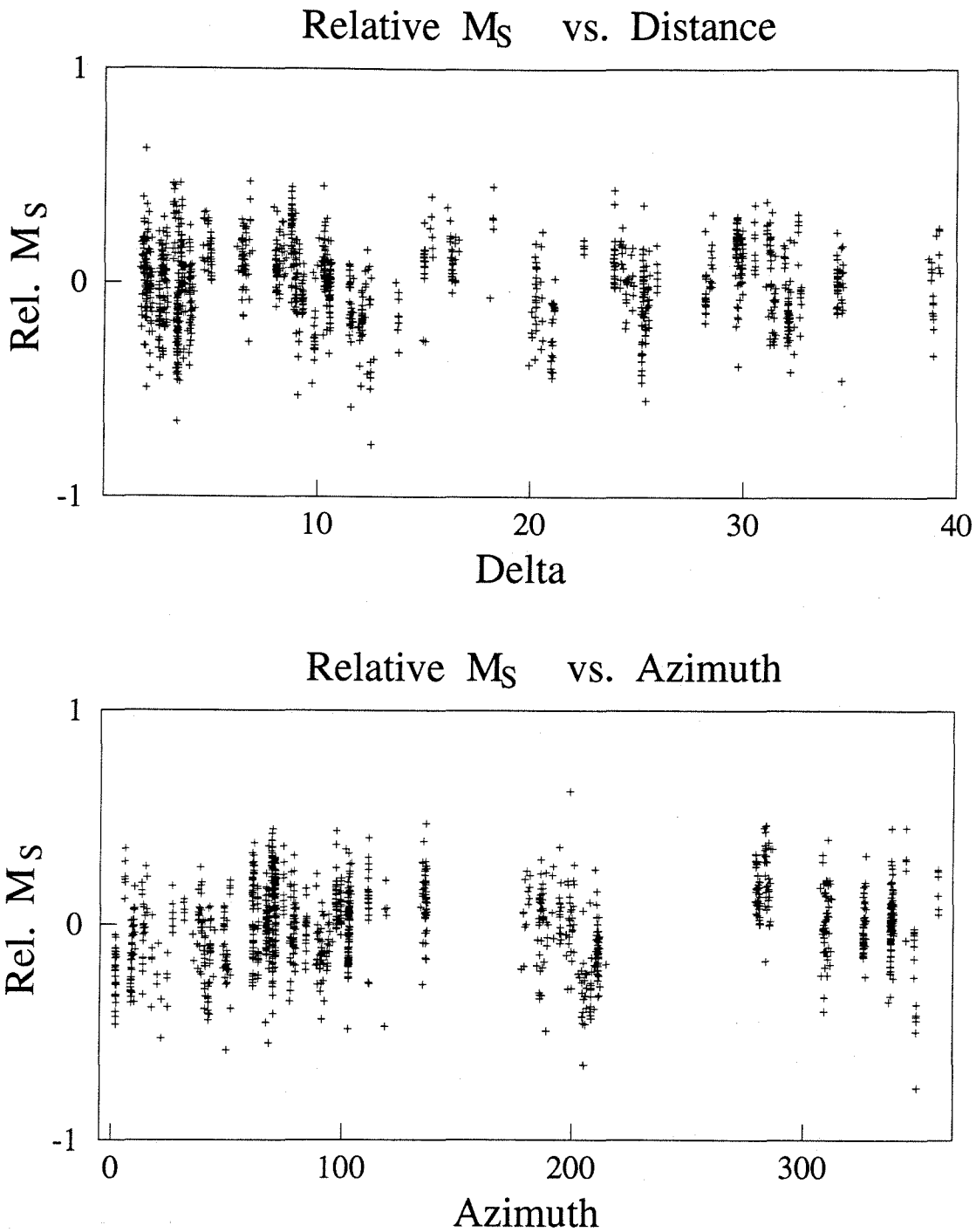

Figure 2.10: Relative M_s (individual station-network average) vs. distance (a) and azimuth (b). M_s values do not appear to be a function of distance. There also is no apparent functional relationship between azimuth and M_s; some azimuths are not covered, however.

relation for individual events and found the evidence more compelling that there is no distance dependence for the M_S values, which makes this M_S method very attractive, particularly for small events, for which Rayleigh wave amplitudes are measurable only at near distances, since there will be no bias in magnitude values between large and small events. Figure 2.10b shows the relative event M_S vs. azimuth. There is some variation with azimuth. This is to be expected for we do not take into account tectonic release in our M_S calculations. Azimuthal variations in propagation paths, caused, perhaps, by different tectonic regions may also contribute to this effect.

Table 2.2 lists the final mixed-path 1, path-corrected M_S values for the 190 events of this study. The first column lists the number of stations recording the event. Next are given the surface wave magnitude and associated error for the event. Next is a three letter shot information code. The first letter denotes its geographic location: Yucca (Y), Pahute (P), Rainer (R), or Climax Stock (C). The second is whether its shot depth was above (A) or below (B) the water table. The last letter describes the shot site rock as tuff (T), rhyolite (R), granite (G), or alluvium (A). An underscore means that the information is not known. The final two columns are the event's name and Julian data, respectively. The events are listed in chronological order.

To determine the portability of this M_S calculation method, the events need to be separated into groups based on their source regions and then compared, one group to another, in order to see if there are systematic differences in M_S values relative to any other magnitude scale. Three main geographic source regions comprise the event data set: Pahute Mesa, Rainier Mesa and Yucca Flat.

Whether or not a shot occurs within saturated material is another criterion by which to separate events in order to look for systematic differences in M_S values. Other studies have found significant seismic coupling differences between explosions detonated above and below the water table (Marshall *et al.*, 1979; Gupta, 1989; Vergino and Mensing, 1989). This seismic coupling effect is important to quantify.

Table 2.2: Table giving final M_S results

Table 2: Event Information

No. Sta.	M_S	M_S s.e.	Shot Info.	Event	Julian Date	No. Sta.	M_S	M_S s.e.	Shot Info.	Event	Julian Date
1	2.49	-	R_	Rainier	57262	5	3.86	0.04	YAT	Yard	67250
1	3.25	-	R_	Logan	58289	1	2.08	-	YAA	Marvel	67264
1	3.73	-	R_	Blanca	58303	9	3.64	0.05	YBT	Cobbler	67312
1	2.96	-	NBG	Hardhat	62046	10	5.40	0.06	NBT	Faultless	68019
1	2.89	-	YAA	Dormouseprime	62095	6	3.53	0.05	RAT	Dorsalfin	68060
1	3.57	-	YA_	Aardvark	62132	4	2.85	0.06	N_	Buggy1	68072
1	3.12	-	YAA	Haymaker	62178	3	5.80	0.01	PBR	Boxcar	68117
1	3.69	-	YAA	Sedan	62187	10	4.75	0.09	PAT	Rickey	68167
1	3.66	-	YA_	Mississippi	62278	11	4.48	0.06	PAR	Chateaugay	68180
2	4.85	0.22	YBT	Bilby	63256	9	3.43	0.08	RAT	Hudsonseal	68268
1	3.77	-	RAT	Clearwater	63289	1	3.14	-	YAA	Crew	68309
2	3.07	0.28	YAL	Handcar	64310	4	3.66	0.10	PAT	Schooner	68343
2	2.54	0.08	YAA	Merlin	65047	4	5.92	0.08	PBT	Benham	68354
1	2.82	-	NAA	Wishbone	65049	11	4.03	0.05	RAT	Wineskin	69015
12	3.97	0.06	YBT	Wagtail	65062	1	3.20	-	RAT	Cypress	69043
6	3.96	0.07	YAT	Cup	65085	15	4.06	0.04	YBT	Blenton	69120
1	2.59	-	PAR	Palanquin	65104	9	5.58	0.05	PBT	Jorum	69259
4	2.40	0.06	PBT	Buteo	65132	9	4.68	0.05	PAR	Pipkin	69281
4	3.08	0.09	NAA	Dilutedwaters	65167	3	2.11	0.06	YAT	Cruet	69302
7	3.66	0.05	YAT	Charcoal	65253	3	2.53	0.12	YAT	Pod	69302
5	3.81	0.09	YBT	Lampblack	66018	4	4.36	0.14	YBT	Calabash	69302
8	3.91	0.12	PBT	Rex	66055	2	3.17	0.02	R_	Dieseltrain	69339
13	3.96	0.07	PAR	Duryea	66104	2	3.34	0.05	RAT	Dianamist	70042
5	3.47	0.11	NAT	Pinstripe	66115	2	3.46	0.05	YAT	Cumarin	70056
3	2.81	0.05	YAA	Cyclamen	66125	2	3.22	0.18	YAA	Yannigan	70057
11	4.01	0.10	PAR	Chartreuse	66126	3	2.14	0.24	YAT	Cyathus	70065
15	4.34	0.04	YBT	Piranha	66133	3	1.66	0.20	YAT	Arabis	70065
6	3.50	0.06	YAT	Discusthrower	66147	2	2.22	0.27	YAA	Jal	70078
26	4.27	0.04	CBG	Piledriver	66153	17	4.29	0.05	YBT	Shaper	70082
18	4.29	0.03	YBT	Tan	66154	8	5.56	0.08	PBT	Handley	70085
3	2.70	0.13	YAA	Vulcan	66176	5	3.35	0.13	RAT	Mintleaf	70125
3	5.06	0.15	PBR	Halfbeak	66181	7	3.76	0.08	YAT	Cornice	70135
3	5.37	0.11	PBT	Greeley	66354	13	3.54	0.06	YAT	Morrones	70141
2	2.39	0.05	YAA	Ward	67039	2	1.79	0.33	YAT	Manzanas	70141
1	2.38	-	YAA	Persimmon	67053	5	3.12	0.06	RAT	Hudsonmoon	70146
5	4.55	0.09	YAA	Agile	67054	16	4.12	0.07	YAT	Flask	70146
7	4.96	0.06	YBT	Commodore	67140	2	2.40	0.10	YAA	Embudo	71167
10	4.64	0.07	PAR	Knickerbocker	67146	4	3.01	0.09	YAT	Laguna	71174
3	3.46	0.05	RAT	Midimist	67177	4	3.21	0.02	YAT	Harebell	71175
2	3.03	0.14	RAT	Doormist	67243	10	3.16	0.06	RAT	Camphor	71180

Table 2: Event Information (cont.)

No. Sta.	M_S	M_S s.e.	Shot Info.	Event	Julian Date	No. Sta.	M_S	M_S s.e.	Shot Info.	Event	Julian Date
15	4.13	0.03	YBT	Miniata	71189	11	4.40	0.05	YAT	Baseball	81015
21	3.63	0.06	YBT	Algodones	71230	10	4.18	0.07	YBT	Rousanne	81316
2	2.59	0.06	YAT	Pedernal	71272	9	4.67	0.05	YBT	Jornada	82028
4	2.59	0.04	YAT	Cathay	71281	10	4.52	0.06	PBR	Molbo	82043
4	2.29	0.17	YAA	Longchamps	72110	8	4.41	0.08	PAR	Hosta	82043
7	3.44	0.10	RAT	Mistynorth	72123	4	2.99	0.10	YAT	Tenaja	82107
5	3.27	0.06	YBT	Monero	72140	6	4.44	0.05	PAT	Gibne	82115
7	3.35	0.06	RBT	Diamondsculls	72202	15	4.29	0.04	YBT	Bouschet	82127
1	2.50	-	YA_	Delphinium	72270	9	4.52	0.05	PAR	Nebbiolo	82175
12	4.09	0.04	YBT	Miera	73067	9	3.04	0.10	YAT	Monterey	82210
22	4.09	0.03	YBT	Starwort	73116	9	4.73	0.05	YBT	Atrisco	82217
8	3.35	0.08	RAT	Didoqueen	73156	8	3.38	0.05	RAT	Huronlanding	82266
5	5.10	0.12	PBR	Almendro	73157	5	3.54	0.11	RAT	Frisco	82266
15	4.35	0.05	YBT	Latir	74058	2	2.49	0.29	YAA	Seyval	82316
8	3.43	0.08	RAT	Mingblade	74170	6	3.13	0.09	YAA	Manteca	82344
20	4.59	0.05	YBT	Escabosa	74191	2	1.80	0.01	YAA	Cerro	82245
13	3.96	0.05	YBT	Stanyan	74269	3	2.52	0.08	YBT	Borrego	82272
15	4.02	0.04	YBA	Cabrillo	75066	11	4.01	0.05	PAR	Cabra	83085
3	3.24	0.18	RAT	Diningcar	75095	20	4.15	0.05	YBT	Torquoise	83104
13	3.74	0.05	YBT	Obar	75120	7	2.83	0.07	YAA	Crowdie	83125
10	4.65	0.06	PBR	Stilton	75154	12	3.34	0.05	YAT	Fahada	83146
23	4.51	0.06	YBT	Mizzen	75154	10	2.93	0.06	YAA	Danablu	83160
3	5.53	0.02	PBT	Camembert	75177	12	4.17	0.06	PAR	Chancellor	83244
1	3.37	-	RAT	Huskypup	75297	3	3.04	0.22	R_	Midnitezephyr	83264
4	5.59	0.07	PBT	Kasseri	75301	5	2.50	0.04	YBT	Techado	83265
3	5.91	0.02	PBT	Muenster	76003	11	3.81	0.06	YAT	Romano	83350
14	4.49	0.05	YBT	Keelson	76035	9	3.42	0.06	RAT	Midasmyth	84046
8	5.56	0.09	PBT	Fontina	76043	1	2.28	-	YAA	Agrini	84091
13	5.15	0.05	PBR	Cheshire	76045	19	4.40	0.04	YBT	Mundo	84122
6	5.62	0.11	PBT	Colby	76074	11	4.48	0.06	YBT	Caprock	84152
3	3.23	0.17	RAT	Mightyepic	76133	4	3.16	0.17	YAT	Duoro	84172
8	4.24	0.05	YBT	Rudder	76363	21	4.18	0.07	PAR	Kappeli	84207
18	4.17	0.04	YBT	Bulkhead	77117	6	2.90	0.09	YAT	Correo	84215
10	4.09	0.05	YBT	Crewline	77145	3	3.08	0.03	YAT	Dolcetto	84243
27	4.29	0.04	YBT	Lowball	78193	5	3.58	0.08	YAT	Breton	84257
4	3.12	0.17	R_	Diablohawk	78256	4	2.80	0.08	YAA	Villita	84315
13	3.87	0.05	YBT	Quargel	78322	12	4.23	0.06	PAT	Egmont	84344
21	4.35	0.04	YBT	Quinella	79039	14	4.22	0.06	PAR	Tierra	84350
22	4.14	0.05	YBT	Pyramid	80107	11	4.43	0.07	YBT	Tortugas	84061
6	3.36	0.13	RAT	Minersiron	80305	5	3.39	0.06	YAT	Vaughn	85074

Table 2: Event Information (cont.)

No. Sta.	M_S	M_S s.e.	Shot Info.	Event	Julian Date	No. Sta.	M_S	M_S s.e.	Shot Info.	Event	Julian Date
4	4.03	0.23	YAT	Cottage	85082	10	4.42	0.07	PAR	Cybar	86198
8	4.72	0.08	YBT	Hermosa	85092	2	2.97	0.02	YAA	Cornucopia	86205
7	3.47	0.12	R_T	Mistyrain	85096	8	4.29	0.07	PAR	Labquark	86273
19	4.37	0.06	PBT	Towanda	85122	7	4.34	0.05	P__	Belmont	86289
13	4.46	0.05	PBR	Salut	85163	5	4.58	0.07	YBT	Gascon	86318
12	4.30	0.05	PAR	Serena	85206	7	4.55	0.08	P__	Bodie	86347
4	3.24	0.13	YAT	Ponil	85270	4	4.38	0.10	P__	Delamar	87108
8	4.19	0.09	YBT	Kinibito	85339	8	4.47	0.07	PAT	Hardin	87120
8	4.19	0.06	P__	Goldstone	85362	4	3.66	0.14	Y__	Midland	87197
4	4.07	0.06	YBT	Glencoe	86081	5	4.60	0.08	Y__	Tahoka	87225
7	3.40	0.09	RAT	Mightyoak	86100	4	4.51	0.13	P__	Lockney	87267
12	4.33	0.07	PAR	Jefferson	86112	3	3.87	0.06	Y__	Borate	87296
2	2.53	0.12	YAA	Panamint	86141	1	4.09	-	PAT	Kernville	88046
7	4.22	0.10	YAT	Tajo	86156	1	4.17	-	PAT	Kearsarge	88230
15	4.31	0.05	P__	Darwin	86176	1	3.36	-	Y__	Kawich	89055

Reviewing figure 2.6, it is also apparent that shots fired-off below the water table have a larger body wave magnitude than those detonated above the water table.

Figure 2.11a shows the M_S:$m_{b(LM)}$ relationship for all NTS events. The surface wave magnitudes were all calculated using mixed-path Green's functions (with the RSSD-1 structure for the generic path part) and path corrections. The vertical error bars represent the one standard deviation confidence interval for each M_S value. A linear least squares regression was performed to determine the scaling relationship. The solid line represents this curve and the dashed lines represent the two sigma confidence level of this curve. Figure 2.11b and 2.11c divide the data populations into above and below the water table, respectively; shots for which water table information was not available were left out. Although all but one Rainier Mesa event were detonated above the water level, we found that their coupling (M_S vs. log yield) was diagnostic of explosions detonated below the water table. Taylor (1983) notes that Rainier Mesa sports a perched aquifer. We believe that the Rainier Mesa events are detonated within this zone, hence they are assumed to be well-coupled events, *i.e.*, the pore space of the shot medium is filled with water and thus pore space crushing will not be a strong effect.

The bottom three figures (2.11d-f) plot the same data, but a constrained least squares fit was performed with the slope=1.50. The off-set in curves between events detonated above and below the water table is 0.10. This amount is within the scatter of the data (*i.e.*, statistically insignificant), but it would appear that shot medium coupling effects associated with pore-filling phenomena are similar for surface waves and P-waves.

Figure 2.15a-c are M_S vs. log-yield plots analogous to Figure 2.11a-c. It is important to note that the individual explosion variances are about the same size for the entire range of yields, so that our predicted yield values for small events should be as as accurate as for the larger events. The slope of the M_S and log-yield scaling

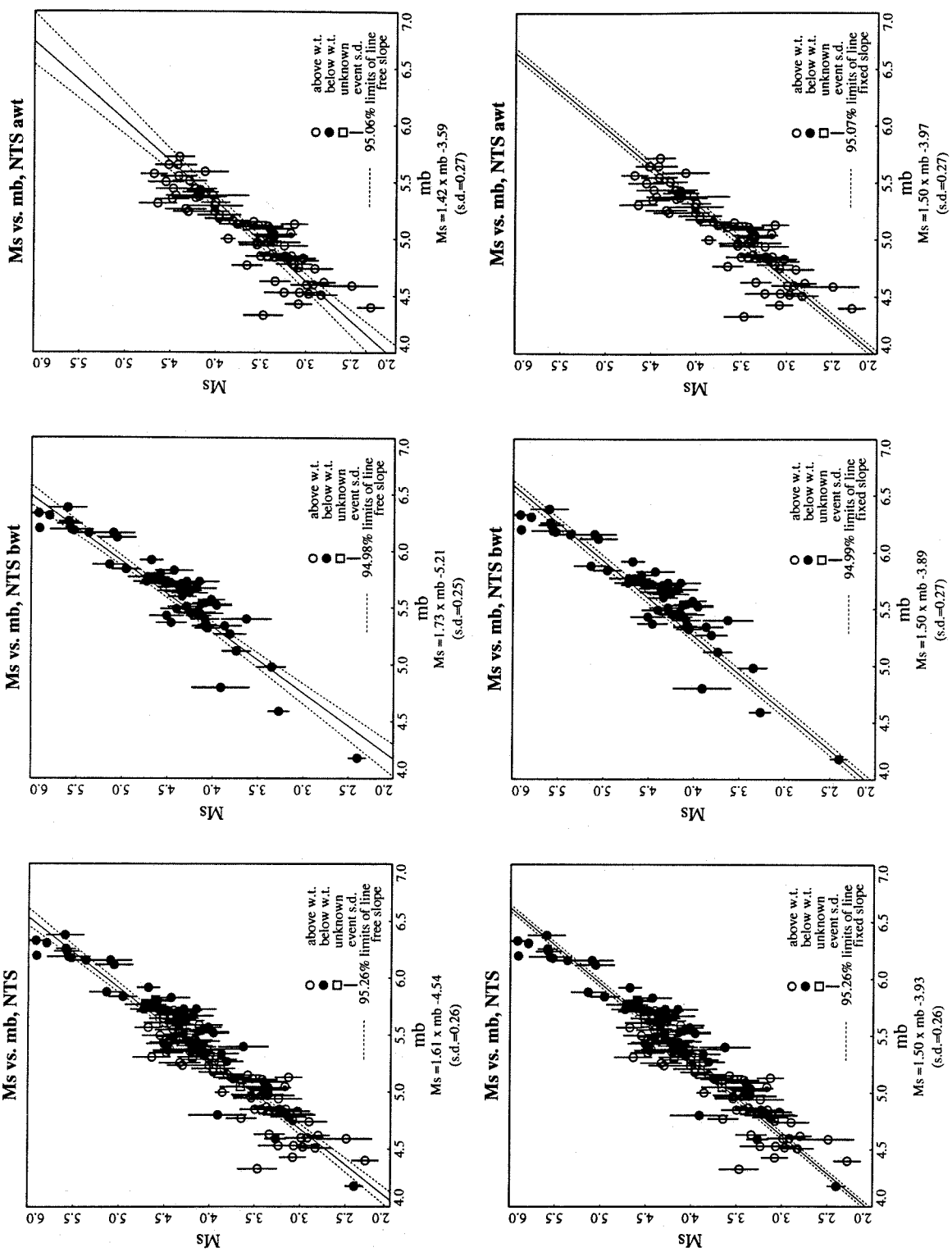

Figure 2.11: M_s regressed vs. m_b for all NTS events. The data are also separated with respect to shot point being above and below the water table. The bottom figures are constrained least-square regressions assuming a slope of 1.5.

relation curves was found to be near unity for all populations. Assuming the scaling relationship has a slope of 1, BWT shots couple more strongly than AWT shots by 0.52 units–a substantial amount; for m_b-yield scaling the coupling effect found in this study is 0.28 units. This coupling factor depends on the slope of the scaling curve and has been found to be as large as 0.7 to 0.9 throughout the literature. For individual source regions, the off-set in the M_S-yield and m_b-yield scaling curves for shots fired above and below the water table vary slightly from these values determined from the entire data set. There is some scatter in the data which is not surprising considering the diversity of the sampled populations. However, the best-fitting M_S-m_b curves are well constrained, for the population covers a wide range of magnitudes.

The various M_S:m_b relationships for Yucca events are shown in figure 2.12a-c. The scatter in the data is reduced by 25 percent over that of the general population (figure 2.11a-c). The free-slope regression curves are not as well constrained as those of figure 2.11 because the yield range for Yucca explosions is smaller than that of the entire data set. Fixing the slope to 1.5 (figure 2.12d-f) leads to AWT shots coupling 0.13 M_S units more strongly than BWT shots for a given m_b. The error in the fit to the curve is larger than this variation, so it is not a statistically significant result. It would appear the pore-filling coupling affects surface wave and body waves similarly. When the Yucca M_S data are regressed with respect to log-yield, as shown in figure 2.15d-f, it is found that BWT events couple four times more efficiently than AWT shots (ΔM_S =0.61). This is a significant amount and the data set on which it is based is more extensive than that of the M_S-m_b regression. Springer (1966) found that high dry porosity (60 percent) shot mediums coupled 4 to 5 times less effectively than in saturated alluvium. Most Yucca Flat shots are detonated in alluvium.

Figure 2.13a plots all Pahute event M_S's vs. their respective m_b's. The scaling relationship is significantly different than that of the Yucca data above. Comparing the unconstrained below and above water table curves (figures 2.13b,c) to their

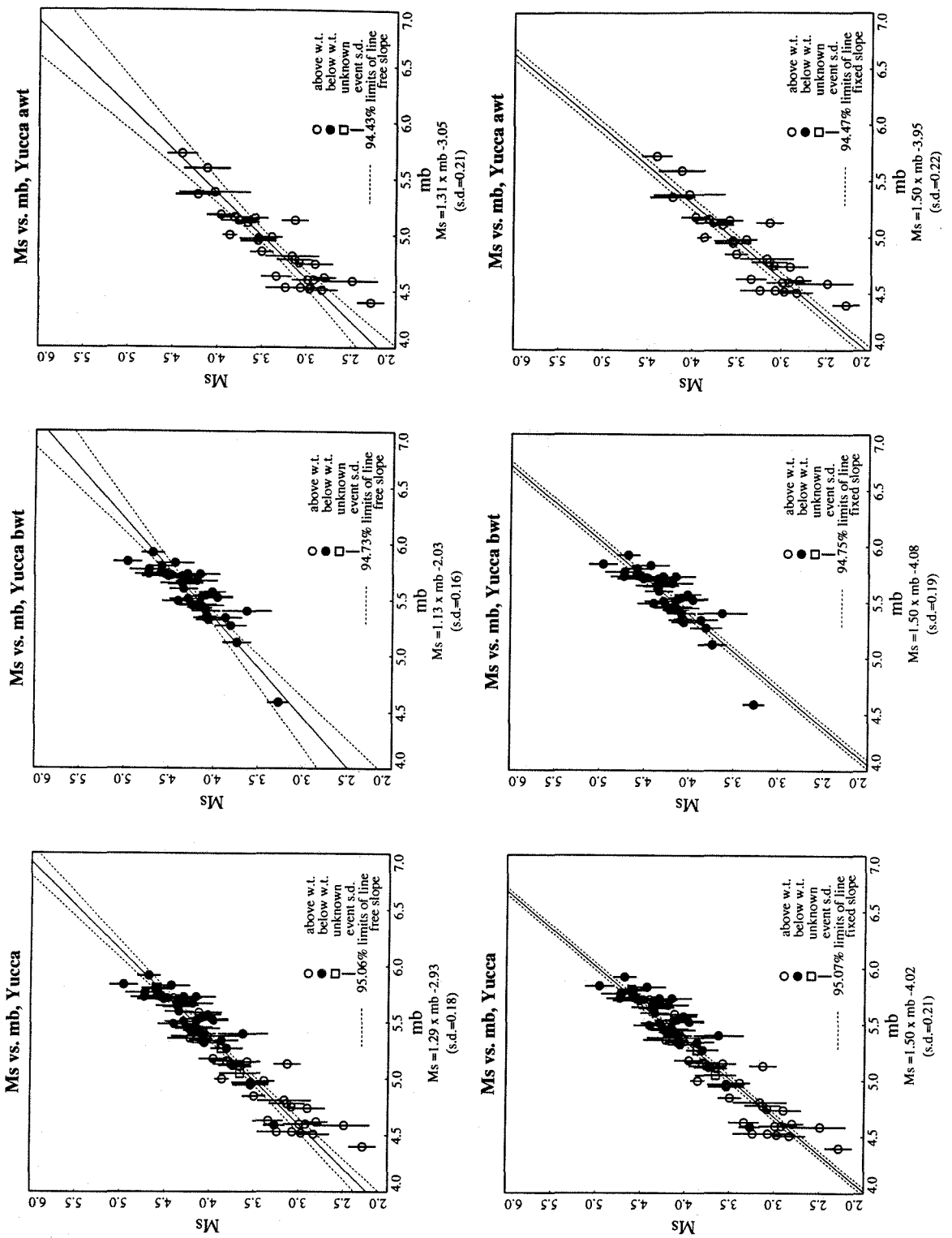

Figure 2.12: M_s regressed vs. $m_{b(LM)}$ for Yucca events. The data are also separated with respect to shot point being above and below the water table. The bottom figures are constrained least-square regressions assuming a slope of 1.5.

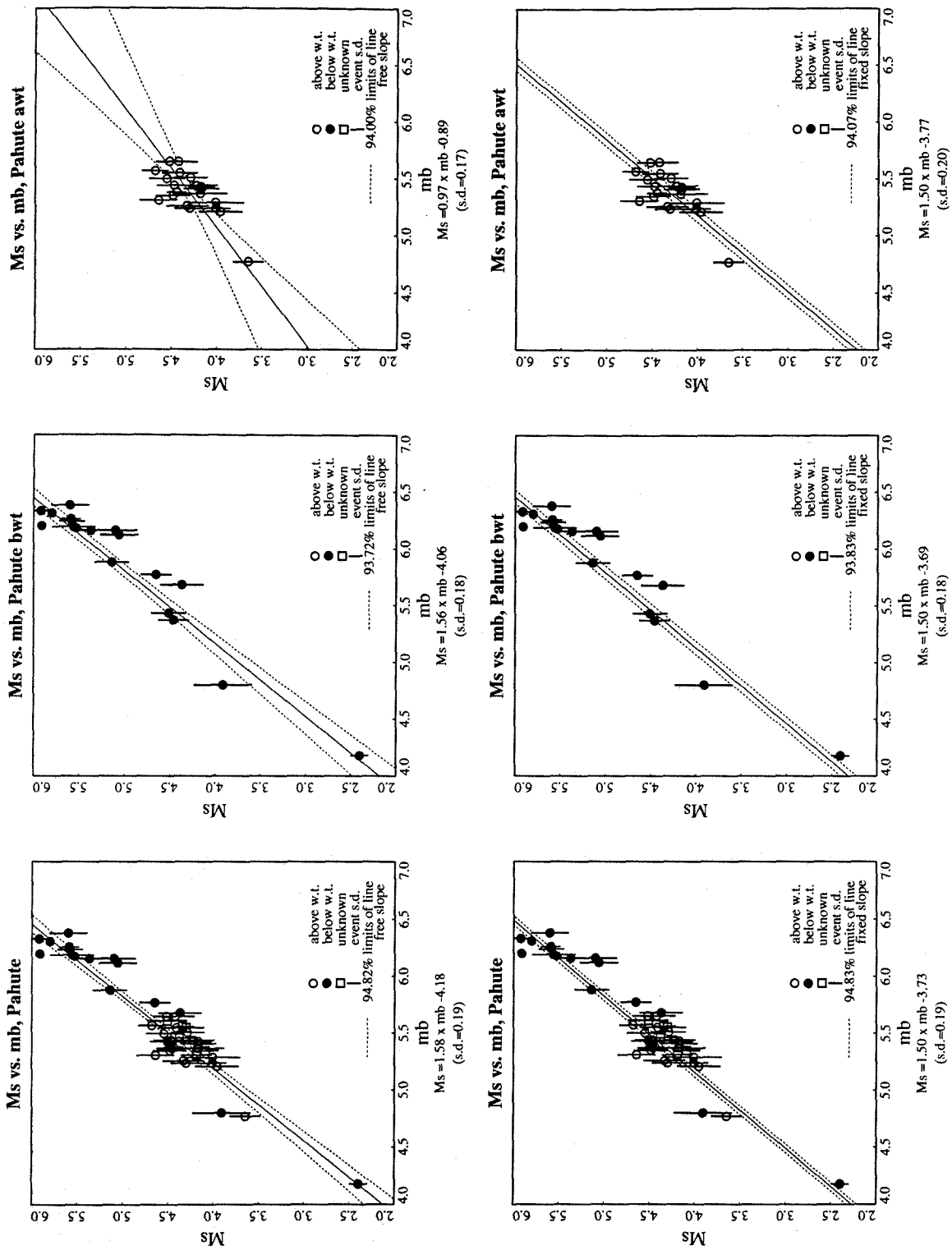

Figure 2.13: M_s regressed vs. $m_{b(LM)}$ for Pahute events. The data are also separated with respect to shot point being above and below the water table. The bottom figures are constrained least-square regressions assuming a slope of 1.5.

Yucca counterparts (figures 2.12b and c), it is apparent that explosions at the two sites do not display the same scaling relationships. One possible explanation for this difference is that there is not enough data to constrain the the scaling curves, particularly for Yucca BWT and Pahute AWT events. Another possible explanation is that this scaling relationship difference is real and may be caused by differences in the source medium, source structure or tectonic-strain release associated with the sites. Figures 2.12e-f and 2.13e-f show constrained (slope=1.5) regression curves for the Yucca and Pahute data, respectively. For a given m_b, surface wave magnitudes for events at Pahute Mesa are larger than those at Yucca Flat by 0.39 and 0.18 log units for BWT and AWT shots, respectively. There is also an appreciable difference in the M_S:log-yield relationship between Yucca and Pahute events detonated in water-saturated material (0.23 units). The Pahute data are plotted in figures 2.16d-f. For the case of events exploded in dry material, there is a significant difference with Yucca events having an M_S 0.44 units smaller than Pahute events.

Figures 2.14a-f display the M_S-m_b regression curves and data for Rainier Mesa events in combination with and without Pahute Mesa data. Figures 2.16a-c are analogous figures for the M_S vs. log-yield data. Although the clustering of Rainier data near $m_b = 5.0$ causes the curve to be poorly constrained, a slope is obtained that is close to that for Pahute and Yucca BWT shots. Comparison of the equations at the bottom of figures 2.13e and 2.14e gives an off-set of 0.47 between M_S estimates at Pahute and Rainier (for a given m_b). Either the Pahute site is more efficient at producing surface waves or the Rainier site is more efficient at coupling body wave energy. Rainier events are tunnel shots. The immediate source region (R < 200 m) may behave like an asymmetric cavity, resulting in a source that is non-isotropic (Zhao and Harkrider, 1991) and/or seismic coupling that has strong frequency dependence. Either of these effects may account for this difference. The difference in M_S-log yield scaling relationship is somewhat less (0.31 units), implying that Rainier

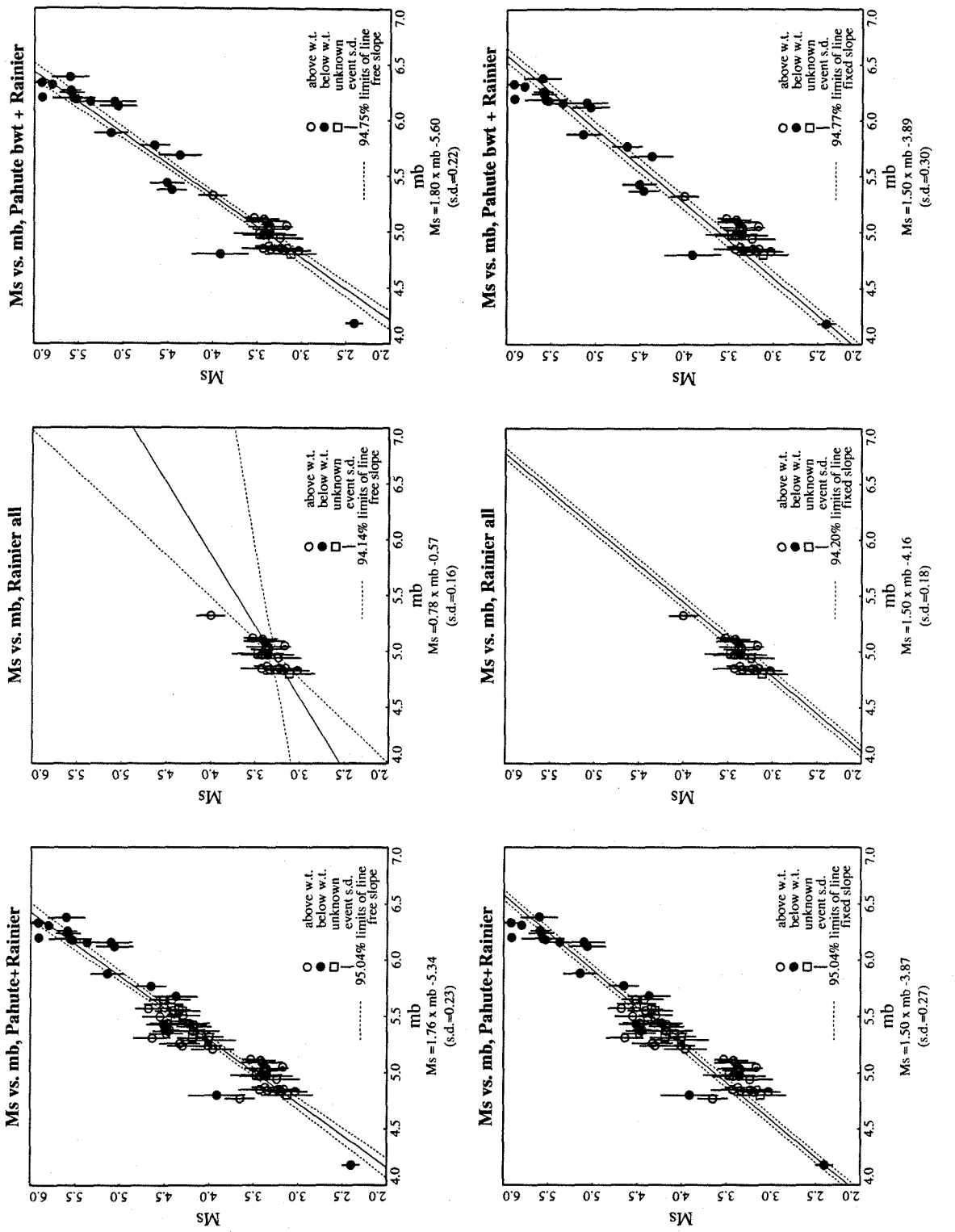

Figure 2.14: M_s regressed vs. $m_{b(LM)}$ for Pahute and Rainier events. Regression of Rainier data alone (middle figures), all Rainier and Pahute events (left figures), and all Rainier events with Pahute shots below the water table (right figures) are shown. The bottom figures are constrained least-square regressions assuming a slope of 1.5.

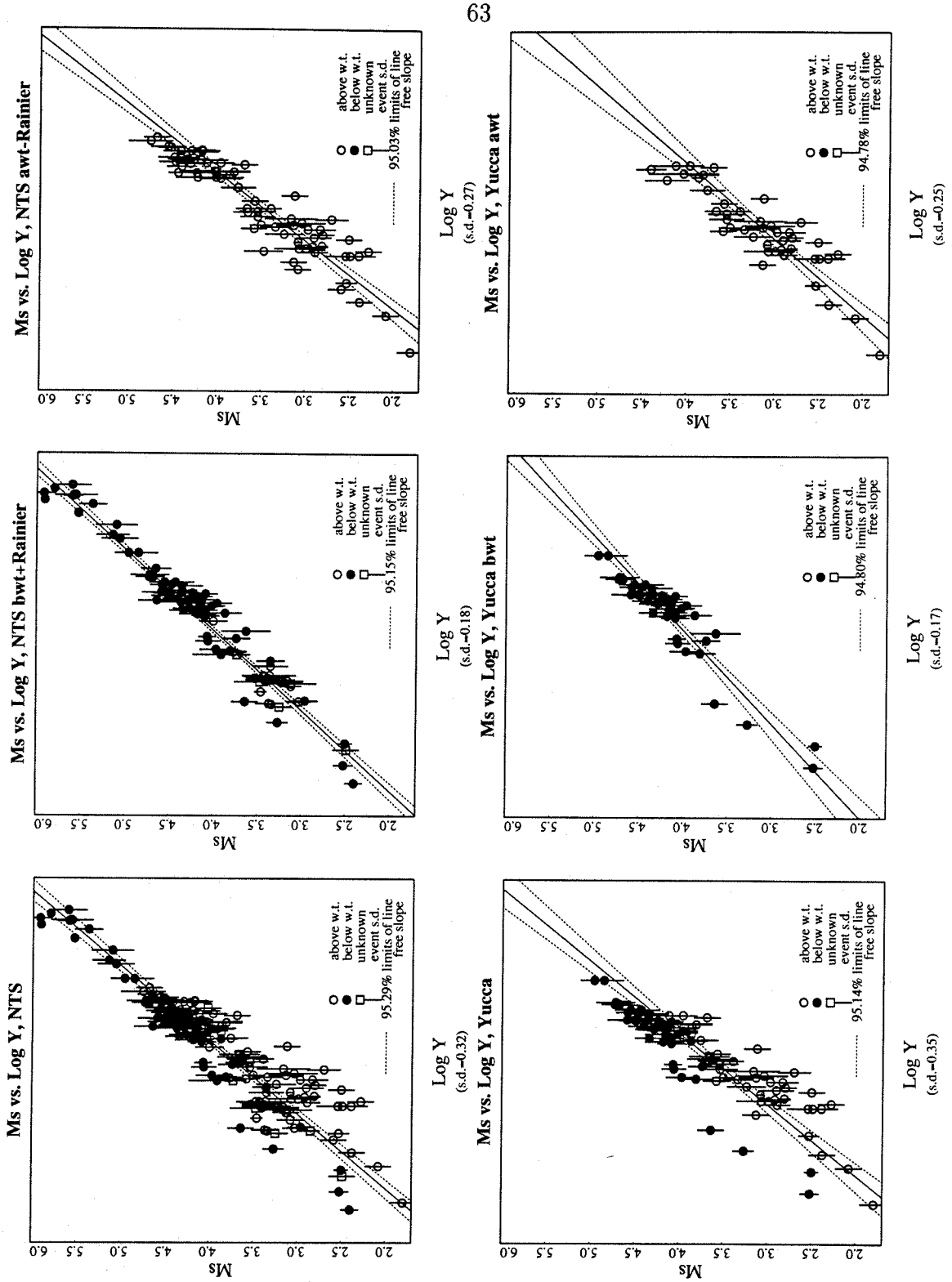

Figure 2.15: M_S regressed vs. Log Yield for all NTS events (top figures) and for Yucca events (bottom figures). Event populations also have been grouped with respect to shot point water table location.

more efficiently couples short-period energy than Pahute.

2.6 Conclusion

The method we have described to calculate surface wave magnitudes makes it possible to quantify the long-period (8 t0 20 seconds) source spectrum of nuclear explosions over a wider magnitude range than was previously possible. These M_S values scale consistently (within a constant factor) with other seismic magnitude scales. Using our technique, it is now possible to use near-regional ($\Delta < 8°$) long-period records, as well as more conventional far-regional ($\Delta < 15°$) and teleseismic observations, in order to measure surface wave magnitudes. As it is a time-domain measurement, it is easy to calculate M_S from historical analog waveforms, since it is only necessary to measure the peak to peak Rayleigh wave amplitude.

This M_S method is very useful for quantifying small explosions, because time-domain magnitude measurements of regional waveforms lowers the effective magnitude threshold. Small events, for which teleseimsic surface waves aren't observed, can now be analyzed with regional surface wave data, thus lowering the effective measuring M_S threshold. Figure 2.17 illustrates this point, showing unrotated three-component data for FLOYDADA (8/15/91, m_b = 4.2) detonated at Yucca Flat and recorded by three TERRAscope stations convolved with a Press-Ewing 30-90 response. The source to receiver distances are between 210 and 390 km. The maximum peak to peak amplitudes are quite small (< 0.5 mm). On the actual analog instrument it would not be possible to measure the surface wave amplitude. Because of the low signal to noise ratio, a spectral moment would be of dubious value. However, the M_S and M_0(PPA) methods described in this paper would furnish an accurate surface wave magnitude with which to estimate its yield.

These small surface wave magnitudes, based on near-regional data, would also

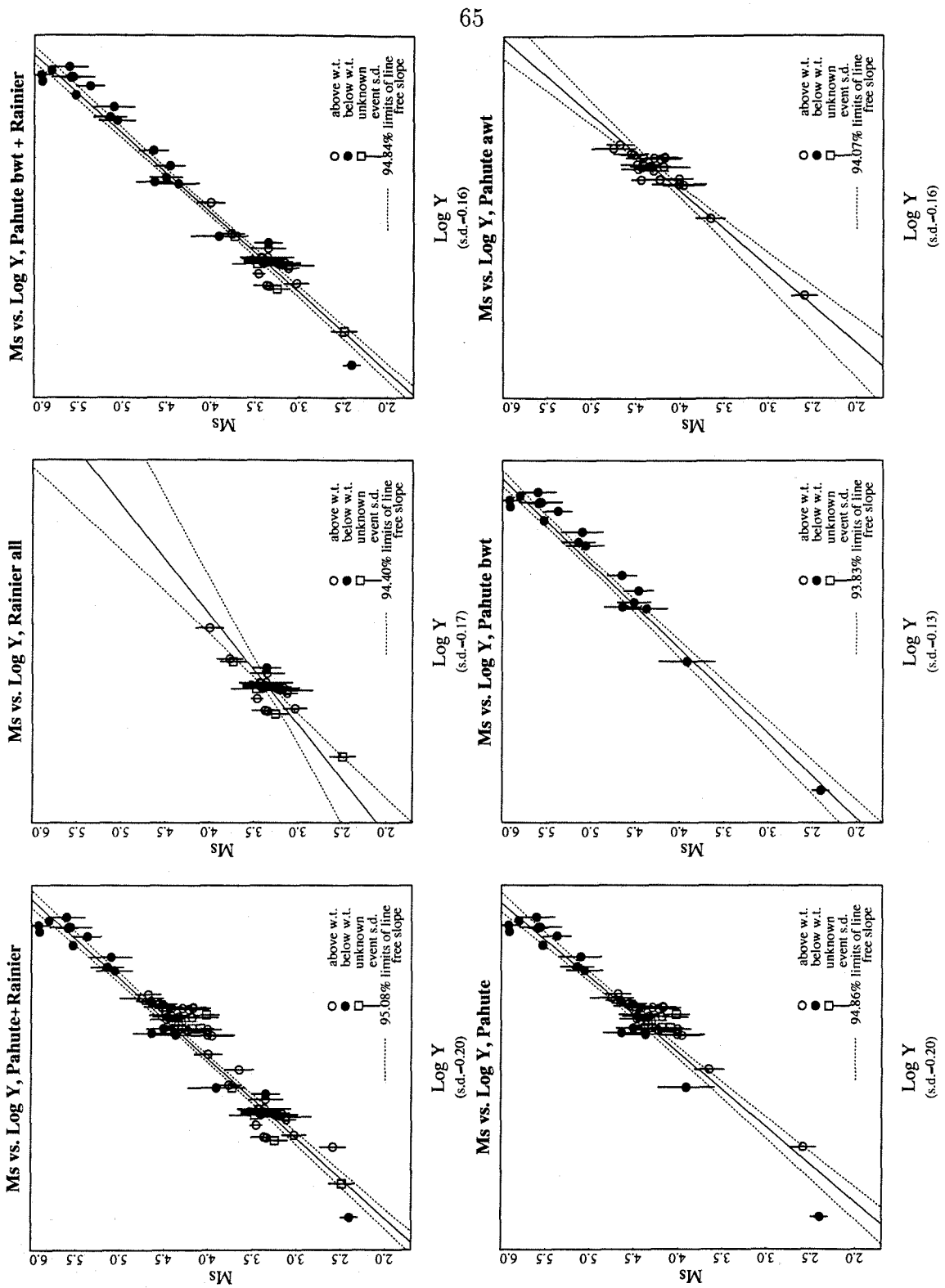

Figure 2.16: M_S regressed vs. Log Yield for Pahute and Rainier events (top figures) and for Pahute events alone (bottom figures). Event populations have also been grouped with respect to shot point water table location.

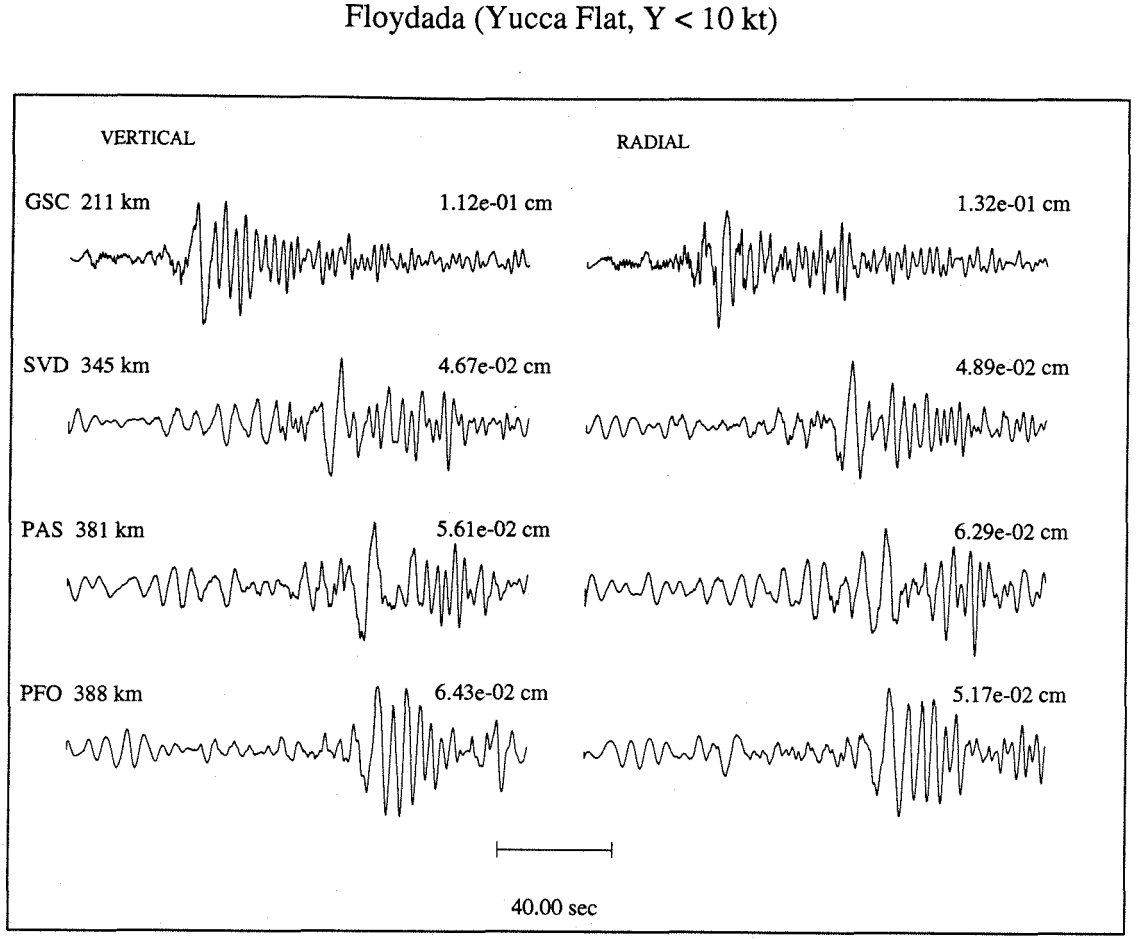

Figure 2.17: TERRAscope Streckeisen recordings of an NTS explosion Floydada at Yucca Flats on 8/15/91 with an estimated yield of < 10 kt ($m_b = 4.2$, $M_L = 4.0$, and log-$M_0 = 14.16$ N-M). The broadband records have been convolved with a Press-Ewing 30-90 instrument response. All four stations record the surface wave-train well enough to measure the Airy phase peak amplitudes. Records from an actual 30-90 long-period instrument would be unusable.

be of considerable value for discrimination methods which make use of the difference in long-period:short-period spectral content of earthquakes and explosions, for it is possible to lower the discrimination threshold using such data.

The increase in nearer observations has several other advantages. Station network coverage is enhanced in terms of overall numbers as well as in azimuthal coverage. In this study stations a few hundred kilometers away from NTS in the southwestern U.S. were included in the network that otherwise would have no coverage to the west or southwest. These improvements make the network M_S's more stable and statistically robust. Potential monitoring areas may well have similar geographical constraints requiring the use of near-regional ($\Delta < 8°$) seismic data. Also, the effect of inaccuracies in estimating Q are negligible for very near-regional recordings.

From the results obtained with the data set used here, there does appear to be significant differences in seismic coupling between NTS sub-sites, with events at Pahute Mesa producing larger surface wave magnitudes for a given m_b than at Rainier Mesa or Yucca Flat. For well-coupled events this discrepancy is largest for Rainier Mesa events. M_S values at Yucca Flat tend to be larger than those at Rainer Mesa by 0.08 magnitude units for a given m_b. There also appears to be some difference in waveforms between events of these two source regions. Pahute Mesa events are 0.39 magnitude units larger than those at Yucca flat for explosions set-off below the water table and with the same m_b.

Although L_g measurements with a calibration shot give more accurate estimates of explosion yields, there may be cases where L_g "blockage," caused by strong lateral variations in the propagation path, may occur and one must use other methods, such as surface wave magnitudes, instead to estimate yields or for discriminating the event.

Chapter 3

Long-Period Explosion Source Spectra of Regional Surface Waves

3.1 Summary

Seismic moments of Nevada Test Site (NTS) explosions are determined from regional surface wave spectra. Two methods are used. In one the moment is solved for assuming only an explosive source, or average scalar moment; in the other a joint inversion for an isotropic (explosive) source plus a constrained double couple moment component representing tectonic strain release (TSR). Although the general moment tensor solution to this joint inversion problem is non-unique, if some assumptions are made concerning the non-isotropic moment components, then the remaining source parameters can be solved by a linear least-squares inversion scheme. We examine the errors in determining the isotropic moment component (M_I) by this latter method of constrained linear inversion solutions in a canonical study using a theoretical network of long-period (6-60 sec.) surface wave data. The network azimuthal coverage was chosen to represent that of a long-period North American super-network of 55 stations used for the actual NTS events. We compare these errors in moment estimate to

those obtained from surface wave magnitude (M_S) and spectral scalar moment (M_O) measurements for the same surface wave observations. For a ratio of $M_{(expl)}/M_{(eq)}$ less than 1.0 we find that the inverted M_I solution is a much better estimate of the actual isotropic moment than either M_S or M_O, and the standard deviation in this estimate is substantially less than that using the other two methods for the great majority of isotropic source + double couple sources. Even when the inversion constraints are off in dip and rake each by 30°, the mis-estimate of the isotropic moment is less than 35 percent of the actual value. In the case of a vertical strike-slip fault, the inverted isotropic moment solution which assumes this fault orientation is exact to three figures, whereas M_S and M_O under-estimate the moment by 45 percent and 32 percent, respectively because of uneven azimuthal coverage. This moment tensor inversion method is applied to determine the isotropic source for 109 NTS underground explosions using vertical and tangential component surface wave data from this regional network. We also calculate M_S and M_O for these same events and compare the results. Isotropic source errors are smallest using the spectral domain inversion method. However, this spectral domain method cannot attain as low a magnitude threshold as the time domain moment or M_S method. The extensive moment data set analyzed here were combined with larger yield explosions from prior moment studies to create a comprehensive data set with which to obtain conclusive, well-constrained long-period explosion source scaling relationships at the separate NTS sub-sites.

3.2 Introduction

The purpose of this work is to determine the precision of seismic moment (M_0) estimates of underground nuclear explosions determined from spectral measurements of intermediate-period (6 to 60 sec.), regional surface waves. Seismic moment is

a measure of low frequency seismic source spectrum. Besides being useful as a quantifier of earthquake sources, it also can be used to estimate seismic yields of explosions and employed in long-period:short-period discriminants (see chapter 4; Woods *et al.*, 1993). Chapter 2 (Woods and Harkrider, 1993) dealt with time-domain moment and magnitude (M_S) measurements of regional surface waves. A criticism of time domain amplitude measurements of regional surface waves is that lateral variations in the crustal structure cause multi-pathing and scattering which affect the peak amplitude of the Airy Phase, particularly for paths shorter than 1000 km for which the longer-period wave-train is not well dispersed. Spectral moment $M(\omega)$ measurements reduce this problem by averaging over the frequency band of interest. They are also insensitive to spall effects which are significant primarily in this 0.2 to 2 Hz frequency bandwidth (Taylor and Randall, 1989), since the spectral moment is calculated between 0.0167 and 0.167 Hz.

Unlike short-period body wave amplitudes, surface waves are relatively insensitive to source region attenuation effects which give rise to m_b biases in yield-magnitude relationships between inter-regional testing sites.

Previous moment studies of explosions have relied on distant regional ($D > 1000$ km) and teleseismic surface wave measurements and as such only the larger explosions ($m_b \geq 5.5$) could be examined. Stevens (1986) determined scalar moments, assuming a pure isotropic (explosive) source, for Nevada Test Site (NTS) and East Kazakhstan Test Site events. Given and Mellman (1986) inverted fundamental-mode Rayleigh and Love wave spectral data to obtain the isotropic component and double-couple component (due to tectonic strain release) of the source moment tensor for virtually the same data set. Both studies relied on seismic networks with poor azimuthal coverage and included mixed continental-oceanic paths which, as discussed in chapter 2, can significantly alter surface wave-train waveforms and spectral content. Although both studies made use of uniquely derived path structures to account for

propagation effects, they also made use of empirically derived "station corrections" directly or indirectly, but which are, in fact, path corrections to reduce the scatter in the network averaged moment caused by apparent errors in modeling the paths. These two studies also relied heavily on hand-digitized data for events in the 70's; the digital data available was, for the most part, from stations with oceanic paths. One would rather use digitized data from pure continental paths, since waveforms should be more reliable and the signal to noise ratio (SNR) should be better, particularly for smaller events. The mixed-path approximation theory for synthetic surface wave generation discussed in chapter 2 (Woods and Harkrider, 1993) works best for paths that aren't radically different, so it is not clear that this approximation would work well for ocean-continent paths.

Evernden *et al.* (1971) suggest, that with high dynamic range digital seismometers, it should be possible to observe surface waveforms from small earthquakes ($m_b \approx 4.0$) up to 6000 km distance away; for explosions which have relatively lower level long-period source spectra, a higher detection threshold would be expected.

This study re-investigates the long-period source spectrum (seismic moment) of explosions using surface wave spectral amplitude measurements from digitally recorded, reasonably high dynamic range, regional (375 km $<$ 5000 km) waveforms. Such data have been used in earthquake source studies (Patton and Zandt, 1991; Yelin and Patton, 1991; and Thio and Kanamori, 1992), but until now has not been applied to underground explosion source studies. We wish to determine whether such data better constrain moment estimates of explosions and whether the observational magnitude threshold for measuring surface moments can be lowered. This study is confined to NTS events; however, it is a more comprehensive data set in that it includes 109 events–nearly three times as many events as the previous studies and events from Rainier Mesa are examined as well. As in chapter 2, localized site effects on moment estimates can be studied. The digital data for this study is not

as comprehensive as that in chapter 2 which included many analog data, so that it will not be possible to constrain the magnitude-moment scaling relationships as well as the in time-domain moment-M_S moment study.

With the use of nearer regional stations, better azimuthal coverage of NTS is attainable. This is important for obtaining unbiased average scalar moments and/or to invert for non-isotropic moment components. Also with shorter paths, errors in propagation effects, principally because of attenuation, Q, will be smaller than for the longer paths.

Particular attention is paid to error analysis in this study, since high confidence levels in nuclear monitoring are a primary concern. Standard deviations in scalar moments estimates by Stevens (1986) ranged between 12 and 200 percent , with most being under 25 percent. While no error analysis appears to have been conducted in the moment tensor inversion study, it was found that some explosions exhibited radiation patterns which have double-couple moment components as large as 50 percent of the isotropic moment component. The explosions with the largest apparent tectonic strain release moments in the Given and Mellman study also tended to have the largest error estimates in the Stevens (1986) scalar moment study. Hence it would be instructive to examine how well correcting for tectonic release effects would reduce the variance in moment estimates.

The assumption that the radiation pattern from an explosive source has no azimuthal dependence, while theoretically sound, is not born out in practice. Many researchers have reported evidence for a non-isotropic component for explosion sources (Press and Archambeau, 1962; Brune and Pomeroy, 1963; Toksöz *et al.*, 1971; Toksöz and Kehrer, 1972; Wallace *et al.*, 1985) and has been attributed predominantly to tectonic strain release (Archambeau and Sammis, 1970) and, more recently, to asymmetric explosion cavities (Zhao and Harkrider, 1992). This additional source can have appreciable long-period content, and as such can effect surface wave radiation

patterns (Helle and Rygg, 1984; Given and Mellman, 1986), and thus bias moment estimates if it is not accounted for.

The most general moment tensor inversion solution for a joint isotropic + double-couple source is non-unique (Mendiguren, 1977; Ekström and Richards, 1993). And for very shallow sources some off-diagonal elements of the moment tensor become unresolvable (Kanamori and Given, 1981; and Patton, 1988a). If one is to invert for source depth and source time functions, the problem becomes non-linear and even more complicated. In the inversion procedure developed herein, several assumptions are made concerning the sources. The tectonic release source and explosion sources are both modeled as step moment source time functions coincident in time and depth, which are reasonable assumptions for the periods measured (6-60 sec.). Secondly, as described later in the Inversion Method Section, certain moment tensor components and source excitation functions are assumed to be negligible when source depth is taken as the limit $h \rightarrow 0$ (see Given and Mellman, 1986, for details). The tectonic release radiation pattern is assumed to be modeled as a double-couple source. Further, the dip and rake of the double-couple fault plane are constrained by previous studies of tectonic release at NTS to be predominantly vertical, strike-slip in nature with a $sin2\phi$ radiation pattern (Toksöz *et al.*, 1965; Aki and Tsai, 1972; Wallace *et al.*, 1983 and 1985; Lay *el al*, 1984; Given and Mellman, 1986), with the strike angle varying between N10^{o}W and N60^{o}W.

The tectonic release strike angle (ϕ), moment (M_{DC}), and the explosion moment (M_I) are then inverted from fundamental-mode Rayleigh wave and Love wave spectra in what is then a one-step linear least-squares inversion. The errors in M_I are compared to those of scalar moments (M_0). The source parameters and yield-magnitude relationships are compared between the three major NTS sub-sites: Pahute Mesa, Rainier Mesa, and Yucca Flats.

3.3 Data Processing and Analysis

The digital and digitized data of chapter 2 (Woods and Harkrider, 1993) are used in this study. Table 3.1 lists, in chronological order, the events used along with available source information. In the date column is the Julian date. The three-letter site code (3rd column) gives the NTS sub-site location (P=Pahute Mesa, Y=Yucca Flat, R=Rainier Mesa (Tunnel shots), or C=Climax Stock), whether the shot was detonated above (A) or below (B) the water table, and rock type (T=Volcanic Tuff, G=Granite, R=Rhyolite, A=Alluvium). When available, the shot point elevation and depth of burial are given. Also listed, when available, are body wave magnitudes determined by the International Seismic Centre (ISC) and Lilwall and Neary (1985) (L), and local magnitudes. Data for events before 1982 are digitized records, while all later events rely on digital recordings. In most cases the vertical and two horizontal components are all available for any particular event-station pair, although for a small minority of the data pairs only the vertical or horizontal component records were usable/existent. Horizontal components were rotated to their great circle path to obtain the transverse component; the radial components were not used as they yield only redundant P-SV wavefield (Rayleigh wave) information and can be contaminated with scattered transverse component energy. Horizontal components also, in general, have a lower SNR than vertical components.

The SNR for some observations is low, particularly for the smaller events ($m_b \approx$ 5.0 and below), with long-period ($T > 60$ sec) noise overwhelming the transient signal. High-pass filtering improved the time-domain SNR significantly, making positive identification of Love waves much easier. In examining the ensemble of records, it became apparent that Love waves were observed for almost all events. The largest Love waves are associated with Pahute Mesa and Rainier events; however, most Yucca shots also showed evidence of Love wave generation. Most of the low-magnitude events were from Yucca Flat, so that the lack of Love wave observations may be due

Table 1 (a): Event Information										
NAME	Date	Site	Lat.	Lon.	Elev.	Depth	$m_{b(I)}$	$m_{b(L)}$	σ_{m_b}	M_L
WAGTAIL	65062	YBT	37.06	-116.04	1237	-750		5.53	0.06	5.0
LAMPBLACK	66018	YBT	37.09	-116.02	1294	-561	5.2	5.27	0.08	5.2
REX	66055	PBT	37.27	-116.43	1998	-672	4.8			4.8
PIRANHA	66133	YBT	37.09	-116.03	1264	-549	5.6	5.60	0.04	5.1
PILEDRIVER	66153	CBG	37.23	-116.06	1535	-463	5.6	5.63	0.04	5.0
TAN	66154	YBT	37.07	-116.04	1249	-561	5.7	5.69	0.03	4.9
MIDIMIST	67177	RAT	37.20	-116.21	2226	-374	5.1			4.5
DOORMIST	67243	RAT	37.18	-116.21	2325	-446	5.0	4.83		4.8
COBBLER	67312	YBT	37.09	-116.04	1269	-671	5.1			
DORSALFIN	68060	RAT	37.18	-116.21	2287	-410	5.0	5.12	0.08	
HUDSONSEAL	68268	RAT	37.20	-116.21	2191	-333	5.0	4.97	0.08	
WINESKIN	69015	RAT	37.21	-116.23	2290	-518	5.3	5.32	0.05	5.0
CYPRESS	69043	RAT	37.17	-116.21	2292	-412		4.83		
BLENTON	69120	YBT	37.08	-116.01	1281	-558	5.3	5.32	0.04	
DIANAMIST	70042	RAT	37.18	-116.21	2225	-399	4.6	4.84	0.08	4.5
SHAPER	70082	YBT	37.09	-116.02	1279	-561	5.5	5.51	0.03	
MINTLEAF	70125	RAT	37.22	-116.18	2121	-405	5.2	5.04	0.06	4.6
HUDSONMOON	70146	RAT	37.18	-116.21	2301	-422	5.0			4.6
CAMPHOR	71180	RAT	37.18	-116.21			4.9	4.85	0.08	
MINIATA	71189	YBT	37.11	-116.05	1274	-529	5.5	5.53	0.03	5.3
ALGODONES	71230	YBT	37.06	-116.04	1233	-528	5.4	5.40	0.04	5.2
MISTYNORTH	72123	RAT	37.21	-116.21	2226	-377	5.0	4.85	0.06	
MONERO	72140	YBT	37.06	-116.00	1272	-537	4.9	4.59	0.04	4.5
DIAMONDSCULLS	72202	RBT	37.21	-116.18	2140	-424	5.0	4.98	0.04	4.6
MIERA	73067	YBT	37.10	-116.03	1306	-569	5.4	5.34	0.03	5.4
STARWORT	73116	YBT	37.12	-116.06	1288	-564	5.6	5.54	0.02	5.3
DIDOQUEEN	73156	RAT	37.18	-116.22	2274	-391	5.1	5.02	0.05	4.8
LATIR	74058	YBT	37.10	-116.05			5.8	5.64	0.02	5.4

Table 3.1: NTS Event source information.

Table 1 (b)

NAME	Date	Site	Lat.	Lon.	Elev.	Depth	$m_{b(I)}$	$m_{b(L)}$	σ_{m_b}	M_L
MINGBLADE	74170	RAT	37.21	-116.21			5.0	4.97	0.04	
ESCABOSA	74191	YBT	37.08	-116.03			5.7	5.74	0.02	5.6
STANYAN	74269	YBT	37.13	-116.07			5.6	5.52	0.03	5.0
CABRILLO	75066	YBA	37.13	-116.08	1315	-600	5.5	5.57	0.03	5.2
DININGCAR	75095	RAT	37.19	-116.21	2265	-305	4.8	4.94	0.03	4.5
OBAR	75120	YBT	37.11	-116.03			5.2	5.12	0.04	5.0
MIZZEN	75154	YBT	37.09	-116.04	1274	-637	5.7	5.71	0.02	5.6
HUSKYPUP	75297	RAT	37.22	-116.18	2063	-348	4.7	4.87	0.05	4.7
KEELSON	76035	YBT	37.07	-116.03	1285	-655	5.8	5.72	0.02	5.8
MIGHTYEPIC	76133	RAT	37.21	-116.21	2251		4.9	4.85	0.05	4.6
RUDDER	76363	YBT	37.10	-116.04	1282	-640	5.5	5.69	0.02	5.5
BULKHEAD	77117	YBT	37.09	-116.03	1286	-594	5.4	5.43	0.03	5.1
CREWLINE	77145	YBT	37.09	-116.04	1252	-564	5.3	5.40	0.03	5.3
LOWBALL	78193	YBT	37.08	-116.04	1252	-564	5.5	5.72	0.02	5.4
QUARGEL	78322	YBT	37.13	-116.08	1302	-542	5.1	5.34	0.03	5.2
QUINELLA	79039	YBT	37.10	-116.05	1302	-542	5.5	5.71	0.02	5.2
PYRAMID	80107	YBT	37.10	-116.03	1293	-579	5.3	5.45	0.03	5.3
MINERSIRON	80305	RAT	37.24	-116.21	2239	-390	4.7	4.97	0.06	4.9
BASEBALL	81015	YAT	37.09	-116.04	1259	-564	5.6	5.72	0.02	5.5
JORNADA	82028	YBT	37.09	-116.05	1260	-640	5.9	5.92	0.02	5.6
MOLBO	82043	PBR	37.22	-116.46	1900	-651	5.6	5.43	0.03	5.4
HOSTA	82044	PAR	37.35	-116.32	2103	-640	5.6	5.55	0.02	5.5
TENAJA	82107	YAT	37.02	-116.01	1210	-357	4.5	4.59	0.15	4.4
GIBNE	82115	PAT	37.26	-116.42	1964	-570	5.4	5.38	0.03	5.4
KRYDDOST	82126	Y__	37.12	-116.13	1390	-325	4.3			4.4
BOUSCHET	82127	YBT	37.07	-116.05	1244	-564	5.7	5.73	0.02	5.4
NEBBIOLO	82175	PAR	37.24	-116.37	2065	-640	5.6	5.65	0.02	5.6
MONTEREY	82210	YAT	37.10	-116.07	1280	-400	4.5	4.97	0.06	4.6

Table 1 (c)

NAME	Date	Site	Lat.	Lon.	Elev.	Depth	$m_{b(I)}$	$m_{b(L)}$	σ_{m_b}	M_L
ATRISCO	82217	YBT	37.08	-116.01	1295	-640	5.7	5.73	0.02	5.4
HURONLANDING	82266	RAT	37.21	-116.01	2260	-408	4.9	5.04	0.04	4.8
BORREGO	82272	YBT	37.09	-116.04	1261	-564				4.1
FRISCO	82267	YAT	37.17	-116.09	1374	-451	4.9	4.97	0.06	4.8
MANTECA	82344	YAA	37.03	-116.07	1263	-413	4.6	4.78	0.06	4.7
CABRA	83085	PAR	37.30	-116.46	1934	-543	5.1	5.24	0.03	5.2
TORQUOISE	83104	YBT	37.07	-116.05	1246	-533	5.7	5.73	0.03	5.5
CROWDIE	83125	YAA	37.01	-116.09	1336	-390	4.5	4.51	0.06	4.3
FAHADA	83146	YAT	37.10	-116.01	1339	-384	4.4	4.63	0.10	4.4
DANABLU	83160	YAT	37.16	-116.09	1353	-320	4.5	4.60	0.06	4.6
CHANCELLOR	83244	PAR	37.27	-116.36	2040	-625	5.4	5.41	0.03	5.3
MIDNITEZEPHYR	83264	RAT	37.21	-116.21	2257	-405				4.1
TECHADO	83265	YBT	37.11	-116.05	1268	-533				4.1
ROMANO	83350	YAT	37.14	-116.07	1314	-515	5.1	5.16	0.04	5.0
MILAGRO	84046	RAT	37.22	-116.18	2076	-361	5.0	5.11	0.04	4.8
TORTUGAS	84061	YBT	37.07	-116.05	1243	-639	5.9	5.83	0.02	5.5
MUNDO	84122	YBT	37.11	-116.02	1319	-567	5.3	5.49	0.03	5.3
CAPROCK	84152	YBT	37.10	-116.05	1264	-600	5.8	5.72	0.02	5.6
DUORO	84172	YAT	37.00	-116.04	1207	-381	4.6	4.81	0.07	4.5
KAPPELI	84207	PAR	37.27	-116.41	2010	-640	5.3	5.37	0.03	5.2
CORREO	84215	YAT	37.02	-116.01	1209	-335	4.7	4.74	0.07	4.4
DOLCETTO	84243	YAT	37.09	-115.99	1318	-366	4.5	4.75	0.10	4.3
BRETON	84257	YAT	37.09	-116.07	1265	-483	5.0	5.15	0.04	5.0
VILLITA	84315	YAA	37.00	-116.02	1205	-373	4.5	4.62	0.10	4.4
EGMONT	84344	PAT	37.27	-116.49	1867	-551	5.5	5.44	0.03	5.4
TIERRA	84350	PAR	37.28	-116.31	2145	-640	5.4	5.44	0.03	5.4
VAUGHN	85074	YAT	37.06	-116.05	1238	-427	4.8	4.98	0.05	4.6
COTTAGE	85082	YAT	37.18	-116.09	1389	-515	5.3	5.38	0.04	5.1

Table 1 (d)

NAME	Date	Site	Lat.	Lon.	Elev.	Depth	$m_{b(I)}$	$m_{b(L)}$	σ_{m_b}	M_L
HERMOSA	85092	YBT	37.10	-116.03	1278	-640	5.7	5.77	0.02	5.6
MISTYRAIN	85096	R_T	37.20	-116.21	1850	-389	4.8	4.98	0.04	4.8
TOWANDA	85122	PBT	37.25	-116.33	2112	-661	5.7	5.68	0.02	5.4
SALUT	85163	PBR	37.25	-116.49	1900	-608	5.5	5.37	0.03	5.3
SERENA	85206	PAR	37.30	-116.44	1969	-597	5.2	5.24	0.03	5.1
PONIL	85270	YAT	37.09	-116.00	1312	-366	4.6	4.53	0.07	4.5
ROQUEFORT	85289	YAT	37.11	-116.12	1368	-415	4.6	4.50	0.07	4.6
KINIBITO	85339	YBT	37.05	-116.05	1235	-600	5.7	5.67	0.02	5.2
GOLDSTONE	85362	P__	37.24	-116.47	1914	-500	5.3	5.31	0.03	5.1
GLENCOE	86081	YBT	37.08	-116.07	1260	-600	5.4	5.35	0.03	5.0
MIGHTYOAK	86100	RAT	37.22	-116.18	2111	-400	4.9	5.09	0.05	4.9
JEFFERSON	86112	PAR	37.26	-116.44	1982	-600	5.3	5.26	0.03	5.4
PANAMINT	86141	YAT	37.13	-116.06	1286	-480	4.8			3.9
TAJO	86156	YAT	37.10	-116.02	1316	-518	5.3	5.36	0.03	5.3
DARWIN	86176	P__	37.27	-116.50	1876	-549	5.5	5.55	0.03	5.3
CYBAR	86198	PAR	37.28	-116.36	2044	-628	5.7	5.65	0.02	5.5
CORNUCOPIA	86205	YAA	37.14	-116.07	1314	-400	4.4	4.52	0.07	4.4
LABQUARK	86273	PAR	37.30	-116.31	2127	-600	5.5	5.51	0.03	5.2
BELMONT	86289	P__	37.22	-116.46	1898	-600	5.6	5.56	0.03	5.5
GASCON	86318	YAT	37.10	-116.05	1263	-600	5.8	5.80	0.03	5.6
BODIE	86347	PAT	37.26	-116.41	2018	-600	5.5	5.50	0.03	5.4
DELAMAR	87108	P__	37.25	-116.51	1902	-500	5.5	5.46	0.03	5.3
HARDIN	87120	PAT	37.23	-116.42	1970	-600	5.5	5.44	0.03	5.3
PANCHUELA	87181	YAA	36.99	-116.04	1206	-300	4.6	4.64		4.0
TAHOKA	87225	Y_A	37.06	-116.05	1239	-600	5.9	5.81	0.03	5.5
LOCKNEY	87267	P__	37.23	-116.38	2072	-600	5.7	5.61	0.03	5.4
BORATE	87296	Y__	37.14	-116.08	1321	-500	5.2	5.27	0.03	5.0

Figure 3.1: Explosion-generated surface waves observed at Albequerque, N.M. (ALQ), some 900 km from NTS.

ALQ (a)

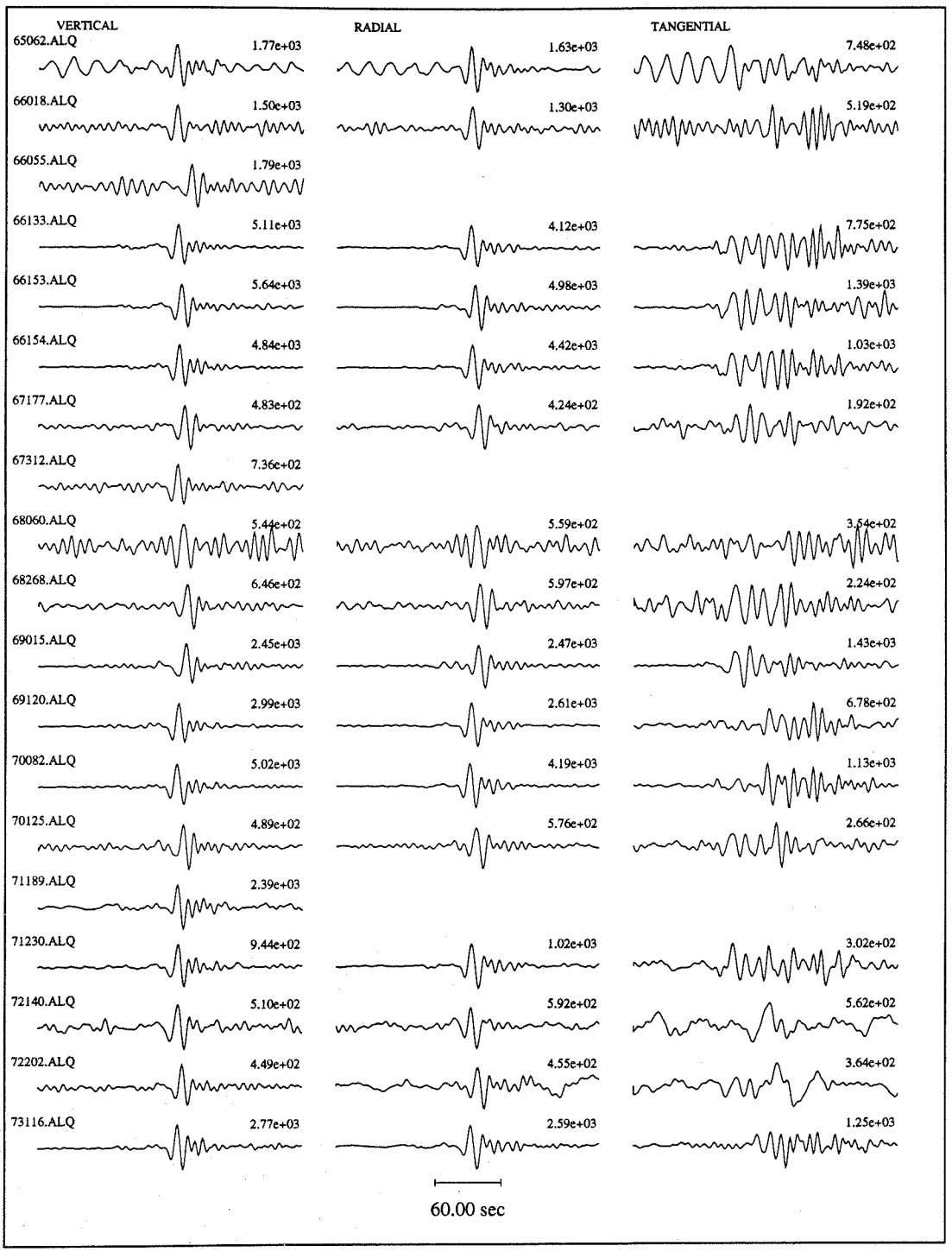
VERTICAL
RADIAL
TANGENTIAL
65062.ALQ
1.77e+03
1.63e+03
7.48e+02
66018.ALQ
1.50e+03
1.30e+03
5.19e+02
66055.ALQ
1.79e+03
66133.ALQ
5.11e+03
4.12e+03
7.75e+02
66153.ALQ
5.64e+03
4.98e+03
1.39e+03
66154.ALQ
4.84e+03
4.42e+03
1.03e+03
67177.ALQ
4.83e+02
4.24e+02
1.92e+02
67312.ALQ
7.36e+02
68060.ALQ
5.44e+02
5.59e+02
3.54e+02
68268.ALQ
6.46e+02
5.97e+02
2.24e+02
69015.ALQ
2.45e+03
2.47e+03
1.43e+03
69120.ALQ
2.99e+03
2.61e+03
6.78e+02
70082.ALQ
5.02e+03
4.19e+03
1.13e+03
70125.ALQ
4.89e+02
5.76e+02
2.66e+02
71189.ALQ
2.39e+03
71230.ALQ
9.44e+02
1.02e+03
3.02e+02
72140.ALQ
5.10e+02
5.92e+02
5.62e+02
72202.ALQ
4.49e+02
4.55e+02
3.64e+02
73116.ALQ
2.77e+03
2.59e+03
1.25e+03
60.00 sec

ALQ (b)

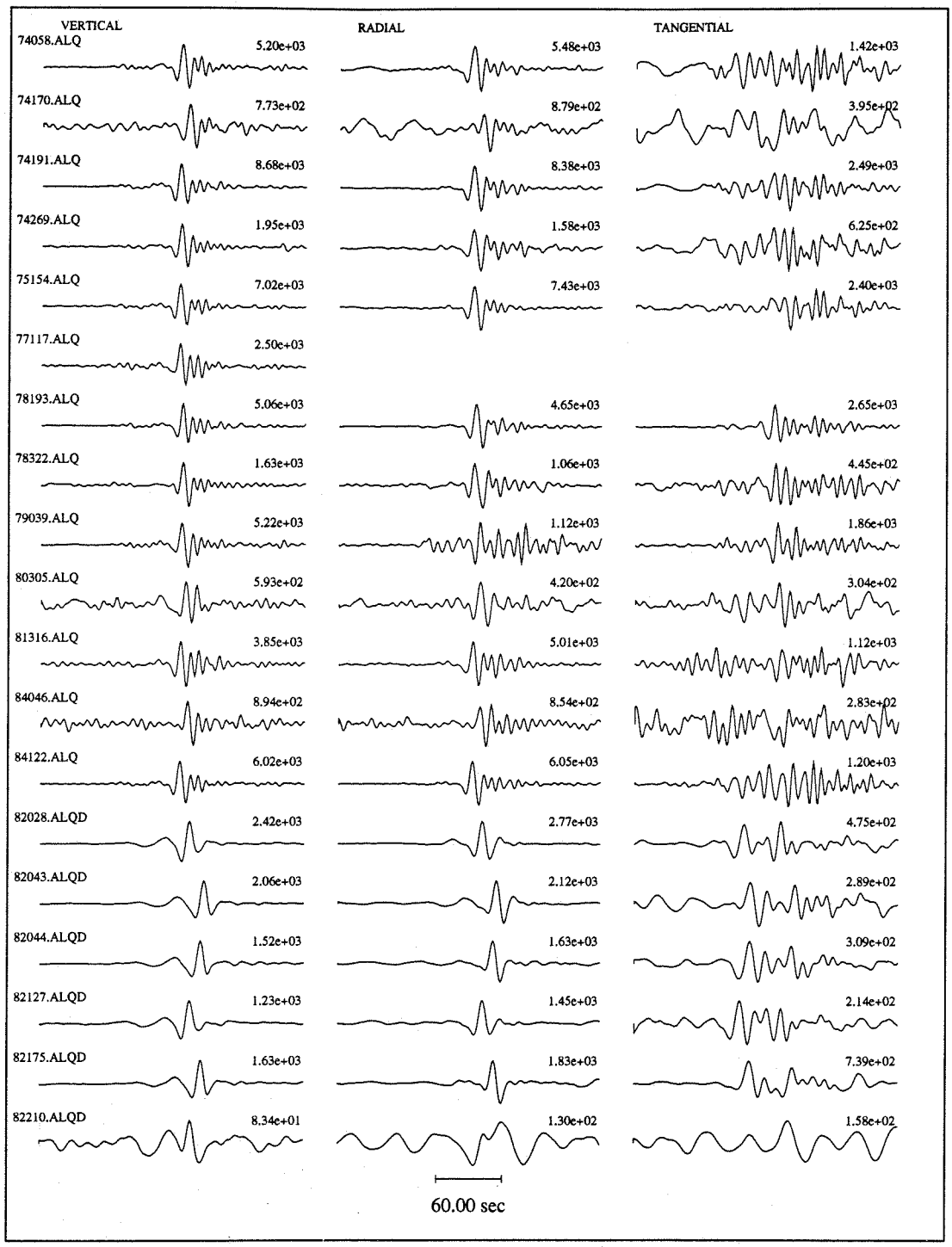
VERTICAL
RADIAL
TANGENTIAL
74058.ALQ
5.20e+03
5.48e+03
1.42e+03
74170.ALQ
7.73e+02
8.79e+02
3.95e+02
74191.ALQ
8.68e+03
8.38e+03
2.49e+03
74269.ALQ
1.95e+03
1.58e+03
6.25e+02
75154.ALQ
7.02e+03
7.43e+03
2.40e+03
77117.ALQ
2.50e+03
78193.ALQ
5.06e+03
4.65e+03
2.65e+03
78322.ALQ
1.63e+03
1.06e+03
4.45e+02
79039.ALQ
5.22e+03
1.12e+03
1.86e+03
80305.ALQ
5.93e+02
4.20e+02
3.04e+02
81316.ALQ
3.85e+03
5.01e+03
1.12e+03
84046.ALQ
8.94e+02
8.54e+02
2.83e+02
84122.ALQ
6.02e+03
6.05e+03
1.20e+03
82028.ALQD
2.42e+03
2.77e+03
4.75e+02
82043.ALQD
2.06e+03
2.12e+03
2.89e+02
82044.ALQD
1.52e+03
1.63e+03
3.09e+02
82127.ALQD
1.23e+03
1.45e+03
2.14e+02
82175.ALQD
1.63e+03
1.83e+03
7.39e+02
82210.ALQD
8.34e+01
1.30e+02
1.58e+02
60.00 sec

ANMO (c)

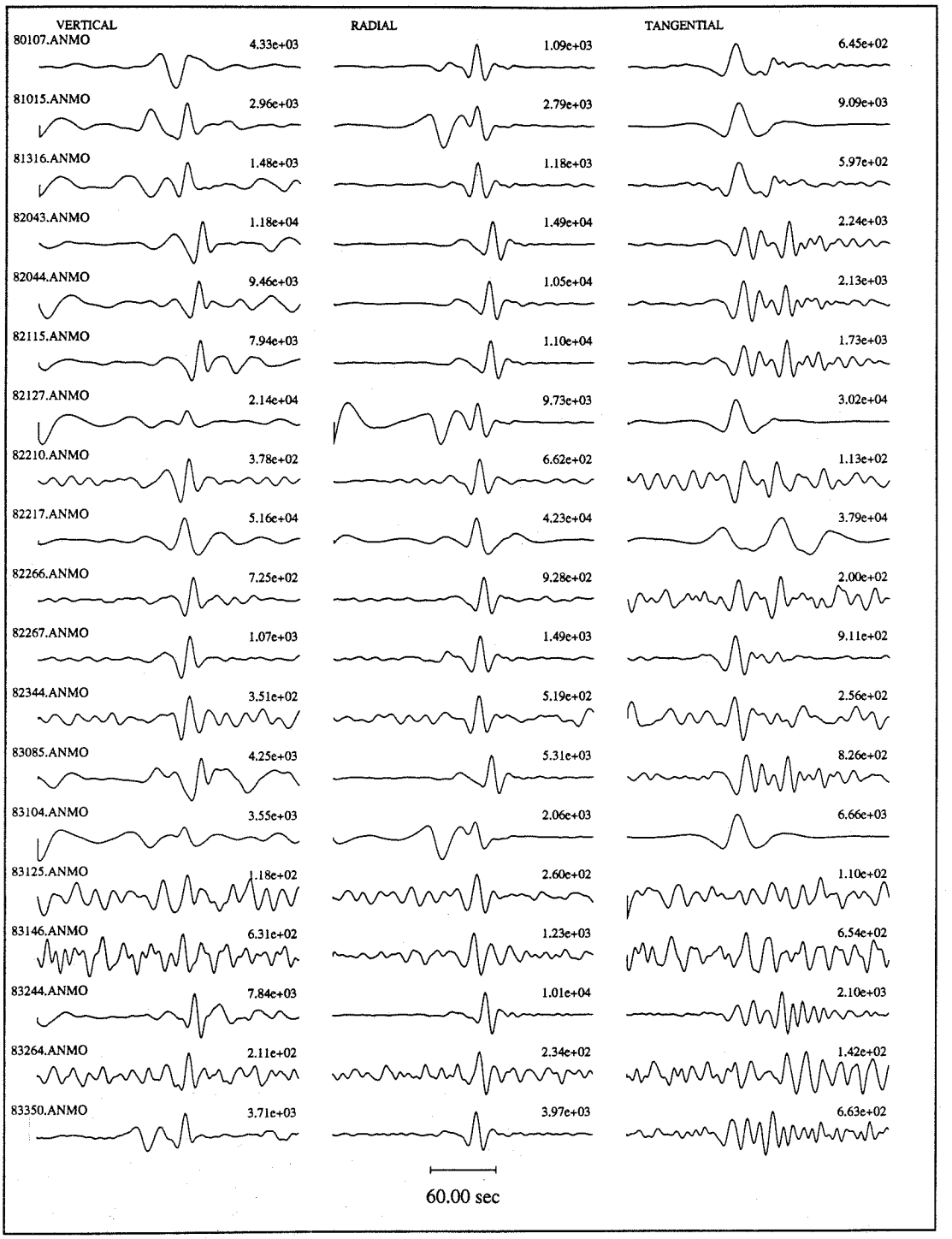
VERTICAL
RADIAL
TANGENTIAL
80107.ANMO
4.33e+03
1.09e+03
6.45e+02
81015.ANMO
2.96e+03
2.79e+03
9.09e+03
81316.ANMO
1.48e+03
1.18e+03
5.97e+02
82043.ANMO
1.18e+04
1.49e+04
2.24e+03
82044.ANMO
9.46e+03
1.05e+04
2.13e+03
82115.ANMO
7.94e+03
1.10e+04
1.73e+03
82127.ANMO
2.14e+04
9.73e+03
3.02e+04
82210.ANMO
3.78e+02
6.62e+02
1.13e+02
82217.ANMO
5.16e+04
4.23e+04
3.79e+04
82266.ANMO
7.25e+02
9.28e+02
2.00e+02
82267.ANMO
1.07e+03
1.49e+03
9.11e+02
82344.ANMO
3.51e+02
5.19e+02
2.56e+02
83085.ANMO
4.25e+03
5.31e+03
8.26e+02
83104.ANMO
3.55e+03
2.06e+03
6.66e+03
83125.ANMO
1.18e+02
2.60e+02
1.10e+02
83146.ANMO
6.31e+02
1.23e+03
6.54e+02
83244.ANMO
7.84e+03
1.01e+04
2.10e+03
83264.ANMO
2.11e+02
2.34e+02
1.42e+02
83350.ANMO
3.71e+03
3.97e+03
6.63e+02
60.00 sec

ANMO (d)

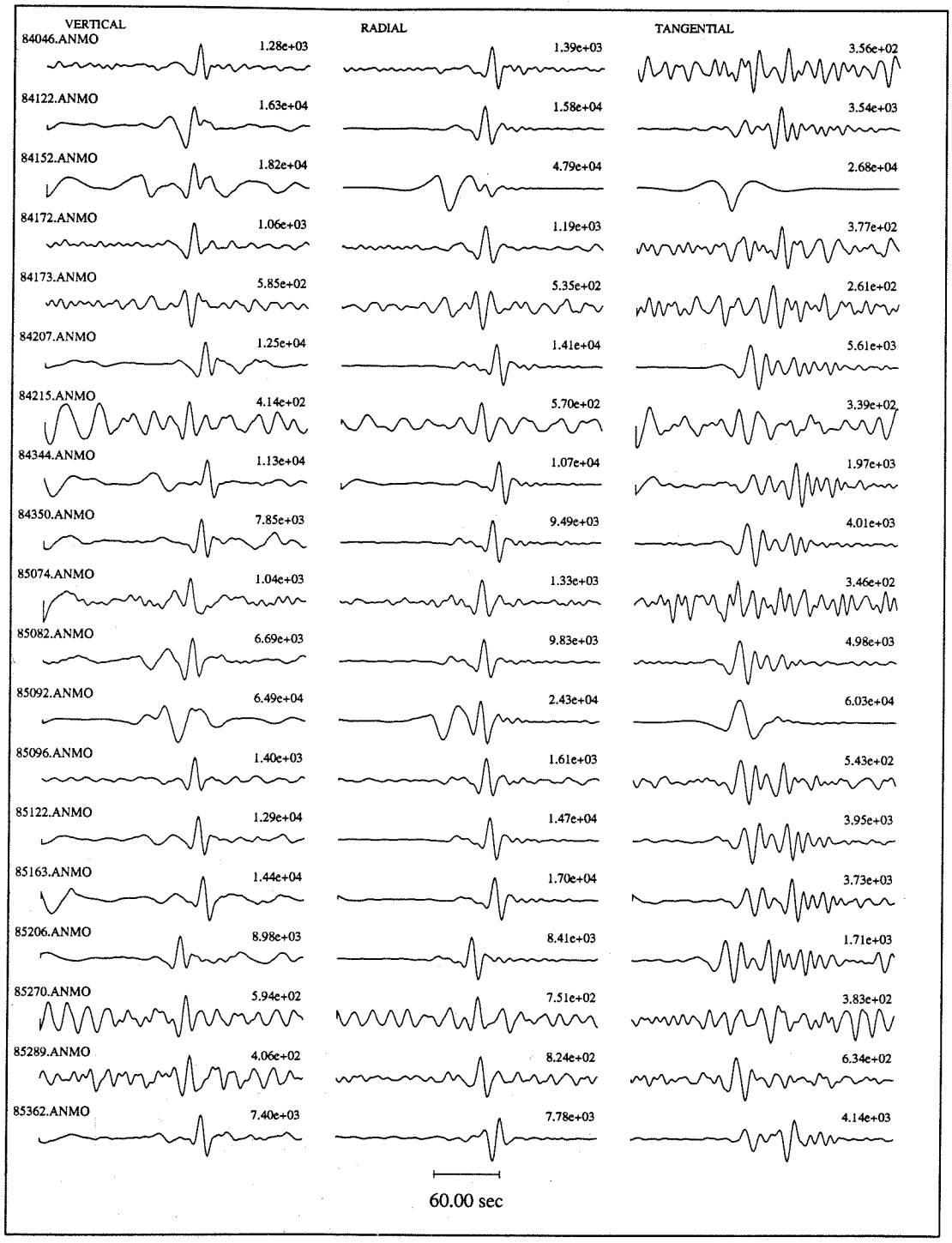
VERTICAL
RADIAL
TANGENTIAL
84046.ANMO
1.28e+03
1.39e+03
3.56e+02
84122.ANMO
1.63e+04
1.58e+04
3.54e+03
84152.ANMO
1.82e+04
4.79e+04
2.68e+04
84172.ANMO
1.06e+03
1.19e+03
3.77e+02
84173.ANMO
5.85e+02
5.35e+02
2.61e+02
84207.ANMO
1.25e+04
1.41e+04
5.61e+03
84215.ANMO
4.14e+02
5.70e+02
3.39e+02
84344.ANMO
1.13e+04
1.07e+04
1.97e+03
84350.ANMO
7.85e+03
9.49e+03
4.01e+03
85074.ANMO
1.04e+03
1.33e+03
3.46e+02
85082.ANMO
6.69e+03
9.83e+03
4.98e+03
85092.ANMO
6.49e+04
2.43e+04
6.03e+04
85096.ANMO
1.40e+03
1.61e+03
5.43e+02
85122.ANMO
1.29e+04
1.47e+04
3.95e+03
85163.ANMO
1.44e+04
1.70e+04
3.73e+03
85206.ANMO
8.98e+03
8.41e+03
1.71e+03
85270.ANMO
5.94e+02
7.51e+02
3.83e+02
85289.ANMO
4.06e+02
8.24e+02
6.34e+02
85362.ANMO
7.40e+03
7.78e+03
4.14e+03
60.00 sec

ANMO (e)

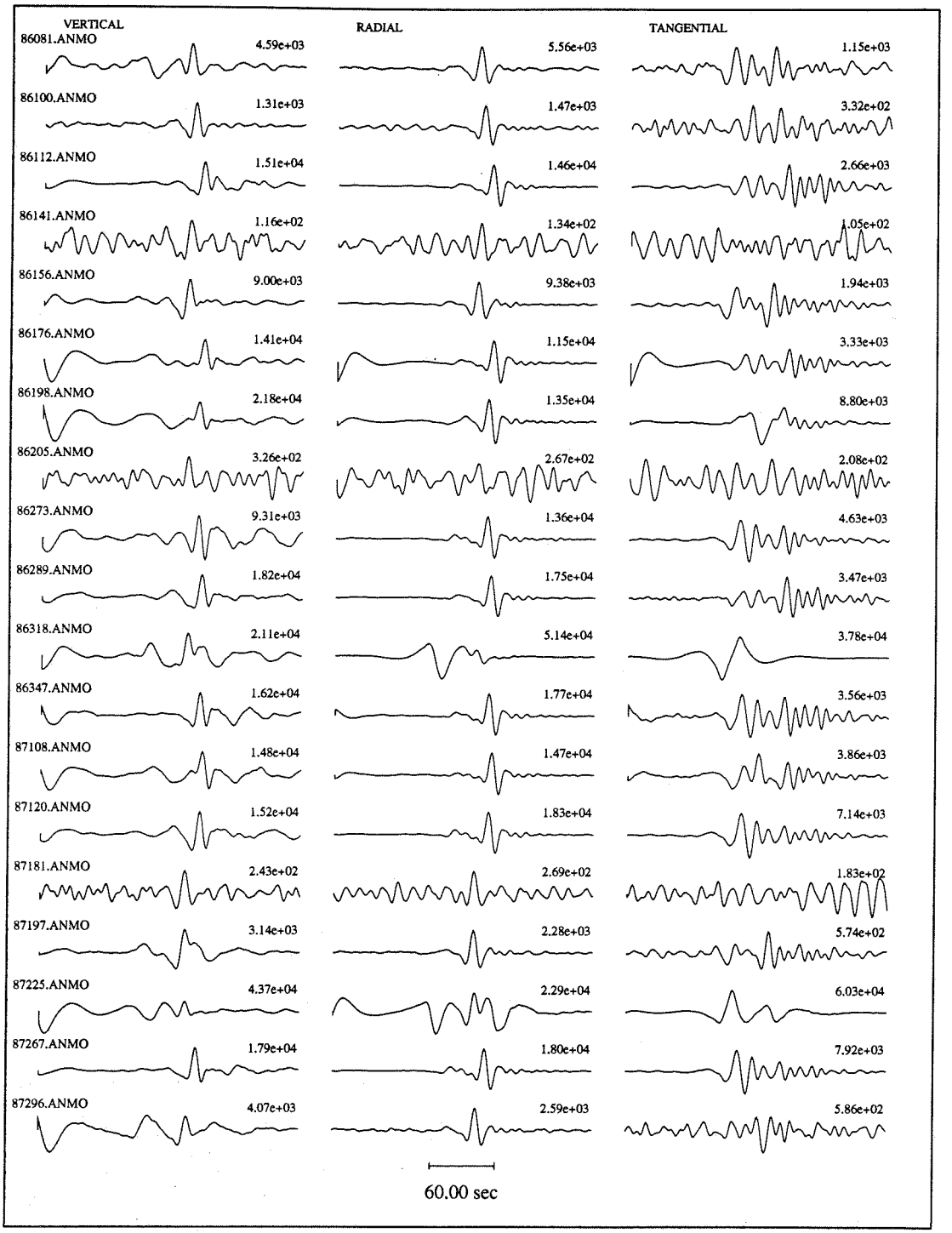
VERTICAL
RADIAL
TANGENTIAL
86081.ANMO 4.59e+03 5.56e+03 1.15e+03
86100.ANMO 1.31e+03 1.47e+03 3.32e+02
86112.ANMO 1.51e+04 1.46e+04 2.66e+03
86141.ANMO 1.16e+02 1.34e+02 1.05e+02
86156.ANMO 9.00e+03 9.38e+03 1.94e+03
86176.ANMO 1.41e+04 1.15e+04 3.33e+03
86198.ANMO 2.18e+04 1.35e+04 8.80e+03
86205.ANMO 3.26e+02 2.67e+02 2.08e+02
86273.ANMO 9.31e+03 1.36e+04 4.63e+03
86289.ANMO 1.82e+04 1.75e+04 3.47e+03
86318.ANMO 2.11e+04 5.14e+04 3.78e+04
86347.ANMO 1.62e+04 1.77e+04 3.56e+03
87108.ANMO 1.48e+04 1.47e+04 3.86e+03
87120.ANMO 1.52e+04 1.83e+04 7.14e+03
87181.ANMO 2.43e+02 2.69e+02 1.83e+02
87197.ANMO 3.14e+03 2.28e+03 5.74e+02
87225.ANMO 4.37e+04 2.29e+04 6.03e+04
87267.ANMO 1.79e+04 1.80e+04 7.92e+03
87296.ANMO 4.07e+03 2.59e+03 5.86e+02
60.00 sec

to the extremely low SNR. Also, the smaller events can only be observed at the nearer stations, so that the Rayleigh and Love wavefields have not separated enough in time by dispersion to identify the Love wave, since the Love wave is a pulse and arriving near and within the Rayleigh wave time window. Figures 3.1 and 3.2 plot the three component records for LON (Longmire, WA) and ALQ-ANMO (Albequerque, NM), respectively. These two stations were the best-reporting for the network used in this study. Both stations were upgraded with longer-period instruments for events after 1982, which explains the oberved difference in frequency content between the two types of records. Love waves are present on all but the lowest SNR records, implying that tectonic strain release or some other effect is generating a non-isotropic source. Given and Mellman (1986) found that all events they studied displayed evidence of tectonic strain release. However, their study was confined to large ($m_b > 5.5$) events.

Poor quality data such as ANMO: 85092, 82217(tang), 82127, 84152, 86318 and 87197(vert) were removed. Low SNR tangential components were removed in cases where the vertical component was kept, such as ANMO: 87181 and 86141, or ALQ: 65062 and 72140. All seismograms were bandpass-filtered between 6 and 60 seconds to best observe the wavetrain and for data analysis. Synthetic seismograms were filtered identically. Next, cosine-tapered time windows were applied to vertical and tangential records in an attempt to remove all but the fundamental-mode Rayleigh wave and Love wave respectively. A more robust alternative to this time-domain windowing would be to phase-match-filter (Herrin and T. Goforth, 1977) the records, particularly the tangential component and all low SNR records, in order to remove noise and Rayleigh contamination, particularly for nearer stations where the fundamental-mode Rayleigh wave and Love wave group arrival times overlap.

Next, the spectral ratio of each windowed record and its appropriate synthetic is computed by averaging over the 0.167 to 0.0167 Hz bandwidth. The standard deviation in the spectral ratio estimate is taken as the error in the observation.

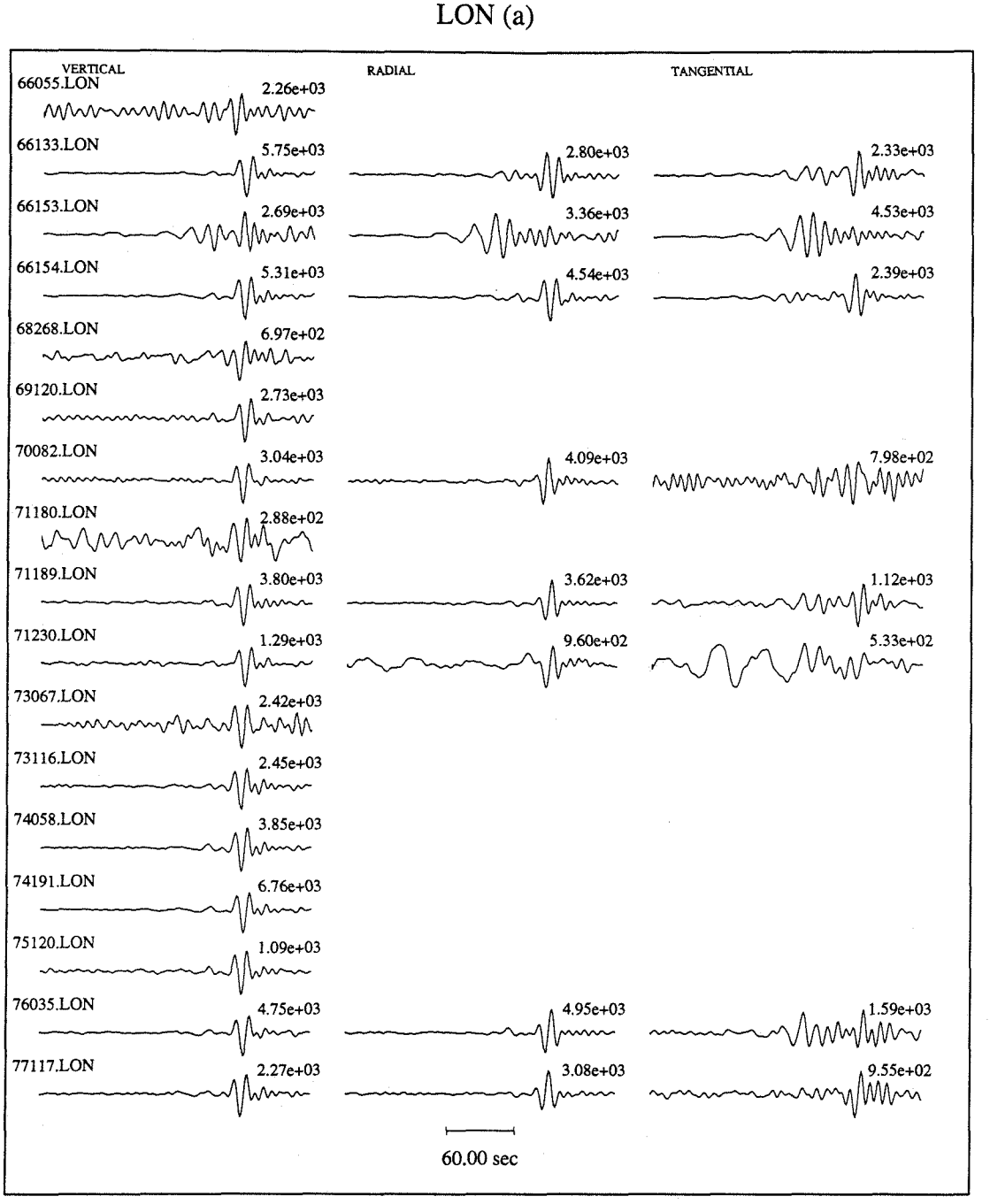

Figure 3.2: Explosion-generated surface waves observed at Longmire, WA (LON), some 1150 km from NTS.

LON (b)

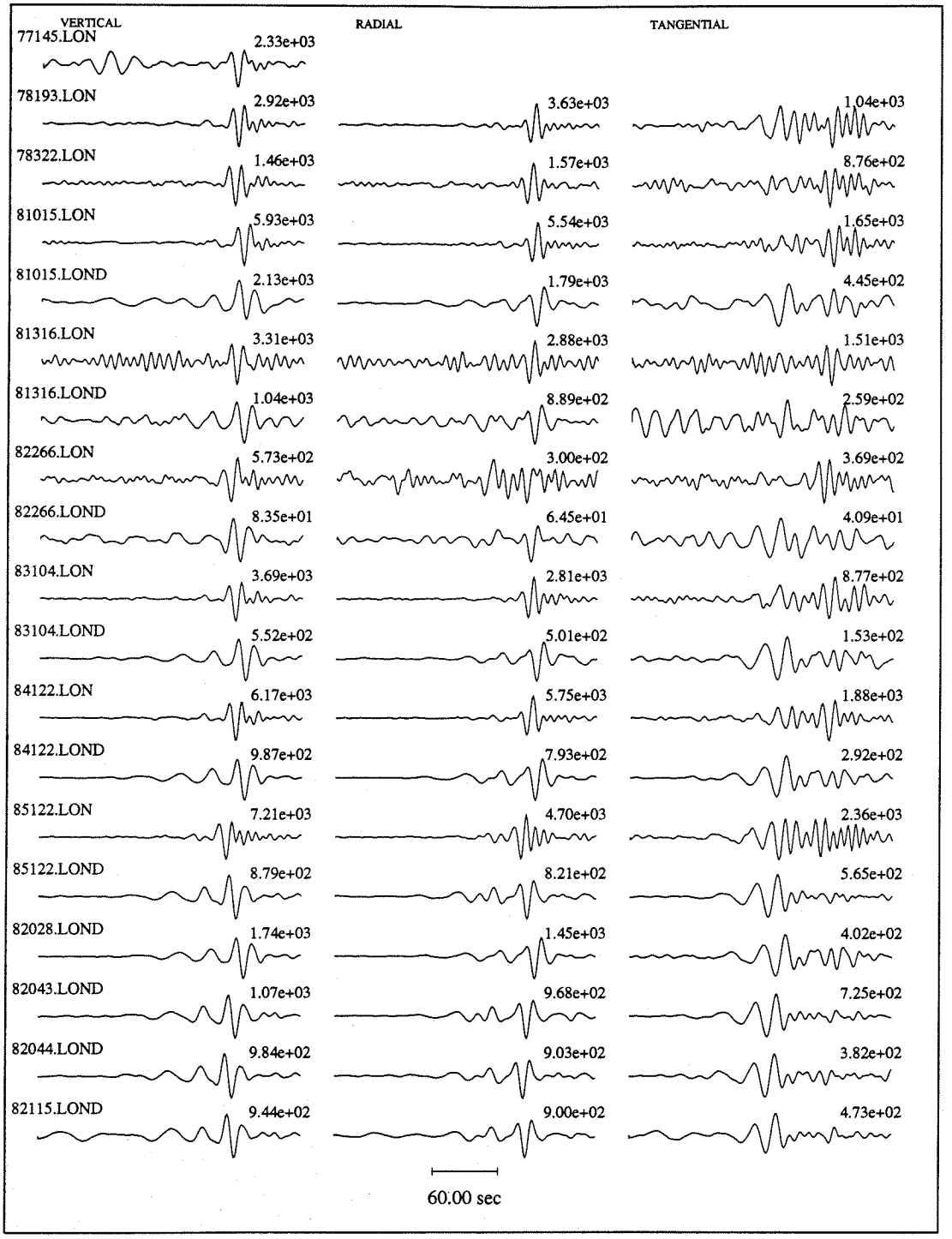
VERTICAL
RADIAL
TANGENTIAL
77145.LON
2.33e+03
78193.LON
2.92e+03
3.63e+03
1.04e+03
78322.LON
1.46e+03
1.57e+03
8.76e+02
81015.LON
5.93e+03
5.54e+03
1.65e+03
81015.LOND
2.13e+03
1.79e+03
4.45e+02
81316.LON
3.31e+03
2.88e+03
1.51e+03
81316.LOND
1.04e+03
8.89e+02
2.59e+02
82266.LON
5.73e+02
3.00e+02
3.69e+02
82266.LOND
8.35e+01
6.45e+01
4.09e+01
83104.LON
3.69e+03
2.81e+03
8.77e+02
83104.LOND
5.52e+02
5.01e+02
1.53e+02
84122.LON
6.17e+03
5.75e+03
1.88e+03
84122.LOND
9.87e+02
7.93e+02
2.92e+02
85122.LON
7.21e+03
4.70e+03
2.36e+03
85122.LOND
8.79e+02
8.21e+02
5.65e+02
82028.LOND
1.74e+03
1.45e+03
4.02e+02
82043.LOND
1.07e+03
9.68e+02
7.25e+02
82044.LOND
9.84e+02
9.03e+02
3.82e+02
82115.LOND
9.44e+02
9.00e+02
4.73e+02
60.00 sec

LON (c)

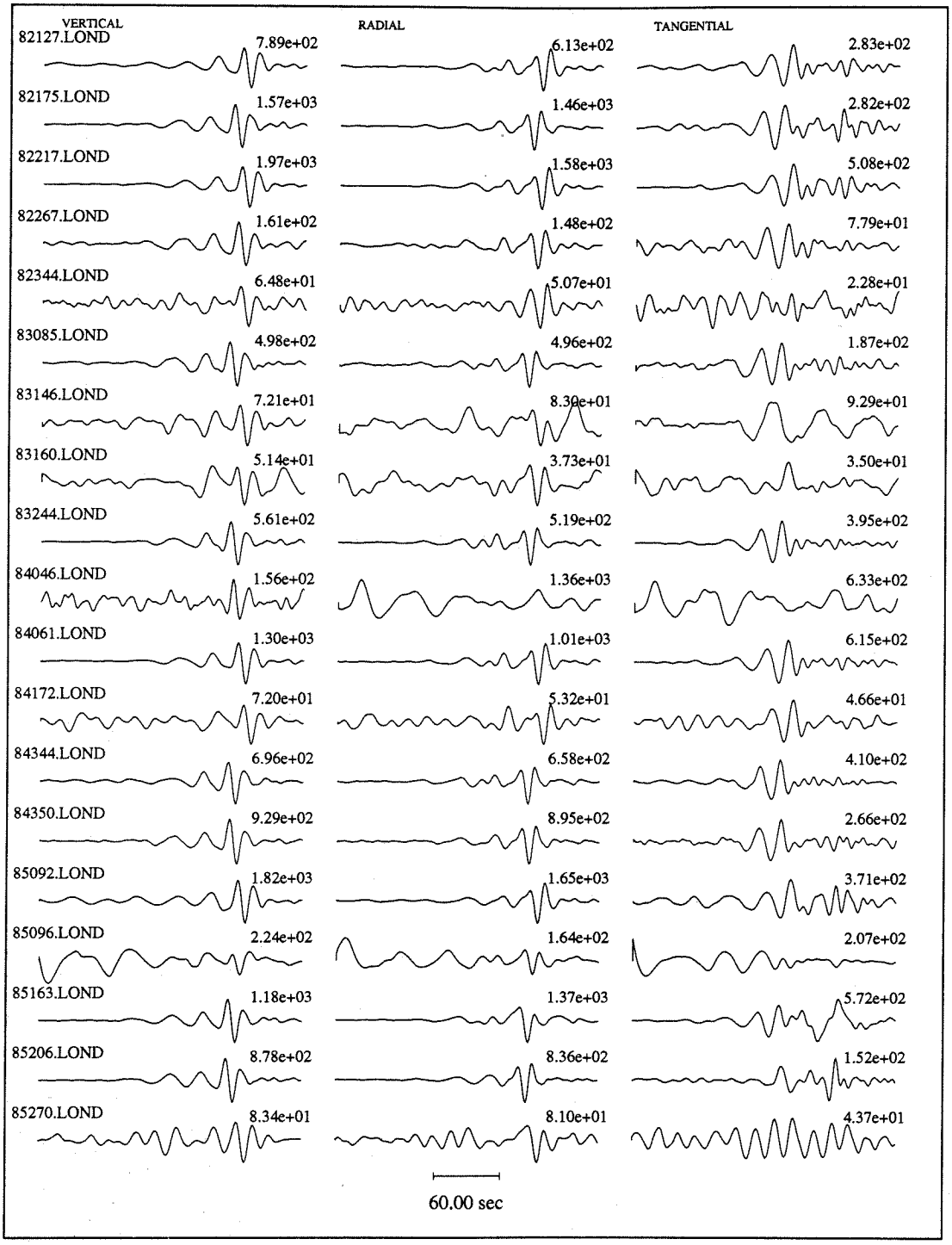
VERTICAL
RADIAL
TANGENTIAL
82127.LOND
7.89e+02
6.13e+02
2.83e+02
82175.LOND
1.57e+03
1.46e+03
2.82e+02
82217.LOND
1.97e+03
1.58e+03
5.08e+02
82267.LOND
1.61e+02
1.48e+02
7.79e+01
82344.LOND
6.48e+01
5.07e+01
2.28e+01
83085.LOND
4.98e+02
4.96e+02
1.87e+02
83146.LOND
7.21e+01
8.30e+01
9.29e+01
83160.LOND
5.14e+01
3.73e+01
3.50e+01
83244.LOND
5.61e+02
5.19e+02
3.95e+02
84046.LOND
1.56e+02
1.36e+03
6.33e+02
84061.LOND
1.30e+03
1.01e+03
6.15e+02
84172.LOND
7.20e+01
5.32e+01
4.66e+01
84344.LOND
6.96e+02
6.58e+02
4.10e+02
84350.LOND
9.29e+02
8.95e+02
2.66e+02
85092.LOND
1.82e+03
1.65e+03
3.71e+02
85096.LOND
2.24e+02
1.64e+02
2.07e+02
85163.LOND
1.18e+03
1.37e+03
5.72e+02
85206.LOND
8.78e+02
8.36e+02
1.52e+02
85270.LOND
8.34e+01
8.10e+01
4.37e+01
60.00 sec

LON (d)

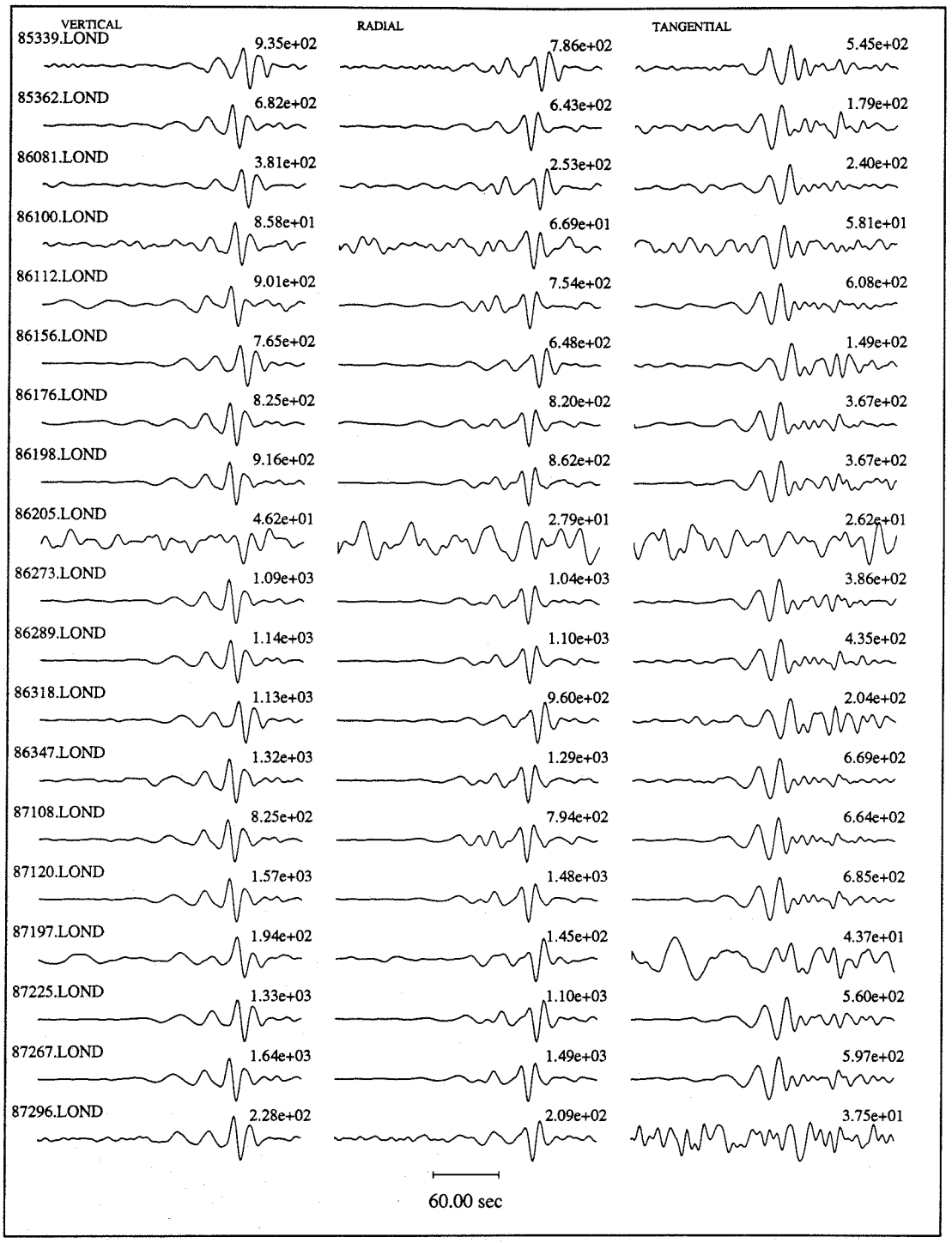
VERTICAL
RADIAL
TANGENTIAL
85339.LOND
9.35e+02
7.86e+02
5.45e+02
85362.LOND
6.82e+02
6.43e+02
1.79e+02
86081.LOND
3.81e+02
2.53e+02
2.40e+02
86100.LOND
8.58e+01
6.69e+01
5.81e+01
86112.LOND
9.01e+02
7.54e+02
6.08e+02
86156.LOND
7.65e+02
6.48e+02
1.49e+02
86176.LOND
8.25e+02
8.20e+02
3.67e+02
86198.LOND
9.16e+02
8.62e+02
3.67e+02
86205.LOND
4.62e+01
2.79e+01
2.62e+01
86273.LOND
1.09e+03
1.04e+03
3.86e+02
86289.LOND
1.14e+03
1.10e+03
4.35e+02
86318.LOND
1.13e+03
9.60e+02
2.04e+02
86347.LOND
1.32e+03
1.29e+03
6.69e+02
87108.LOND
8.25e+02
7.94e+02
6.64e+02
87120.LOND
1.57e+03
1.48e+03
6.85e+02
87197.LOND
1.94e+02
1.45e+02
4.37e+01
87225.LOND
1.33e+03
1.10e+03
5.60e+02
87267.LOND
1.64e+03
1.49e+03
5.97e+02
87296.LOND
2.28e+02
2.09e+02
3.75e+01
60.00 sec

Spectral ratio curves for Rayleigh waves were generally smooth and flat, implying a good fit between observed and synthetic spectra. Love wave data-to-synthetic spectral ratios were not as flat. It is suspected that the Rayleigh wavetrain energy, contaminating the Love wavetrain primarily is responsible for this effect.

The polarity of the waveform, used as phase information, was determined by visual inspection. This was primarily of importance for Love wave observations. Only in the case of PILEDRIVER were there any reversed-polarity Rayleigh waves. The resultant spectral ratios and phase information were used in the source inversion. The inversion technique is described in section 5 (Moment Inversion Technique) as is the method for generating synthetics. The results of the source inversion are discussed later.

3.4 Path Modeling

To determine accurate source parameters it is necessary to correct for propagation effects along the surface wave travel-paths. This involves determining an average earth structure for each path from a general source region to a particular receiver. The paths are modeled as 1-dimensional laterally homogeneous structures. Paths from the Nevada Test Site (NTS) to 23 World Wide Seismic Station Network (WWSSN) and Canadian Seismograph Network (CSN) stations were determined for a surface wave study by Stevens (1986 and personal communication). These stations are shown as circles in Figure 2.1. The path Green's functions were determined by a two step inversion of shear wave velocity and Q as discussed in Stevens (1986). For other stations in the network (shown as triangles in Figure 2.1) path models were chosen or developed through a variety of means. Whenever possible, pre-existing models were used for path structures for any given NTS-station path. For some paths several models were tried. To determine whether or not a particular earth model was ap-

propriate for a particular path, a synthetic seismogram was generated and compared to the highest signal to noise (SNR) observed record. The quality of the fit was determined by visual inspection of time domain records. Absolute travel time and amplitude comparisons between observed and synthetic intermediate-period (6<T<60 sec.) Rayleigh waveforms as well as fundamental-mode dispersion data were the criteria used to judge the goodness of fit of the paths.

Most of the intermediate-range to distant station paths ($\Delta > 1500$ km) were successfully modeled using a structure from Stevens' ensemble of structures. However, for regional stations at lesser distances (i.e., the southwestern United States), alternative earth models were necessary. Station coverage in this area is especially important for several reasons. At regional distances the threshold magnitude for observing surface waves is lower than that of more distant receiver, since the effects of geometrical spreading and attenuation (due both to anelastic absorption and scattering) are less for shorter paths. Amplitude errors due to using incorrect Q values for path corrections will also be less for shorter paths for the same reason. Because NTS is situated in the southwest corner of the U. S., the azimuthal coverage for more distant paths is limited, so that there are no seismographic stations 600 to 5000 km to the west or southwest of NTS (i.e., in the Pacific Ocean). Station coverage to the south (for pure continental paths) is also very limited, as there were few long-period seismographic stations recording in Mexico and Central America during the time period in which events for this study were taken.

Broad azimuthal coverage is also important for constraining the seismic moment. For example, a vertical strike slip double-couple source, which has a $(\sin 2\theta)$ radiation pattern superimposed with an isotropic source will generate a Rayleigh wave radiation pattern with quadrants of increased and decreased amplitude, which is caused by the constructive and destructive interference of the two sources. For the case of perfect azimuthal coverage, the network-averaged scalar moment will be that

of the isotropic source. Lack of coverage in one of these quadrants will cause the observed network-averaged moment to be larger or smaller than the actual value, depending upon whether constructive or destructive interference occurs in the unobserved quadrant. If phase and amplitude information are to be inverted to obtain the moment tensor, broad azimuthal coverage improves the constraints of the moment tensor inversion.

A large proportion of the regional stations in this study have paths which predominantly traverse the Basin and Range province. Fortunately this region has been the focus of many crustal and upper mantle structure studies, so that there are a good many earth structures derived from both surface wave and body wave studies available from which to choose to model the paths of interest in this study.

Mooney and Braile (1989) review P-wave velocity structures, determined from P-wave refraction studies, for the different physiographic regions of North America, including the Basin and Range province. Saikia and Burdick (1991) forward-modeled P_{nl} waveforms from NTS explosions to many of the same regional stations used in this study in order to determine a general crustal model for the area.

Press (1960) used a combined refraction, surface wave phase velocity, and gravity data to infer a seismic velocity structure for, primarily, the Mojave block. Hadley and Kanamori, in more recent studies, have interpreted this same area both in terms of P-wave refraction data (1977) and interstation phase velocities from teleseismic Rayleigh waves (1979).

Keller *et al.* (1976) used regional, explosion-generated, short-period (4 to 22 sec.) Rayleigh wave group velocities to determine crustal structure for several areas in the Western U. S., including the eastern Basin and range Province. Priestly and Brune (1978) made use of teleseismic, wide-band (4 to 120 sec.), interstation fundamental-mode Rayleigh wave and Love wave phase velocities modes to determine the shear-wave velocity structure for the Nevada and Western Utah Great Basin area. The

dispersion results of this study are corroborated in a study by Patton (1982) in which single-station Rayleigh wave phase velocities were determined using regional, digital, broadband data.

Patton and Taylor (1984) determined shear-wave Q structure from regional Love wave and Rayleigh wave amplitude data. The shear velocity model used in their method is a hybrid of the Priestly-Brune (PB, 1978) upper mantle model and a NTS-TUC (Tuscon, Arizona) crustal model developed by Bache *et al.* (1978) discussed below. Their results imply a much lower Q in the crust and upper mantle than a more general study of attenuation in western North America by Mitchell (1975), which they attribute to partial melting in the upper mantle. This attenuation model was used in conjunction with all earth models examined in this study for paths in this region, which don't have an associated Q structure.

The model that generally best fit the Rayleigh wave and Love wave observed waveforms for the Basin and Range stations (DUG, GSC, ELK, KNB, LAC and MNV) from the above cited models was found to be the PB model. The Patton and Taylor (PT) Basin and Range attenuation model was used in conjunction with the PB velocity model.

Bache *et al.* (1978) determined flat-layered velocity structures for paths from NTS to ALQ and TUC using surface wave dispersion data. Attenuation values were taken from the previously cited study of regional Rayleigh attenuation study by Mitchell (1975). Langston and Helmberger (1974) also modeled the NTS-TUC path by forward-modeling body wave phases and by trial and error inversion of group velocity data. Both studies have similar crustal thicknesses for the NTS-TUC path, as body wave phases were used to constrain the depth to the Moho; however, the shear velocity is higher at the top of the mantle in the Langston-Helmberger model than in the other (v_s = 4.6, vs. v_s = 4.42). The Bache model was chosen for this study. Synthetic fundamental-mode surface waves generated with the Bache

models match observed surface wave records significantly better than the Langston-Helmberger model. Comparisons of observed and syntethic surface wave waveforms for the NTS to ALQ and TUC paths, along with all others, are shown in figure 2.2 (for Rayleigh waves) and figure 3.10 (for Love waves).

Path structures determined in this study were arrived at through a combination of forward modeling and inversion of dispersion data for shear-wave structure. Compressional velocity and density were calculated from functional relationships with shear-wave structure as per Stevens (1986). The philosophy behind these path structures is to obtain earth models that will give accurate path corrections or Green's functions with which to generate synthetic seismograms which fit the observed waveforms with respect to amplitude and arrival times, rather than to recover the lithospheric structure or the earth along the path, although the models also should not diverge too drastically from realistic gross earth structure. NTS surface waves for many of the stations in this study's network traverse several tectonic/geologic provinces. A flat-layered earth model obviously cannot accurately describe a crust and upper mantle cross-section traversing various portions of the Western Cordillera (the Basin and Range, Rocky Mountains, and the Colorado Plateau) and the North American craton. However, one can obtain a model which describes an average earth model for a given path which fits the observed dispersion data and spectral amplitude curves, as well as the time-domain waveforms.

The starting models used for this path determination scheme come from studies in which the earth structures for similar/nearby paths were inverted for using rigorous inversion procedures and resolution analysis and geophysical constraints. The first step was to see how well the initial structure modeled Rayleigh waveforms. As it turned out, none of these structures fit both arrival times and waveforms very well for the desired paths. Next, for each path the initial structure was perturbed in an effort to better fit synthetic seismograms generated with the structure to the

observed waveforms. This included adding and removing low-velocity surface layers (representing sedimentary basins), increasing and decreasing the gross (or average) velocity in the crust and/or upper mantle, and increasing and decreasing the crustal thickness. This exercise also gives one a feel for the effects of these model changes. Perturbations to the initial model were retained if they improved the wave-train arrival and/or waveform.

The depth to the moho and the shear-velocity contrast are the most important influences upon the surface wave-field. Independent geophysical constraints on these factors was desired. Mooney and Braile (1989) summarize crustal models for North America (NA) inferred from seismic refraction and reflection studies. Their map of NA crustal thickness and representative P-wave velocity structures for the various geologic regions were useful as guidelines for estimating average depths to the moho for the various paths investigated, as well as for inferring the crust-mantle shear-wave velocity contrast. In inverting for shear velocity structure, as described below, it was found that using a starting model with a correct crustal thickness (constrained by reflection and refraction data) was important in order to obtain earth structures which produced well-fitting dispersion values and time-series. Inverted shear-wave earth models obtained from starting models with crustal depths which differed from what was believed to be a reasonable estimate of the average crustal thickness (constrained by independent geophysical data) usually did not produce dispersion values compatible with the data or time series which adequately modeled observed seismograms.

As an independent test of crustal thickness, a stochastic inversion of the dispersion data was conducted with a generic model ($v_p = 7.0, v_s = 4.0$) to find the depth to the moho. It was found in each case that the structure converged, to first order, to a layer over a half-space. The depth of the basal crustal layer was found to agree with the values inferred from the Mooney and Braile (1989) map. In the case of JAS, where

the travel path transverses the Sierra Nevada, it was unclear what the average crustal thickness should be, so the preliminary inversion inferred mantle depth of 37.5 km was taken to be representative of the average NTS-JAS path, and the Priestly-Brune Basin and Range based starting model was modified accordingly.

Paths from NTS to PAS, JAS, and RSTN stations were modeled in this study. Elastic parameters for these paths were determined by inverting fundamental-mode Rayleigh wave dispersion data to obtain the shear wave velocity (β) structure for the model. The surface wave analysis and velocity inversion computer codes used come from the Computer Programs in Seismology software package developed at the University of St. Louis (Herrmann, 1988). The shear-wave velocity (V_S) structure is found by simultaneously inverting for group and phase velocity data (for Rayleigh waves measured between 0.015 and 0.150 Hz) and minimizing the integral of $\|d\beta/dz\|$ over the structure, except across discontinuities at layer boundaries. This linear inversion scheme is similar to the one described in Bache *et al.* (1978) and Stevens (1986).

Q values for paths to RSTN stations were taken from the Stevens' attenuation model with the most similar path. All RSTN stations were on or near great circle paths of North American WWSSN or CSN stations. The PAS and JAS structures used the Patton and Taylor (1984) attenuation model. These two stations have paths to NTS which traverse a portion of the Basin and Range region.

Although Q structure was not determined by inversion, it was modified from the starting Q model by forward modeling of synthetic time series to be compatible with observations. For some paths it was necessary to create narrow, very high Q ($Q \approx 1000$) zones in the upper crust (5 to 15 km depth) in order to model the data. This was needed when the observed Airy Phase amplitudes ($8 < T < 15$) were considerably larger relative to the longer period data than the synthetic counterpart. The actual cause for these amplitude discrepancies are likely to be

lateral variations in the waveguide which tend to generate shorter period surface waves, rather than extreme Q values in the crust or mantle. However, to model these paths with flat-layered models, amplitude discrepancies must be accounted for in the attenuation structure. The amplitude discrepancy between relative long period and shorter period Rayleigh waves is in all likelihood due to anomalous short-period energy, as it is much harder to account for differences in Q at longer periods, since the long-period wave-field completes fewer cycles for a given path distance than do the shorter period waves.

Surface wave dispersion is not strongly dependent on the compressional velocity (V_P) or density (ρ), hence they aren't directly solved for in the inversion, but rather treated as functions of the medium's shear velocity, to which surface wave velocities are most sensitive. The compressional velocity (V_P) is constrained to be consistent with a Poisson's ratio of 0.27, while the density is constrained by a Birch's law formula:

$$\rho = 0.65 \times \beta + 400. \tag{3.1}$$

This formula is an empirical relationship developed from data in Dobrin (1976) and is in MKS units.

The maximum depth of the inversion model was set to the approximate longest wavelength ($\lambda = c/f$) observations. For a 0.015 Hz Rayleigh wave phase velocity ($c \approx 4.0$), this depth would be 270 km. Little resolution is to be expected at the lower bounds of this depth estimate, however. Layer thicknesses in the crust were chosen to be 5 km, with the top-most layer being divided in two, allowing for some resolution of possible shallow sedimentary basins. The upper 40 km of mantle is divided into 10 km thick sections and below this to 200 km, it is divided into layers 20 km thick. These layer thicknesses are close in value to the resolution length.

Single-station group velocity (U) dispersion values were determined from multiple filter analysis (Dziewonski *et al.*, 1969) of vertical component Rayleigh waves. In this

method the predominant arrival (peak amplitude phase) at a given frequency ω_0 is found by convolving the time series with a Gaussian filter

$$H(\omega) = \begin{cases} exp(-\alpha(\omega - \omega_c)^2/\omega_0^2) & \omega_0 - \omega_c \leq |\omega| \leq \omega_0 + \omega_c \\ 0 & \text{otherwise} \end{cases} \tag{3.2}$$

where

$$\omega_c = \omega_0(\pi/\alpha)^{1/2}$$

and α parameterizes the half-width of the filter. This parameter, in turn, affects the resolution of the group velocity determinations. After some experimentation, it was found that $\alpha = 8\pi$ gave the combination of resolution and smoothness in the group velocity curve.

After obtaining group velocities ($U(\omega)$), the time series are iteratively phase matched filtered (Herrin and Goforth, 1977; and Stevens, 1986) to remove scattered energy, noise and higher modes, so that the signal can be more accurately analyzed for phase and group velocity and amplitude information. The premise of this method is to cross-correlate the observed surface wave signal $s(t)$ (plus incoherent noise) with a signal known $s(t)$', which is an approximation to $s(t)$ in order to remove noise and the dispersive propagation effects. In this case $s(t)$ is the surface wavetrain and $s(t)$' is determined from the initial iteration of dispersion data.

Since the filter is matched to the seismograms and to the noise, the signal energy is compressed to times near t =0, while the noise is not. Therefore, a spectral estimate of $h(t)$, evaluated from a time window near t =0, is less contaminated by noise. A multipathed, or a higher-mode arrival with group arrival time t_S, rather than t_P (that of the primary arrival), will be time-shifted to $t = t_P - t_S$ which is not t =0.

Seismograms used for dispersion analysis were chosen from large magnitude explosions with the least observed tectonic release. Events which did not show evidence

of long-period tangential energy in the approximate Love wave time window were assumed to be good candidates. KEARSARGE data were used for PAS and JAS (CMB) to NTS paths. Dispersion analysis was done for other events, too. For all events examined, coherent spectral amplitudes were observed up to 30 sec. At periods greater than this, the error in velocity measurements are considerably larger. The propagation paths are less than 400 km in length, so longer-period surface waves have traveled very few wavelengths and thus are not yet fully developed and/or are not dispersed enough to measure their group energy packets.

For the RSTN stations, seismic waveforms came from a variety of events. For these stations at greater distances (D $<$ 230 km), coherent signal was observed up to 50 sec. The RSSD, RSCP, and RSNT paths used DARWIN data. The DARWIN group velocity curves for RSON and RSNY had several inflection points between 15 and 50 seconds. This feature is believed to be due to signal noise or processing artifacts. These two stations' deconvolved displacement records showed long-period noise throughout the records. For other larger events, with higher signal to noise ratios, this phenomenon may be due to tectonic-release generated signals. These deviations from the correct dispersion curve are significant and adversely affect inversion results.

The group velocity dispersion for a suite of seven events (both from Pahute Mesa and Yucca Flat) for the two paths were compared. The group velocity curves generally correlated quite well by visual inspection between 8 and 40 sec. Above and below these levels, only some events had coherent smoothly continuous dispersion curves. In the period range between 15 and 50 sec. perturbations from a smooth, near-constant slope group velocity curve varied in shape from event to event and sometimes were absent, implying that they are some sort of noise effect and not a propagation phenomenon. The final dispersion data came from BELMONT for RSON and HERMOSA for RSNY. Deconvolved displacement seismograms for these

events show low long-period noise levels.

Phase velocities were obtained using a phase-matched filtering (Herrin and Goforth, 1977; Stevens 1986) scheme. Using the formulation of Rayleigh wave displacement given in equation (1) (chapter 2), the phase delay is

$$T = T_s + \frac{r}{c} + \frac{3\pi}{4\omega}, \tag{3.3}$$

where T_s is the source function phase delay, r is the range and c is the phase velocity. For explosive sources theoretical (Bache *et al* , 1975) and empirical (Haskell, 1967) studies find T_s to be no more than a fraction of a second for the periods of interest, so its contribution to the phase delay can be neglected, so that equation (1) can be re-arranged in order to obtain an expression for the phase velocity:

$$c(\omega) = \frac{-r\omega}{\phi - \phi_0 + 2\pi n} \tag{3.4}$$

where ϕ is the unwrapped phase, ϕ_0 is the initial source phase and n is an integer selected to give realistic earth model phase velocity values. For vertical component, positive up, explosion-generated Rayleigh wave displacements, $\phi_0 = -3\pi/4$. For short paths the correct value of n can be determined from the long-period limit of the phase velocity, since an incorrect choice of n will lead to unreasonable values. For longer paths n was chosen so that phase velocity at 0.015 Hz was closest to the world-wide average of 4.0 km/sec. (Oliver, 1962). After this step, improved/revised group velocity and amplitude measurements are obtained from multiple narrow band-pass filtering of the filtered fundamental-mode time series. Single-station phase velocities are also determined from this filtered signal, using equation 3.4 and Fourier analysis.

Another iteration of the phase matched filtering is performed with the revised group and phase velocities. The second iteration, phase matched filtered fundamental-mode time series from this procedure is used to obtain the revised, final phase and group velocity measurements using the methods described earlier. These dispersion data are used to invert for the shear-wave velocity structure.

The best-fitting forward-modeled velocity structure was then used as the initial model for the shear-wave inversion procedure. A weighted, least-squares inversion of fundamental-mode Rayleigh wave group and phase velocity is performed. Details of the inversion method are given in Russell (1986). The procedure is non-linear in nature, so iterative solutions are obtained. Q structure was not inverted for these paths. Instead the attenuation model associated with the initial inversion model was used. Here the assumption is that the gross attenuation structure is the same between nearby paths. To robustly solve for attenuation, one must employ two-station attenuation measurements or joint moment-Q inversions. The combination of data and paths in this study does not lend it to the two-station method. For the shorter paths (JAS and PAS), attenuation effects are minimal for surface waves, as they propagate relatively few wavelengths and consequently undergo a corresponding low number of attenuation cycles.

The initial model for the inversion was chosen to be a pre-existing earth model for a similar path or region. The RSTN paths used models by Stevens (1986) and the JAS and PAS paths used modified versions of the Priestly and Brune (1978) Basin and Range model. The starting models all came from studies in which the earth structures were inverted for using rigorous inversion procedures and resolution analysis. Each earth model is comprised of 15 to 22 layers. The highest resolution of the travel paths is in the crust and upper mantle, so the finest (thinnest) layers are in that portion of the model. The basal crustal layer of each model was modified to put it in line with the North American crustal depth map of Mooney and Braile (1989). Of particular note the path to JAS, which transverses the Sierra Nevada, had the crustal depth increased by over 25 percent over the thin 31 km thick Basin and Range Model.

The shear wave inversion is a non-linear process, so many iterations were performed. The weighting factors used for the dispersion observations were proportional

to the inverse of the spectral amplitude at a given period. Approximately every fourth iterated model was saved in case later iteration models converged towards a "pathological" one with unrealistically large velocity-contrast low velocity zones in the crust. Early inversion attempts made, using a damped least-squares stochastic inversion, resulted in such low velocity zones. Applying a weighted, damped differential least-squares inversion produced "smoother" velocity models which were geophysically reasonable (*i.e.*, did not have oscillating high and low velocity zones or unreasonably large velocity contrasts). The final inverted models were obtained using the latter method.

As mentioned earlier, the criterion to determine the goodness of fit of an earth structure were visual comparisons of the observed and Green's Function derived dispersion and waveform fits of the fundamental Rayleigh wave. Figures 3.3 through 3.9 compare observed and modeled group and phase velocity dispersion for the seven paths. All dispersion curve fits are quite good. The largest mismatch between observed and inverted model dispersion values are at the longest and shortest periods. These periods had the lowest spectral amplitudes, so they are weighted least in the inversion scheme. It is somewhat surprising that such good fits were obtained, considering the significant lateral variations in the waveguide, particularly for the JAS and PAS paths which each traverse several mountain ranges and valleys.

Figure 2.2 compares observed to synthetic seismograms for the fundamental-mode, vertical component Rayleigh waves for the seven paths modeled in this study as well as for the other network paths used in this study. All time series were band-passed filtered between 60 and 6 seconds. Each path is well modeled with respect to waveform and arrival time ($\Delta t < 1.0$). A confirmation of how well the models reflect the average earth structure of the path are comparisons of observed and synthetic fundamental-mode Love waves. The error in timing of the Rayleigh wave-train is in all cases small and is estimated to be less than 2 seconds. Figure 3.10 compares

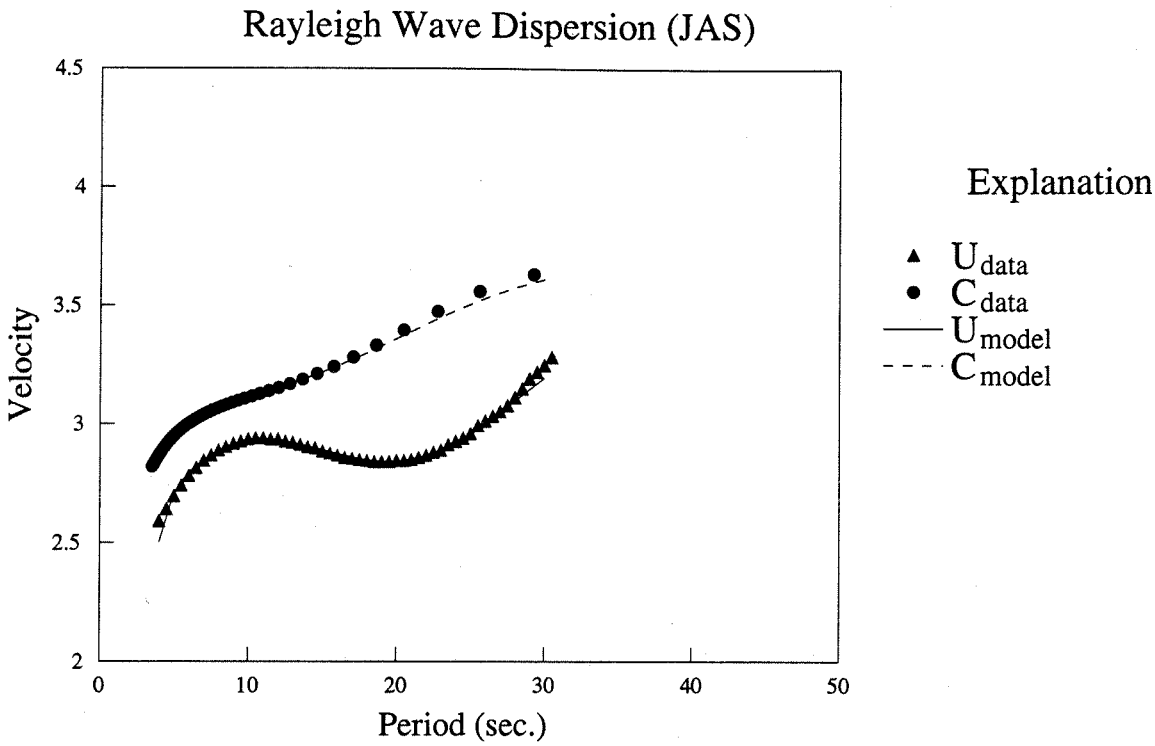

Figure 3.3: Fundamental-mode Rayleigh wave dispersion curves for JAS.

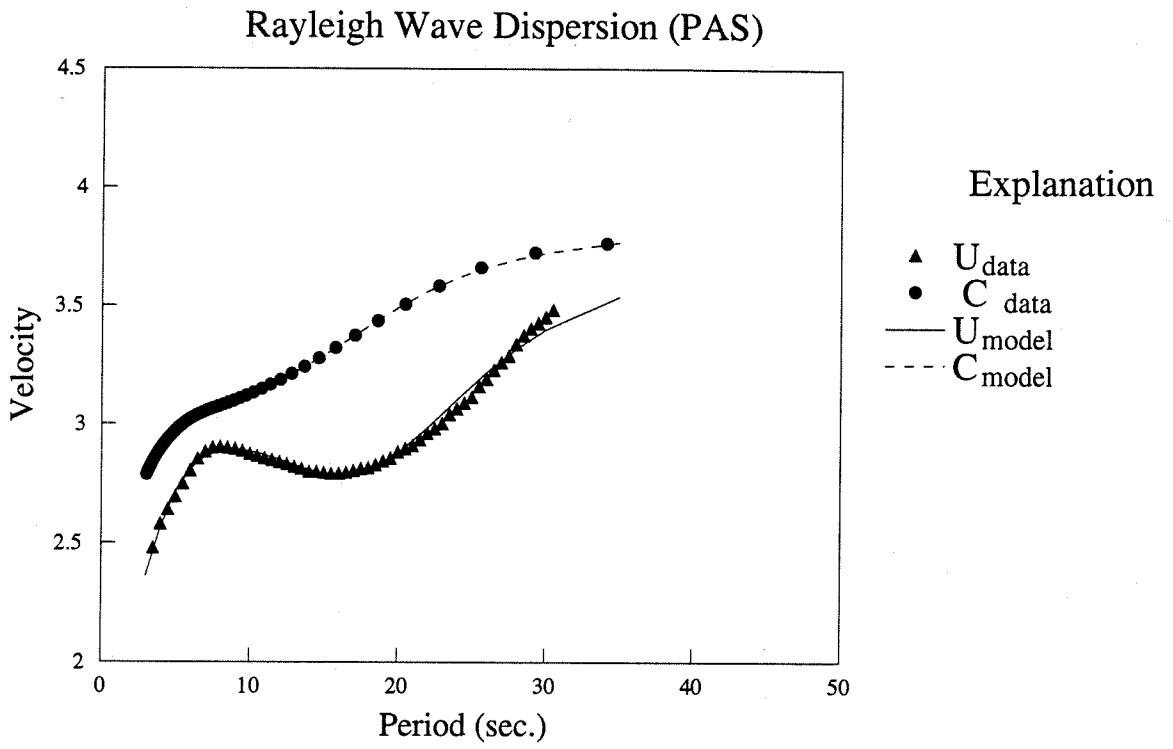

Figure 3.4: Fundamental-mode Rayleigh wave dispersion curves for PAS.

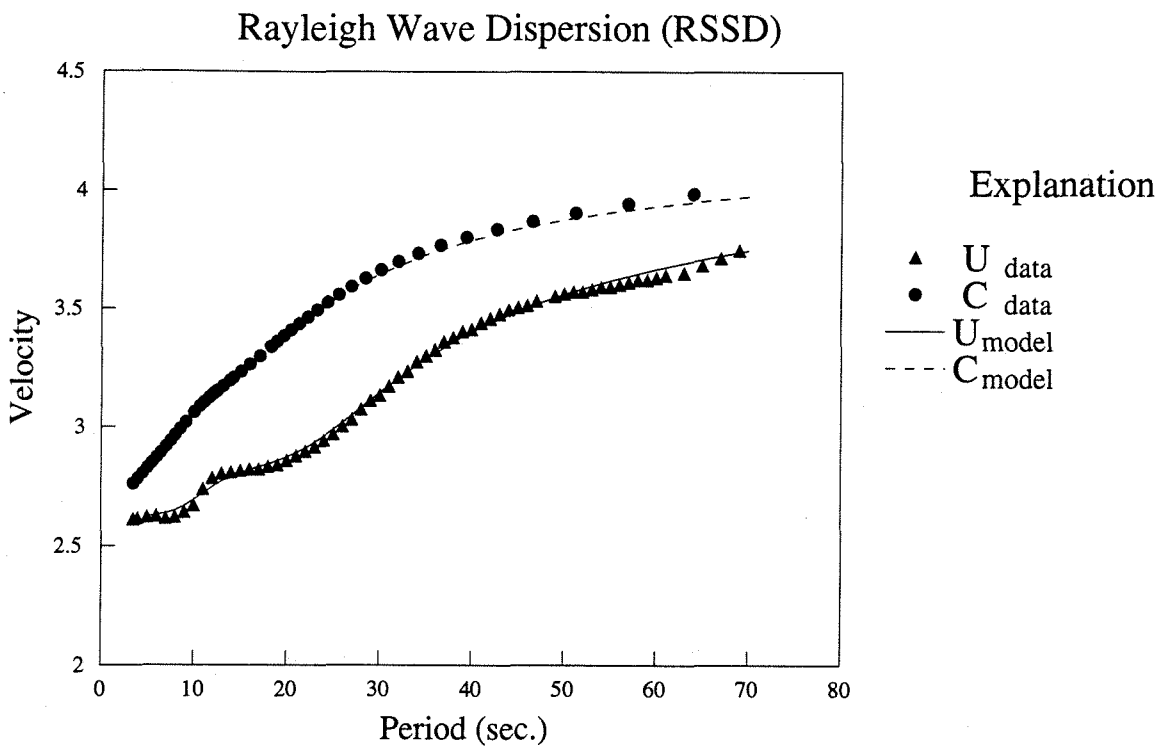

Figure 3.5: Fundamental-mode Rayleigh wave dispersion curves for RSSD.

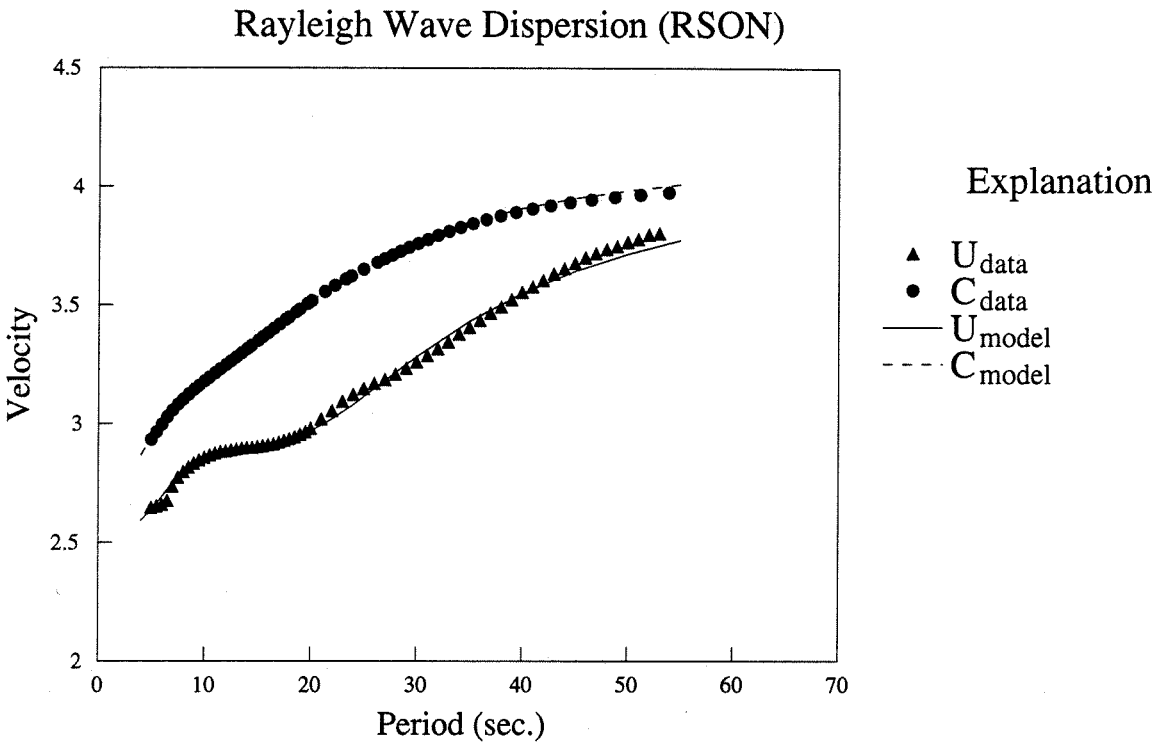

Figure 3.6: Fundamental-mode Rayleigh wave dispersion curves for RSON.

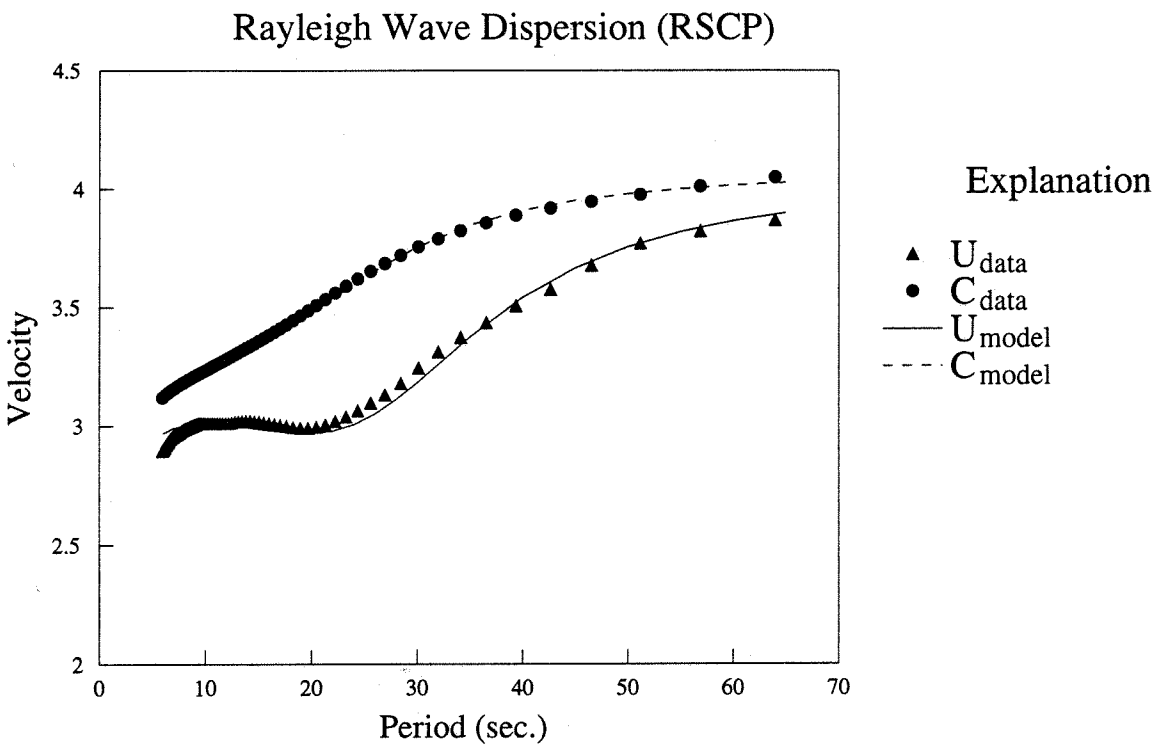

Figure 3.7: Fundamental-mode Rayleigh wave dispersion curves for RSCP.

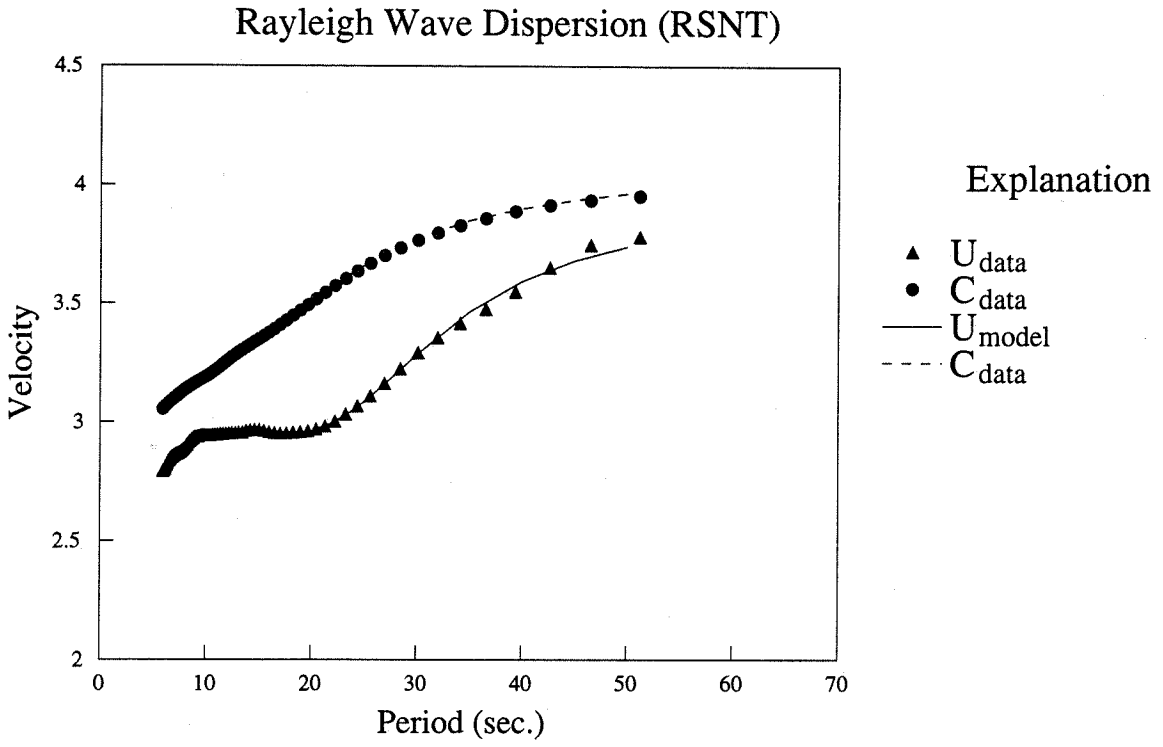

Figure 3.8: Fundamental-mode Rayleigh wave dispersion curves for RSNT.

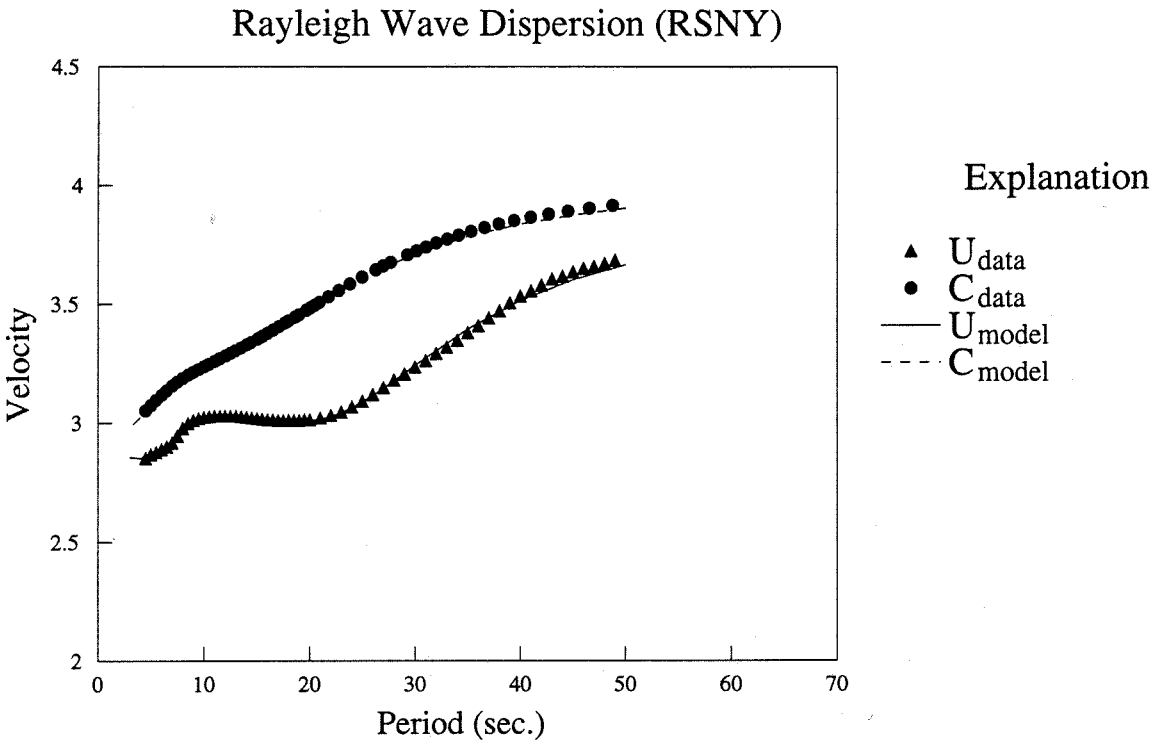

Figure 3.9: Fundamental-mode Rayleigh wave dispersion curves for RSNY.

observed and synthetic Love waves. Unlike the case of explosion generated Rayleigh waves, the polarity of tangential waves is ambiguous, because the source mechanism is not necessarily known. The correct polarity or phase was determined by comparing the best combined waveform fit/travel time residual minimum in conjunction with assumptions on the radiation pattern from previous studies. The waveform fits are sufficient for inversion purposes and aren't bad predictions of the observed Love waves, although the wave-train arrival time errors are larger (from 2 to 10 seconds), with the largest errors correlating, in general, to the more distant paths.

Figure 3.11 displays the data/synthetic seismograms for the seven paths modeled in this study. Both fundamental-mode Rayleigh waves (vertical component) and Love waves are plotted.

Figures 3.12 through 3.18 show the final inverted path models. The P-wave and S-wave velocities, Q values and densities are plotted separately. As discussed previously, the Q structures are based on pre-existing Q models, which are then modified by forward modeling the waveforms and only β was directly inverted. Estimated errors (1 standard deviation) in S velocity are on the order of 0.05 to 0.1 km/sec. Errors are smallest in the upper crust and largest in the lower crust and upper mantle. The resolving kernel widths were approximately 5 km in the upper crust and 10 to 15 km in the lower crust and upper mantle. Little or no resolution was found below 60 km. Tables 3.2 through 3.8 list the parameters of the structures. These path models have typical continental path structures with crustal thicknesses in line with refraction and reflection constraints. No large low velocity zones are within the crust. Where an overlying layer does have a greater S velocity, the contrast is small ($\Delta V_S < 0.2$ km/sec.), and the errors in V_S are nearly of the same order of magnitude.

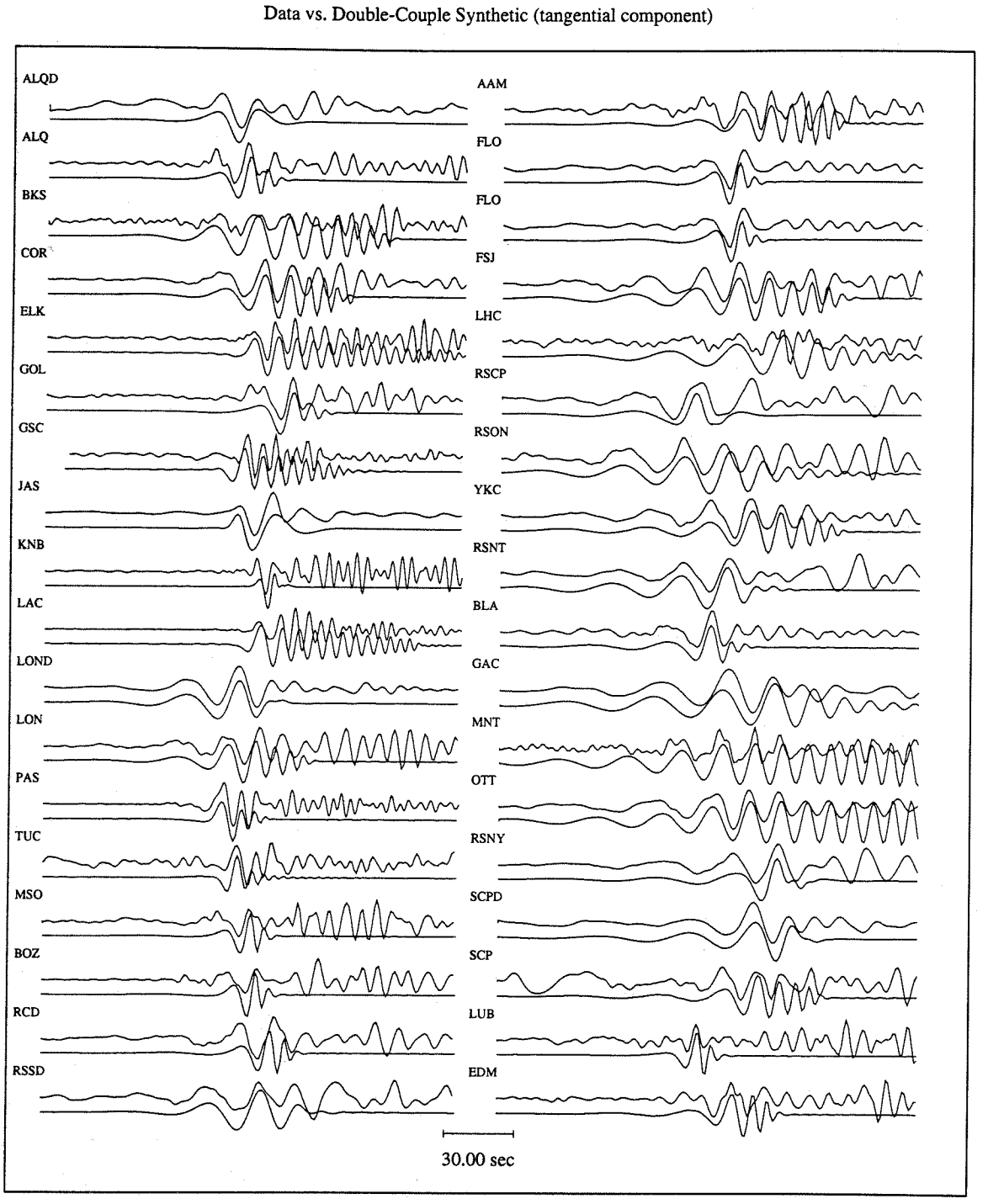

Figure 3.10: Comparison of observed and synthetic fundamental-mode Love waves.

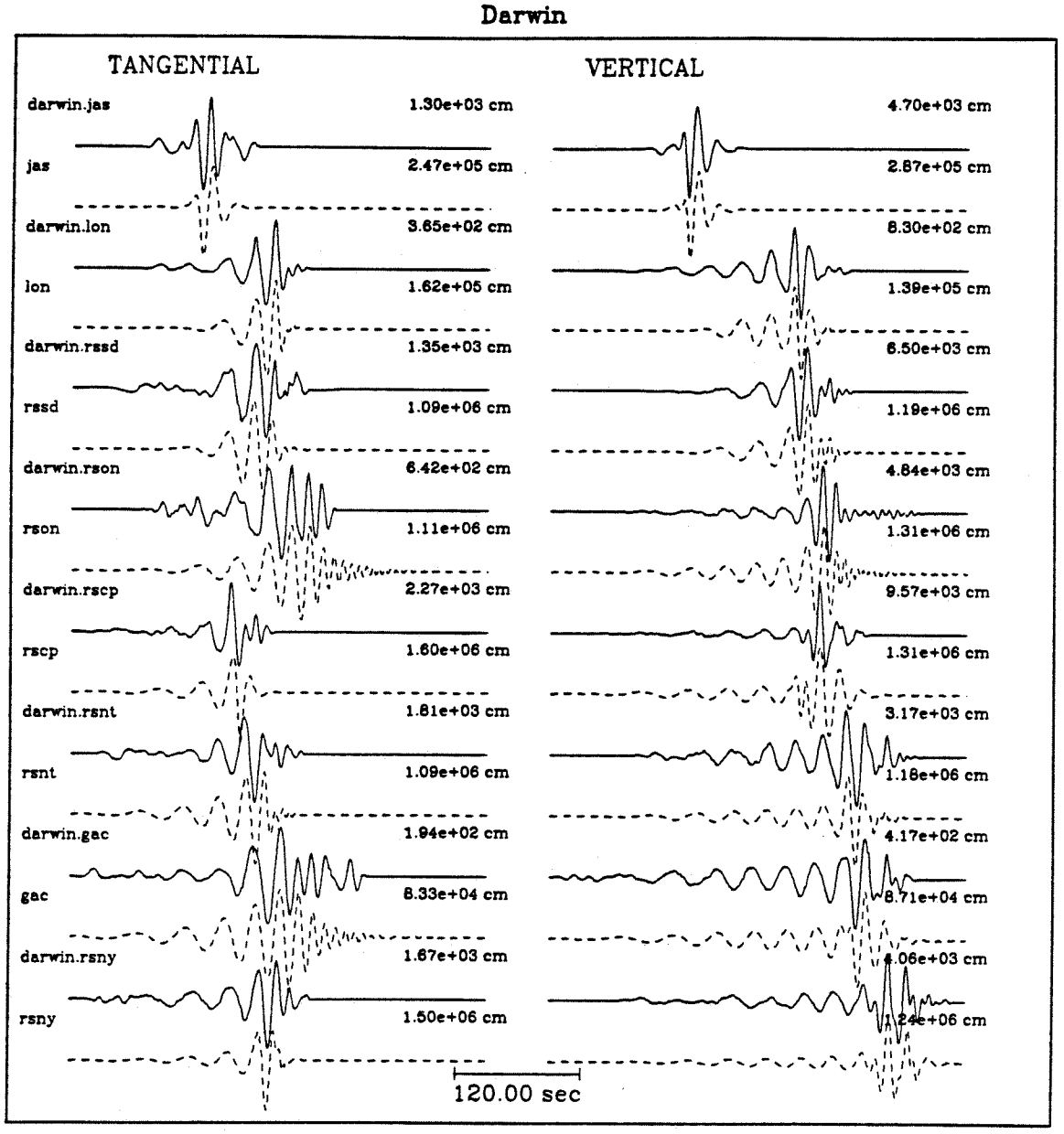

Figure 3.11: Comparison of observed and synthetic seismograms for paths modeled in this study.

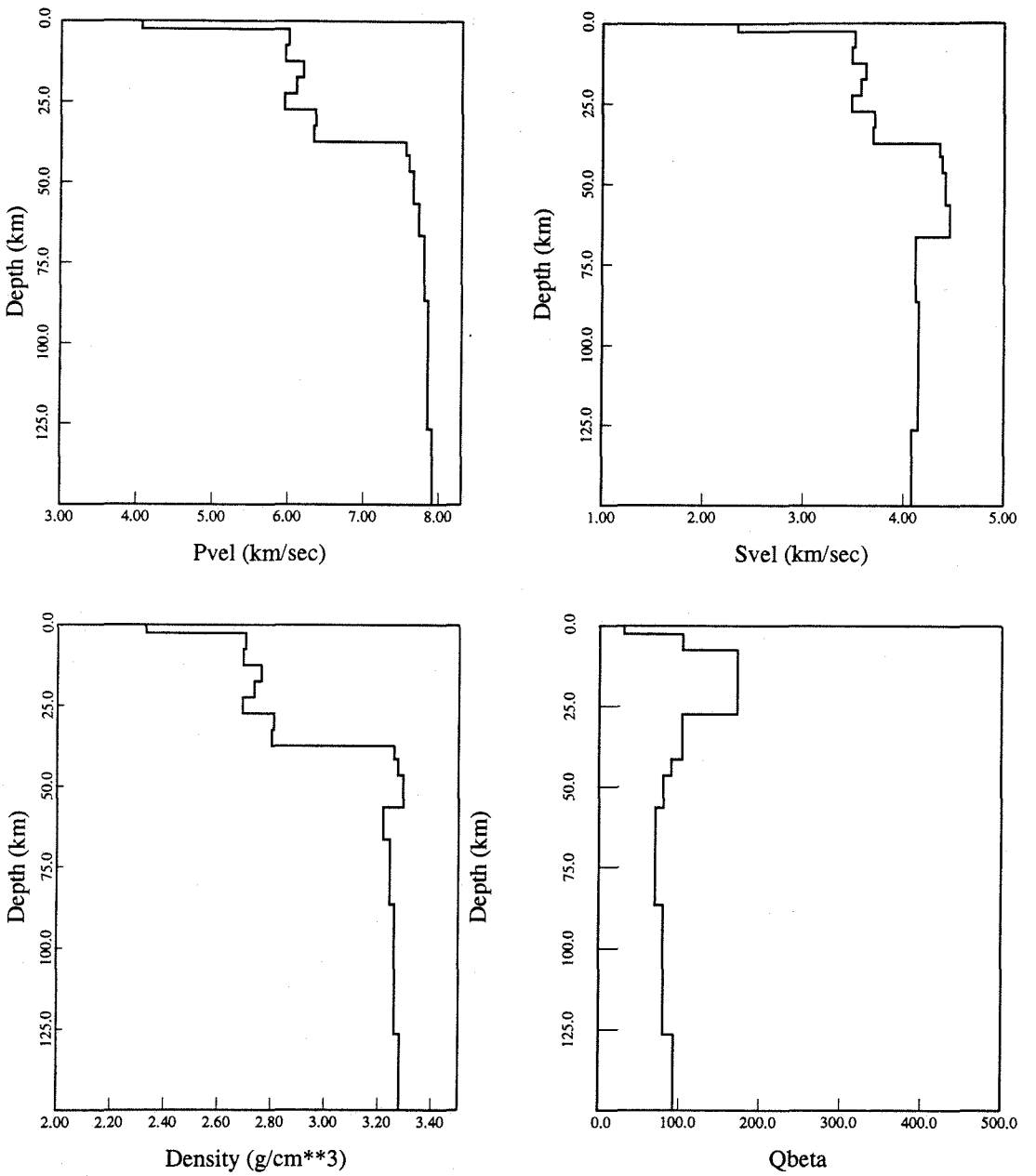

Figure 3.12: Path structure for NTS to JAS.

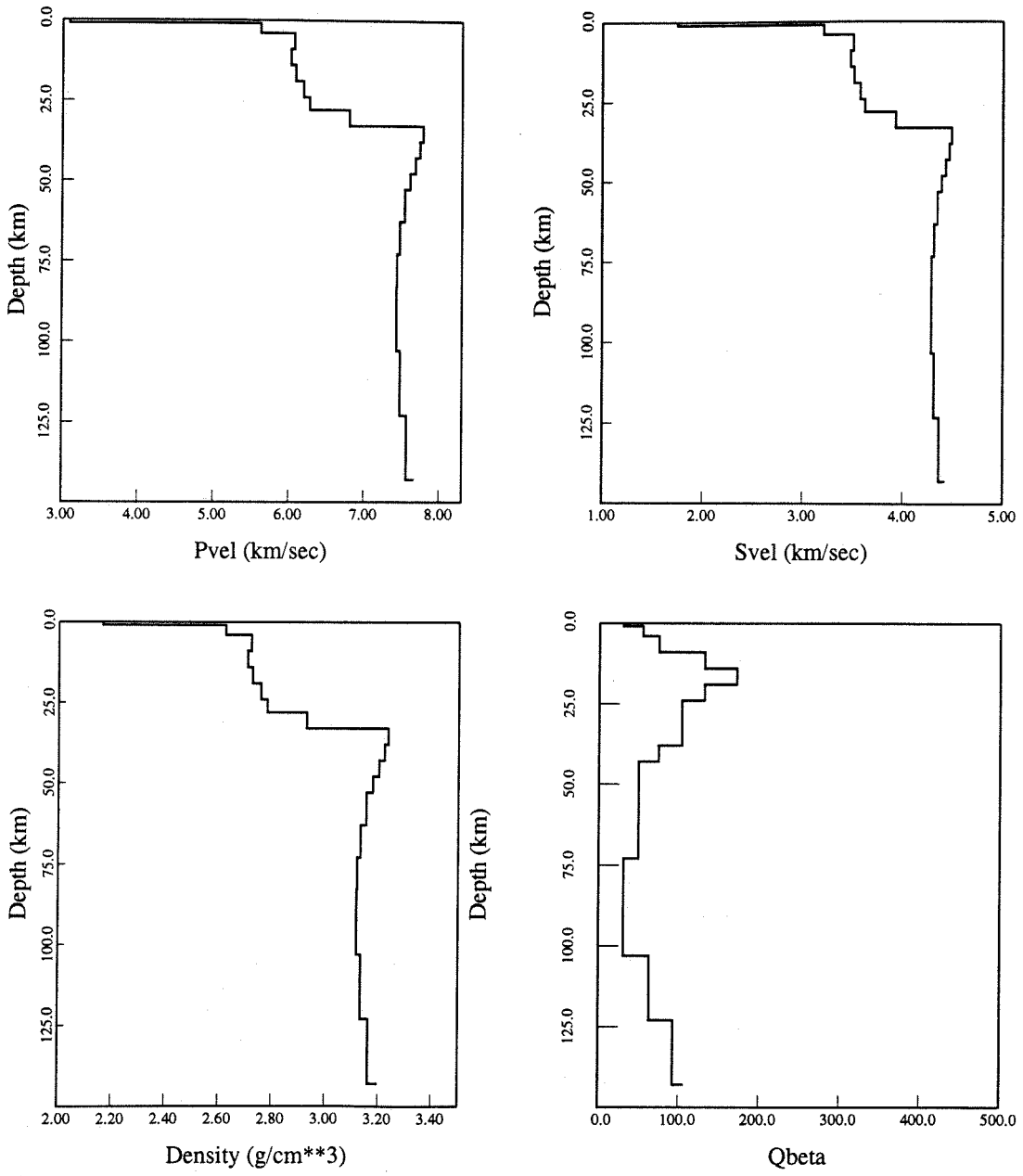

Figure 3.13: Path structure for NTS to PAS.

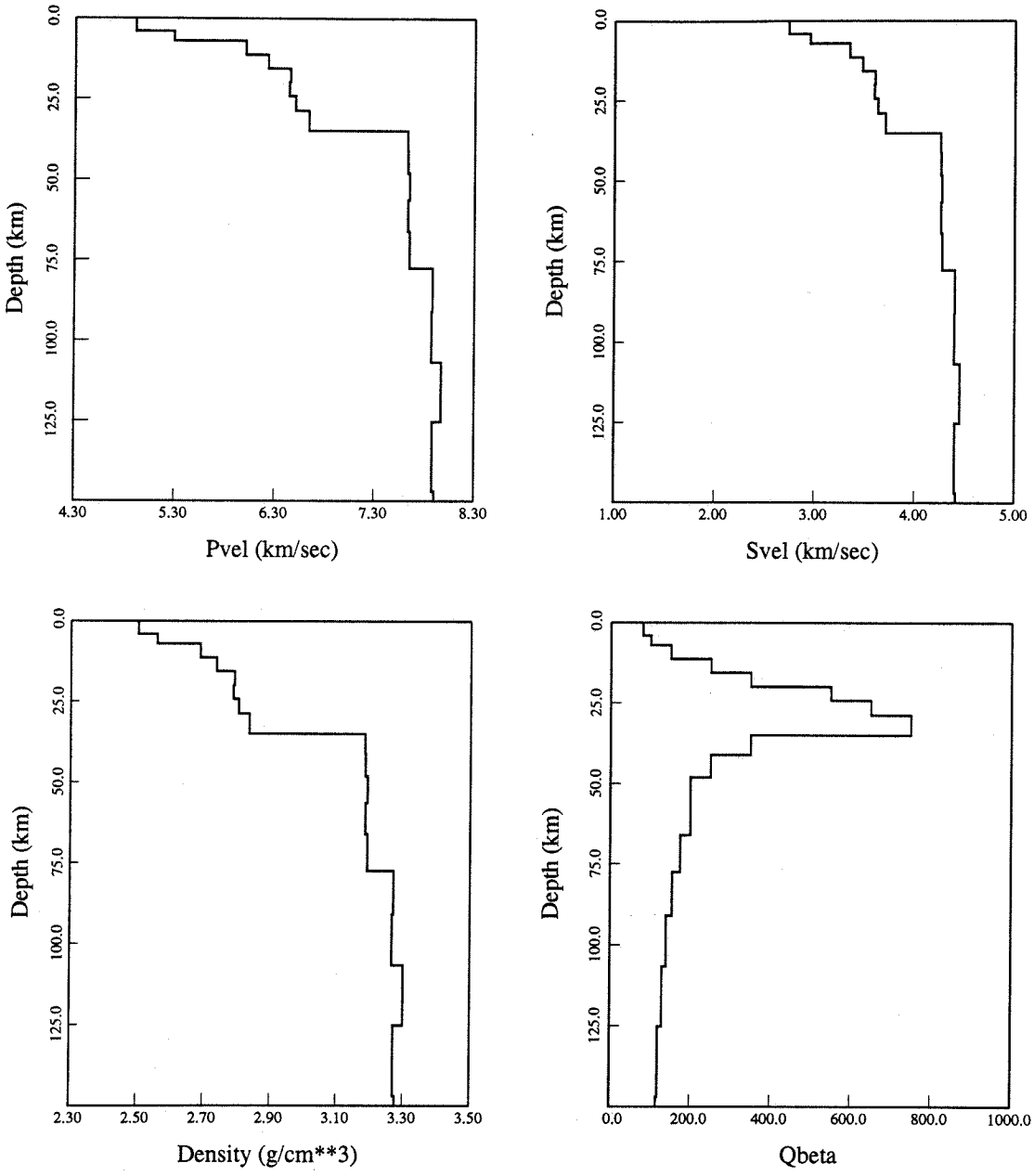

Figure 3.14: Path structure for NTS to RSSD.

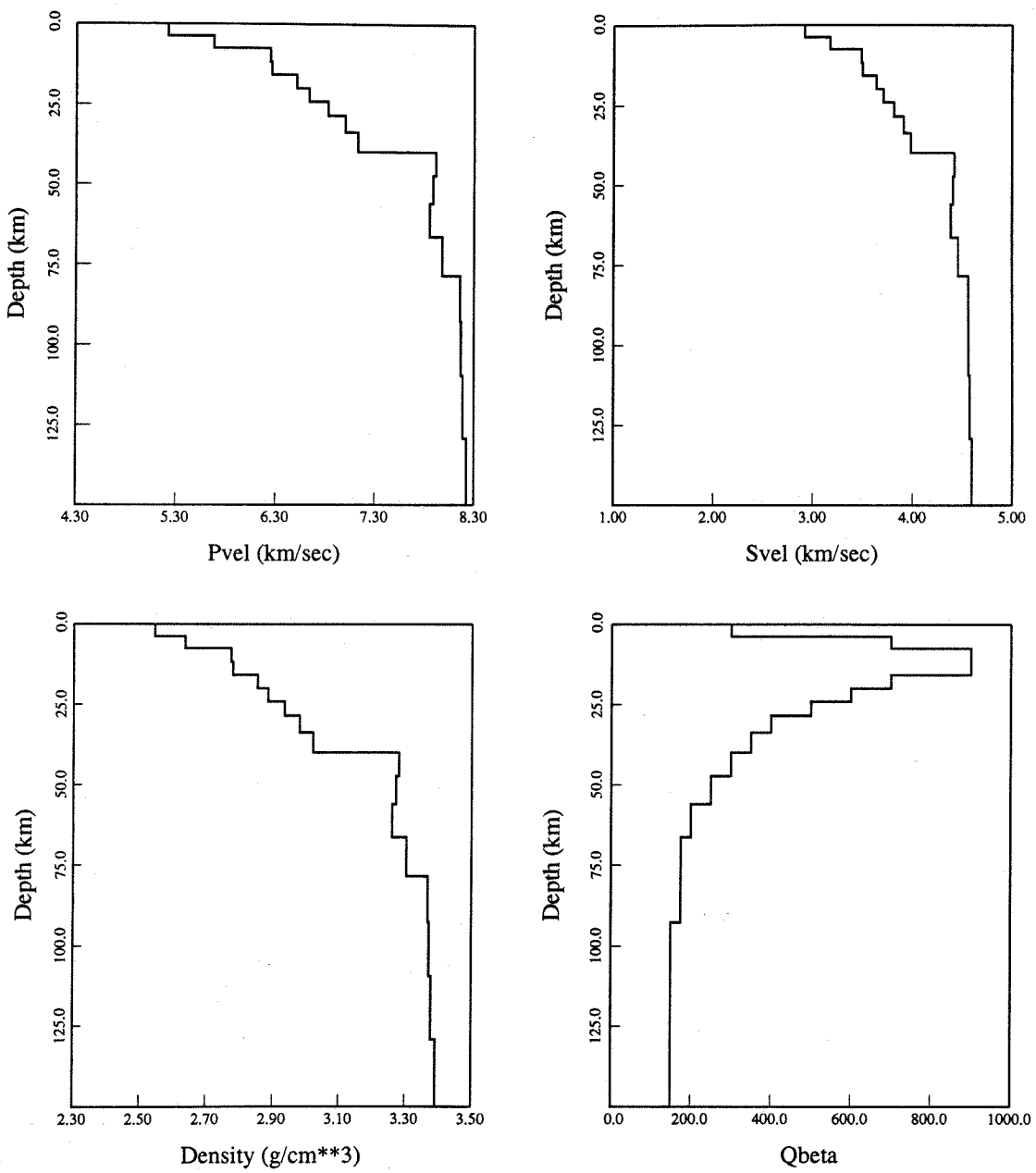

Figure 3.15: Path structure for NTS to RSON.

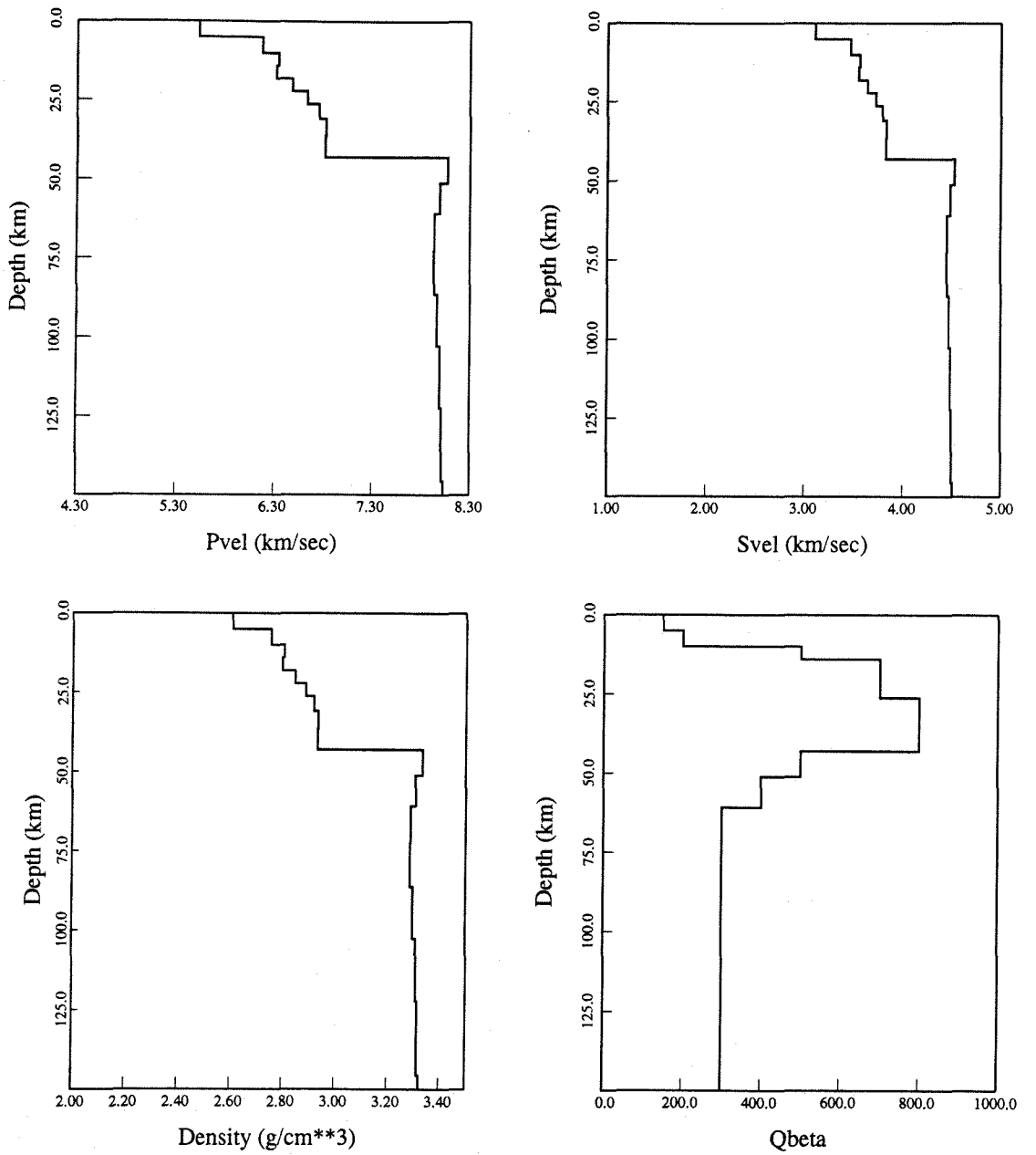

Figure 3.16: Path structure for NTS to RSCP.

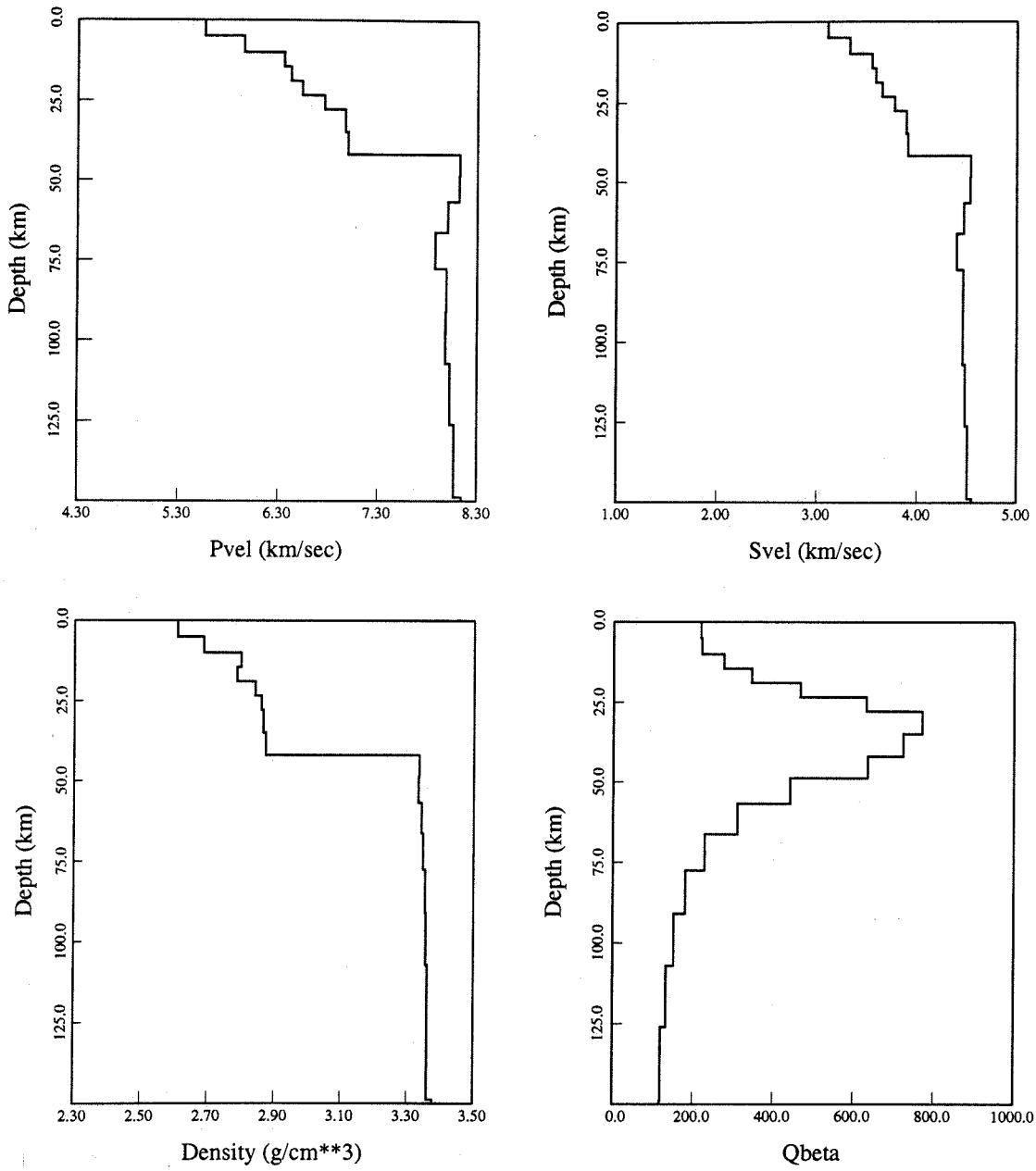

Figure 3.17: Path structure for NTS to RSNT.

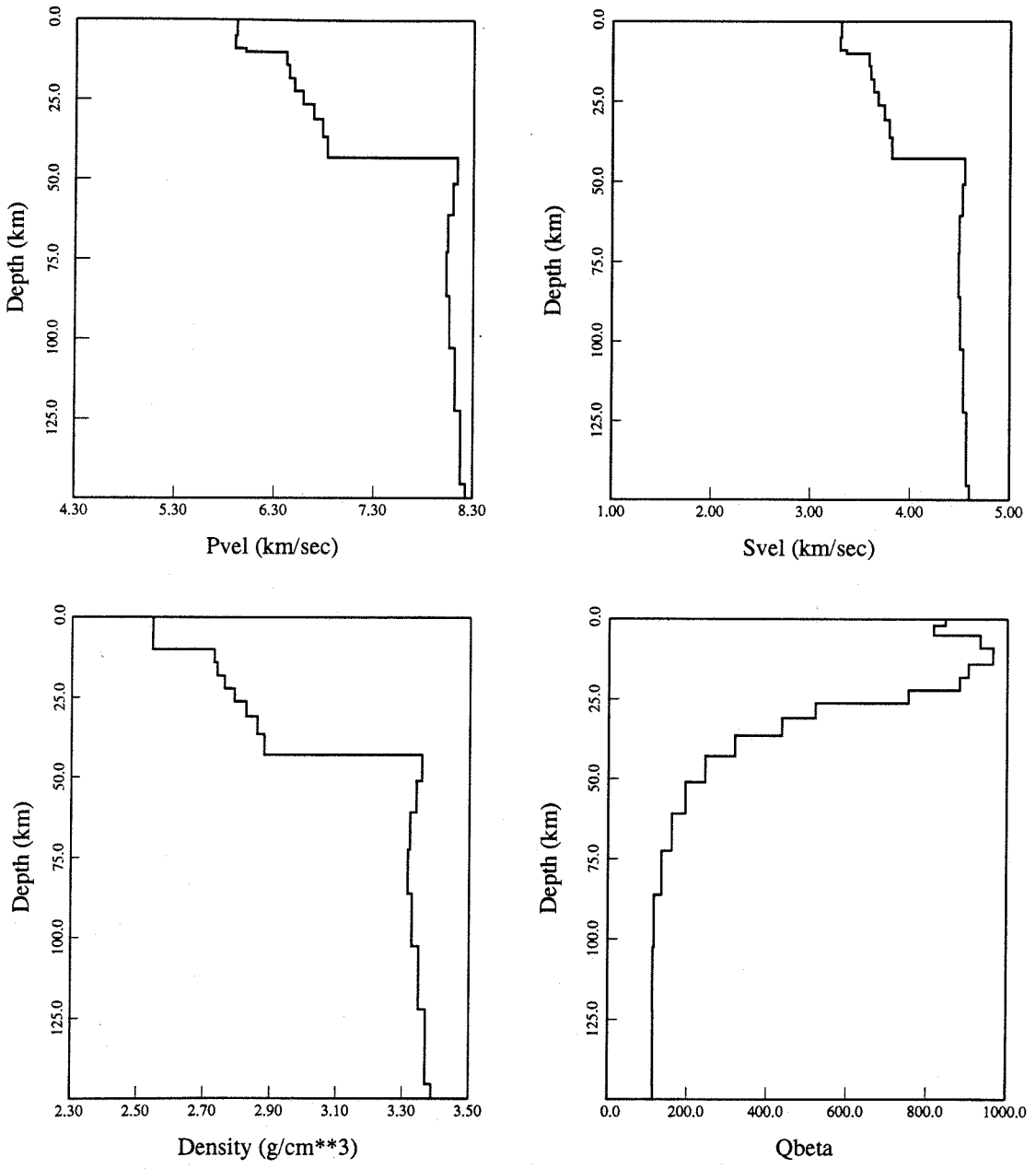

Figure 3.18: Path structure for NTS to RSNY.

Table 2: NTS to JAS Earth model				
thickness (km)	α (km/ sec)	β (km/ sec)	ρ ($g/\ cm^3$)	Q_β
2.5	4.06	2.35	2.33	30.0
5.0	6.00	3.51	2.70	103.4
5.0	5.96	3.49	2.69	171.6
5.0	6.20	3.63	2.76	171.6
5.0	6.11	3.58	2.73	171.6
5.0	5.95	3.48	2.69	171.6
5.0	6.36	3.71	2.81	103.4
5.0	6.33	3.69	2.80	103.4
4.0	7.55	4.36	3.26	103.4
5.0	7.60	4.38	3.27	90.0
10.0	7.66	4.42	3.29	80.0
10.0	7.73	4.46	3.22	70.0
20.0	7.80	4.12	3.24	70.0
20.0	7.86	4.15	3.26	80.0
20.0	7.91	4.08	3.28	93.4
20.0	7.98	4.09	3.30	106.8
20.0	8.04	4.40	3.33	106.8
20.0	8.13	4.43	3.36	106.8
20.0	8.22	4.45	3.39	106.8
∞	8.36	4.54	3.44	106.8

Table 3.2: NTS to JAS path model.

Table 3: NTS to PAS Earth model				
thickness (km)	α (km/ sec)	β (km/ sec)	ρ (g / cm^3)	Q_β
1.0	3.09	1.75	2.16	30.0
3.0	5.62	3.21	2.62	54.6
5.0	6.07	3.51	2.72	74.6
5.0	6.02	3.48	2.71	131.6
5.0	6.08	3.52	2.73	171.6
5.0	6.19	3.58	2.76	131.6
4.0	6.27	3.62	2.78	103.4
5.0	6.80	3.93	2.93	103.4
5.0	7.78	4.49	3.24	103.4
5.0	7.74	4.47	3.22	74.6
5.0	7.68	4.43	3.20	49.6
5.0	7.61	4.39	3.18	49.6
10.0	7.54	4.35	3.15	49.6
10.0	7.48	4.31	3.13	49.6
10.0	7.44	4.29	3.12	31.2
20.0	7.43	4.29	3.12	31.2
20.0	7.48	4.32	3.13	63.4
20.0	7.58	4.37	3.16	93.4
∞	7.67	4.43	3.20	106.8

Table 3.3: NTS to PAS path model.

Table 4: NTS to RSSD Earth model				
thickness (km)	α (km/ sec)	β (km/ sec)	ρ ($g/\ cm^3$)	Q_β
4.000	4.91	2.74	2.50	80.0
3.000	5.29	2.96	2.56	100.0
4.306	6.0	3.35	2.69	150.0
4.306	6.23	3.48	2.74	250.0
4.306	6.45	3.61	2.79	350.0
4.306	6.44	3.60	2.79	550.0
4.495	6.51	3.64	2.80	650.0
6.277	6.64	3.71	2.84	750.0
6.020	7.63	4.26	3.18	350.0
7.067	7.63	4.27	3.19	250.0
8.297	7.65	4.28	3.19	200.0
9.741	7.63	4.27	3.19	200.0
11.430	7.65	4.28	3.19	175.0
13.420	7.88	4.40	3.27	155.0
15.760	7.87	4.40	3.27	140.0
18.500	7.97	4.46	3.30	130.0
21.720	7.89	4.41	3.27	120.0
25.500	7.91	4.42	3.28	116.0
∞	7.91	4.42	3.28	116.0

Table 3.4: NTS to RSSD path model.

Table 5: NTS to RSON Earth model				
thickness (km)	α (km/ sec)	β (km/ sec)	ρ ($g/\ cm^3$)	Q_β
3.75	5.22	2.92	2.54	300.0
3.75	5.68	3.17	2.64	700.0
4.16	6.25	3.49	2.78	900.0
4.16	6.26	3.50	2.78	900.0
4.16	6.51	3.64	2.85	700.0
4.16	6.64	3.71	2.89	600.0
4.45	6.83	3.81	2.94	500.0
5.24	7.00	3.91	2.98	400.0
6.17	7.13	3.98	3.02	350.0
7.39	7.92	4.42	3.28	300.0
8.71	7.89	4.41	3.27	250.0
10.26	7.86	4.39	3.26	200.0
12.08	7.98	4.46	3.30	175.0
14.24	8.16	4.56	3.37	175.0
16.77	8.17	4.57	3.37	150.0
19.76	8.19	4.58	3.38	150.0
23.28	8.23	4.60	3.39	150.0
27.43	8.25	4.61	3.40	125.0
32.32	8.23	4.60	3.39	115.0
∞	8.23	4.60	3.39	115.0

Table 3.5: NTS to RSON path model.

Table 6: NTS to RSCP Earth model				
thickness (km)	α (km/ sec)	β (km/ sec)	ρ ($g/\ cm^3$)	Q_β
5.00	5.54	3.11	2.61	150.0
5.00	6.18	3.47	2.75	200.0
4.06	6.33	3.56	2.80	500.0
4.06	6.33	3.55	2.80	700.0
4.06	6.49	3.64	2.85	700.0
4.06	6.64	3.73	2.89	700.0
4.64	6.76	3.80	2.92	800.0
5.52	6.82	3.83	2.94	800.0
6.58	6.82	3.83	2.93	800.0
8.18	8.07	4.53	3.34	500.0
9.73	7.99	4.49	3.31	400.0
11.58	7.94	4.46	3.29	300.0
13.78	7.93	4.45	3.29	300.0
16.41	7.97	4.47	3.30	300.0
19.53	8.00	4.49	3.31	300.0
23.25	8.02	4.50	3.32	300.0
27.67	8.04	4.51	3.32	300.0
32.94	8.08	4.53	3.34	300.0
39.21	8.15	4.57	3.36	300.0
∞	8.15	4.58	3.37	300.0

Table 3.6: NTS to RSCP path model.

Table 7: NTS to RSNT Earth model				
thickness (km)	α (km/ sec)	β (km/ sec)	ρ (g / cm^3)	Q_β
5.00	5.57	3.11	2.61	217.4
5.00	5.96	3.33	2.69	219.9
4.45	6.36	3.55	2.80	275.4
4.45	6.43	3.58	2.79	344.3
4.45	6.54	3.65	2.84	466.0
4.45	6.76	3.78	2.86	631.4
7.09	6.97	3.90	2.87	770.2
7.06	7.00	3.91	2.87	723.0
6.70	8.13	4.54	3.34	634.9
7.98	8.11	4.53	3.33	441.2
9.50	8.00	4.47	3.34	310.3
11.31	7.88	4.40	3.35	229.2
13.46	7.99	4.46	3.35	181.0
16.03	7.98	4.46	3.36	152.3
19.08	8.03	4.49	3.36	133.5
22.72	8.07	4.51	3.36	120.2
27.05	8.15	4.55	3.38	118.6
32.20	8.22	4.59	3.37	119.0
38.33	8.26	4.61	3.39	119.3
45.63	8.26	4.62	3.39	119.5

Table 3.7: NTS to RSNT path model.

Table 8: NTS to RSNY Earth model				
thickness (km)	α (km/ sec)	β (km/ sec)	ρ ($g/\ cm^3$)	Q_β
2.00	5.92	3.31	2.54	844.0
3.00	5.92	3.31	2.54	815.0
4.00	5.90	3.30	2.54	932.0
1.00	6.01	3.36	2.54	965.0
4.06	6.42	3.59	2.73	964.0
4.06	6.44	3.60	2.74	902.0
4.06	6.50	3.63	2.76	881.0
4.06	6.58	3.68	2.79	752.4
4.64	6.69	3.74	2.83	520.0
5.52	6.78	3.79	2.86	436.1
6.58	6.83	3.82	2.88	318.5
8.18	8.14	4.55	3.36	243.4
9.73	8.10	4.52	3.34	194.3
11.58	8.04	4.49	3.32	160.5
13.78	8.03	4.49	3.32	135.1
16.41	8.06	4.50	3.33	116.0
19.53	8.12	4.54	3.35	113.4
23.25	8.18	4.57	3.37	114.1
27.67	8.23	4.60	3.39	114.6
32.94	8.27	4.62	3.40	115.0
39.21	8.31	4.64	3.42	115.0
∞	8.34	4.66	3.43	115.0

Table 3.8: NTS to RSNY path model.

3.5 Synthetic Seismogram Generation and Moment Inversion Technique

As in chapter 2, only fundamental-mode surface wave observations are modeled. Since explosions are shallow sources ($d < 1$ km) and tectonic strain release is also thought to be not much deeper, higher modes are not strongly excited. Patton (1988a) found that spall can generate higher modes. However, such excited energy is relatively short-period, so that it's effect on the long-period function is minimal.

The vertical spectral displacement (positive down) for an explosion is

$$w_0 = -ik_R A_R \frac{\beta^2}{\alpha^2} M_I(\omega) K_R H_0^{(2)}(k_R r), \tag{3.5}$$

following the notation of Harkrider (1964 and 1981). The vertical displacement for a double-couple source is

$$w_0 = -ik_R A_R \frac{M_{DC}(\omega)}{2} \{B_{DC} H_0^{(2)} \Lambda_O(k_R r) - C_{DC} \Lambda_1 H_1^{(2)}(k_R \cdot r) + A_{DC} \Lambda_2 H_2^{(2)}(k_R r)\}, \tag{3.6}$$

where

$$K_R = y_3^R(h) - \frac{1}{2\mu k_R r} y_2^R(h), \tag{3.7}$$

$$A_{DC} = -y_3^R(h), \tag{3.8}$$

$$B_{DC} = -\{(3 - 4\frac{\beta^2}{\alpha^2}) y_3^R(h) + \frac{2y_2^R(h)}{\rho\alpha^2 k_R}\}, \tag{3.9}$$

$$C_{DC} = \frac{y_4^R(h)}{\mu k_R}, \tag{3.10}$$

and

$$\Lambda_0 = \frac{1}{2} \sin\lambda \sin 2\delta, \tag{3.11}$$

$$\Lambda_1 = \cos\lambda \cos\delta \cos\phi - \sin\lambda \cos 2\delta \sin\phi, \tag{3.12}$$

$$\Lambda_2 = \frac{1}{2} \sin\lambda \sin 2\delta \cos 2\phi + \cos\lambda \sin\delta \sin 2\phi. \tag{3.13}$$

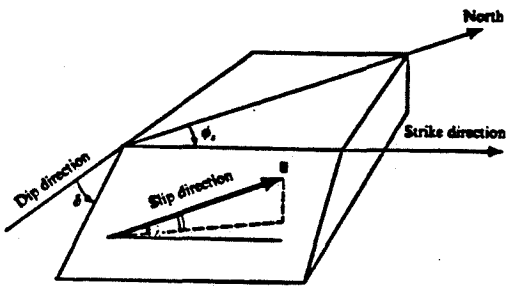

Definition of the fault-orientation parameters (strike ϕ_s, dip δ), and slip-direction. ϕ_s is measured clockwise round from north, with the fault dipping down to the right of the strike direction: $0 \leq \phi_s < 2\pi$. δ is measured down from the horizontal: $0 \leq \delta \leq \pi/2$.

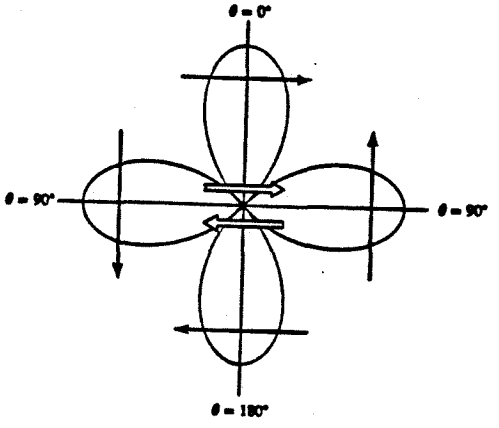

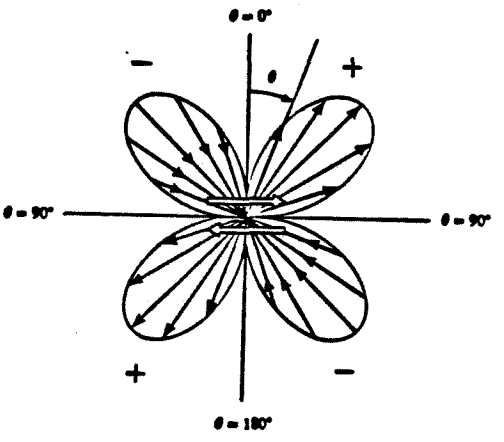

Figure 3.19: (a) Fault plane geometry for tectonic strain release mechanism. (b) Rayleigh wave radiation pattern for a vertical strike-slip mechanism. (c) Love wave radiation pattern for a vertical strike-slip mechanism.

The angles λ, δ, and ϕ are defined in figure 3.19a.

For Love waves, the tangential component displacement due to an arbitrary fault plane is:

$$v_0 = -iA_L \frac{M_{DC}(\omega)}{4} \{ y_1^L \frac{\partial \Lambda_2}{\partial \phi} \frac{d}{dr} H_2^{(2)}(k_L r) + \frac{2}{\mu k_L} y_2^L \frac{\partial \Lambda_1}{\partial \phi} \frac{d}{dr} H_1^{(2)}(k_L r) \}. \qquad (3.14)$$

A_R and A_L are given by equation 2.7:

$$A = \frac{1}{2cUI}$$

From equations 3.12 and 3.13 one obtains:

$$\frac{\partial \Lambda_1}{\partial \phi} = \sin\lambda \cos 2\delta \cos\phi - \cos\lambda \cos\delta \sin\phi \qquad (3.15)$$

and

$$\frac{\partial \Lambda_2}{\partial \phi} = 2\cos\lambda \sin\delta \cos 2\phi - \sin\lambda \sin 2\delta \sin 2\phi. \qquad (3.16)$$

Equations 3.15 and 3.16 follow the development by Harkrider (1964 and 1970) and are more explicitly given in Stevens *et al.* (1982).

Assuming that tectonic release can be modeled as a double couple source and that at the periods of interest ($T > 6sec$) the explosion and tectonic release source occur simultaneously, the full vertical Rayleigh wave displacement field is (combining equations 3.5 and 3.6):

$$\begin{aligned} w_0 \;=\; & -ik_R A_R \{ M_I \frac{\beta^2}{\alpha^2} K_R(h_I) H_0^{(2)}(k_R r) \\ & + \frac{M_{DC}}{2} [\frac{\sin\lambda \sin 2\delta}{2} B_{DC}(h_{DC}) H_0^{(2)}(k_R r) \\ & - (\cos\lambda \cos\delta \cos\phi - \sin\lambda \cos 2\delta \sin\phi) C_{DC}(h_{DC}) H_1^{(2)}(k_R r) \\ & + (\frac{\sin\lambda}{2} \sin 2\delta \cos 2\phi + \cos\lambda \sin\delta \sin 2\phi) A_{DC}(h_{DC}) H_2^{(2)}(k_R r)] \}. \end{aligned} \qquad (3.17)$$

At distances large in comparison to the wavelength ($k \cdot r \gg 1$), the following approximations can be made:

$$H_0^{(2)}(kr) \cong (\frac{2}{\pi kr})^{1/2} e^{-ikr} e^{i\pi/4}, \qquad (3.18)$$

$$H_1^{(2)}(kr) \cong i(\frac{2}{\pi kr})^{1/2} e^{-ikr} e^{i\pi/4}, \tag{3.19}$$

$$\frac{dH_1^{(2)}}{dr}(kr) \cong k(\frac{2}{\pi kr})^{1/2} e^{-ikr} e^{i\pi/4}, \tag{3.20}$$

$$H_2^{(2)}(kr) \cong -(\frac{2}{\pi kr})^{1/2} e^{-ikr} e^{i\pi/4}, \tag{3.21}$$

$$\frac{dH_2^{(2)}}{dr}(kr) \cong ik(\frac{2}{\pi kr})^{1/2} e^{-ikr} e^{i\pi/4}, \tag{3.22}$$

yielding the following far-field displacements for vertical and tangential components

$$\begin{aligned} w_0 \cong\ & -ik_R A_R (\frac{2}{\pi k_R r})^{1/2} e^{-ik_R r} e^{i\pi/4} [M_I \frac{\beta^2}{\alpha^2} K_R(h_I) \\ & + \frac{M_{DC}}{2} \{ \frac{1}{2} \sin\lambda \sin 2\delta [B_{DC}(h_{DC}) - A_{DC}(h_I) \cos 2\phi] \\ & - \cos\lambda \sin\delta \sin 2\phi A_{DC}(h_{DC}) \\ & - i(\cos\lambda \cos\delta \cos\phi - \sin\lambda \cos 2\delta \sin\phi) C_{DC}(h_{DC}) \}] \end{aligned} \tag{3.23}$$

and

$$\begin{aligned} v \cong\ & k_L A_L (\frac{2}{\pi k_L r})^{1/2} e^{-ik_L r} e^{i\pi/4} \frac{M_{DC}}{2} \\ \cdot\ & [(\cos\lambda \sin\delta \cos 2\phi - \frac{\sin\lambda}{2} \sin 2\delta \sin 2\phi) y_1^L(h_{DC}) \\ & + i(\sin\lambda \cos 2\delta \cos\phi - \cos\lambda \cos\delta \sin\phi) \frac{y_2^L(h_{DC})}{k_L \mu}] \end{aligned} \tag{3.24}$$

Assuming that h_I and h_{DC}, the respective explosion and double couple source depths, are shallow, then as $h \to 0$, $y_2^R(h) \to 0$, $y_4^R(h) \to 0$, and $y_2^L(h) \to 0$ and $K_R(0) = y_3^R(0) = -A_{DC}(0) = \frac{1}{3-4\frac{\beta^2}{\alpha^2}} B_{DC}(0)$ and $C_{DC}(0) = 0$ and $y_1^L(0) = 1$. Making use of these relations reduces the displacement equations to:

$$\begin{aligned} w_0 \cong\ & -ik_R A_R (\frac{2}{\pi k_R r})^{1/2} e^{-ik_R r} e^{i\pi/4} y_3^R(0) \frac{\beta^2}{\alpha^2} \\ \cdot\ & \{ M_I + \frac{M_{DC}}{2} \frac{\alpha^2}{\beta^2} [\frac{1}{2} \sin\lambda \sin 2\delta (\cos 2\phi - 3 + 4\frac{\beta^2}{\alpha^2}) \\ & + \cos\lambda \sin\delta \sin 2\phi] \} \end{aligned} \tag{3.25}$$

and

$$v \cong k_L A_L (\frac{2}{\pi k_L r})^{1/2} e^{-ik_L r} e^{i\pi/4} \frac{M_{DC}}{4} \tag{3.26}$$

$$\cdot \quad (2\cos\lambda \sin\delta \cos 2\phi - \sin\lambda \sin 2\delta \sin 2\phi). \tag{3.27}$$

At NTS the assumed mechanism for tectonic release is believed to be predominantly vertical, right-lateral strike slip in nature (Toksöz *et al.*, 1965;d Wallace *et al.*, 1983, 1985) ($\lambda = 180^o and \delta = 90^o$). This assumption is made in part to help simplify the inversion procedure and leads to:

$$w_0 \cong -ik_R A_R (\frac{2}{\pi k_R r})^{1/2} e^{-ik_R r} e^{i\pi/4} y_3^R(0) \frac{\beta^2}{\alpha^2} [M_I - \frac{M_{DC}}{2} \frac{\alpha^2}{\beta^2} \sin 2\phi] \tag{3.28}$$

and

$$v = -k_L A_L (\frac{2}{\pi k_R r})^{1/2} e^{-ik_R r} e^{i\pi/4} \frac{M_{DC}}{2} \cos 2\phi, \tag{3.29}$$

so that measure moment becomes a function of M_I, M_{DC} and ϕ (three parameters), where ϕ is the azimuth measured clockwise from the strike of the fault plane.

The SH and P-SV radiation patterns (in map view) for vertical strike-slip fault plane are shown in figures 3.19b and 3.19c, respectively.

To invert for the combined isotropic/double couple source mechanism, the measured fundamental Rayleigh and Love wave amplitudes are averaged over a spectral bandwidth between 10 and 60 seconds. For a receiver at azimuth θ, measured clockwise from North, and with a vertical strike slip fault with strike ψ, also measured clockwise from North (see figure 3.19a), the observed Rayleigh amplitude will be:

$$A_{Ray} \propto M_I - \frac{M_{DC}}{2} \frac{\alpha^2}{\beta^2} \sin 2(360^o - \psi + \theta), \tag{3.30}$$

which can be simplified to:

$$A_{Ray} \propto M_I - \frac{M_{DC}}{2} \frac{\alpha^2}{\beta^2} [\sin 2\theta \cos 2\psi - \cos 2\theta \sin 2\psi]. \tag{3.31}$$

This equation can be formulated as a linear least-squares inversion problem of the form:

$$\mathbf{A} \cdot \mathbf{x} = \mathbf{b},$$

or

$$A_{Ray} = 1 \cdot x_1 - \frac{\sin 2\theta}{2}\frac{\alpha^2}{\beta^2} \cdot x_2 + \frac{\cos 2\theta}{2}\frac{\alpha^2}{\beta^2} \cdot x_3 \tag{3.32}$$

where $x_1 = M_I$, $x_2 = M_{DC} \cdot \cos 2\psi$, and $x_3 = M_{DC} \cdot \sin 2\psi$.

Similarly for the Love wave case, the amplitude is

$$A_{Lov} \propto M_{DC} \cos 2\phi = M_{DC} \cos 2(360^o - \psi + \theta), \tag{3.33}$$

or

$$A_{Lov} \propto M_{DC}[\cos 2\theta \cos 2\psi + \sin 2\theta sin2\psi] \tag{3.34}$$

or in terms of a least-square problem in the form

$$A_{Lov} \propto \cos 2\theta \cdot x_1' + \sin 2\theta \cdot x_2' = \cos 2\theta \cdot x_2 + \sin 2\theta \cdot x_3. \tag{3.35}$$

The errors in this inversion can be calculated directly. For a function $x = f(u, v)$, the variance (σ_x^2) is defined as

$$\sigma_x^2 = \sigma_u^2(\frac{\partial x}{\partial u})^2 + \sigma_v^2(\frac{\partial x}{\partial v})^2 + 2\sigma_{uv}^2(\frac{\partial x}{\partial u})(\frac{\partial x}{\partial v}). \tag{3.36}$$

For the case of u and v being uncorrelated $\sigma_{uv}^2 = 0$. σ_x is defined as:

$$\sigma_X = \sqrt{\frac{\sum(X_{obs}^i - X_{model}^i)^2}{N - m}}, \tag{3.37}$$

with N being the number of observations and m the number of parameters.

For the Rayleigh wave inversion (equation 36) case, the variance in the explosion estimate, x_1 is $\sigma_E^2 = \sigma_1^2$. For the tectonic release component $(TR = \sqrt{x_2^2 + x_3^2})$,

$$\sigma_{TR}^2 = \sigma_2^2 \cdot \frac{x_2^2}{(x_2^2 + x_3^2)} + \sigma_3^2 \cdot \frac{x_3^2}{(x_2^2 + x_3^2)}. \tag{3.38}$$

For the strike azimuth ($\psi = \frac{90^o}{\pi} \arctan(x_3/x_2)$),

$$\sigma_\psi^2 = \sigma_2^2 \cdot (\frac{90^o}{\pi})^2 \frac{x_2^2}{(x_2^2 + x_3^2)} + \sigma_3^2 \cdot (\frac{90^o}{\pi})^2 \frac{x_3^2}{(x_2^2 + x_3^2)}. \tag{3.39}$$

Since in the Love wave case $TR = \sqrt{x_2^2 + x_3^2}$ as well, the variances σ_{TR}^2 and σ_ψ^2 are also given by equations 3.37 and 3.39, respectively.

3.6 Results

Several variations of spectral source inversions were conducted. First a weighted average spectral moment was calculated assuming only a scalar moment from an explosive source. No station corrections were included in these calculations. Variance reciprocals were used as the weighting coefficients. These source parameters are given in table 3.9; for each event the upper entry is the source parameter and the lower one is its standard deviation. Moment values are in units of 10^{15} Newton-Meters $(N - M)$ and the strike angle is in degrees. In the second column the upper entry is the number of Rayleigh observations and the lower entry is the number of Love wave observations used.

Next, the isotropic (M_I) and double-couple (M_{DC}) moment components and strike angle (ϕ) were then determined using the least-squares inversion method described in the previous section. Separate inversions were performed for the Rayleigh waves ($M_{*(R)}$, $M_{DC(R)}$, and $\phi_{(R)}$), Love waves $M_{DC(L)}$ and $\phi_{(L)}$), and the combined data ($M_{*(R+L)}$, $M_{DC(R+L)}$, and $\phi_{(R+L)}$). The values and standard deviations are also listed in table 9. Again variance reciprocals were used as the weighting coefficients in the inversion. In the last column is the F factor, defined by Toksöz *et al.* (1965) as:

$$F = \frac{M_{DC}}{M_I} \frac{\alpha^2}{2\beta^2} \approx \frac{3}{2} \frac{M_{DC}}{M_I} \tag{3.40}$$

for near-Poisson solids ($\alpha^2/\beta^2 \approx 3$).

Table 9 (a): Inverted Explosion and Tectonic Release Source Parameters											
Event	# obs.	M_0	$M_{I(R)}$	$M_{dc(R)}$	$\phi_{(R)}$	$M_{dc(L)}$	$\phi_{(L)}$	$M_{I(R+L)}$	$M_{dc(R+L)}$	$\phi_{(R+L)}$	$F_{(R+L)}$
65062	13	1.762	2.220	0.804	335.3	1.395	340.9	2.261	0.900	342.4	0.597
	4	0.345	0.223	0.263	9.6	0.207	4.4	0.208	0.145	4.6	0.111
66018	4	1.740	1.650	0.693	307.2			1.661	0.629	307.9	0.568
	1	0.438	0.323	0.315	15.6			0.237	0.190	12.1	0.189
66055	7	0.965	1.725	1.	342.7	2.696	353.9	1.760	1.155	344.7	0.984
	2	0.382	0.175	0.206	4.9	0.178	2.4	0.211	0.255	4.9	0.247
66133	16	5.952	5.672	0.702	334.1	1.544	329.8	5.493	1.021	331.3	0.279
	7	0.363	0.416	0.359	14.9	0.323	5.6	0.369	0.252	7.0	0.071
66153	26	4.242	4.846	1.269	51.5	6.032	326.0	3.811	1.023	330.8	0.403
	13	0.416	0.407	0.395	7.5	1.507	6.3	0.949	0.769	19.8	0.319
66154	19	5.544	5.368	0.384	325.2	0.826	330.7	5.243	0.656	329.1	0.188
	8	0.331	0.378	0.335	26.4	0.482	19.1	0.390	0.252	12.2	0.073
67177	3	0.697	0.628	0.054	320.2	0.388	346.8	0.248	0.378	345.4	2.288
	2	0.018	0.018			0.016	0.6	0.064	0.	2.5	0.638
67243	1	0.195									
	0										
67312	8	1.110	0.954	0.206	295.4			0.871	0.315	296.4	0.543
	1	0.101	0.234	0.206	27.8			0.193	0.163	14.6	0.306
68060	5	0.647	0.721	0.261	344.0						0.543
	0	0.165	0.101	0.087	11.3						0.196
68268	7	0.694	0.639	0.233	335.6						0.546
	0	0.133	0.127	0.115	13.7						0.290
69015	8	2.578	2.942	0.654	5.2	2.012	358.8	2.871	1.237	357.4	0.646
	2	0.245	0.711	0.250	25.5	0.710	3.3	0.886	0.300	16.3	0.253
69043	1	0.451									
	0										
69120	15	3.131	3.007	0.173	332.0			2.944	0.262	333.6	0.134
	1	0.203	0.299	0.251	45.0			0.265	0.214	25.3	0.110
70042	1	0.582									
	0										
70082	14	5.360	5.713	1.289	297.3			5.605	1.357	301.6	0.363
	1	0.572	0.597	0.588	13.5			0.540	0.472	11.2	0.131

Table 3.9: Source parameters for explosions and associated tectonic release.

Table 9 (b): Inverted Explosion and Tectonic Release Source Parameters											
Event	# obs.	M_0	$M_{I(R)}$	$M_{dc(R)}$	$\phi_{(R)}$	$M_{dc(L)}$	$\phi_{(L)}$	$M_{I(R+L)}$	$M_{dc(R+L)}$	$\phi_{(R+L)}$	$F_{(R+L)}$
70125	3	0.856	70.761	63.643	79.7	0.431	346.2	0.386	0.431	350.5	1.675
	2	0.122	0.122			0.109	3.8	0.235	0.168	8.0	1.209
70146	2	0.354									
	0	0.041									
71180	7	0.291	0.362	0.103	354.5						0.427
	0	0.048	0.028	0.022	8.0						0.096
71189	15	3.561	3.896	0.567	58.4	1.007	1.1	3.433	0.400	346.2	0.175
	3	0.212	0.299	0.315	14.6	0.216	7.3	0.286	0.209	16.3	0.092
71230	18	1.426	1.370	0.109	339.0	0.582	356.3	1.276	0.286	347.7	0.336
	5	0.068	0.079	0.072	18.5	0.071	3.3	0.	0.075	6.5	0.091
72123	5	0.444	0.712	0.265	354.0			0.655	0.255	343.6	0.584
	1	0.127	0.101	0.078	10.9			0.114	0.093	11.3	0.237
72140	3	0.573	0.607	0.184	313.1			0.576	0.049	29.6	0.127
	1	0.043	0.043					0.081	0.075	36.8	0.197
72202	5	0.477	0.475	0.138	347.9						0.436
	0	0.095	0.049	0.046	11.8						0.150
73067	10	3.228	3.353	0.270	81.5			2.785	0.455	321.2	0.245
	1	0.199	0.428	0.273	37.6			0.365	0.280	14.0	0.154
73116	20	2.851	2.865	0.124	351.6			2.886	0.287	339.3	0.149
	1	0.279	0.296	0.304	60.2			0.299	0.269	25.9	0.141
73156	6	0.634	0.574	0.140	357.9						0.367
	0	0.071	0.	0.022	6.2						0.061
74058	15	6.	5.533	1.390	328.9	2.078	345.2	5.333	1.761	336.5	0.495
	8	0.474	0.385	0.342	8.1	0.209	2.7	0.341	0.239	3.9	0.074
74170	7	0.690	0.761	0.228	344.2			0.830	0.314	356.1	0.568
	1	0.123	0.083	0.091	10.2			0.079	0.067	5.7	0.134
74191	21	10.389	10.422	1.692	315.0	3.168	347.5	10.427	1.935	323.8	0.278
	6	0.806	0.724	0.652	12.3	0.359	3.0	0.681	0.543	8.8	0.080
74269	12	2.265	2.194	0.150	315.7			2.169	0.236	325.4	0.163
	1	0.136	0.157	0.144	28.0			0.164	0.143	17.5	0.100
75066	15	2.692	2.470	0.300	298.2						0.182
	0	0.156	0.192	0.161	16.0						0.099

Table 9 (c): Inverted Explosion and Tectonic Release Source Parameters											
Event	# obs.	M_0	$M_{I(R)}$	$M_{dc(R)}$	$\phi_{(R)}$	$M_{dc(L)}$	$\phi_{(L)}$	$M_{I(R+L)}$	$M_{dc(R+L)}$	$\phi_{(R+L)}$	$F_{(R+L)}$
75095	1	0.649									
	0										
75120	12	1.492	1.486	0.236	325.1						0.238
	0	0.122	0.107	0.098	14.9						0.101
75154	20	8.947	8.503	1.682	284.4	11.806	20.5	8.613	1.299	290.6	0.226
	3	0.737	0.714	0.748	10.8	4.249	10.2	0.787	0.679	14.5	0.120
75297	1	0.289									
	0										
76035	13	7.244	7.740	1.076	282.6	1.682	351.7	7.254	1.534	319.4	0.317
	4	0.665	0.701	0.902	23.6	1.967	29.8	0.680	0.393	8.0	0.086
76133	1	0.853									
	0										
76363	7	4.736	4.411	1.211	282.9						0.412
	0	0.403	0.364	0.524	8.4						0.181
77117	16	3.297	3.926	0.896	274.7			3.154	0.395	323.1	0.188
	1	0.248	0.329	0.337	6.5			0.359	0.267	21.5	0.129
77145	8	4.051	4.664	0.901	80.9						0.290
	0	0.366	0.466	0.368	12.5						0.122
78193	21	4.728	5.275	1.288	297.5	0.462	342.7	5.186	1.025	302.0	0.296
	4	0.408	0.318	0.286	6.7	1.140	69.9	0.394	0.294	8.8	0.088
78322	12	1.889	1.923	0.301	288.3						0.234
	0	0.188	0.240	0.219	19.0						0.173
79039	18	2.611	4.389	1.886	332.4						0.644
	0	0.594	0.709	0.601	11.1						0.230
80107	17	3.118	3.201	0.982	84.7	0.777	319.3	3.103	0.514	282.9	0.249
	3	0.419	0.378	0.446	9.5	0.122	5.7	0.437	0.338	15.8	0.167
80305	5	0.526	0.611	0.374	329.3			0.812	0.354	352.1	0.654
	1	0.193	0.188	0.194	12.1			0.132	0.089	10.7	0.196
81015	10	7.871	7.504	0.760	337.1			7.414	0.916	339.1	0.185
	1	0.626	0.834	0.763	29.1			0.676	0.512	15.6	0.105
82028	8	11.200	11.512	0.895	335.8	1.939	344.9	11.436	1.548	349.5	0.203
	4	0.520	0.402	0.509	17.4	0.292	5.3	0.389	0.324	5.4	0.043

Table 9 (d): Inverted Explosion and Tectonic Release Source Parameters											
Event	# obs.	M_0	$M_{I(R)}$	$M_{dc(R)}$	$\phi_{(R)}$	$M_{dc(L)}$	$\phi_{(L)}$	$M_{I(R+L)}$	$M_{dc(R+L)}$	$\phi_{(R+L)}$	$F_{(R+L)}$
82043	4	10.253	10.199	1.714	299.9	3.326	335.2	8.253	3.236	335.2	0.588
	4	1.379	1.748	1.401	30.7	0.160	1.3	0.960	0.319	2.6	0.090
82044	7	7.402	6.958	1.493	355.2	1.870	345.6	7.046	1.612	349.6	0.343
	7	0.652	0.590	0.704	8.7	0.094	1.9	0.366	0.151	3.4	0.037
82107	4	0.210	0.197	0.086	351.0	0.250	47.2	0.210	0.045	342.0	0.325
	3	0.054	0.031	0.033	9.3	0.081	2.3	0.056	0.032	24.1	0.248
82115	7	6.638	6.633	0.302	306.2	1.925	337.0	6.594	1.213	348.3	0.276
	5	0.362	0.398	0.384	76.7	0.151	2.2	0.469	0.186	6.1	0.047
82126	4	0.109	0.111	0.009	287.2						0.120
	0	0.007	0.012	0.022	52.6						0.296
82127	8	4.896	4.969	0.648	345.2	1.351	339.1	5.	1.023	345.3	0.306
	8	0.353	0.314	0.429	14.0	0.107	2.4	0.267	0.127	4.1	0.041
82175	8	9.711	9.151	1.956	13.0	1.592	3.9	9.	1.666	9.4	0.275
	8	0.711	0.515	0.460	5.6	0.112	7.6	0.433	0.120	4.5	0.024
82210	8	0.280	0.274	0.096	322.4	0.188	334.1	0.261	0.132	337.6	0.755
	3	0.057	0.029	0.033	20.8	0.008	1.1	0.031	0.014	3.1	0.121
82217	8	12.794	12.692	0.666	340.8	2.152	341.5	12.559	1.571	348.0	0.188
	5	0.547	0.561	0.717	27.1	0.077	1.1	0.529	0.343	5.9	0.042
82266	5	0.590	0.632	0.061	86.2	0.227	339.0	0.387	0.172	339.7	0.666
	3	0.	0.255	0.189	84.0	0.008	1.0	0.133	0.079	13.4	0.382
82267	4	0.969	0.951	0.202	15.0	0.510	353.6	0.737	0.436	359.4	0.886
	4	0.131	0.223	0.198	23.7	0.	0.9	0.144	0.063	5.7	0.215
82272	4	0.096	0.092	0.013	15.1						0.214
	0	0.005			0.3						0.003
82344	7	0.352	0.317	0.047	356.1	0.092	2.1	0.282	0.089	4.4	0.474
	5	0.024	0.031	0.028	15.1	0.016	16.8	0.028	0.	7.1	0.072
83085	11	3.452	3.293	0.790	2.3	0.944	34	3.068	0.789	345.2	0.386
	10	0.284	0.139	0.109	4.8	0.078	2.5	0.171	0.081	3.5	0.045
83104	10	3.564	3.631	0.596	352.1	0.697	333.4	3.583	0.608	344.1	0.255
	7	0.312	0.311	0.372	12.1	0.	2.9	0.235	0.167	7.2	0.072
83125	6	0.121	0.189	0.084	287.0						0.662
	0	0.025	0.027	0.022	7.4						0.199

Table 9 (e): Inverted Explosion and Tectonic Release Source Parameters

Event	# obs.	M_0	$M_{I(R)}$	$M_{dc(R)}$	$\phi_{(R)}$	$M_{dc(L)}$	$\phi_{(L)}$	$M_{I(R+L)}$	$M_{dc(R+L)}$	$\phi_{(R+L)}$	$F_{(R+L)}$
83146	7	0.545	0.528	0.081	331.9			0.525	0.084	335.7	0.240
	1	0.066	0.	0.076	32.1			0.062	0.068	24.6	0.197
83160	6	0.296	0.301	0.087	341.8	0.084	7.5	0.301	0.103	348.9	0.512
	4	0.047	0.017	0.019	5.7	0.048	41.8	0.028	0.012	5.5	0.078
83244	13	3.855	4.301	1.671	338.0	1.533	334.8	4.272	1.547	335.4	0.543
	13	0.514	0.204	0.191	3.3	0.094	1.6	0.176	0.086	1.5	0.038
83264	2	0.162									
	0	0.003									
83265	4	0.078	0.	0.031	284.0			0.087	0.015	287.9	0.259
	1	0.004	0.018	0.028	18.1			0.018	0.023	37.7	0.409
83350	10	1.983	1.887	0.233	335.2	0.278	352.2	1.863	0.281	345.9	0.227
	5	0.144	0.134	0.132	16.7	0.112	28.0	0.111	0.071	8.6	0.058
84046	7	0.594	0.631	0.307	331.3			0.631	0.307	331.2	0.731
	1	0.137	0.036	0.035	2.9			0.032	0.	2.5	0.081
84061	10	8.401	8.009	1.893	346.5	2.656	338.4	7.975	2.179	344.8	0.410
	7	0.722	0.335	0.353	4.5	0.219	2.4	0.312	0.229	3.0	0.046
84122	10	7.374	6.373	1.282	336.5	1.318	333.5	6.374	1.315	334.5	0.309
	9	0.510	0.582	0.507	11.1	0.114	2.5	0.333	0.190	4.1	0.048
84152	10	8.081	8.132	0.935	352.6	1.147	330.3	8.084	0.920	336.5	0.171
	7	0.476	0.467	0.750	12.2	0.144	3.7	0.404	0.228	7.2	0.043
84172	4	0.660	0.507	0.217	337.5			0.507	0.217	337.5	0.642
	1	0.134	0.058	0.051	6.8			0.039	0.035	4.6	0.114
84207	9	3.637	4.839	2.736	354.5	3.344	351.0	4.927	2.952	354.2	0.899
	9	0.838	0.234	0.245	1.8	0.186	2.1	0.201	0.150	1.4	0.059
84215	5	0.210	0.206	0.043	349.2	0.104	342.6	0.203	0.	354.5	0.445
	3	0.022	0.013	0.018	8.1	0.129	45.7	0.022	0.018	7.7	0.143
84243	3	0.359	0.389	0.104	291.2			0.388	0.099	291.5	0.384
	1	0.055	0.055					0.003	0.004	1.0	0.014
84257	4	1.179	1.190	0.223	356.3	0.395	348.9	1.207	0.328	358.3	0.407
	4	0.055	0.048	0.199	5.7	0.031	3.9	0.028	0.026	1.6	0.034
84315	4	0.125	0.140	0.029	306.1	0.478	316.6	0.157	0.066	295.5	0.626
	2	0.017	0.012	0.	13.1	0.013	0.7	0.048	0.035	14.4	0.384

Table 9 (f): Inverted Explosion and Tectonic Release Source Parameters

Event	# obs.	M_0	$M_{I(R)}$	$M_{dc(R)}$	$\phi_{(R)}$	$M_{dc(L)}$	$\phi_{(L)}$	$M_{I(R+L)}$	$M_{dc(R+L)}$	$\phi_{(R+L)}$	$F_{(R+L)}$
84344	13	4.334	4.332	1.225	346.1	1.528	336.3	4.338	1.258	342.6	0.435
	11	0.371	0.178	0.199	3.8	0.102	1.9	0.157	0.111	2.5	0.041
84350	13	5.255	5.123	1.680	6.6	1.691	351.3	4.897	1.603	358.9	0.491
	10	0.524	0.323	0.298	4.8	0.233	4.6	0.325	0.195	3.8	0.068
85074	5	0.837	0.795	0.173	353.1						0.326
	0	0.106	0.437	0.206	68.1						0.427
85082	3	4.251	-1.623	5.157	318.3	3.008	350.6	3.012	2.487	344.3	1.239
	3	1.233	1.233			0.524	4.3	0.861	0.509	6.1	0.435
85092	11	12.581	13.191	1.409	345.8	1.758	324.6	13.327	1.653	341.8	0.186
	5	1.	1.219	1.562	22.3	0.246	6.0	0.912	0.871	12.8	0.099
85096	3	1.125						0.598	0.440	345.2	1.106
	1	0.208						0.901	0.418	32.6	1.970
85122	13	6.448	5.892	2.473	351.3	2.438	346.6	5.734	2.407	348.6	0.630
	13	0.685	0.512	0.540	4.8	0.163	2.1	0.342	0.211	2.4	0.067
85163	14	8.196	8.239	1.330	356.4	1.777	340.5	8.450	1.262	346.3	0.224
	13	0.502	0.429	0.414	8.0	0.106	1.9	0.318	0.155	4.4	0.029
85206	13	3.139	4.300	2.184	43.0	0.745	353.0	3.426	0.847	24.4	0.371
	11	0.690	0.515	0.495	5.5	0.168	6.8	0.556	0.342	11.4	0.161
85270	3	0.514	-1.462	2.375	356.8						*****
	0	0.095	0.095								0.159
85289	2	0.553									
	1	0.073									
85339	7	5.167	5.140	2.560	353.6	1.976	336.5	5.012	2.076	350.7	0.621
	4	1.178	0.962	0.881	9.1	0.736	10.4	0.777	0.486	7.8	0.174
85362	9	4.671	4.301	1.573	348.1	0.895	357.3	4.477	0.997	351.3	0.334
	3	0.606	0.506	0.527	8.3	0.199	10.6	0.455	0.224	8.0	0.082
86081	5	3.197	2.908	0.500	310.7	1.071	342.7	2.216	1.032	340.8	0.698
	3	0.337	0.652	0.311	39.8	0.254	7.6	0.337	0.187	5.2	0.165
86100	7	0.651	0.600	0.162	338.0	0.276	340.6	0.592	0.199	341.5	0.504
	2	0.099	0.	0.084	14.9	0.	9.3	0.078	0.059	8.5	0.162
86112	13	4.784	6.023	2.531	341.1	2.404	334.6	5.957	2.297	337.7	0.578
	10	0.698	0.377	0.344	3.8	0.186	1.9	0.294	0.177	2.2	0.053

Table 9 (g): Inverted Explosion and Tectonic Release Source Parameters											
Event	# obs.	M_0	$M_{I(R)}$	$M_{dc(R)}$	$\phi_{(R)}$	$M_{dc(L)}$	$\phi_{(L)}$	$M_{I(R+L)}$	$M_{dc(R+L)}$	$\phi_{(R+L)}$	$F_{(R+L)}$
86141	1	0.115									
	0										
86156	8	4.633	4.611	1.436	353.1	0.536	347.0	4.622	0.676	353.0	0.219
	4	0.847	0.805	0.803	14.3	0.146	11.6	0.662	0.308	19.0	0.105
86176	9	4.002	5.229	1.584	347.2	1.191	343.0	4.875	1.233	344.5	0.379
	8	0.510	0.510	0.417	8.3	0.124	3.3	0.307	0.138	3.6	0.049
86198	11	6.852	6.704	2.003	336.2	1.589	320.9	6.704	1.625	329.0	0.363
	7	0.799	0.534	0.521	7.3	0.202	4.2	0.489	0.263	4.7	0.064
86205	1	0.264									
	0										
86273	9	7.362	6.697	2.175	0.2	2.092	358.5	6.689	2.122	358.6	0.476
	9	1.	0.286	0.199	6.0	0.226	3.5	0.321	0.144	2.6	0.040
86289	7	6.947	7.683	2.018	340.8	1.766	338.5	7.554	1.786	339.1	0.355
	7	0.712	0.312	0.299	4.4	0.103	1.7	0.242	0.100	1.7	0.023
86318	6	8.049	9.990	2.595	296.1	1.009	340.6	9.950	2.582	298.0	0.389
	3	0.668	1.439	1.269	13.7	1.635	45.0	1.076	0.914	10.1	0.144
86347	8	9.412	8.703	1.747	1.3	2.780	347.2	7.687	2.391	351.2	0.467
	8	1.039	2.089	1.783	23.0	0.268	3.8	1.	0.409	6.9	0.102
87108	5	7.904	6.126	1.797	336.5	3.019	340.7	5.201	2.826	340.8	0.815
	5	0.688	0.579	0.455	7.4	0.151	1.5	0.404	0.251	2.6	0.096
87120	8	11.109	8.724	3.177	5.9	4.186	4.8	7.957	3.958	4.2	0.746
	6	0.962	0.629	0.436	3.7	0.589	6.3	0.703	0.368	3.5	0.096
87181	2	0.148									
	0	0.009									
87225	4	10.809	11.835	1.797	278.4	4.340	311.7	10.454	2.782	325.6	0.399
	3	1.051	0.159	0.176	2.2	0.470	3.1	1.262	0.704	7.4	0.112
87267	4	10.772	10.134	1.361	3.6	3.769	0.6	8.644	3.294	357.8	0.572
	4	0.495	0.247	0.229	3.2	0.071	0.7	0.640	0.391	3.5	0.080
87296	4	1.650	1.996	0.474	78.9						0.356
	0	0.119	0.031	0.033	1.1						0.025

The different inversion schemes, with a few exceptions, all yield similar explosion moment estimates for a given event. Also, most strike angles for the double-couple source are in the Northwest quadrant (280^o E $< \phi <$ 5^o E). The $15^o - 20^o$ NW strike angle inferred/observed by other studies of NTS tectonic release lies within the 2σ confidence levels for most events, implying that the results obtained here are consistent with others' observations. In general, for a given event, $\phi_{(R)}$ and $\phi_{(L)}$ correlate reasonably well and $M_{DC(R)}$ and $M_{DC(L)}$ are within a factor of two of each other. Notable exceptions to these observations are PILEDRIVER (66153), HURONLANDING-DIAMONDACE (82267) and MIZZEN (75154). PILEDRIVER is the only event in this data set detonated at Climax Stock, a granite pluton and is believed to have generated tectonic release with a thrust-like mechanism (Stevens, 1986), so the inversion scheme employed here would not accurately model it. HURONLANDING-DIAMONDACE was a double event, which is a possible explanation for its anomalous radiation pattern. It is also very close in location to the PILEDRIVER shot, so that the tectonic release faulting mechanisms may be similar. The Rayleigh and Love wave double-couple moments vary by a factor of seven and the strikes are off by 90 degrees for this Rainier Mesa event. However, the Love wave source solution is poorly constrained having only a minimum number of observations. It may be that the tectonic release mechanism for this event may vary significantly from the assumed vertical strike-slip one. MIZZEN belongs to subgroup of Yucca shots north of latitude 37.09 N, many of which yield double-couple mechanisms with strikes near $N80^oE$. Given and Mellman (1986) found an offset in the M_0 vs. m_b curves between northern and southern Yucca Flat, which was interpreted as a difference in Poisson ratios between shot sites or as having different stress regimes which would give rise to differing tectonic release mechanisms.

In most cases, the double-couple moment determined from Love wave observations is within a factor of two of the moment determined from Rayleigh waves alone. The

relative errors of the double-couple moment estimates are appreciably larger than those of the isotropic moment estimates, so the 2σ confidence levels of the two independent double-couple moment estimates overlap and are thus compatable. The joint inversion results in significantly better constrained M_{DC} estimates.

Many of the Rainier Mesa shots were relatively small ($m_b \approx 5.0$) and consequently not enough observations were available to invert for a source, so it is hard to ascertain the predominant tectonic release mechanism at this sub-site. However, barring the double event HURONLANDING-DIAMONDACE, all events with sufficient observations for inversion yielded strikes appropriate for a vertical strike-slip fault with the strike angle in the North West quadrant. Patton (1988a) speculates that block thrust or rotation may be the prime mechanism at Rainier Mesa; however, the results here imply that strike-slip motion can explain the fundamental-mode surface wave radiation pattern observations adequately.

Figure 3.20 plots the estimated tectonic release (from combined Rayleigh and Love wave inversion) vs. the isotropic moment. Events with no observed Love waves or too few observations to invert for a double-couple source are treated as having no tectonic release ($M_{DC} = 0$). For all events $M_I > M_{DC}$. All Pahute events show evidence of tectonic release. Only about half of the Yucca events do so. Otherwise, there are no clear trends in the data. The amount of tectonic strain release does not appear to depend on whether the shot takes place above or below the water table, either.

The explosion moments and errors were converted to log_{10} units and listed, along with time domain moments (and their errors) for overlapping events determined in chapter 2, in table 3.10. The time-domain moments are plotted versus the spectral moments in figure 2.5. Spectral domain moment errors are significantly smaller than those of time-domain moments by over 0.1 magnitude units on average, resulting in a reduction in standard deviation from 41.3 to 12.2 percent. However, the time-

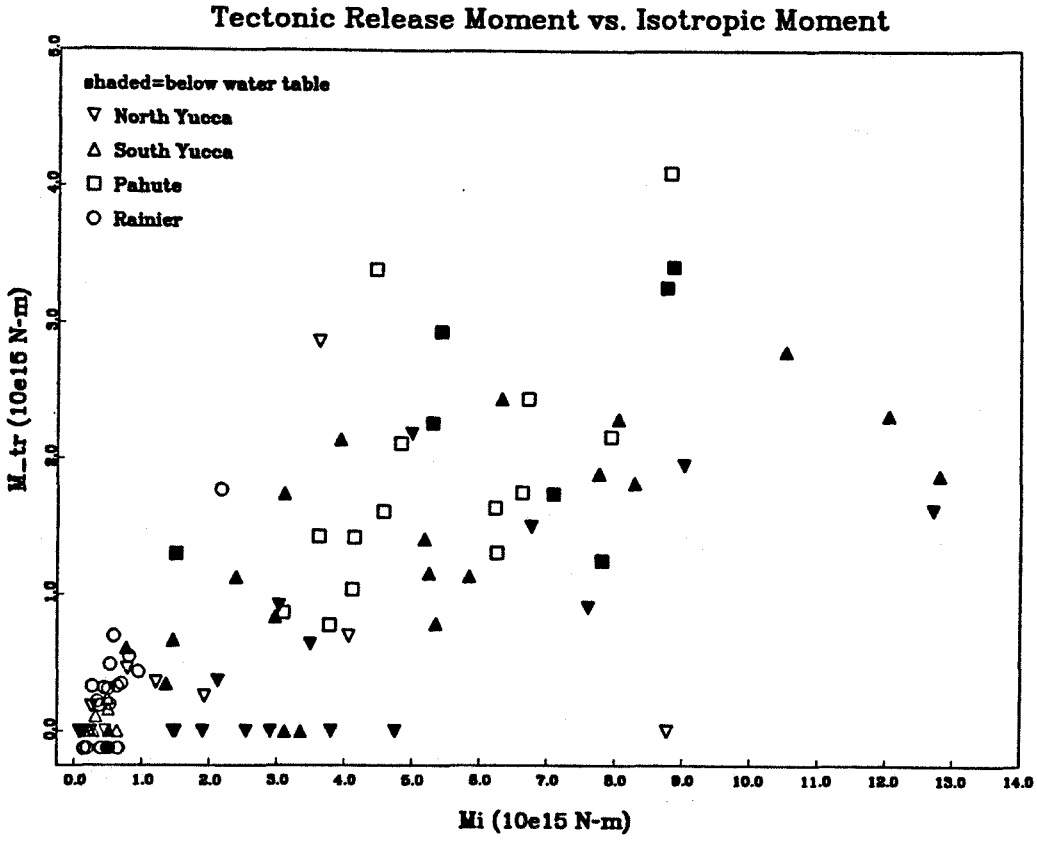

Figure 3.20: Tectonic release moment plotted vs. isotropic moment.

domain log-moments are in close agreement with the scalar spectral log-moments; yielding estimates within 15 to 30 percent of one another. There is no discernible improvement in error reduction between the different types of spectral moment estimates. Differences between constrained explosion (M_0) and inverted isotropic (M_I) log-moments are generally less than 0.1 log units (25 percent); often the difference is much smaller.

Since reducing the error in explosion moment estimates is critical to their worth, it is important to appreciate the margin of error introduced by assumptions in the analysis. One such question is how reasonable is the vertical strike-slip mechanism assumption for determining the tectonic release moment and what are the associated errors in the explosion moment estimate.

A theoretical source inversion study was conducted in order to get a handle on such errors. A hypothetical network with the same station azimuth make-up as that of the observed data set was used; however, all paths used the same structure and were of the same path length ($\Delta = 40^o$). An explosion of given moment ($10^{16} N-M$) is superimposed with a double-couple source of varying focal mechanism and F-factor.

Time-domain and spectral moments and isotropic moments and their standard deviations are calculated from the synthetic "data." The results are shown in table 3.11. At the top of each box the rake (λ) and dip (δ) are given. A negative λ denotes a normal fault, a positive λ, a thrust fault. The left-most column gives the ratio of double-couple to isotropic moment. The first column gives the ratio of input tectonic release moment (M_{DC}) to explosion moment (M_I). For comparison, log-moments are converted to surface wave magnitudes by the relation

$$M_S = \log(M_0) - 11.36, \tag{3.41}$$

developed in chapter 2 for the generic path, so that the correct M_S (or converted M_0) of the explosion alone should be 4.64 on this scale. Only Rayleigh wave synthetic data were used to determine the source information. Otherwise moments were determined

Table 10 (a): $\log(M_0)$ and $\log(\sigma_{M_0})$ comparisons										
Event Date	# Obs.(t)	M_0	σ	# Obs.(ω)	M_0	σ	$M_{I(R)}$	σ	$M_{I(R+L)}$	σ
65062	12	15.44	0.15	13	15.25	0.03	15.35	0.02	15.35	0.02
66018	5	15.30	0.16	4	15.24	0.02	15.22	0.02	15.22	0.01
66055	8	15.44	0.16	7	14.98	0.03	15.24	0.01	15.25	0.02
66133	15	15.79	0.13	16	15.77	0.04	15.75	0.04	15.74	0.04
66153	26	15.74	0.13	26	15.63	0.06	15.69	0.05	15.58	0.12
66154	18	15.74	0.11	19	15.74	0.04	15.73	0.04	15.72	0.04
67177	3	14.90	0.06	3	14.84	0.01	14.80	0.01	14.39	0.01
67243	2	14.47	0.12	1	14.29					
67312	9	15.10	0.14	8	15.05	0.01	14.98	0.02	14.94	0.02
68060	6	14.97	0.09	5	14.81	0.01	14.86	0.01		
68268	9	14.90	0.15	7	14.84	0.01	14.81	0.01		
69015	11	15.46	0.14	8	15.41	0.02	15.47	0.05	15.46	0.07
69043	1	14.63		1	14.65					
69120	15	15.51	0.10	15	15.50	0.02	15.48	0.03	15.47	0.03
70042	2	14.77	0.05	1	14.77					
70082	17	15.77	0.16	14	15.73	0.06	15.76	0.06	15.75	0.05
70125	5	14.83	0.15	3	14.93	0.01	16.85	0.01	14.59	0.01
70146	5	14.57	0.10	2	14.55	0.01				
71180	10	14.63	0.15	7	14.46	0.01	14.56	0.01		
71189	15	15.58	0.15	15	15.55	0.02	15.59	0.03	15.54	0.03
71230	21	15.14	0.18	18	15.15	0.01	15.14	0.01	15.11	0.01
72123	7	14.92	0.18	5	14.65	0.01	14.85	0.01	14.82	0.01
72140	5	14.71	0.10	3	14.76	0.01	14.78	0.01	14.76	0.01
72202	7	14.81	0.15	5	14.68	0.01	14.68	0.01		
73067	12	15.54	0.12	10	15.51	0.02	15.53	0.04	15.44	0.03
73116	22	15.55	0.12	20	15.45	0.03	15.46	0.04	15.46	0.04
73156	8	14.82	0.12	6	14.80	0.01	14.76	0.01		

Table 3.10: Explosion log moments and associated errors.

Table 10 (b): $\log(M_0)$ and $\log(\sigma_{M_0})$ comparisons										
Event Date	# Obs.(t)	M_0	σ	# Obs.(ω)	M_0	σ	$M_{I(R)}$	σ	$M_{I(R+L)}$	σ
74058	15	15.82	0.15	15	15.78	0.05	15.74	0.04	15.73	0.04
74170	8	14.91	0.17	7	14.84	0.01	14.88	0.01	14.92	0.01
74191	20	16.06	0.16	21	16.02	0.09	16.02	0.08	16.02	0.08
74269	13	15.42	0.14	12	15.36	0.01	15.34	0.02	15.34	0.02
75066	15	15.48	0.12	15	15.43	0.02	15.39	0.02		
75095	3	14.72	0.18	1	14.81					
75120	13	15.20	0.14	12	15.17	0.01	15.17	0.01		
75154	23	16.01	0.18	20	15.95	0.08	15.93	0.08	15.94	0.09
75297	1	14.80		1	14.46					
76035	14	15.96	0.16	13	15.86	0.06	15.89	0.06	15.86	0.06
76133	3	14.70	0.16	1	14.93					
76363	8	15.69	0.12	7	15.68	0.03	15.64	0.03		
77117	18	15.62	0.13	16	15.52	0.03	15.59	0.04	15.50	0.04
77145	10	15.55	0.14	8	15.61	0.03	15.67	0.04		
78193	27	15.77	0.16	21	15.67	0.05	15.72	0.04	15.71	0.05
78322	13	15.34	0.19	12	15.28	0.02	15.28	0.02		
79039	21	15.82	0.16	18	15.42	0.07	15.64	0.08		
80107	22	15.64	0.19	17	15.49	0.05	15.51	0.04	15.49	0.05
80305	6	14.87	0.19	5	14.72	0.01	14.79	0.01	14.91	0.01
81015	11	15.86	0.16	10	15.90	0.05	15.88	0.07	15.87	0.05
82028	9	16.13	0.11	8	16.05	0.04	16.06	0.03	16.06	0.03
82043	10	15.98	0.13	4	16.01	0.07	16.01	0.09	15.92	0.05
82044	8	15.87	0.13	7	15.87	0.04	15.84	0.04	15.85	0.03
82107	4	14.45	0.15	4	14.32	0.01	14.29	0.01	14.32	0.01
82115	8	15.88	0.09	7	15.82	0.03	15.82	0.03	15.82	0.03
82126	4	14.10	0.13	4	14.04	0.01	14.05	0.01		
82127	15	15.75	0.14	8	15.69	0.03	15.70	0.02	15.70	0.02
82175	9	15.98	0.12	8	15.99	0.05	15.96	0.04	15.96	0.03

Table 10 (c): $\log(M_0)$ and $\log(\sigma_{M_0})$ comparisons

Event Date	# Obs.(t)	M_0	σ	# Obs.(ω)	M_0	σ	$M_{l(R)}$	σ	$M_{l(R+L)}$	σ
82210	9	15.55	0.20	8	14.45	0.01	14.44	0.01	14.42	0.01
82217	9	16.18	0.12	8	16.11	0.04	16.10	0.04	16.10	0.04
82266	8	14.83	0.12	5	14.77	0.01	14.80	0.02	14.59	0.01
82267	5	15.02	0.16	4	14.99	0.01	14.98	0.01	14.87	0.01
82272	3	13.97	0.10	4	13.98	0.01	13.96	0.01		
82344	6	14.60	0.17	7	14.55	0.01	14.50	0.01	14.45	0.01
83085	11	15.47	0.13	11	15.54	0.03	15.52	0.01	15.49	0.02
83104	20	15.64	0.17	10	15.55	0.03	15.56	0.03	15.55	0.02
83125	7	14.30	0.17	6	14.08	0.01	14.28	0.01		
83146	12	14.80	0.14	7	14.74	0.01	14.72	0.01	14.72	0.01
83160	10	14.39	0.15	6	14.47	0.01	14.48	0.01	14.48	0.01
83244	12	15.65	0.16	13	15.59	0.05	15.63	0.02	15.63	0.02
83264	3	14.56	0.25	2	14.21	0.01				
83265	5	13.94	0.08	4	13.89	0.01	13.96	0.01	13.94	0.01
83350	11	15.28	0.14	10	15.30	0.01	15.28	0.01	15.27	0.01
84046	9	14.88	0.14	7	14.77	0.01	14.80	0.01	14.80	0.01
84122	19	15.86	0.14	10	15.87	0.04	15.80	0.05	15.80	0.03
84061	11	15.90	0.15	10	15.92	0.06	15.90	0.03	15.90	0.03
84152	11	15.94	0.14	10	15.91	0.04	15.91	0.04	15.91	0.03
84172	4	14.67	0.22	4	14.82	0.01	14.70	0.01	14.70	0.01
84207	21	15.70	0.20	9	15.56	0.07	15.68	0.02	15.69	0.02
84215	6	14.37	0.16	5	14.32	0.01	14.31	0.01	14.31	0.01
84243	3	14.52	0.03	3	14.55	0.01	14.59	0.01	14.59	0.01
84257	5	15.03	0.12	4	15.07	0.01	15.08	0.01	15.08	0.01
84315	4	14.25	0.12	4	14.10	0.01	14.15	0.01	14.20	0.01
84344	12	15.71	0.17	13	15.64	0.04	15.64	0.02	15.64	0.02
84350	14	15.71	0.18	13	15.72	0.05	15.71	0.03	15.69	0.03
85074	5	14.84	0.12	5	14.92	0.01	14.90	0.03		

Table 10 (d): $\log(M_0)$ and $\log(\sigma_{M_0})$ comparisons										
Event Date	# Obs.(t)	M_0	σ	# Obs.(ω)	M_0	σ	$M_{I(R)}$	σ	$M_{I(R+L)}$	σ
85082	4	15.59	0.27	3	15.63	0.06			15.48	0.04
85092	8	16.19	0.15	11	16.10	0.08	16.12	0.10	16.12	0.07
85096	7	14.98	0.19	3	15.05	0.01			14.78	0.04
85122	19	15.86	0.17	13	15.81	0.06	15.77	0.05	15.76	0.03
85163	13	15.92	0.16	14	15.91	0.05	15.92	0.04	15.93	0.03
85206	12	15.76	0.15	13	15.50	0.06	15.63	0.05	15.53	0.05
85270	4	14.71	0.14	3	14.71	0.01				
85289	1	14.80		2	14.74	0.01				
85339	8	15.67	0.19	7	15.71	0.08	15.71	0.07	15.70	0.05
85362	8	15.65	0.16	9	15.67	0.05	15.63	0.04	15.65	0.04
86081	4	15.52	0.09	5	15.50	0.02	15.46	0.04	15.35	0.02
86100	7	14.88	0.18	7	14.81	0.01	14.78	0.01	14.77	0.01
86112	12	15.81	0.19	13	15.68	0.06	15.78	0.04	15.78	0.03
86141	2	13.97	0.11	1	14.06					
86156	7	15.71	0.20	8	15.67	0.06	15.66	0.06	15.66	0.05
86176	15	15.79	0.19	9	15.60	0.04	15.72	0.04	15.69	0.02
86198	10	15.90	0.20	11	15.84	0.07	15.83	0.05	15.83	0.04
86205	2	14.40	0.02	1	14.42					
86273	8	15.76	0.16	9	15.87	0.08	15.83	0.02	15.83	0.03
86289	7	15.79	0.11	7	15.84	0.05	15.89	0.02	15.88	0.02
86318	5	16.03	0.13	6	15.91	0.04	16.00	0.09	16.00	0.07
86347	7	16.02	0.19	8	15.97	0.07	15.94	0.14	15.89	0.07
87108	4	15.84	0.14	5	15.90	0.04	15.79	0.03	15.72	0.02
87120	8	15.94	0.14	8	16.05	0.07	15.94	0.05	15.90	0.05
87181	1	14.29		2	14.17	0.01				
87225	5	16.06	0.12	4	16.03	0.05	16.07	0.01	16.02	0.06
87267	4	15.98	0.16	4	16.03	0.03	16.01	0.01	15.94	0.03
87296	3	15.31	0.07	4	15.22	0.01	15.30	0.01		

using the same methods used on the data in this chapter and chapter 2. The M_s's in the second column were obtained by time domain measurements of the maximum peak to trough amplitude using the Von Seggern formula for well dispersed Rayleigh waves as in chapter 2.

The F factor results in table 9 imply that for NTS, the M_{DC}/M_I ratio is never above 0.6, so the maximum moment ratio of 2.0 was considered an extreme value for this area. The rake varied between -45 and 45 in 15 degree increments and the strike varied between 90 (vertical) and 45 degrees in 15 degree increments. These fault parameters are reasonable variations from the assumed vertical ($\delta = 0$), pure strike-slip (λ) mechanism for NTS tectonic release.

Unlike the observational results, there is a significant reduction in variance of the explosion moment estimate by inverting for the isotropic moment component over the average spectral moment estimate. For all but the most extreme deviations in source parameters and F factor, the estimated isotropic moments standard deviations are small, usually under 0.01 magnitude units. The actual data errors (table 3.10) are somewhat bigger. This can be attributed to the fact that in the synthetic study case the seismograms have no noise contamination, hence there is no problem measuring the signal accurately. Also in the synthetic study case, far better azimuthal coverage was attainable, since only a small proportion of the network was available for any one event. In the theoretical case the synthetic seismograms are identical to the synthetic "data," so that there will be no error in the spectral ratio measurements, whereas in the observational case, errors in modeling the propagation path can lead to inaccuracies in moment estimates.

The average spectral scalar moment (M_0) standard deviations are significantly larger than those of the inverted moment estimates, being similar in size to errors in time-domain moment estimates. These errors are significant even for relatively low F-factor events ($M_{DC}/M_I < 0.75$), being, on average, 0.07 for $M_{DC}/M_I = 0.25$ events

λ=45° δ=90°						
$M_\#/M_*$	M_S	s.d.	logM_0	s.d.	logM_I	s.d.
0.00	4.64	0.00	4.64	0.00	4.64	0.00
0.25	4.63	0.06	4.63	0.07	4.64	0.00
0.50	4.56	0.17	4.61	0.14	4.64	0.00
0.75	4.52	0.26	4.58	0.22	4.64	0.00
1.00	4.46	0.37	4.51	0.36	4.64	0.00
1.25	4.41	0.46	4.46	0.45	4.64	0.01
1.50	4.44	0.45	4.48	0.45	4.65	0.01
1.75	4.48	0.44	4.53	0.43	4.66	0.02
2.00	4.55	0.38	4.59	0.37	4.67	0.02

λ=45° δ=60°						
$M_\#/M_*$	M_S	s.d.	logM_0	s.d.	logM_I	s.d.
0.00	4.64	0.00	4.64	0.00	4.64	0.00
0.25	4.56	0.08	4.56	0.08	4.57	0.00
0.50	4.41	0.24	4.45	0.21	4.50	0.00
0.75	4.06	0.70	4.13	0.65	4.42	0.00
1.00	4.31	0.33	4.34	0.33	4.32	0.02
1.25	4.36	0.38	4.39	0.36	4.20	0.04
1.50	4.42	0.38	4.45	0.37	4.06	0.07
1.75	4.49	0.36	4.52	0.34	3.78	0.17
2.00	4.54	0.36	4.58	0.33	5.03	0.05

λ=45° δ=75°						
$M_\#/M_*$	M_S	s.d.	logM_0	s.d.	logM_I	s.d.
0.00	4.64	0.00	4.64	0.00	4.64	0.00
0.25	4.59	0.07	4.59	0.07	4.60	0.00
0.50	4.47	0.21	4.53	0.18	4.56	0.00
0.75	4.36	0.37	4.39	0.38	4.52	0.00
1.00	4.30	0.44	4.35	0.43	4.50	0.01
1.25	4.39	0.38	4.43	0.36	4.46	0.03
1.50	4.45	0.38	4.48	0.37	4.40	0.03
1.75	4.52	0.31	4.55	0.31	4.35	0.04
2.00	4.54	0.39	4.57	0.36	4.27	0.04

λ=45° δ=45°						
$M_\#/M_*$	M_S	s.d.	logM_0	s.d.	logM_I	s.d.
0.00	4.64	0.00	4.64	0.00	4.64	0.00
0.25	4.55	0.07	4.56	0.07	4.56	0.00
0.50	4.42	0.20	4.43	0.20	4.47	0.00
0.75	4.08	0.60	4.13	0.57	4.38	0.00
1.00	4.24	0.36	4.29	0.33	4.27	0.04
1.25	4.31	0.37	4.35	0.36	4.03	0.03
1.50	4.41	0.31	4.45	0.30	3.68	0.12
1.75	4.47	0.33	4.51	0.31	4.92	0.04
2.00	4.54	0.30	4.57	0.28	4.95	0.06

Table 3.11: Source inversion results for theoretical study.

λ=−45° δ=90°						
$M_\#/M_*$	M_S	s.d.	logM_0	s.d.	logM_I	s.d.
0.00	4.64	0.00	4.64	0.00	4.64	0.00
0.25	4.62	0.07	4.63	0.07	4.64	0.00
0.50	4.60	0.14	4.61	0.14	4.64	0.00
0.75	4.57	0.22	4.58	0.22	4.64	0.00
1.00	4.49	0.37	4.51	0.36	4.64	0.00
1.25	4.44	0.46	4.47	0.44	4.64	0.01
1.50	4.47	0.45	4.49	0.44	4.65	0.01
1.75	4.51	0.43	4.53	0.42	4.66	0.02
2.00	4.56	0.38	4.60	0.37	4.67	0.02

λ=−30° δ=90°						
$M_\#/M_*$	M_S	s.d.	logM_0	s.d.	logM_I	s.d.
0.00	4.64	0.00	4.64	0.00	4.64	0.00
0.25	4.62	0.08	4.62	0.08	4.64	0.00
0.50	4.59	0.18	4.60	0.17	4.64	0.00
0.75	4.52	0.33	4.53	0.31	4.64	0.00
1.00	4.42	0.51	4.44	0.48	4.64	0.00
1.25	4.44	0.51	4.47	0.48	4.64	0.01
1.50	4.51	0.46	4.54	0.44	4.64	0.01
1.75	4.59	0.38	4.61	0.37	4.64	0.01
2.00	4.62	0.40	4.66	0.39	4.64	0.02

λ=−45° δ=75°						
$M_\#/M_*$	M_S	s.d.	logM_0	s.d.	logM_I	s.d.
0.00	4.64	0.00	4.64	0.00	4.64	0.00
0.25	4.65	0.06	4.66	0.06	4.67	0.00
0.50	4.67	0.11	4.68	0.11	4.70	0.00
0.75	4.68	0.17	4.69	0.16	4.73	0.00
1.00	4.68	0.22	4.69	0.22	4.75	0.00
1.25	4.67	0.30	4.69	0.27	4.78	0.00
1.50	4.66	0.35	4.68	0.34	4.80	0.00
1.75	4.65	0.42	4.66	0.41	4.82	0.00
2.00	4.64	0.47	4.66	0.45	4.84	0.01

λ=−30° δ=75°						
$M_\#/M_*$	M_S	s.d.	logM_0	s.d.	logM_I	s.d.
0.00	4.64	0.00	4.64	0.00	4.64	0.00
0.25	4.64	0.08	4.65	0.07	4.66	0.00
0.50	4.64	0.15	4.65	0.14	4.68	0.00
0.75	4.63	0.23	4.64	0.22	4.70	0.00
1.00	4.59	0.35	4.61	0.33	4.72	0.00
1.25	4.53	0.49	4.55	0.47	4.73	0.01
1.50	4.55	0.49	4.57	0.47	4.73	0.02
1.75	4.59	0.47	4.60	0.46	4.72	0.03
2.00	4.63	0.45	4.65	0.44	4.71	0.04

λ=−45° δ=60°						
$M_\#/M_*$	M_S	s.d.	logM_0	s.d.	logM_I	s.d.
0.00	4.64	0.00	4.64	0.00	4.64	0.00
0.25	4.67	0.06	4.68	0.05	4.69	0.00
0.50	4.71	0.10	4.72	0.10	4.74	0.00
0.75	4.74	0.14	4.75	0.14	4.78	0.00
1.00	4.77	0.17	4.78	0.17	4.82	0.00
1.25	4.79	0.20	4.80	0.20	4.86	0.00
1.50	4.81	0.23	4.82	0.23	4.89	0.00
1.75	4.82	0.27	4.84	0.26	4.92	0.00
2.00	4.83	0.31	4.86	0.28	4.95	0.00

λ=−30° δ=60°						
$M_\#/M_*$	M_S	s.d.	logM_0	s.d.	logM_I	s.d.
0.00	4.64	0.00	4.64	0.00	4.64	0.00
0.25	4.66	0.07	4.67	0.06	4.67	0.00
0.50	4.68	0.12	4.69	0.12	4.71	0.00
0.75	4.69	0.18	4.70	0.18	4.74	0.00
1.00	4.70	0.23	4.71	0.23	4.77	0.00
1.25	4.68	0.31	4.71	0.29	4.80	0.00
1.50	4.68	0.37	4.70	0.36	4.83	0.00
1.75	4.65	0.46	4.68	0.44	4.85	0.00
2.00	4.66	0.50	4.68	0.48	4.87	0.02

λ=−45° δ=45°						
$M_\#/M_*$	M_S	s.d.	logM_0	s.d.	logM_I	s.d.
0.00	4.64	0.00	4.64	0.00	4.64	0.00
0.25	4.68	0.05	4.69	0.05	4.70	0.00
0.50	4.73	0.09	4.74	0.09	4.75	0.00
0.75	4.77	0.12	4.78	0.12	4.80	0.00
1.00	4.80	0.15	4.81	0.14	4.84	0.00
1.25	4.83	0.17	4.84	0.17	4.88	0.00
1.50	4.86	0.19	4.87	0.19	4.92	0.00
1.75	4.89	0.21	4.90	0.20	4.95	0.00
2.00	4.91	0.23	4.92	0.22	4.99	0.00

λ=−30° δ=45°						
$M_\#/M_*$	M_S	s.d.	logM_0	s.d.	logM_I	s.d.
0.00	4.64	0.00	4.64	0.00	4.64	0.00
0.25	4.67	0.06	4.67	0.05	4.68	0.00
0.50	4.70	0.10	4.70	0.10	4.72	0.00
0.75	4.72	0.14	4.73	0.14	4.76	0.00
1.00	4.74	0.18	4.75	0.18	4.79	0.00
1.25	4.76	0.21	4.77	0.21	4.82	0.00
1.50	4.76	0.26	4.78	0.25	4.85	0.00
1.75	4.77	0.30	4.79	0.28	4.88	0.00
2.00	4.78	0.33	4.80	0.32	4.91	0.00

λ=−15° δ=90°						
$M_\#/M_*$	M_S	s.d.	logM_0	s.d.	logM_I	s.d.
0.00	4.64	0.00	4.64	0.00	4.64	0.00
0.25	4.62	0.09	4.62	0.09	4.64	0.00
0.50	4.58	0.20	4.59	0.20	4.64	0.00
0.75	4.47	0.42	4.49	0.40	4.64	0.00
1.00	4.43	0.50	4.45	0.48	4.64	0.00
1.25	4.46	0.51	4.49	0.49	4.64	0.00
1.50	4.55	0.42	4.59	0.39	4.64	0.00
1.75	4.61	0.43	4.64	0.41	4.64	0.00
2.00	4.67	0.40	4.70	0.38	4.64	0.00

λ=0° δ=90°						
$M_\#/M_*$	M_S	s.d.	logM_0	s.d.	logM_I	s.d.
0.00	4.64	0.00	4.64	0.00	4.64	0.00
0.25	4.62	0.09	4.62	0.09	4.64	0.00
0.50	4.58	0.21	4.58	0.21	4.64	0.00
0.75	4.47	0.44	4.47	0.44	4.64	0.00
1.00	4.45	0.49	4.45	0.49	4.64	0.00
1.25	4.53	0.45	4.49	0.52	4.64	0.00
1.50	4.60	0.39	4.60	0.39	4.64	0.00
1.75	4.63	0.48	4.63	0.47	4.64	0.00
2.00	4.71	0.37	4.71	0.37	4.64	0.00

λ=−15° δ=75°						
$M_\#/M_*$	M_S	s.d.	logM_0	s.d.	logM_I	s.d.
0.00	4.64	0.00	4.64	0.00	4.64	0.00
0.25	4.63	0.09	4.64	0.08	4.65	0.00
0.50	4.61	0.18	4.62	0.18	4.66	0.00
0.75	4.57	0.30	4.57	0.30	4.67	0.00
1.00	4.46	0.52	4.48	0.51	4.68	0.00
1.25	4.49	0.50	4.51	0.48	4.69	0.01
1.50	4.52	0.49	4.55	0.48	4.70	0.01
1.75	4.60	0.44	4.62	0.43	4.71	0.02
2.00	4.64	0.43	4.67	0.42	4.72	0.02

λ=0° δ=75°						
$M_\#/M_*$	M_S	s.d.	logM_0	s.d.	logM_I	s.d.
0.00	4.64	0.00	4.64	0.00	4.64	0.00
0.25	4.62	0.09	4.62	0.09	4.64	0.00
0.50	4.58	0.20	4.59	0.20	4.64	0.00
0.75	4.48	0.41	4.49	0.40	4.64	0.00
1.00	4.42	0.51	4.45	0.49	4.64	0.00
1.25	4.46	0.51	4.49	0.50	4.64	0.00
1.50	4.55	0.42	4.59	0.40	4.64	0.00
1.75	4.61	0.45	4.63	0.43	4.64	0.00
2.00	4.68	0.40	4.70	0.37	4.64	0.00

λ=−15° δ=60°						
$M_\#/M_*$	M_S	s.d.	logM_0	s.d.	logM_I	s.d.
0.00	4.64	0.00	4.64	0.00	4.64	0.00
0.25	4.64	0.08	4.65	0.07	4.66	0.00
0.50	4.64	0.15	4.64	0.15	4.68	0.00
0.75	4.62	0.23	4.63	0.23	4.69	0.00
1.00	4.57	0.36	4.59	0.34	4.71	0.00
1.25	4.51	0.50	4.54	0.48	4.72	0.01
1.50	4.54	0.49	4.56	0.47	4.72	0.01
1.75	4.58	0.46	4.60	0.46	4.71	0.02
2.00	4.60	0.47	4.63	0.46	4.73	0.03

λ=0° δ=60°						
$M_\#/M_*$	M_S	s.d.	logM_0	s.d.	logM_I	s.d.
0.00	4.64	0.00	4.64	0.00	4.64	0.00
0.25	4.62	0.08	4.62	0.08	4.64	0.00
0.50	4.59	0.17	4.60	0.17	4.64	0.00
0.75	4.52	0.31	4.53	0.31	4.64	0.00
1.00	4.41	0.52	4.43	0.50	4.64	0.00
1.25	4.43	0.52	4.46	0.50	4.64	0.00
1.50	4.50	0.47	4.53	0.45	4.64	0.00
1.75	4.57	0.41	4.61	0.38	4.64	0.01
2.00	4.61	0.42	4.65	0.40	4.64	0.01

λ=−15° δ=45°						
$M_\#/M_*$	M_S	s.d.	logM_0	s.d.	logM_I	s.d.
0.00	4.64	0.00	4.64	0.00	4.64	0.00
0.25	4.64	0.06	4.65	0.06	4.66	0.00
0.50	4.65	0.12	4.66	0.12	4.68	0.00
0.75	4.65	0.17	4.66	0.17	4.70	0.00
1.00	4.65	0.23	4.66	0.23	4.72	0.00
1.25	4.62	0.33	4.64	0.31	4.74	0.00
1.50	4.59	0.43	4.61	0.41	4.76	0.00
1.75	4.57	0.48	4.60	0.46	4.75	0.01
2.00	4.59	0.47	4.62	0.45	4.70	0.03

λ=0° δ=45°						
$M_\#/M_*$	M_S	s.d.	logM_0	s.d.	logM_I	s.d.
0.00	4.64	0.00	4.64	0.00	4.64	0.00
0.25	4.62	0.07	4.63	0.07	4.64	0.00
0.50	4.60	0.14	4.61	0.14	4.64	0.00
0.75	4.57	0.22	4.58	0.22	4.64	0.00
1.00	4.49	0.38	4.51	0.36	4.64	0.00
1.25	4.43	0.48	4.45	0.46	4.64	0.00
1.50	4.44	0.48	4.47	0.47	4.64	0.00
1.75	4.49	0.45	4.53	0.43	4.65	0.00
2.00	4.54	0.40	4.59	0.39	4.65	0.00

λ=15° δ=90°						
$M_\#/M_*$	M_S	s.d.	logM_0	s.d.	logM_I	s.d.
0.00	4.64	0.00	4.64	0.00	4.64	0.00
0.25	4.62	0.09	4.62	0.09	4.64	0.00
0.50	4.57	0.22	4.59	0.20	4.64	0.00
0.75	4.46	0.43	4.49	0.40	4.64	0.00
1.00	4.42	0.51	4.45	0.48	4.64	0.00
1.25	4.46	0.52	4.48	0.50	4.64	0.00
1.50	4.57	0.41	4.59	0.40	4.64	0.00
1.75	4.62	0.42	4.64	0.41	4.64	0.00
2.00	4.67	0.39	4.70	0.39	4.64	0.00

λ=30° δ=90°						
$M_\#/M_*$	M_S	s.d.	logM_0	s.d.	logM_I	s.d.
0.00	4.64	0.00	4.64	0.00	4.64	0.00
0.25	4.62	0.08	4.62	0.08	4.64	0.00
0.50	4.56	0.21	4.60	0.17	4.64	0.00
0.75	4.49	0.34	4.53	0.31	4.64	0.00
1.00	4.40	0.50	4.44	0.49	4.64	0.00
1.25	4.42	0.51	4.46	0.50	4.64	0.01
1.50	4.50	0.46	4.53	0.45	4.64	0.01
1.75	4.58	0.39	4.61	0.37	4.64	0.01
2.00	4.62	0.40	4.65	0.39	4.64	0.02

λ=15° δ=75°						
$M_\#/M_*$	M_S	s.d.	logM_0	s.d.	logM_I	s.d.
0.00	4.64	0.00	4.64	0.00	4.64	0.00
0.25	4.60	0.09	4.61	0.09	4.62	0.00
0.50	4.55	0.21	4.56	0.21	4.61	0.00
0.75	4.37	0.53	4.40	0.50	4.60	0.00
1.00	4.38	0.53	4.40	0.51	4.58	0.00
1.25	4.47	0.45	4.50	0.44	4.57	0.00
1.50	4.56	0.36	4.59	0.35	4.56	0.00
1.75	4.62	0.36	4.65	0.35	4.54	0.00
2.00	4.66	0.35	4.70	0.34	4.53	0.00

λ=30° δ=75°						
$M_\#/M_*$	M_S	s.d.	logM_0	s.d.	logM_I	s.d.
0.00	4.64	0.00	4.64	0.00	4.64	0.00
0.25	4.60	0.08	4.60	0.09	4.61	0.00
0.50	4.50	0.24	4.54	0.20	4.59	0.00
0.75	4.32	0.52	4.37	0.49	4.56	0.00
1.00	4.36	0.44	4.39	0.45	4.54	0.01
1.25	4.44	0.41	4.48	0.40	4.51	0.01
1.50	4.53	0.32	4.56	0.32	4.47	0.01
1.75	4.57	0.35	4.60	0.35	4.44	0.02
2.00	4.62	0.35	4.65	0.35	4.41	0.02

λ=15° δ=60°						
$M_\#/M_*$	M_S	s.d.	logM_0	s.d.	logM_I	s.d.
0.00	4.64	0.00	4.64	0.00	4.64	0.00
0.25	4.60	0.08	4.60	0.08	4.61	0.00
0.50	4.54	0.20	4.54	0.20	4.59	0.00
0.75	4.38	0.48	4.40	0.45	4.57	0.00
1.00	4.34	0.52	4.38	0.49	4.54	0.01
1.25	4.42	0.47	4.46	0.44	4.52	0.00
1.50	4.52	0.32	4.56	0.32	4.50	0.01
1.75	4.57	0.34	4.61	0.33	4.47	0.02
2.00	4.59	0.41	4.64	0.39	4.45	0.02

λ=30° δ=60°						
$M_\#/M_*$	M_S	s.d.	logM_0	s.d.	logM_I	s.d.
0.00	4.64	0.00	4.64	0.00	4.64	0.00
0.25	4.58	0.08	4.58	0.08	4.59	0.00
0.50	4.49	0.21	4.49	0.21	4.54	0.00
0.75	4.18	0.67	4.22	0.64	4.49	0.00
1.00	4.35	0.36	4.39	0.36	4.43	0.00
1.25	4.41	0.40	4.45	0.38	4.37	0.01
1.50	4.48	0.35	4.51	0.34	4.30	0.03
1.75	4.54	0.34	4.57	0.33	4.20	0.04
2.00	4.56	0.37	4.60	0.35	4.09	0.06

λ=15° δ=45°						
$M_\#/M_*$	M_S	s.d.	logM_0	s.d.	logM_I	s.d.
0.00	4.64	0.00	4.64	0.00	4.64	0.00
0.25	4.59	0.07	4.60	0.07	4.61	0.00
0.50	4.54	0.16	4.55	0.16	4.58	0.00
0.75	4.44	0.33	4.46	0.31	4.56	0.00
1.00	4.30	0.52	4.33	0.50	4.54	0.01
1.25	4.40	0.40	4.42	0.39	4.53	0.02
1.50	4.45	0.34	4.50	0.32	4.48	0.01
1.75	4.48	0.34	4.55	0.32	4.47	0.02
2.00	4.53	0.34	4.59	0.33	4.42	0.04

λ=30° δ=45°						
$M_\#/M_*$	M_S	s.d.	logM_0	s.d.	logM_I	s.d.
0.00	4.64	0.00	4.64	0.00	4.64	0.00
0.25	4.57	0.07	4.58	0.07	4.58	0.00
0.50	4.48	0.18	4.49	0.18	4.53	0.00
0.75	4.27	0.47	4.29	0.45	4.46	0.00
1.00	4.30	0.36	4.34	0.35	4.45	0.03
1.25	4.34	0.35	4.40	0.33	4.30	0.01
1.50	4.40	0.33	4.46	0.32	4.22	0.03
1.75	4.41	0.45	4.48	0.41	4.11	0.08
2.00	4.47	0.43	4.52	0.41	3.98	0.15

and 0.12 for $M_{DC}/M_I = 0.5$ events. For large F-factor events ($M_{DC}/M_I > 1$), the variances become exceedingly high, implying large scatter in the moment estimate.

The inverted isotropic moment is, in most all cases, closer in estimating the explosion moment than either average moment estimate. For all but the most extreme cases (say, $\lambda = -45^o$ and $\delta = 60^o$ and $M_{DC}/M_I > 0.75$), the difference between the estimated and actual isotropic moment is less than 0.1 magnitude units and is often less than 0.01 log units, whereas for the $M_{0(ptpk)}$ and $M_{0(\omega)}$, this difference is larger sometimes as great as 0.24 magnitude units. For a pure vertical strike-slip tectonic release mechanism, the average estimated moment or M_S determined from a network with complete azimuthal coverage should be that of the explosion, with the variations due to the tectonic release canceling itself out, on average (Helle and Rygg, 1984). However, the network used does not have equal coverage for each lobe of the $\sin 2\theta$ radiation pattern, so that the apparent moment or magnitude differs from the actual value for even the smaller F factor cases. For the case of $M_{DC}/M_I = 0.75$, this difference is 0.17 (48 percent). These canonical test results show that estimating the explosion moment by inverting for the isotropic component, in conjunction with a double-couple component, should yield the most accurate measurements.

The error in moment estimate due the difference between the modeled source depth (600 m) and actual source depth (between 300 and 750 m) is minimal (0.25 percent), unless the difference in depth should place the shot in a medium with a significantly different α^2/β^2 ratio. The error in using one generic centralized NTS location to calculate the distance for all station-path synthetic is also minimal, being at the most 0.5 percent for the extreme case of short regional paths ($d_o \approx 400km, \delta d = 20$ km).

Another source of error in explosion moment determinations is caused by mismodeling the near-source region, in particular the shot-point medium elastic properties, since, by equation 3.5, the displacement generated by an explosion is inversely

proportional to α^2/β^2 which, in turn, is related to Poisson's ratio (σ). Various studies have determined the P-wave velocity structure for the various NTS sub-regions; however, the S-wave velocity structure is far less well constrained. Depending on the shot depth and particular model, α^2/β^2 varies between 3.25 and 2.75 (3 for a Poisson solid), leading to potential systematic errors on the order of 8 percent (0.035 log units).

This effect is significant and could be corrected for in terms of sub-site coupling coefficients or calibration constants. In a global nuclear monitoring environment, this factor may only be ascertainable by indirect means (such as estimating α^2/β^2 from the ratio of $M_{DC(Ray)}/M_{DC(Lov)}$). This effect is investigated, as in chapter 2, by examining the moment-m_b and moment-yield scaling relationships for various explosion populations and sub-populations at NTS. Unfortunately the spectral moment data set is significantly smaller and less comprehensive than the data set used in chapter 2, since many of those moments/M_S's were determined from historical analog data. However, the available data set does contain events from Rainier Mesa as well as smaller events from the other sub-sites, down to $m_b = 4.9$, and in a few cases down to the $m_b = 4.4$ level, whereas previous (Stevens, 1986; Given and Mellman, 1986) studies have only examined $m_b = 5.5$ and larger events. Hence the moment scaling relationships can be better constrained for Pahute Mesa and Yucca Flats, and the Rainier Mesa long-period scaling relationships can be established using this data set. Including the large-yield explosions from the previous studies makes the data set even more comprehensive in scale range. By comparing the relationships obtained from these three NTS sub-sites, one can get a handle on the effect of near-source structure and shot medium effects on these scaling relationships.

Figure 3.21a plots all final explosion moments from this study vs. teleseismic m_b taken from, or calculated using the method of Lilwall and Neary (1985). Vertical error bars on the data points are the estimated error (standard deviation, s.d.) of the data

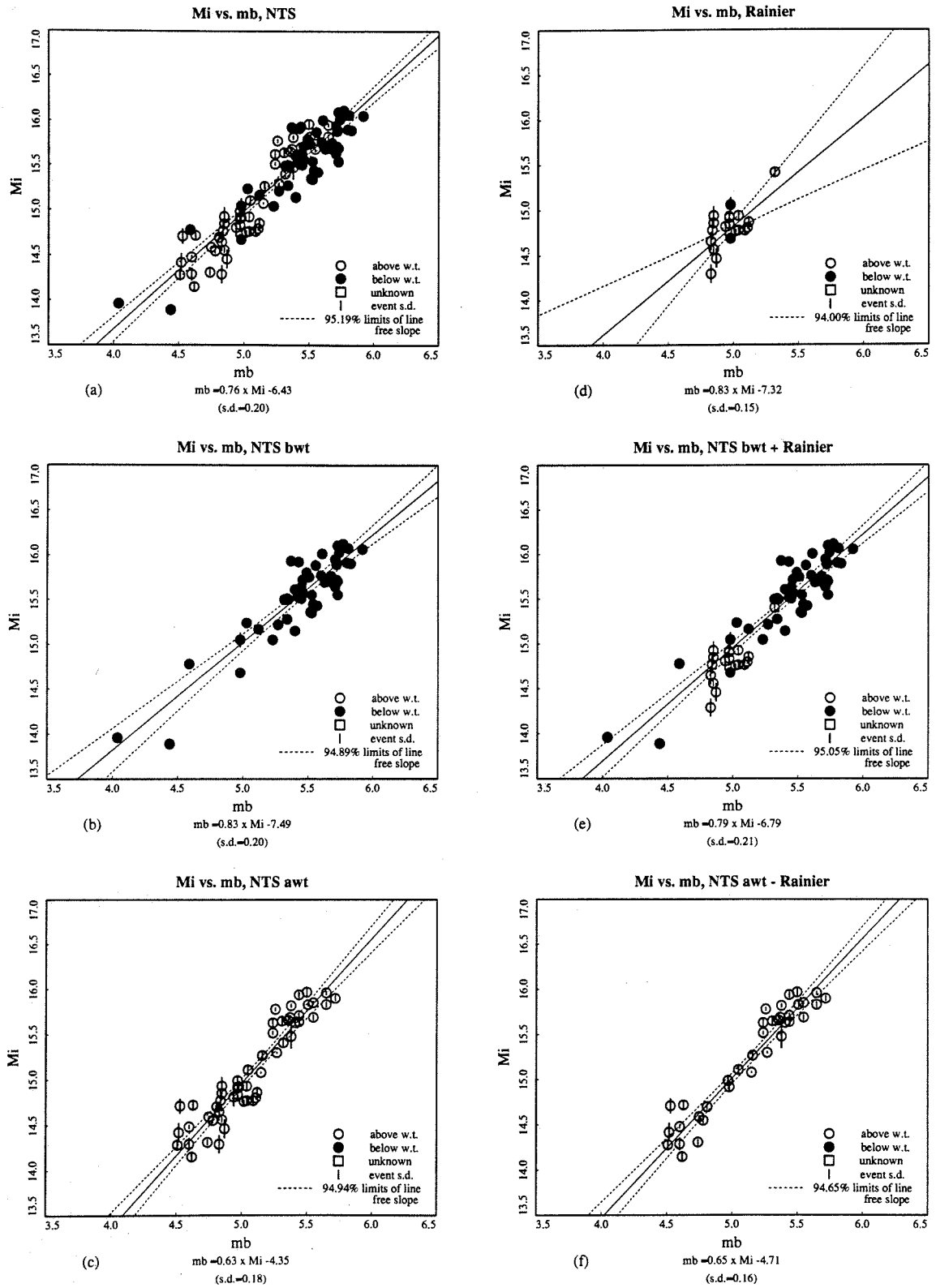

Figure 3.21: M_0 vs. m_b regression curves for the aggregate NTS population and for Rainier Mesa.

(note that for most solid points the scaled errors are smaller than the symbols and hence are not viewable). A weighted linear least-squares regression was performed to obtain the M_0:m_b scaling relationship. Below the curve is the regressed scaling relationship and below that, in parentheses, is the standard deviation in the fit of the data to the curve. Given and Mellman (1986) formulate the M_0:m_b (or M_I:m_b) scaling law as a function of M_0, so for consistency in comparisons the same is done here. Here, unlike in their study, the slope is not set to 0.9, an artificial constraint, needed because of the narrow range of data and based on assumptions in m_b:yield and moment:yield scaling laws. The solid line is the fit to the data and the dashed lines are the 2σ error bars for this line. The scaling relationship is well constrained; however, the standard deviation is large, being 0.2 log-moment units (58 percent). Separating the events into populations detonated below and above the water table (figures 3.21b and 3.21c, respectively) does not reduce the scatter significantly, but it does change the slope of the curve some (10-15 percent), giving an indication of how well the regression curves are constrained.

Figure 3.21d is a regression-curve plot of Rainier Mesa explosions. Although the curve is not well-constrained, the slope is close in value to that of the other curves. Rainier shots are detonated in large horizontal tunnels, unlike other shots which are detonated in boreholes. So there is some question as to the complexity of Rainier sources. As discussed in chapter 2, the M_S-yield relationship is similar to that of well-coupled Pahute detonations below the water table (BWT) from which it is assumed that the Rainier shots can be treated as being in saturated rock. This inference is substantiated by Taylor (1983), who reports that the Mesa sports a perched aquifer. Treating the Rainier detonations as having been below the water, the entire NTS data set is again separated into shots occurring below and above the water table populations in figures 3.21e and 3.21f, respectively. The inclusion or exclusion of Rainier events does not appreciably change either curve, so it not clear from these

results whether Rainier shots are detonated in water-saturated rock or not.

Figure 3.22a is the moment-m_b regression curve for Yucca Flats explosions. Figures 3.22b and 3.22c separate the Yucca population into shots below and above the water table. All three of these curves are well-constrained and have slopes near 0.8, similar to the complete NTS population curves. The standard deviations of these curves are slightly smaller than that of the aggregate NTS data curves, indicating that the sub-sites do have relative excitation levels for surface waves and body wave.

Figures 3.22d, 3.22e and 3.22f are analogous curves for Pahute Mesa. These curves are poorly constrained, because of the limited data set, and have quite different slopes. To obtain useful scaling relationships for Pahute Mesa, more data is necessary. In an effort to better constrain these curves, Rainier shots were added to this population under the premise that the two source regions have similar geology (volcanic mesas of tuff and rhyolite). Although the resultant curves are well-constrained (figures 3.23a, 3.23b and 3.23c), their slope values are quite different from the other populations. It appears that the Rainier shots have a larger m_b for a given moment than Pahute events. This point will be further examined after examining the moment:log-yield scaling laws.

In order to better constrain the m_b:moment scaling relationships, data from the Stevens (1986) and Given and Mellman (1986) studies were included after correcting for their modeled shot points. Figures 3.24 and 3.25 are regression curve plots for the combined data sets analogous to figures 3.21 and 3.22. The main improvement is to better constrain the Pahute Mesa curves (figures 3.25d and 3.25e) which have slopes in line with the regression curves for the other populations (≈ 0.8). The Pahute awt curve is no better constrained however.

From these results it appears that the m_b:moment scaling relationship curve slope is near to 0.8 for all well-constrained cases. The data sets were then regressed again with a fixed slope of 0.8. The difference in off-sets, relative to the aggregate NTS

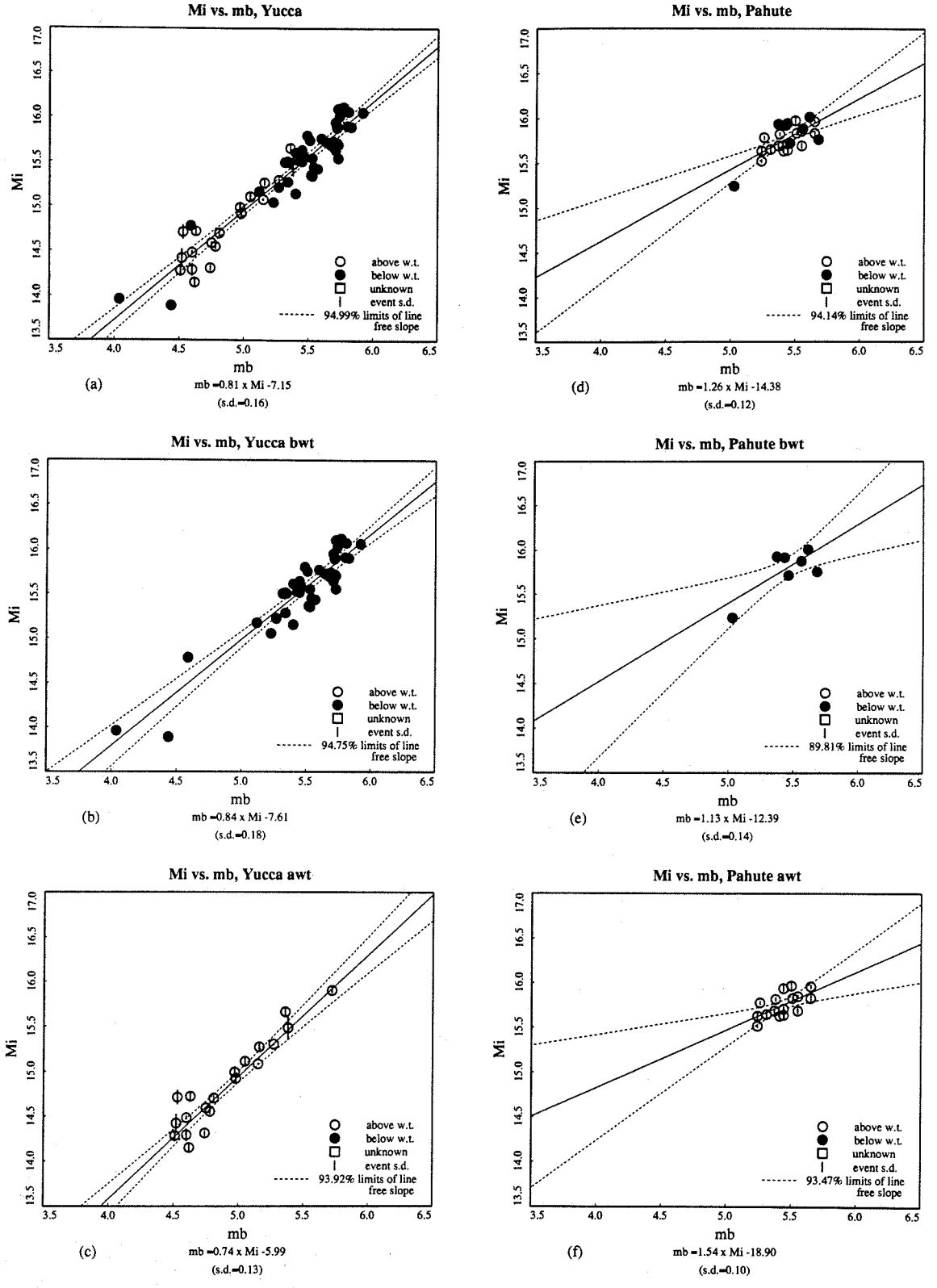

Figure 3.22: M_0 vs. m_b for regression curves Yucca and Pahute Events.

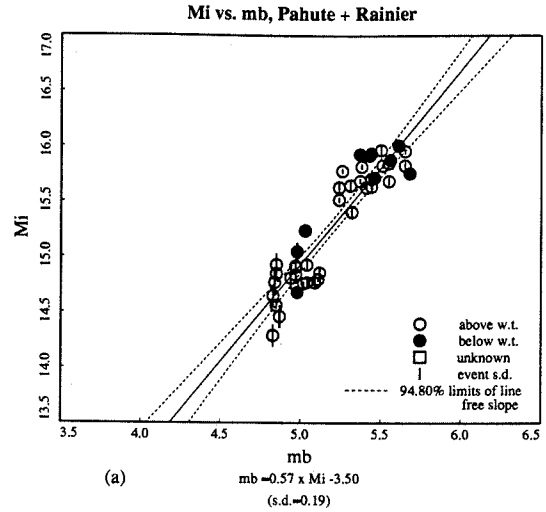

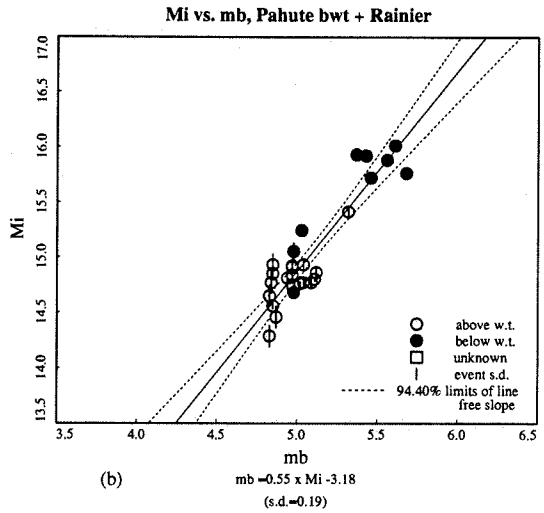

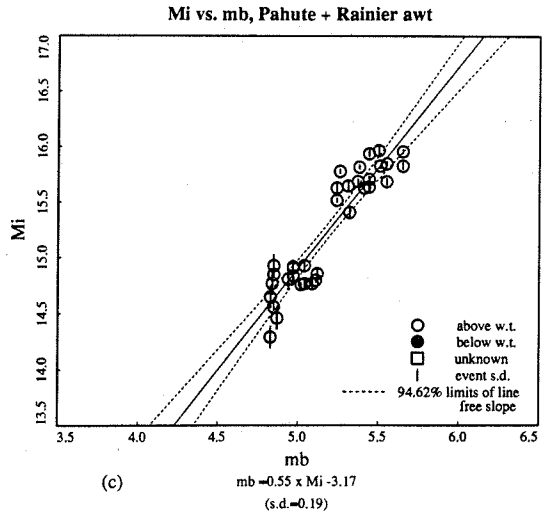

Figure 3.23: M_0 vs. m_b regression curves for Pahute and Rainier events.

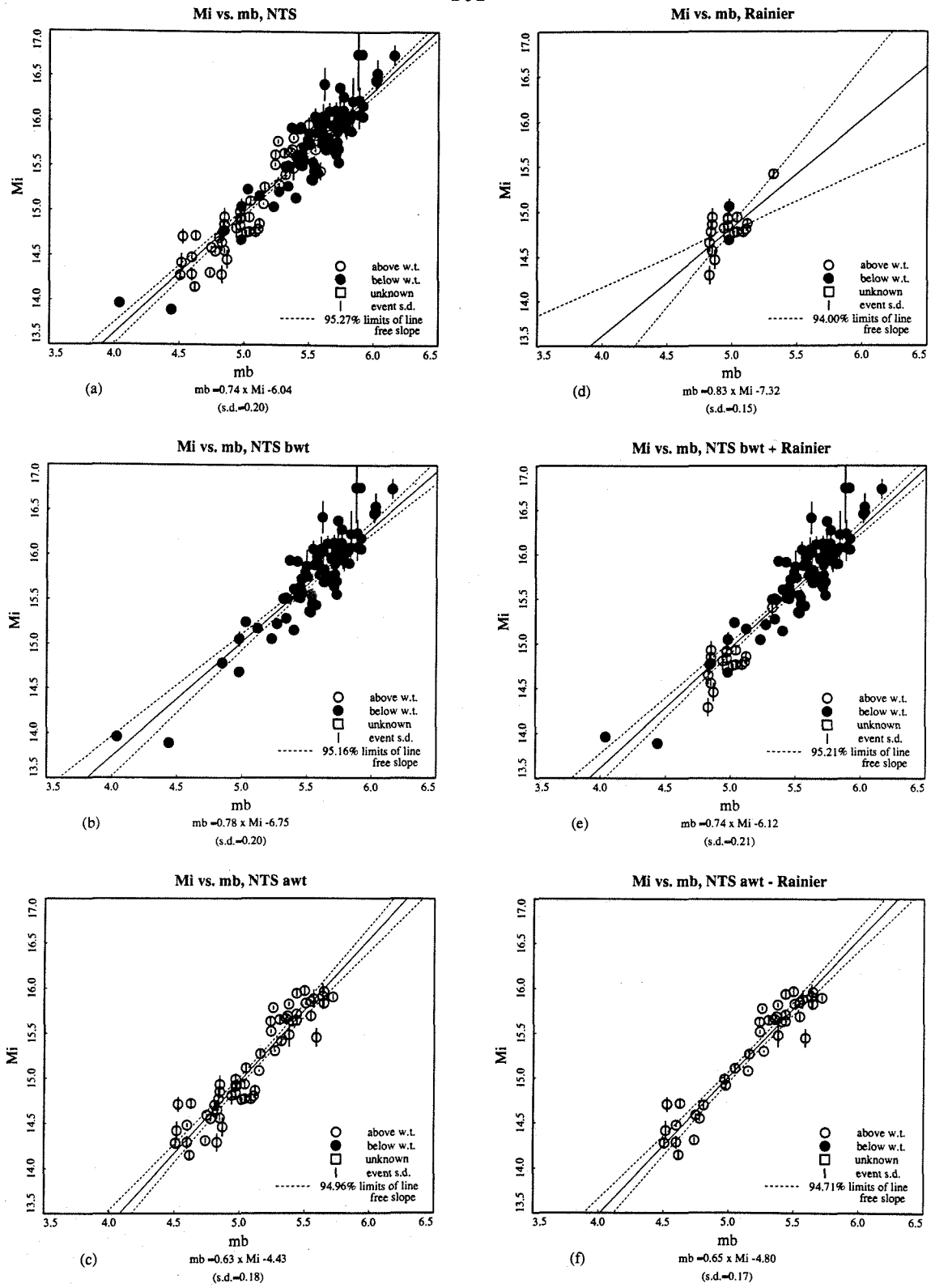

Figure 3.24: M_0 vs. m_b regression curves for all NTS events and for Rainier events. Data from Stevens (1986) and Given and Mellman (1986) are included.

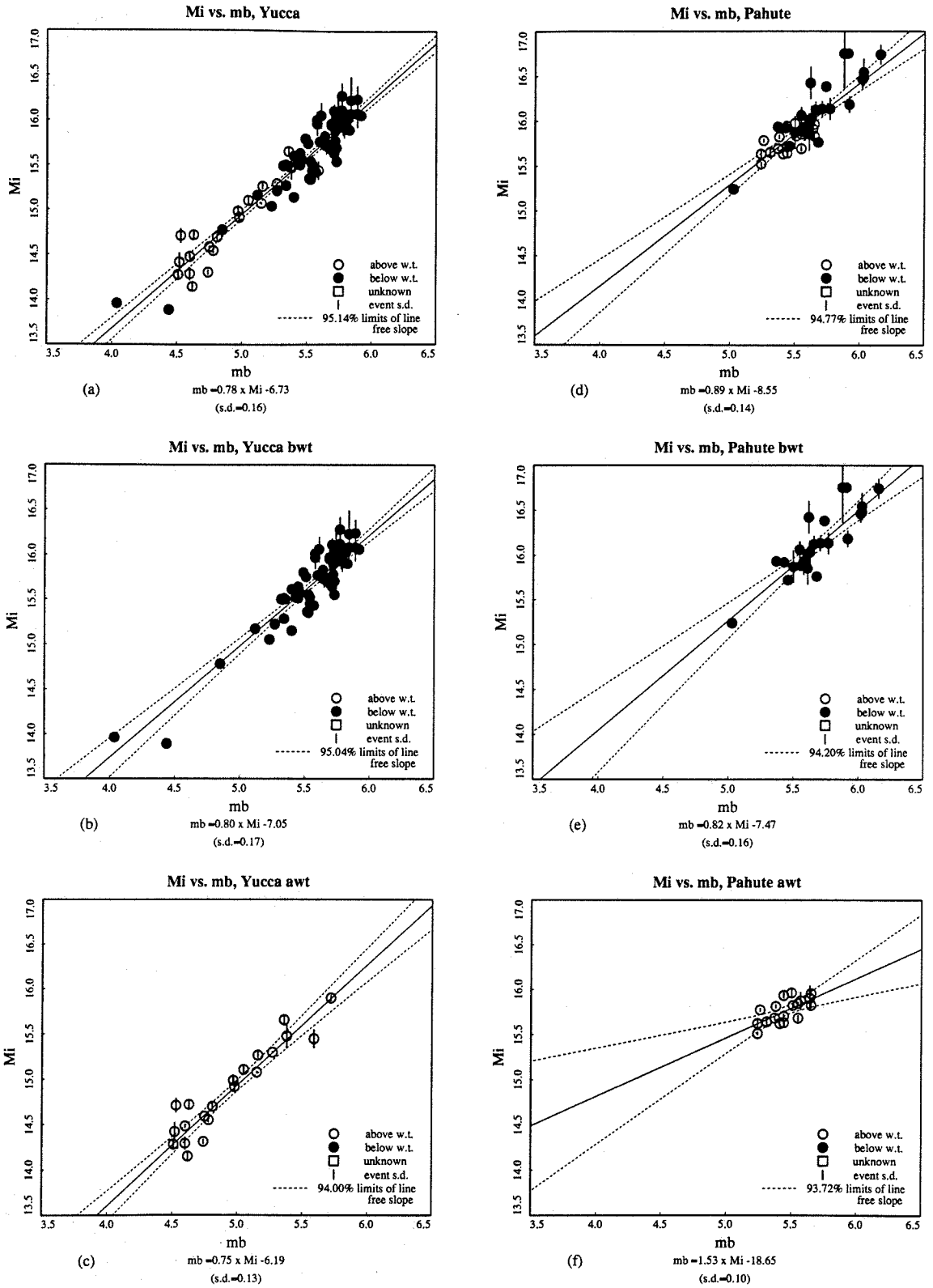

Figure 3.25: M_0 vs. m_b regression curves for Yucca and Pahute events. Data from Stevens (1986) and Given and Mellman (1986) are included.

curve, are given in table 3.12, with a positive value meaning that for a given moment, the m_b value will be larger by that many magnitude units. The standard deviation of the data fit to the curve is also given, so that goodness of fit of the unconstrained and constrained curves can be compared. In all cases, except for Pahute events alone, this difference is negligible. For Pahute the errors are slightly smaller for the unconstrained curve. For the entire NTS data set the fixed-slope scaling relationship is

$$m_b = 0.8 \times M_0 - 7.0. \tag{3.42}$$

Here the M_0 can be interchangeably used with M_I. There is no appreciable off-set between shots detonated above or below the water table at an individual site implying that P-wave and Rayleigh wave coupling effects are very similar. There are differences between sites, however, the largest difference being between Pahute and Rainier. From these results Pahute Mesa will have the smallest m_b for a given moment, followed by Yucca and then Rainier, implying that it is the richest in long-period energy excitation. The scaling curve off-set difference between shots above and below the water table are negligible.

In order to determine seismic coupling effects and moment-scaling independent of another seismic scale, the seismic moments were also regressed against yield. Figures 3.26, 3.27 and 3.28 are log-moment vs. log-yield regression plots analogous to the M_0 vs. m_b plots of figures 3.21, 3.22 and 3.23, respectively.

For the complete NTS data set (figure 3.26a) the curve is well-constrained, with a slope near unity (1.04). The group of data points grouped away from the regression curve are Yucca Flat explosions detonated above the water table (AWT), about half of these were detonated in alluvium as well. Werth *et al.* (1963), in a previous study of P-wave coupling found that alluvium had the lowest seismic coupling coefficient amongst the shot medium rock types that were studied. It is also known that saturated rock tends to be a more effective medium for seismic coupling. Compres-

m_b=0.8×log (M_0)−7.0+D			
Site	Case	D	s.e.
NTS	all	0.0	0.02
NTS	bwt	0.0	0.03
NTS	awt	-0.01	0.03
Rainier	all	0.15	0.03
Yucca	all	0.04	0.02
Yucca	bwt	0.04	0.03
Yucca	awt	0.05	0.03
Pahute	all	-0.17	0.03
Pahute	bwt	-0.18	0.06
Pahute	awt	-0.17	0.03

Table 3.12: Offsets in M_0:m_b regression curves for NTS subsites.

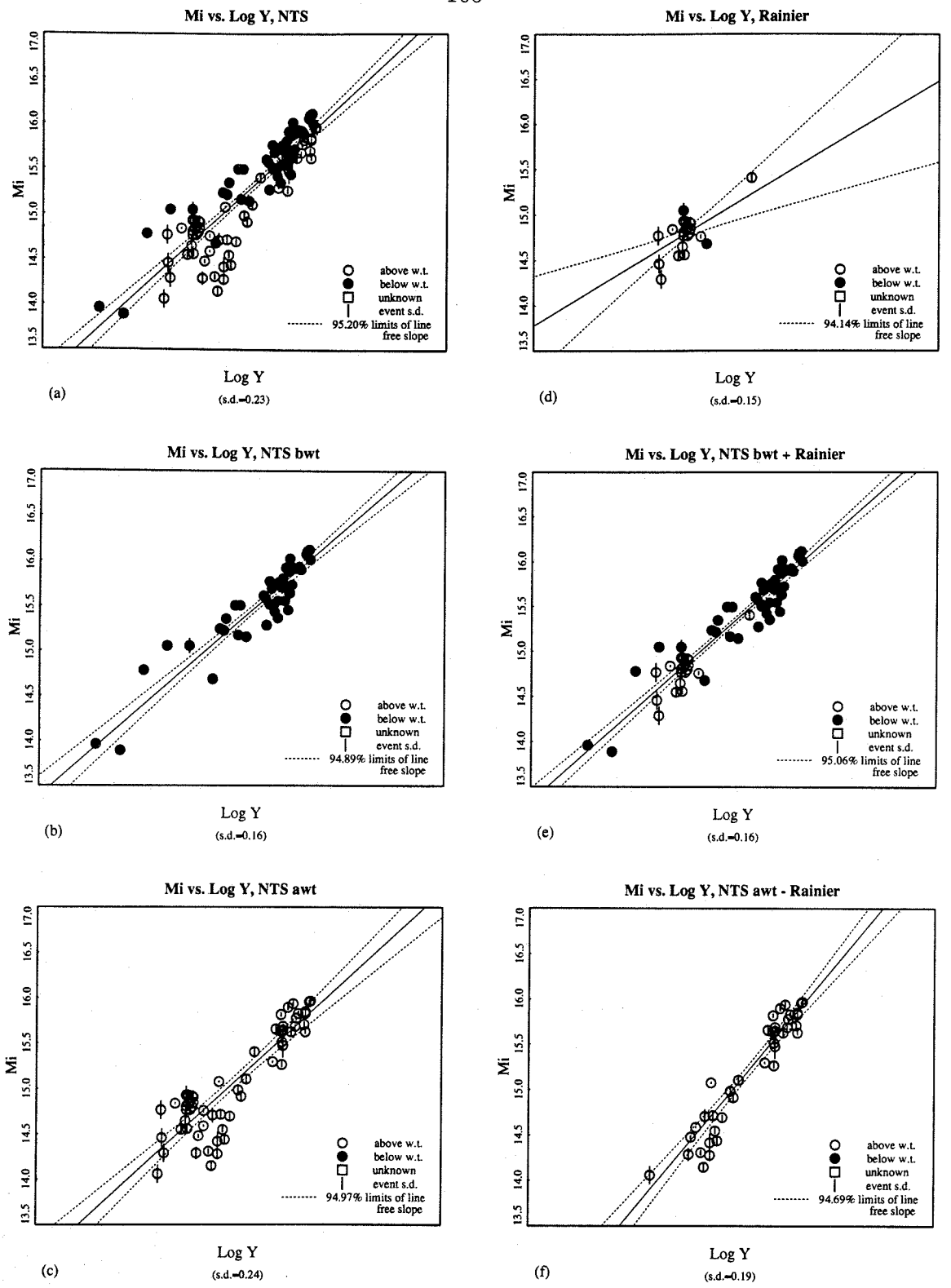

Figure 3.26: M_0 vs. log-yield for aggregate NTS and Rainier data sets.

sional velocity tends to increase with decreasing dry porosity, as the bulk modulus increases, so by equation 3.5 an increase in α lowers the observed displacement for a given moment, M_I. So it is not surprising that bombs detonated in such muffling material will give lower apparent moments. Splitting the NTS population into shots detonated in water-saturated or unsaturated rocks leads to similar sloping curves, with values near unity (0.98, 1.03 and 1.00 for curves b, c and e, respectively) but with different intercepts. The scaling relationship for Rainier events (figure 3.26d) is poorly constrained; however, a slope of unity is within the 2σ confidence level of the curve.

For the case of AWT explosions, excluding Rainier shots (figure 3.26f), the slope of the curve is considerably larger than for any of the other cases. This data set falls into two clusters (above and below $\log(M_I) = 15.5$), the upper group being predominantly Pahute events and the lower being all Yucca events. If there is a difference in coupling between the two sites, there should be a corresponding offset in scaling curves. So the best-fitting curve for the combined data set will give a very skewed, incorrect curve (slope=1.35).

Separated Yucca and Pahute population log-moment:log-yield curves are shown in figures 3.27a through 3.27f. The variance is significantly smaller for the Pahute populations, particularly for BWT events (figure 3.27e). The slope for this curve (0.86) is heavily-constrained by the one low-yield event (REX), where as the Pahute and Pahute AWT curves both have slopes near 0.69 in value. In fact, the best-constrained curve is for Yucca BWT shots (figure 3.27b, slope=0.97). The Yucca AWT regression curve (slope=1.27) is not well-constrained, due to the highly scattered nature of the data.

Combining the Pahute and Rainier data leads to a better constrained curve for BWT events by making the assumption that all of the Rainier shots are fired in saturated rock. For all events above and below the water table, the slope is 0.95

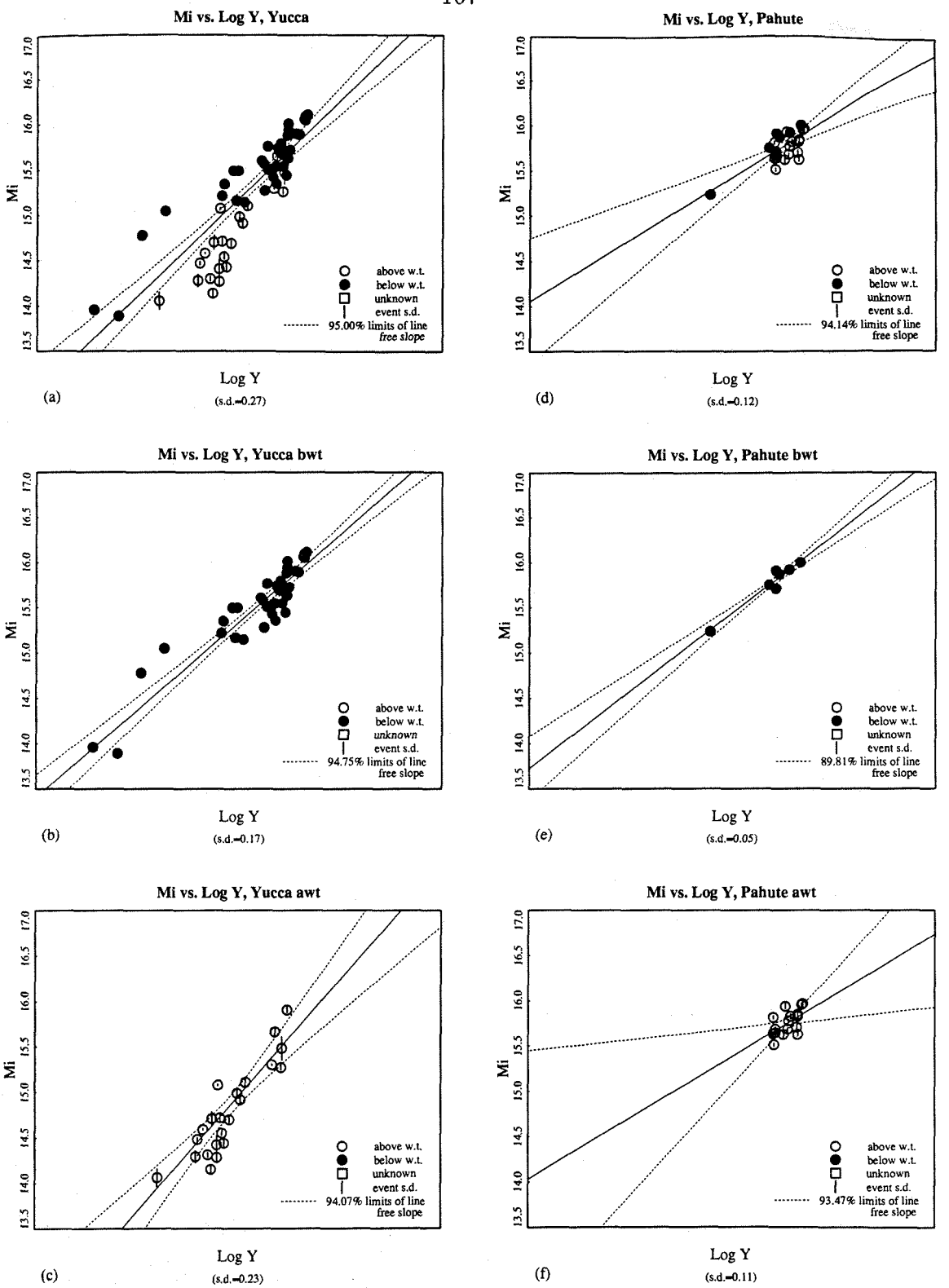

Figure 3.27: M_0 vs. log-yield for Yucca Flats and Pahute Mesa data sets.

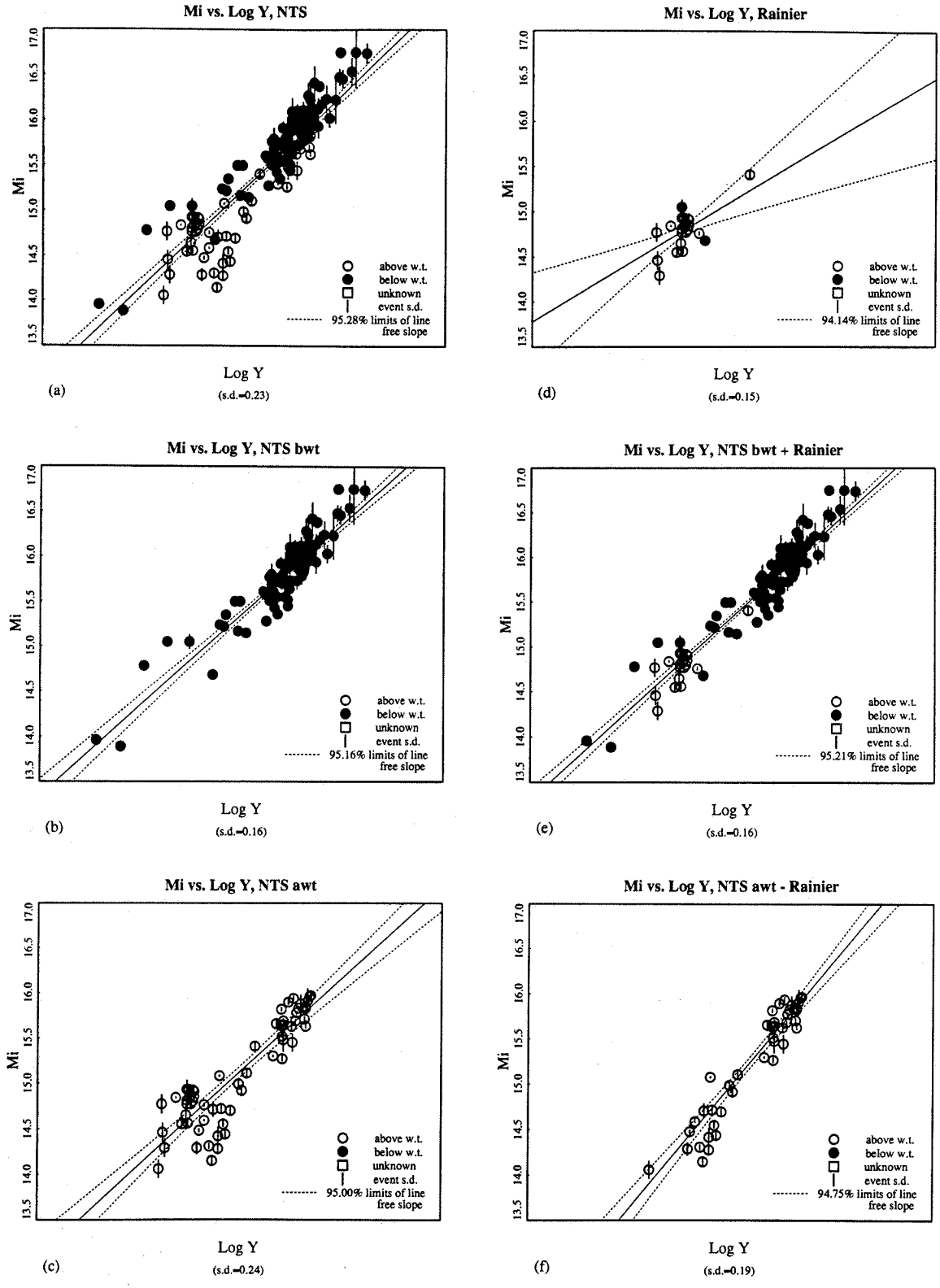

Figure 3.28: M_0 vs. log-yield for combined Yucca Flat and Pahute Mesa data sets.

(figure 3.28a). For the case of BWT shots, the slope is 1.06 (figure 3.28b). Combining Pahute AWT shots with Rainier shots gives a slope of 0.90 (figure 3.28c). The fact that the Pahute AWT + Rainier slope is furthest from unity is interpreted to mean that the Rainier events couple intermediate to Pahute shots detonated below and above the water table.

In order to better constrain the larger-yield portion of the regression curves (particularly for Pahute events), the other studies' moments are also added to the data set, bringing the total number of events to 155 from 109. Figure 3.29a is for all NTS BWT events; the slope of the scaling relationship is 1.01. Including Rainier shots leads to a slope of 1.03 (figure 3.29b).

None of the AWT curves are appreciably changed by the addition of only a few points (1 to 3) at most. The most improvement in constraining the data is for those data sub-sets including Pahute events. Figure 3.29c is for all Pahute alone and the slope, 1.09, is better constrained than that of the curve in figure 3.27d. Including Rainer data gives a slope of 1.01 (figure 3.29d). The Pahute BWT data and corresponding scaling curve are shown in figure 3.29e (slope=1.14), unfortunately the lower end of the scale is still poorly constrained. Figure 3.29f is for Yucca BWT data. Its slope (0.96) is close to the case for this study's data only (figure 3.27b).

From these results the estimated average slope of the moment:yield scaling curves is near unity, with a 2σ margin of error of 0.05. A constrained (fixed-slope) least-squares regression for each data set was also performed. The tabulated results for this study's data set and the combined data set are in Table 3.13 and Table 3.14, respectively. The first column of each table describes the data set sub-population. The second column is the off-set relative to the complete NTS data set determined in this study (δD). The last column is the standard deviation for each fix-slope regression curve, which are generally not appreciably larger than for the free-slope

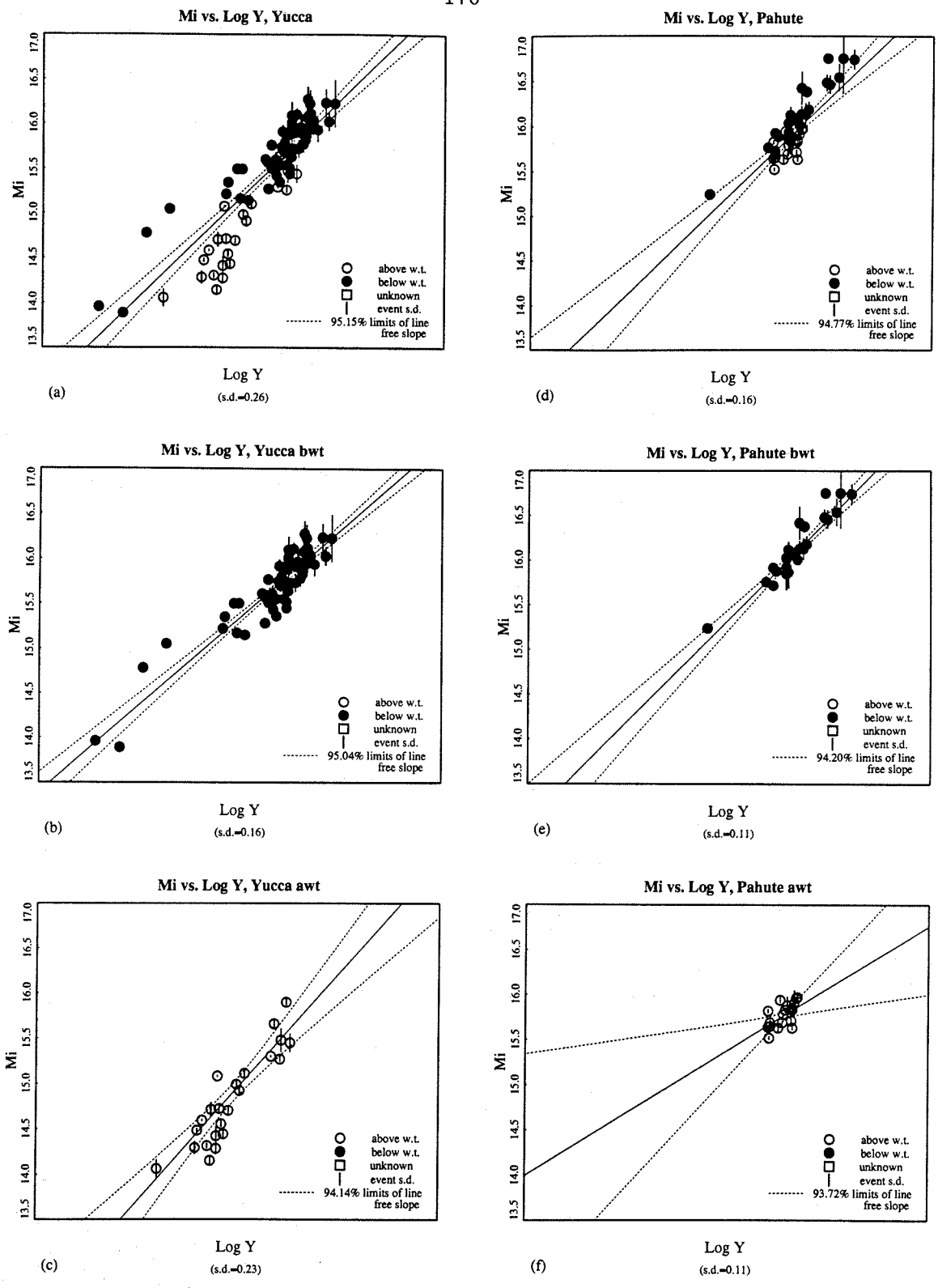

Figure 3.29: M_0 vs. log-yield for the Rainier and complete NTS data sets which include moment data from Stevens (1986) and Given and Mellman (1986).

regression curves. The standard error, $\sigma_{\bar{X}}$, defined as

$$\sigma_{\bar{X}} = \frac{\sigma}{\sqrt{n}}, \tag{3.43}$$

with σ being the standard deviation and n being the number of observations, is between 0.01 and 0.04 for δD in all cases. So δD's larger than this amount are statistically significant.

Using either data set (this study's or the combined data set) a large offset is seen in the log-moment:log-yield intercept between shots detonated above and below the water table. For Pahute this offset is 0.22 log units (a difference of 66 percent). For Yucca the offset is 0.41 log units (a 275 percent difference). The difference in apparent coupling between Pahute and Yucca shots detonated in saturated rock is only 0.08 log units or 20 percent. The Rainier scaling curve intercept appears to be intermediate to that of the Pahute BWT and Pahute AWT curves. Yucca AWT shots have the lowest apparent coupling, being 0.3 log units (200 percent) lower than that of the aggregate NTS data curve. The difference in offset between composite (BWT+AWT) data sets is small for all subsites, being less than 0.07 (17 percent) in all cases. Hence, site source effects are relatively small; however, whether or not the shot occurs in saturated material is a significant effect.

3.7 Conclusion

Spectral moments were determined for 109 NTS explosions using regional surface wave data. This data set is significantly larger and more comprehensive than previous published studies of long-period explosion sources. Whereas these studies (Stevens, 1986 and Given and Mellman, 1986, for example) are confined to explosions greater than $m_b = 5.4$; in this study, events down to $m_b = 4.9$ were consistently observed and analyzed (in some cases even smaller). With this extensive data set it is possible to

log(M_0)=log(yield) + D		
dataset: this study		
Case	ΔD	s.e.
NTS (all)		0.02
NTS bwt	0.11	0.16
NTS awt	-0.12	0.03
Rainier	0.04	0.03
NTS bwt+Rainier	0.10	0.02
NTS awt-Rainier	-0.18	0.03
Yucca (all)	-0.03	0.03
Yucca bwt	0.10	0.03
Yucca awt	-0.30	0.05
Pahute (all)	0.03	0.03
Pahute bwt	0.14	0.02
Pahute awt	-0.04	0.03

Table 3.13: Offsets in constrained M_0:yield regression curves for NTS subsites.

$\log(M_0)$=log(yield) + D		
combined data set		
Case	ΔD	s.e.
NTS (all)	0.02	0.02
NTS bwt	0.14	0.02
NTS awt	-0.12	0.03
NTS bwt+Rainier	0.13	0.01
NTS awt-Rainier	-0.16	0.04
Pahute (all)	0.08	0.02
Pahute bwt	0.21	0.03
Pahute awt	-0.1	0.02
Pahute+Rainier	0.08	0.02
Pahute bwt+Rainier	0.14	0.02
Pahute awt+Rainier	0.0	0.02
Yucca (all)	0.01	0.03
Yucca bwt	0.13	0.02
Yucca awt	-0.28	0.05

Table 3.14: Offsets in constrained M_0:yield regression curves for NTS subsites using the combined data set.

make more robust inferences concerning long-period source scaling for underground nuclear explosions.

The reduced magnitude threshold is due, in part, to the inclusion of near-regional (d<700 km) surface wave records for source inversions. Only with such data were the smallest events ($m_b \leq 4.9$) measurable. Systematic errors due to incorrectly modeling path attenuation effects are minimized using such stations as well. It was also found that regional digital long-period stations, specifically RSTN and DWWSN stations, were superior for observing the smaller events than were the earlier-model analog WWSSN stations.

Moment estimates assuming a pure explosion source (*i.e.*, the average of the station moments) do not vary significantly, in almost all cases, from estimates determined from joint isotropic + double-couple inversions. Moment standard errors (1σ) are also comparable, being on average approximately 7 percent (0.03 log units), with the smaller events tending to have larger errors. This is a significant improvement over the time domain moments determined in chapter 2 ($\bar{\sigma} = 0.15$). Past investigations of surface wave magnitudes and seismic moments did not achieve this level of accuracy, even when secondary path corrections (or more exactly station corrections) were incorporated. The improvement in accuracy in the moment estimates found in this study are attributed to using near-regional stations and having better azimuthal coverage.

The results of the canonical source inversion study predict errors for the joint source inversion compatible with observations; however, the observed errors for the constrained explosion source estimates are smaller than the predicted values. A possible explanation for this fact is that the path Green's functions were inverted from bomb data contaminated with tectonic release energy, so that azimuthal radiation effects are incorporated into them. Thus azimuthal amplitude variations will be smeared-out, making the observed non-isotropic component appear smaller.

The constrained tectonic-release moment results are not as well resolved, with standard deviations varying from 10 to 50 percent (0.04 to 0.18 log units). Moment estimates determined separately by Rayleigh wave and Love wave varied by as much as a factor of 2.5. The inferred strike angles obtained from the constrained moment inversion generally were found to confirm earlier studies that found the predominant tectonic release mechanism could be modeled as a near-vertical strike-slip double-couple source with a strike near N20°W.

As a goal of this study was to re-evaluate the utility of surface wave measurements to quantify explosions for yield and discrimination purposes, particular attention was paid to error analysis of the moment estimates. To this end it is important to determine how much near-source effects can modify apparent moments. Moment scaling relationships for the various NTS sub-sited were determined using this study's analyzed events in conjunction with larger yield explosion data from other studies in order to better constrain their curves. It was found that $m_b \propto 0.8(\pm 0.05) \times \log(M_0)$, while $M_0 \propto Y^{(1.0 \pm 0.05)}$.

The off-set in scaling curve intercept between sub-sites is at most 0.07 log units (17 percent) for the super data set and only 0.02 log units (5 percent) when only data from this study was considered. A much greater difference in scaling curve intercepts exists between events detonated above and below the water table, being between 0.22 log units for Pahute Mesa and 0.41 log units for Yucca Flats. This coupling affect appears to be similar for P-wave amplitudes. If this coupling effect cannot be accounted for in practice, then predicted yield estimates could off by a factor of two. Gupta *et al.* (1989) found that the spectral content of P-waves could be used to determine whether a shot occurred above or below the water table. In an actual monitoring environment where only remote-sensing may be possible, employing this technique would enable one to correct explosion moment estimates for the shot medium coupling, thus significantly improving surface wave moment

estimates, as well as body wave magnitudes.

The improvement in estimating the long-period source spectrum of explosions found in this study makes such measurements more useful for seismic nuclear monitoring. The resolution attained in this study makes surface wave moment estimates a prime candidate as companion measurement to L_g magnitude ($m_{b(Lg)}$) (Nuttli, 1986; Patton, 1988). The magnitude threshold for L_g is lower than that of surface wave measurements, being near $m_b = 3.1$ for comparable distances; however, for paths in which the L_g wavetrain is "pinched out," a term for which is "L_g blockage," other methods are necessary.

Chapter 4

M_L:M_0 as a Regional Seismic Discriminant

4.1 Summary

The m_b:M_S ratio determined by teleseismic observations has proven to be an effective discriminant, for explosive sources tend to be significantly richer in short-period energy than earthquakes. Unfortunately, this method is limited by the detection threshold of teleseismic surface waves. However, recent advances in instrumentation allowing low amplitude surface wave measurements coupled with new analytical techniques make it feasible to use regional waveform data to determine the long-period source excitation level of low magnitude events. We propose using the ratio of M_L (local magnitude) to M_0 (scalar seismic moment) as an analogous regional discriminant. We applied this criterion to a data set of 299 earthquakes and 178 explosions and found that this ratio appears to be diagnostic of source type, with explosions generally having a M_L 0.5 magnitude units larger than that of an earthquake with an equivalent seismic moment. This separation of populations with respect to source type can be attributed to the fact that M_L is a short-period (1 Hz) energy measure-

ment, whereas seismic moment is determined from long-period body wave phases (period > 4 seconds) and surface waves (10 to 40 seconds). Using regional stations with sources 200 to 600 km away, the effective threshold for magnitude measurements for this discriminant is found to be $M_L = 3.1$ for earthquakes and $M_L = 3.6$ for explosions. This method does require the determination of regional crustal models and path calibrations from master events or by other means.

4.2 Introduction

In this era of increased concern regarding the proliferation of nuclear weapons, the need for effective seismic discrimination techniques is as important as ever. As more countries attain or near the technology threshold needed to develop nuclear weapons, more regions of the world need to be monitored for verification purposes. Effective discrimination methods which can make use of historical seismic data and don't require elaborate, costly large-scale arrays, are of considerable interest.

One of the most successful seismic discriminants proven so far is the classical comparison of body wave magnitude (m_b) to surface wave magnitude (M_S) (Basham, 1969; Lieberman and Pomeroy, 1969; Marshall *et al.*, 1971; Stevens and Day, 1985), which exploits the observation that for a given m_b, explosions have a significantly smaller M_S than do earthquakes. This observation implies that explosive sources are richer in high frequency energy than are earthquakes for a given long-period energy level and is attributed, in part, to the differences in characteristic temporal and spatial source dimensions between the two source types. Savino *et al.* (1971), Aki *et al.* (1974) and Müller (1973) find that explosions exhibit characteristics of an impulsive source. Empirical explosion source models developed by Haskell (1967) and Müller and Murphy (1971) yield source time functions with rise times which are only fractions of second in length. Aki (1967), Brune (1970) and Marshall (1970) find that

earthquake source functions, on the other hand, are best-modeled as ramps or step functions with combined duration and rise times greater than one second. Dreger and Helmberger (1991a) found that even moderate-sized earthquakes ($M_L \sim 5.2$) have source durations greater than a second. Stevens and Day (1985) conclude from numerical modeling experiments that the difference between earthquake and explosion source spectra is only partially responsible for explaining m_b:M_S observations. They also cite focal mechanism, near-source elastic properties and pP interference effects as contributing factors to the separation of populations with this type of discriminant.

The drawback to the m_b:M_S method is the threshold at which teleseismic surface wave magnitudes can be determined and the apparent convergence of populations at small magnitudes. Lieberman and Pomeroy (1969) found the surface wave detection level for earthquakes to be m_b >4.3 and for explosions to be $m_b > 4.8$, but found that the populations converged below $m_b = 5.0$ for discrimination purposes. Evernden *et al.* (1971) suggest that with high-dynamic-range digital instruments, surface waves from earthquakes with m_b >4.0 (which corresponds roughly to a m_b =5.0 explosion) can be measured out to 6000 km to 7000 km–distances at which well-dispersed 20 second surface waves can be measured. Broadband, high-dynamic-range seismic stations, such as those in the IRIS network, achieve this observational capability.

Below these threshold levels the surface wave signals are within the noise level, and analogous discriminants using regional phases must be employed. Evernden *et al.* (1971), Lambert and Alexander (1971), and Peppin and McEvilly (1974) found that they could distinguish between source types on the basis of regional P_n amplitude (or $m_{b(Pn)}$) to regional Airy phase Rayleigh wave amplitude (or magnitude) comparisons for events down to $m_{b(Pn)} = 3.6$ to 4.0–the detection threshold for explosion generated surface waves.

Two significant advances in observational seismology occurred since these studies:

one is the large-scale upgrade and augmentation of seismic networks with broadband, high dynamic range instruments; the other is the increased sophistication in source parameterization of earthquakes and explosions in terms of the excitation of Green's functions and the seismic moment tensor (Dziewonski *et al.*, 1981), which more precisely quantify seismic sources. With several three component, broadband stations, it is feasible to invert for the source function using regional body waves (Dreger and Helmberger, 1990 and 1992), surface waves (Kanamori and Given, 1981; Thio and Kanamori, 1992; Patton, 1988) or a combination of the two wave types (Zhao and Helmberger, 1993). M_0 should better reflect the long-period source characteristics of a source than does M_S, so that its use should improve discriminants which make use of long-period seismic phases.

We re-examine the utility of short-period vs. long-period energy measures in the context of regional seismic records. Figure 4.1 displays the study area, which includes Central and Southern California, Western Nevada and Northern Baja, Mexico. Waveform data is presented in this paper for the events shown in the figure (stars). This region is unique in that there is a large amount of natural seismicity, as well as that of Nevada Test Site (NTS) explosions and their aftershocks. The large number of seismic networks monitoring this regions has created a wealth of data useful for discrimination studies.

With M_0 serving as a long-period energy measure, we employ the classical local magnitude, M_L, (Richter, 1935 and 1958) as a measure of short-period energy. M_L is computed from the peak horizontal displacements on a Wood-Anderson torsion instrument, which is a high pass filter peaked around 1.0 second. Teleseismic P-wave phases measured to determine body wave magnitudes are typically of the same period, so M_L, too, can be considered a fair measure of the short-period source spectrum. There are several advantages of using M_L. One is that it is a simple measurement to make and is easy to obtain to very small magnitudes. Secondly, it is

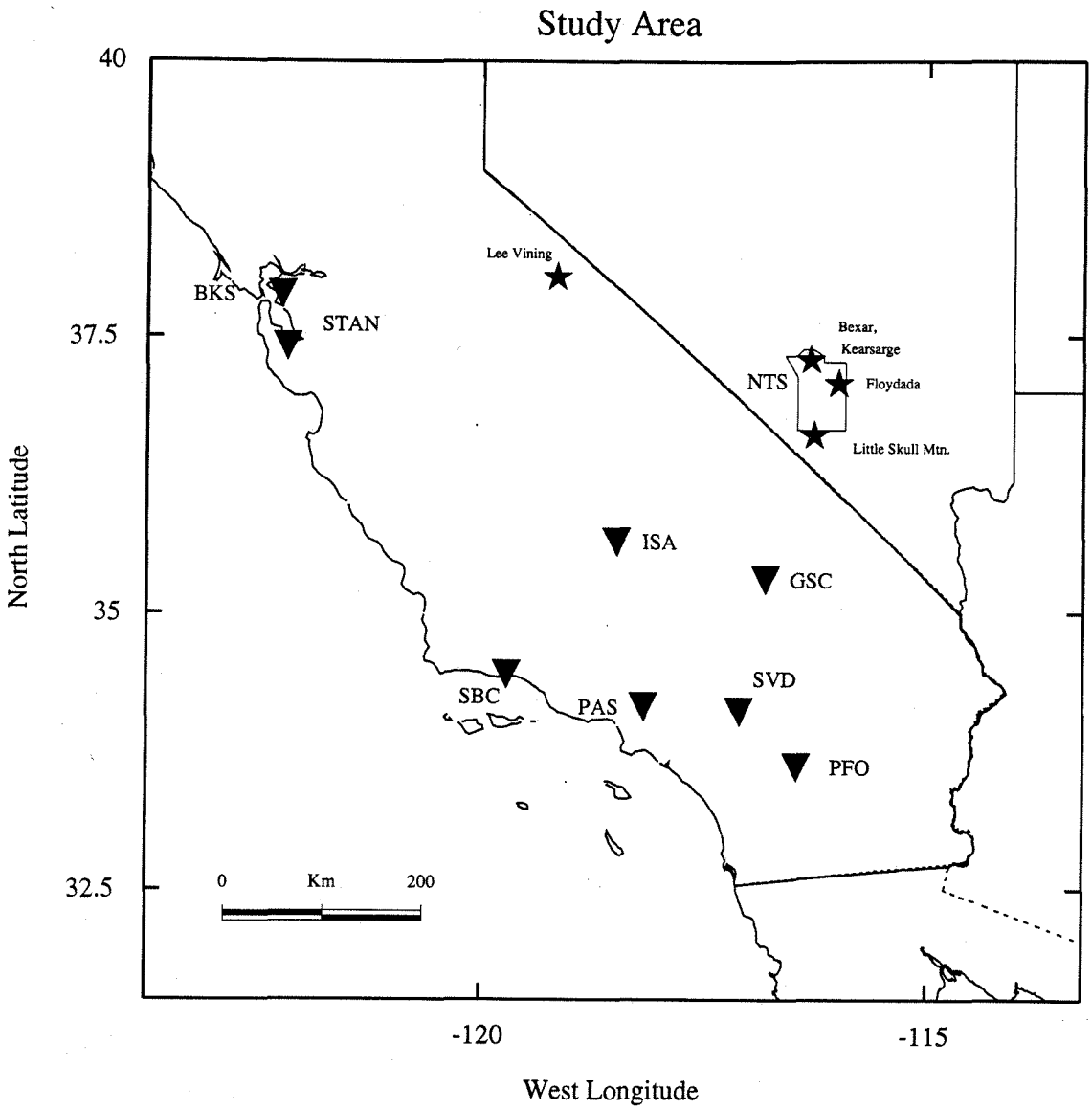

Figure 4.1: Map showing the study area. Broadband stations used to determine M_0 and M_L for 1988+ events are shown with triangles. Events shown in this study are denoted by stars.

a routine source quantification used by many seismic networks. We will make use of M_L magnitudes from several network catalogs. One drawback to measuring M_L is that it is not determined from a particular seismic phase. Normally it is a measure of shear-wave amplitude, but depending on distance and source spectrum for extreme circumstances, a P-wave or surface wave may be the largest amplitude phase on a short-period record.

From visual inspection of broadband recordings of regional earthquakes and explosions, it is apparent that these two source types show distinctly different spectral content. Figure 4.2a (upper box) compares records of the explosion Kearsarge (the 150 kt, $m_b = 5.5$, Joint Verification Event detonated at Pahute Mesa) to two earthquakes: Lee Vining (10/24/90, $m_b = 5.0$) and Little Skull Mountain (6/29/92, $m_b = 5.7$). The three events, all recorded digitally at Pasadena, California (PAS), have roughly the same epicentral distance (see Figure 4.1). For each event the broadband displacement records are displayed (middle trace), as well as the displacements convolved with a Press-Ewing 30-90 (PE) long-period instrument (top trace) and with a Wood-Anderson short-period (WA) instrument (bottom trace). Peak amplitudes are to the right of each trace. For Kearsarge, the ratio of peak short-period (WA trace) to long-period (PE trace) amplitude is 0.325, 0.265 and 0.625 for the vertical, radial and tangential component, respectively.

On the long-period tangential component, no fundamental Love wave is apparent; only later arriving, high frequency, higher-mode waves (L_g and possibly multipathing crustal waveguide surface waves) are evident. The absence of a Love wave is also evidence of an isotropic source, since explosions, in the absence of tectonic strain release do not generate long-period SH-waves. For Lee Vining the ratio of peak short-period to long-period amplitude is 0.152, 0.223 and 0.210 for the vertical, radial and tangential components. The tangential component also has a large fundamental mode Love wave. For Little Skull Mountain the ratio of peak short-period

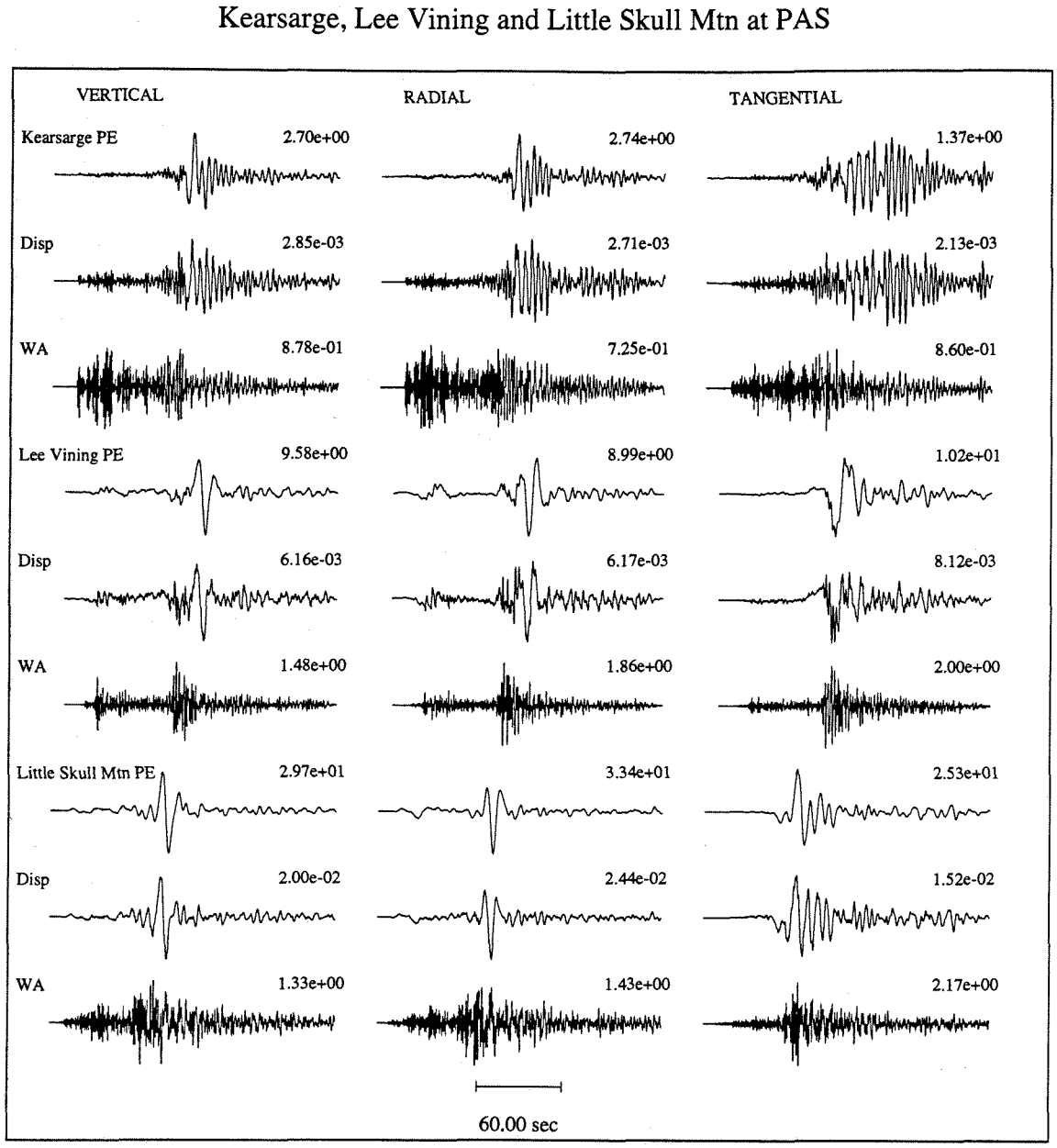

Figure 4.2: **(a)** Broadband displacement (middle trace) records of the JVE event Kearsarge and the Lee Vining and Skull Mountain earthquakes recorded at PAS and played out with long-period (top trace) and short-period (lower trace) instruments. **(b)** Analogous plot for the explosion Bexar and the Lee Vining and Skull Mountain earthquakes recorded at GSC.

Bexar, Lee Vining and Little Skull Mtn at GSC

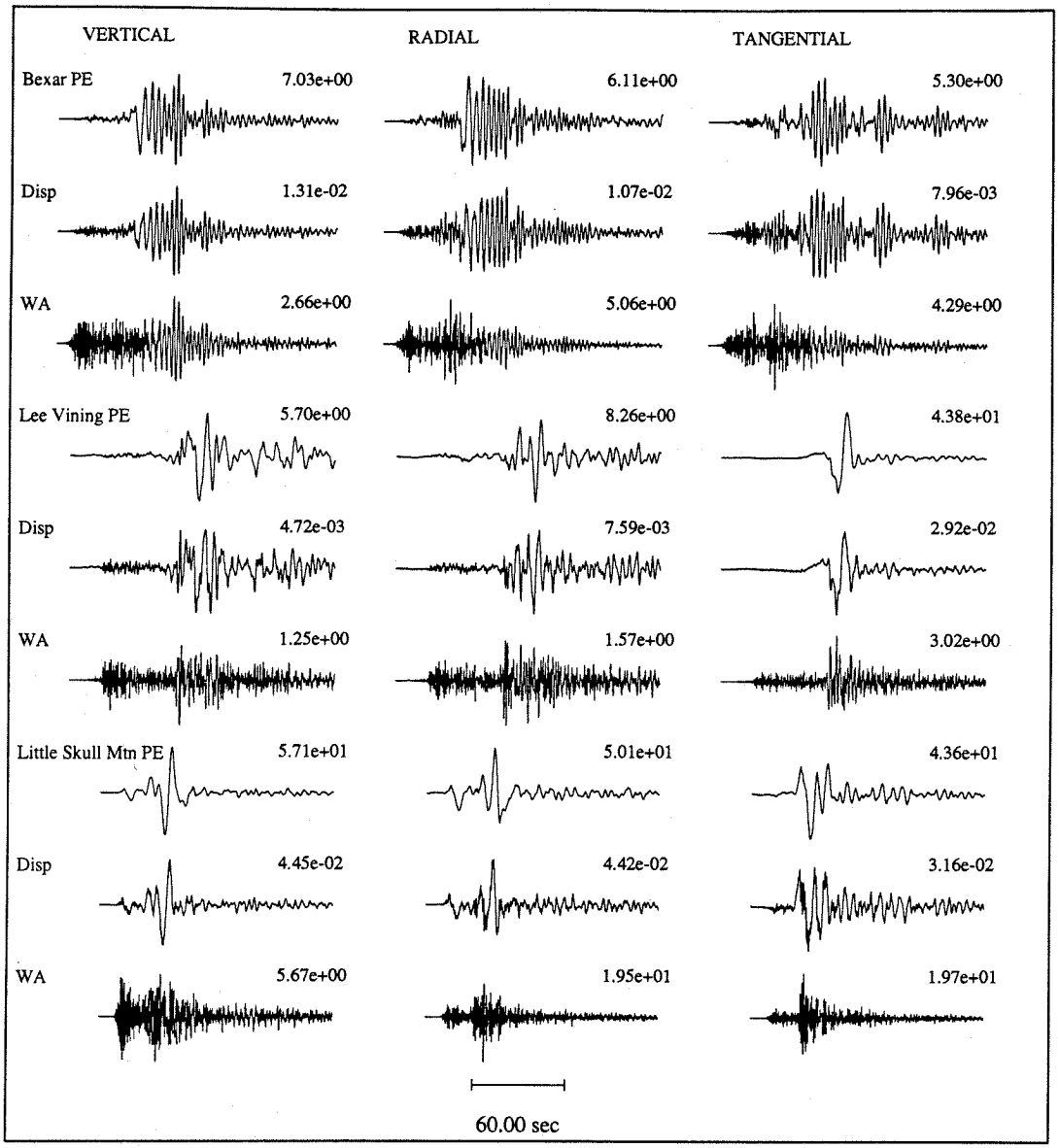

to long-period amplitude is 0.0451, 0.0433 and 0.0872 for the vertical, radial and tangential components. Again a large Love wave is observed. Of these three events, the explosion has the largest short-period to long-period amplitude ratio for each component.

Figure 4.2b shows an analogous plot of seismograms recorded at the digital station Goldstone, California (GSC), for the explosion Bexar (m_b =5.6 and detonated within a kilometer of the Kearsarge shot point) and the two earthquakes of figure 4.2. As with Kearsarge, little or no long-period Love wave is evident on the tangential component; only shorter period crustal waveguide surface waves are visible. The ratio of peak short-period to long-period amplitude for Bexar is 0.379, 0.794 and 0.794 for vertical, radial and tangential component, respectively. For Lee Vining the ratio of peak short-period to long-period amplitude is 0.221, 0.189 and 0.0694 for the vertical, radial and tangential components. For Little Skull Mountain the respective ratios are 0.0989, 0.394 and 0.455. Again, the explosion has the largest short-period to long-period amplitude ratio for each component.

Another comparative difference between the explosions and earthquakes in these figures is the spectral content of the Rayleigh waves. The explosion Rayleigh waves exhibit large, relatively short-period (3 to 8 second) "ringing" or coda waves after the Airy phase, whereas the earthquakes display primarily the dominant long-period Airy phase. This effect is believed to be a depth dependent phenomena. Kafka (1990) found, in a study of New England earthquakes and quarry blasts, that shallow events produce larger short-period (0.4 to 2.5 Hz) R_g waves than do deeper events. Such Rayleigh wave information is useful as a depth discriminant to help distinguish source types.

These sets of records corroborate the observation that explosions are richer in short-period energy relative to long-period energy as compared to earthquakes. Events recorded at both PAS and GSC have been plotted in order to illustrate that this ob-

servation is path independent. Of the network shown in Figure 4.1, only PAS and GSC recorded the Lee Vining event. We shall show, using a large data set, that this spectral difference becomes even more evident after applying propagational corrections and can be used as an effective regional discriminant.

4.3 Data Analysis and Results

We compiled seismic moments (M_0) and local magnitudes (M_L) for NTS explosions and earthquakes throughout the Western United States and Northern Baja California, Mexico from numerous sources. M_L values were taken from the CIT and Berkeley catalogs and from the Northwestern Mexico Seismic Network (Vidal and Munguia, 1991). For recent events (1988-1992) in Nevada and the California-Nevada Border region, M_L's were determined from the array of eight broadband stations shown in Figure 4.1. To calculate these M_L's, an attenuation curve developed by Kanamori *et al.* (1992) was used. All the M_L's used were determined in essentially the same fashion.

The seismic moments collected for this study, however, were determined through a variety of means. Dreger and Helmberger (1990, 1991a, 1991b, and 1992), Ma and Kanamori (1991), and Zhao and Helmberger (1993) inverted local and regional broadband waveforms to obtain source parameters, including moment. Cohn *et al.* (1982) forward modeled near-field broadband records to determine earthquake moments. Moments determined from combined regional phase (P_{nl}) and teleseismic body waves (P and SH) studies were also gathered. Bent and Helmberger (1991) used a combination of forward modeling comparative amplitude ratios to estimate moments for historical Southern California. We also included moments and local magnitudes compiled from various source studies for historical Western United States earthquakes (Doser and Smith, 1989; Doser, 1990).

Moments from several short-period array source studies were incorporated into our data set. Mori and Frankel (1990) obtained moment estimates from deconvolved displacement pulses. Employing the method of Brune (1970), several studies calculated M_0 from the low-frequency amplitude of shear-wave spectra (Johnson and McEvilly, 1974; Fletcher *et al.*, 1984; Frankel, 1984; Vidal and Munguia, 1991).

Surface wave moments were also obtained from a variety of sources. Thio and Kanamori (1992) obtained source parameters from broadband TERRAscope data for earthquakes throughout Southern California for a wide range of magnitudes. Their inversion method uses both Rayleigh wave and Love wave spectra and employs the technique of Kanamori and Given (1981). Patton and Zandt (1991) determined moment tensor solutions for earthquakes throughout the Western U. S. using a linear moment inversion scheme developed for Rayleigh wave spectra by Romanowicz (1982) and extended to Love wave spectra by Patton (1988). Wyss and Brune (1968) determined moments from Love wave spectra for Central California events.

Table 4.1 is a list of the local magnitudes and log-moments for earthquakes for which source parameters were determined from broadband data. It includes all available data from the studies by Dreger and Helmberger (1990, 1991a, 1991b, 1992), Ma and Kanamori (1991), and Thio and Kanamori (1992).

Table 4.2 lists the local magnitudes and log-moments for explosions cited in this study. Seven explosion moments were determined from near-field observations (Aki *et al.*, 1974; Helmberger and Hadley, 1981; Stump and Johnson, 1984; and Johnson, 1988), although most were obtained from surface wave studies. Stevens (1986) calculated spectral moments from Rayleigh wave spectra for large NTS explosions. Given and Mellman (1986) performed moment tensor inversions of large NTS blasts, too, using the path structures developed by Stevens (1986). They used Rayleigh wave and Love wave spectra to solve for the isotropic source as well as a double couple source associated with tectonic release. The data sets for these last two studies over-

Table 4.1: Earthquakes with Moments Determined Using Regional Broadband Data.

Table 1: Earthquakes with Moments Determined Using Broadband Data

Date	M_L	$\log(M_0)$	Event	Date	M_L	$\log(M_0)$	Event
88/06/10	5.4	17.11 [a]	Gorman	92/03/03	3.4	14.49 [a]	Walker Pass
88/06/26	4.6	15.78 [d]	Chino	92/03/04	4.2	15.14 [a]	San Clemente
88/06/27	5.5	16.77 [c]	San Juan Botista	92/03/05	3.8	14.59 [a]	Bakersfield
88/07/06	3.7	14.88 [d]	Chino A.S.	92/04/10	3.4	14.60 [a]	Borrego
88/12/03	4.9	16.38 [b]	Pasadena M.S.	92/04/15	3.4	14.00 [a]	Lytle Creek
11:49:	2.1	12.41 [b]	Pasadena A.S. 1	92/04/23	4.6	15.49 [a]	Joshua Tree F.S.
12:08:	2.0	13.02 [b]	Pasadena A.S. 3	92/04/23	6.1	18.29 [a]	Joshua Tree M.S.
12:13:	2.4	13.02 [b]	Pasadena A.S. 4	13:58:	4.1	15.01 [a]	" " A.S. 1
12:15:	1.6	12.40 [b]	Pasadena A.S. 5	22:55:	3.8	14.54 [a]	" " A.S. 2
13:36:	1.8	12.09 [b]	Pasadena A.S. 6	23:52:	3.8	14.54 [a]	" " A.S. 3
14:46:	1.9	11.88 [b]	Pasadena A.S. 7	92/04/24	3.5	14.37 [a]	" " A.S. 4
88/12/04	2.0	12.24 [b]	Pasadena A.S. 8	18:06:	3.7	14.52 [a]	" " A.S. 5
88/12/08	2.2	12.64 [b]	Pasadena A.S. 9	18:20:	3.7	14.61 [a]	" " A.S. 6
89/01/19	5.0	16.51 [a]	Malibu	92/04/25	3.7	14.73 [a]	" " A.S. 7
89/02/18	4.3	15.34 [e]	Upland	18:56:	4.4	15.05 [a]	" " A.S. 8
89/08/08	5.3	16.41 [c]	Los Gatos	92/04/26	3.7	14.27 [a]	" " A.S. 9
89/10/18	7.0	19.48 [c]	Loma Prieta	6:26:	4.2	15.69 [a]	" " A.S. 10
90/02/28	3.7	14.65 [e]	Upland F.S.	17:21:	4.3	15.39 [a]	" " A.S. 11
90/02/28	5.2	17.40 [e]	Upland M.S.	92/04/27	4.2	15.41 [a]	" " A.S. 12
90/03/01	4.7	15.70 [e]	Upland A.S.	92/04/28	3.7	14.90 [a]	" " A.S. 13
90/03/02	4.6	15.60 [e]	Upland A.S.	11:33:	3.8	15.12 [a]	" " A.S. 14
90/04/17	4.6	15.78 [e]	Upland A.S.	92/04/30	3.7	14.70 [a]	" " A.S. 15
90/10/24	5.0	16.70 [g]	Lee Vining	92/05/01	3.8	14.71 [a]	" " A.S. 16
90/12/17	3.7	14.38 [a]	Big Bear I	92/05/02	4.1	14.64 [a]	" " A.S. 17
90/12/18	3.7	15.04 [a]	White Wolf Fault	19:10:	3.4	14.35 [a]	" " A.S. 18
91/05/20	3.7	14.48 [a]	San Jacinto I	92/05/04	4.0	15.04 [a]	" " A.S. 19
91/05/20	3.7	14.20 [a]	San Jacinto II	16:19:	4.8	16.19 [a]	" " A.S. 20
91/06/28	5.4	17.41 [f]	Sierra Madre	92/05/06	4.5	15.87 [a]	" " A.S. 21
15:37:	3.9	14.61 [f]	Sierra Madre A.S.	92/05/12	4.4	15.60 [a]	" " A.S. 22
17:00:	4.3	15.60 [f]	Sierra Madre A.S.	92/05/18	3.5	14.39 [a]	" " A.S. 23
91/06/29	4.0	14.60 [a]	Mojave	15:44:	4.9	16.10 [a]	" " A.S. 24
91/07/06	3.8	14.59 [f]	Sierra Madre A.S.	92/06/11	4.3	15.29 [a]	" " A.S. 25
91/10/12	4.0	15.04 [a]	Blue Cut	92/05/31	3.2	13.78 [a]	Lenwood Flat I
91/10/27	3.4	14.26 [a]	San Jacinto	92/05/31	3.5	14.28 [a]	Lenwood Flat II
91/12/03	5.4	16.72 [g]	San Miguel	92/06/28	3.7	14.29 [a]	Landers A.S.
91/12/04	4.2	14.95 [a]	Julian	92/06/29	5.4	16.85 [a]	Landers A.S.
91/12/04	4.0	14.62 [a]	Big Bear II	14:41:	4.4	16.90 [a]	Landers A.S.
92/02/17	3.5	14.66 [a]	Coso	16:01:	5.2	17.16 [a]	Landers A.S.
92/02/19	4.0	14.85 [a]	Coso I	92/06/29	5.6	17.40 [c]	Little Skull Mtn
92/02/19	3.7	14.41 [a]	Coso II	92/06/29	3.7	14.66 [a]	La Canada

[a] Thio and Kanamori, 1992; [b] Ma and Kanamori, 1991; [c] Zhao and Helmberger, 1993;
[d], [e], [f], [g] Dreger and Helmberger, 1990, 1991a, 1991b, 1992;

Table 4.2: Explosions in this study.

Table 2: Explosions in This Study

Date	M_L	$\log(M_0)$	Event	Date	M_L	$\log(M_0)$	Event
57/09/19	4.25	14.30 [a]	Rainier	70/03/19	4.05	13.65 [g]	Jal
61/12/03	3.91	13.86 [a]	Fisher	70/03/23	5.29	15.73 [g]	Shaper
62/06/27	4.63	14.55 [g]	Haymaker	70/03/26	6.17	17.72 [c]	Handley
65/02/16	4.21	13.98 [g]	Merlin	70/05/01	4.18	14.35	Beeblam
65/03/03	5.04	15.41 [g]	Wagtail	70/05/05	4.82	14.70 [g]	Mintleaf
65/04/14	4.23	14.02 [g]	Palanquin	70/05/15	5.00	15.19 [g]	Cornice
65/05/12	3.91	13.84 [g]	Buteo	70/05/21	3.60	13.23 [g]	Manzanas
66/04/25	4.69	14.90 [g]	Pinstripe	70/05/21	5.00	14.98 [g]	Morrones
66/04/14	5.02	15.39 [g]	Duryea	70/05/26	4.63	14.60 [g]	Hudsonmoon
66/05/05	4.04	14.24 [g]	Cyclamen	70/05/26	5.20	15.56 [g]	Flask
66/05/13	5.01	15.75 [g]	Piranha	71/06/19	4.20	13.83 [g]	Embudo
66/06/02	4.98	15.73 [g]	Piledriver	71/06/23	4.50	14.45 [g]	Laguna
66/06/25	4.33	14.13 [g]	Vulcan	71/06/29	4.90	14.64 [g]	Harebell
66/06/30	5.90	16.49 [g]	Halfbeak	71/10/29	4.10	14.03 [g]	Pedernal
66/12/20	6.07	16.98 [g]	Greeley	71/10/08	4.10	14.02 [g]	Cathay
67/02/08	4.09	13.82 [g]	Ward	72/04/19	4.20	13.73 [g]	Longchamps
67/02/23	3.89	13.81 [g]	Persimmon	72/05/19	4.48	14.66 [g]	Monero
67/04/07	3.97	13.76	Fawn	72/10/03	4.40	13.93 [g]	Delphinium
67/04/21	3.83	13.51	Effendi	73/06/06	5.68	16.78 [e]	Almendro
67/04/21	3.89	13.72	Chocolate	75/05/14	5.86	16.50 [e]	Tybo
67/05/23	5.57	16.46 [e]	Scotch	75/06/19	5.74	16.58 [e]	Mast
67/06/26	4.54	14.42 [g]	Midimist	75/06/26	5.95	16.96 [g]	Camembert
67/08/31	4.73	14.46 [g]	Doormist	75/10/24	4.86	14.80 [g]	Huskypup
67/09/21	3.87	13.51 [g]	Marvel	75/10/28	6.08	17.03 [g]	Kasseri
67/09/27	5.66	16.32 [e]	Zaza	76/02/12	6.12	17.00 [g]	Fontina
68/01/19	5.74	16.83 [g]	Faultless	76/02/26	5.86	16.79 [e]	Cheshire
68/03/12	3.96	14.28 [g]	Buggy	76/03/09	5.83	16.79 [e]	Estuary
68/04/26	6.09	17.24 [g]	Boxcar	76/03/17	5.77	16.52 [e]	Pool
68/09/24	5.06	14.85 [g]	Hudsonseal	77/04/05	5.20	16.01 [e]	Marsilly
68/11/04	4.46	14.57 [g]	Crew	77/04/27	4.90	15.62 [g]	Bulkhead
68/12/19	6.14	17.35 [g]	Benham	77/05/25	5.00	15.52 [g]	Crewline
69/02/12	4.81	14.63 [g]	Cypress	77/11/09	5.40	16.27 [e]	Sandreef
69/05/07	5.68	16.42 [e]	Purse	77/12/14	5.30	16.22 [e]	Farallones
69/09/16	6.19	16.82 [b]	Jorum	78/03/23	5.30	16.02 [d]	Iceberg
69/10/08	5.50	16.19 [c]	Pipkin	78/04/11	5.10	15.89 [d]	Backbeach
69/10/29	4.40	13.55 [g]	Cruet	78/07/12	5.20	15.75 [g]	Lowball
69/10/29	4.60	13.97 [g]	Pod	78/08/31	5.30	15.92 [d]	Panir
69/10/29	5.50	15.79 [g]	Calabash	78/09/13	4.40	14.55 [g]	Diablohawk
70/02/11	4.67	14.77 [g]	Diamamist	78/09/27	5.30	16.15 [d]	Rummy
70/02/25	4.60	14.89 [g]	Cumarin	78/11/02	4.23	14.36	Emmenthal
70/02/26	4.80	14.65 [g]	Yannigan	78/11/18	5.00	15.30 [g]	Quargel
70/03/06	4.20	13.57 [g]	Cyathus	78/12/16	5.20	16.40 [c]	Farm
70/03/06	4.10	13.09 [g]	Arabis	79/02/08	5.20	15.80 [g]	Quinella

Table 2 (cont.): Explosions in This Study

Date	M_L	$\log(M_0)$	Event	Date	M_L	$\log(M_0)$	Event
79/06/11	5.30	16.13 [d]	Pepato	84/03/31	4.20	13.71 [g]	Agrini
79/06/20	3.92	13.91	Chess	84/05/01	5.10	15.76 [g]	Mundo
79/09/06	5.30	16.16 [d]	Hearts	84/05/31	5.30	15.89 [g]	Caprock
79/09/26	5.20	15.98 [d]	Sheepshead	84/06/20	4.40	14.48 [g]	Duoro
79/11/29	3.89	13.66	Backgammon	84/07/25	5.30	15.42 [g]	Kappeli
80/03/08	3.89	13.43	Norbo	84/08/02	4.30	14.28 [g]	Correo
80/04/26	5.10	15.91 [e]	Colwick	84/08/30	4.50	14.52 [g]	Dolcetto
80/04/30	5.10	15.61 [g]	Pyramid	84/09/13	4.80	15.01 [g]	Breton
80/07/25	5.10	16.10 [d]	Tafi	84/11/10	4.30	14.21 [g]	Villita
80/10/31	4.50	14.77 [g]	Minersiron	84/12/09	5.10	15.63 [g]	Egmont
81/01/15	5.20	15.79 [g]	Baseball	84/12/15	5.00	15.63 [g]	Tierra
81/06/06	5.40	15.87 [f]	Harzer	85/03/15	4.60	14.77 [g]	Vaughn
81/11/12	5.00	15.61 [g]	Rousanne	85/03/23	5.00	15.31 [g]	Cottage
82/01/28	5.30	16.08 [g]	Jornada	85/04/02	5.40	16.12 [g]	Hermosa
82/02/12	5.00	15.95 [g]	Molbo	85/04/06	4.50	14.86 [g]	Misty-rain
82/02/12	5.00	15.90 [g]	Hosta	85/06/12	5.10	15.85 [g]	Salut
82/04/17	4.40	14.35 [g]	Tenaja	85/07/25	5.20	15.73 [g]	Serena
82/04/25	5.00	15.79 [g]	Gibne	85/12/05	5.20	15.56 [g]	Kinibito
82/05/07	5.20	15.76 [g]	Bouschet	85/12/28	5.00	15.57 [g]	Goldstone
82/06/24	5.20	15.96 [g]	Nebbiolo	86/03/22	5.10	15.46 [g]	Glencoe
82/07/29	4.10	14.45 [g]	Monterey	86/04/10	4.50	14.78 [g]	Mightyoak
82/08/05	5.40	16.16 [g]	Atrisco	86/04/22	5.00	15.71 [g]	Jefferson
82/09/02	3.50	13.23 [g]	Cerro	86/05/21	4.00	13.96 [g]	Panamint
82/09/23	4.60	14.82 [g]	Huronlanding	86/06/05	5.30	15.58 [g]	Tajo
82/09/23	4.60	14.88 [g]	Frisco	86/06/25	5.30	15.61 [g]	Darwin
82/09/29	3.80	13.98 [g]	Borrego	86/07/17	5.20	15.08 [g]	Cybar
82/11/12	4.10	13.92 [g]	Seyval	86/07/24	4.70	14.40 [g]	Cornucopia
82/12/10	4.40	14.56 [g]	Manteca	86/09/30	5.40	15.72 [g]	Labquark
83/03/26	4.90	15.44 [g]	Cabra	86/10/16	5.30	15.77 [g]	Belmont
83/04/14	5.20	15.59 [g]	Torquoise	87/04/18	5.30	15.77 [g]	Delamar
83/05/26	4.30	14.26 [g]	Fahada	87/04/30	5.30	15.88 [g]	Hardin
83/06/09	4.30	14.29 [g]	Danablu	87/06/18	4.00	13.90	Brie
83/09/01	5.30	15.77 [f]	Chancellor	87/10/23	5.40	15.31 [g]	Borate
83/09/22	4.00	13.90 [g]	Techado	88/04/07	3.60	12.75	Abliene
83/12/16	4.80	15.22 [g]	Romano	90/06/21	4.30	13.91	Austin
83/05/05	4.20	14.26 [g]	Crowdie	91/08/15	4.00	14.10	Floydada
84/02/15	4.50	14.78 [g]	Milagro	92/09/18	4.00	14.02	Hunters-trophy
84/03/01	5.30	15.85 [g]	Tortugas	92/09/23	4.41	14.27	Divider

[a] Aki *et al*, 1974; [b] Helmberger and Hadley, 1981; [c] Stump and Johnson, 1984; [d] Given and Mellman, 1986; [e] Stevens, 1986a; [f] Johnson, 1988; [g] Woods and Harkrider, 1993

lap substantially. The moment values were found to be similar, so that for events for which two moments were available, the Stevens' (1986) moment was used.

Time domain surface wave moments of explosions were also included in this study. In chapter 2 time-domain were determined from the peak to peak amplitude (PPA) of the dominant Airy phase of the Rayleigh wave for NTS explosions. With the technique, moment is determined from the ratio of the observed PPA to that of a synthetic seismogram with a given input moment. The correlation between moments obtained by this time domain moment method and a more standard spectral scheme performed on a 108 event subset (see chapter 3) of this study is very good (see chapter 2), implying that this time domain moment method yields accurate, robust moment measurements. Using this method we obtained moments for other small NTS events.

Figure 4.3a displays M_L vs. log Moment (N-m) plotted for 299 earthquakes and 178 explosions. Solid symbols represent earthquakes, while open symbols and crosses represent NTS explosions. Moments determined from near-field body wave studies are plotted as circles. Earthquake moments determined from surface wave studies and body wave studies are represented by triangles and diamonds, respectively. Explosion moments determined from surface source studies are denoted by stars (Given and Mellman, 1986), squares (Stevens, 1986) and crosses (chapter 2 of this study). This figure shows how well this discriminant works. There is a significant separation of earthquakes and explosions, with no real overlap of the two populations. This discriminant also works at all scales, with explosions and earthquakes following their respective scaling laws over a wide range of magnitudes and moments; for earthquakes this is true over seven and a half orders of magnitude. It should be noted that the earthquakes with a $\log(M_0)$ below 13.0 were determined from local stations (D $<$ 75 km) and would not be detectable at regional distances. They are included here only to show the continuity of the linear scaling relationship between M_L and $\log(M_0)$ for earthquakes.

Figure 4.3: **(a)** M_L vs. log M_0 for 299 earthquakes (solid symbols) and 178 explosions (open symbols and crosses). Circles are moments from near-field source studies. Triangles are surface wave moments and diamonds are body wave moments. Explosion moments determined from surface waves are shown as stars (Given and Mellman, 1985), squares (Stevens, 1986a) and crosses (chapter 2 of this study). **(b)** Blow-up of that part of the plot which contains explosions.

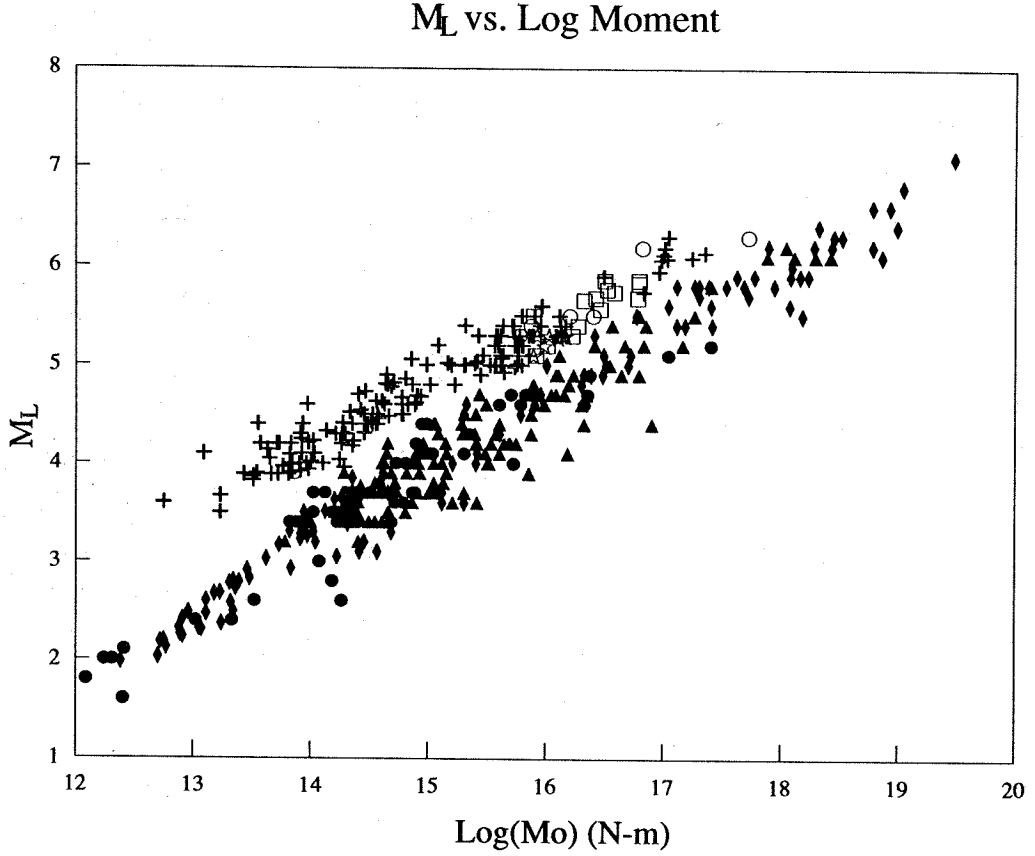

Explanation

- Eq: Near-field studies
- Eq: Surface wave studies
- Eq: Body wave studies
- Ex: Given-Mellman
- Ex: Stevens
- Ex: Woods-Harkrider
- Ex: Near-field studies

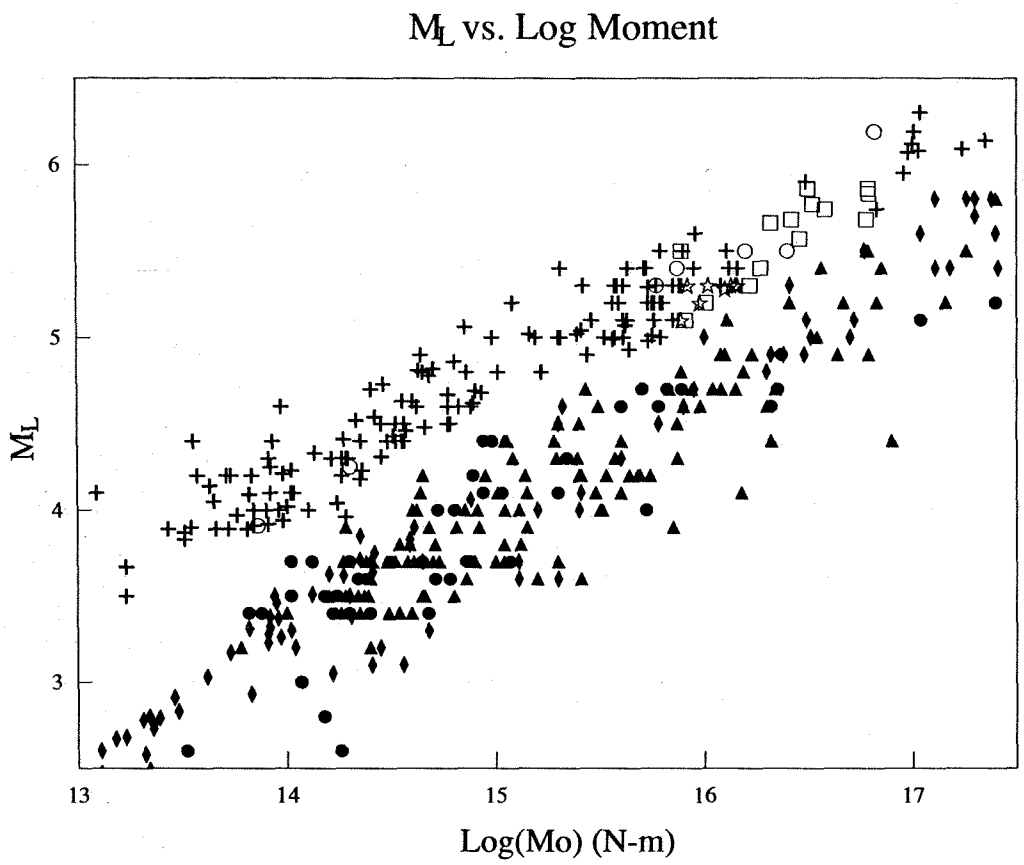

Explanation

- ● Eq: Near-field studies
- ▲ Eq: Surface wave studies
- ♦ Eq: Body wave studies
- ☆ Ex: Given-Mellman
- □ Ex: Stevens
- \+ Ex: Woods-Harkrider
- ○ Ex: Near-field studies

Figure 4.3b is a blow-up of the portion of figure 4.3a containing explosion data. It is important to note when examining these two plots that the data are taken from a number of sources. M_L's were determined from different networks and the moments were calculated in a variety of ways. Yet a distinct separation of the two populations is still obtained. There is one anomalous explosion, Buggy (M_L = 3.96, log(M_0)=14.28), which lies very close to the earthquake population. This was a Plow Shares event in which four nuclear charges with an announced combined yield of 5.4 kt were detonated. We would expect that a multiple-source event like this one would display characteristics similar to a distributed earthquake source, *i.e.*, it should be enriched in long-period energy relative to a point source explosion of the same yield.

4.4 Discussion and Conclusions

The M_L:M_0 criterion appears to be a robust method to discriminate regional seismic events. For a given moment, the M_L of an explosion is more than 0.5 units larger than that of an earthquake. This difference can be attributed to M_L being a short-period (1 Hz) energy measurement, whereas the moment is determined from long-period body wave phases (period > 4 seconds) and Rayleigh waves (10 to 40 seconds).

There are several explanations for the observed difference in short-period:long-period spectral character between earthquakes and explosions. Earthquakes tend to be asperity-driven distributed sources, as opposed to explosions which can more aptly be modeled as point-sources with impulsive time functions. Dreger and Helmberger (1991a) showed that broadband seismograms from small local earthquakes ($4.0 < M_L < 5.0$) can be modeled as distributed finite sources rather than as point-sources. Such distributed slip time functions will generally result in reduced high-frequency spectra relative to a point-source step moment. It is possible that even very small earthquakes (M_L <4) behave similarly. Another possible reason that this

discriminant works at low magnitudes is that for small events the quantities being measured are the P-wave low frequency spectrum (M_L) and the S-wave low frequency spectrum (M_0), in which case, for explosions, the S-wave energy is predominantly generated by secondary P to S converted phases. If this is so, the moment should not be determined solely from P-wave information.

Spall effects may also be a cause of observed high-frequency (0.15 Hz $< f <$ 2.0 Hz) enrichment of explosion source spectra. Theoretical results (Day and McLaughlin, 1991) and various observational studies (Viecelli, 1973; Stump, 1985; Taylor and Randall, 1989; and Patton, 1990) conclude that spallation can be a significant contributor to short period energy, while Patton (1988) and Day *et al.* (1983) find no appreciable spall energy at periods greater than eight seconds. Spall energy would tend to increase M_L measurements.

This discriminant is only limited by the detection threshold capability of long-period data, as the two populations do not converge at small magnitudes. This observation implies that the convergence in the M_S:m_b ratio for small magnitude events seen in some previous studies is due to approaching the effective signal to noise level for measuring surface amplitudes. Previous studies relied on data recorded on lower grade (usually analog) instruments that did not have the recording capabilities of modern, high dynamic range, digital seismometer systems. Modern data combined with digital processing techniques increases the resolution of long-period transient signals. Figure 4.4 shows the Yucca Flat blast Floydada recorded at four TERRAscope stations (epicentral distances being between 200 and 400 km), played-out with PE and WA instruments. The amplitudes indicate that these signals would not be discernible on the actual analog instruments. M_L for this event is 4.0 and its log moment is 14.20. Assuming it is a shallow explosion above the water table, the yield can be inferred to be less than 10 kt from the moment-yield scaling relationships determined for NTS in chapter 2. Were it detonated in hard rock below the water

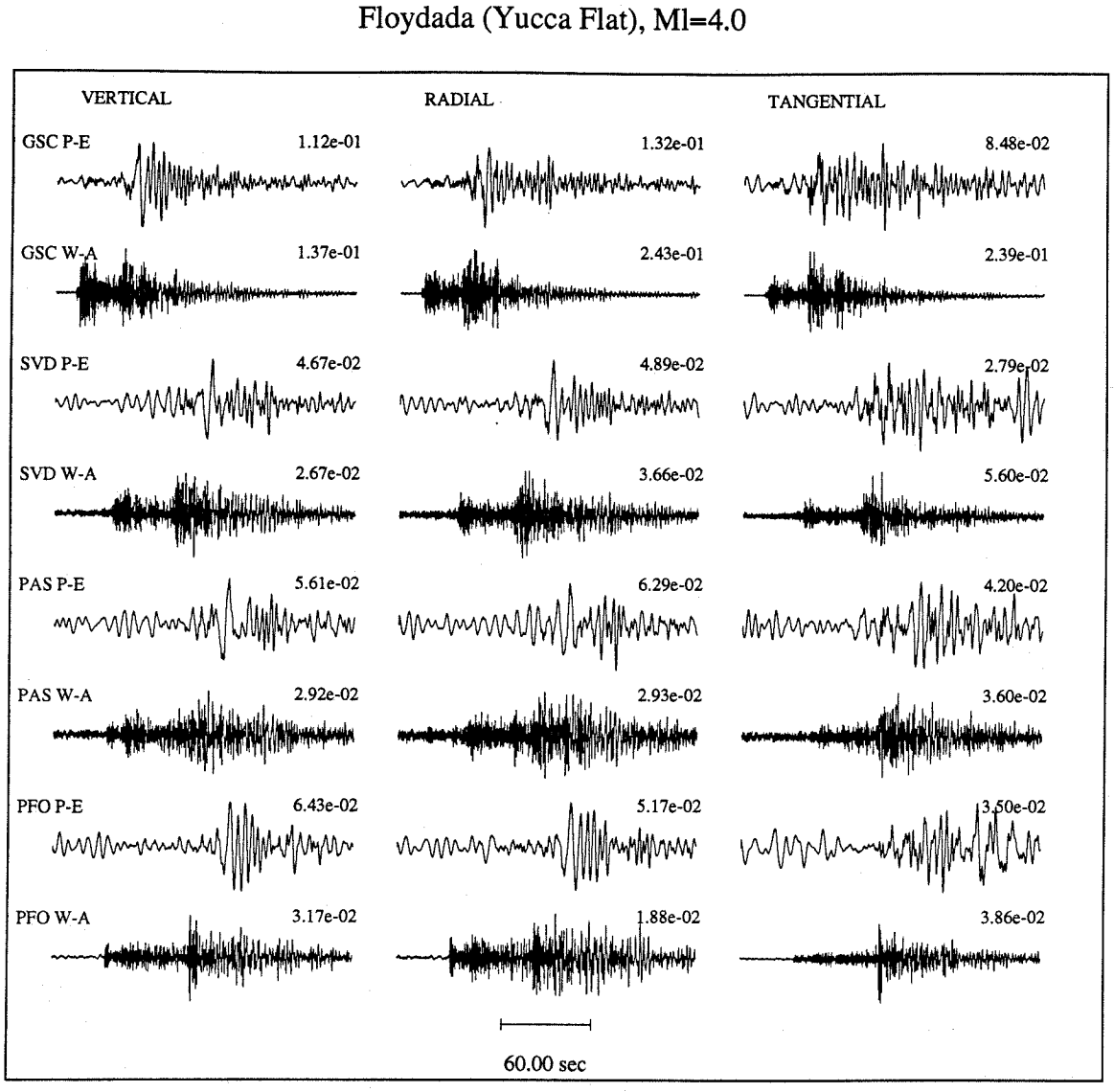

Figure 4.4: A small Yucca Flat explosion, Floydada (Y < 10 kt, $m_b = 4.2$, $M_L = 4.0$), recorded at TERRAscope stations and played-out on Press-Ewing (long-period) and Wood-Anderson (short-period) instruments.

table, it would correspond to a two kiloton explosion. We estimate that were this event 2.5 times lower in yield, it would still be possible to obtain its moment, yielding a magnitude threshold of $M_L > 3.6$ for explosions.

Low SNR seismograms also may be phase match filtered (Herrin and Goforth, 1977; and Stevens, 1986a) in order to retrieve the signal of very small events for spectral amplitude estimates. However, there is some debate on the accuracy of using this method, see Der (1986) and Stevens (1986b) for a discussion of this problem. Employing one or another means of time domain measurements in order to obtain the seismic moment avoids such problems.

Simple time domain moment measurements included in this study are straightforward and can be directly applied to historical analog data sets in order to establish earthquake M_L:M_0 curves for other regions. Since only peak amplitude measurements are necessary for such methods, the required signal to noise ratio (SNR) effectively decreases, too. Time domain peak amplitude measurements are also less susceptible to noise contamination than are spectral amplitude measurements. The other parameter M_L is a simple time-domain measurement which can be made on the smallest detectable seismic sources. Modern source inversion techniques that make use of regional body wave phases (such as P_{nl} and S_{nl}) recorded at sparse regional networks also make for powerful moment determination tools as shown in studies using the TERRAscope broadband network (Dreger and Helmberger, 1992; and Zhao and Helmberger, 1993).

A disadvantage to determining moment tensor solutions is that many methods require Green's functions in order to obtain accurate moments. However, with modern broadband, high dynamic range instrumentation, it is quite feasible to use moderate-sized to small events to determine regional path structures. Zhao and Helmberger (1991) detail the forward modeling of P_{nl}, S_{nl} and Rayleigh wave regional phases along a continental shield path. Dreger and Helmberger (1990) were able to for-

ward model velocity structure using waveform data from small (m_b = 3.7 - 4.0) local events. Shallow crustal structure can also be inferred from the inversion of surface wave dispersion data generated by small, regional seismic sources (Saikia *et al.*, 1990) as well as in conjunction with teleseismic surface waves (Thio and Kanamori, 1991). These path structures needn't be overly complicated or detailed. Dreger and Helmberger (1991b, 1992) found that they could model broadband regional body wave phases from events located throughout Southern California and recorded at various TERRAscope stations with one relatively simple crustal model (with an underlying mantle half-space). Using their regional Green's functions in conjunction with a time-domain source inversion method yielded source parameter solutions consistent with other studies. Zhao and Helmberger (1993) extended this technique to include surface waves and found that this inversion scheme worked well with simple regional earth models as well.

An important point to address concerns the *a priori* source type assumptions made in determining the seismic moments. All earthquake moments were determined assuming either a double couple source (for moment tensor and Green's function inversion methods) or a circular fault model (for corner frequency moment estimates). Most of the NTS explosion moments were determined by modeling the Rayleigh waves as being generated by a shallow, isotropic source excitation function in the absence of an azimuthally dependent radiation pattern. The Given and Mellman (1986) moments, however, were determined by inverting Rayleigh and Love wave spectra to obtain the isotropic and double couple components of the moment tensor solution. An obvious problem with classifying events with respect to their M_L:M_0 ratio is that for an unidentified seismic event, one doesn't know which source model to assume in order to estimate the moment. This point leads to the question, how distinguishable would the two populations be, had they all been treated as double couple sources for moment estimation purposes? For a given seismic moment, the

average radiation pattern amplitude (assuming absolute values) for Rayleigh waves generated by a predominantly strike-slip fault motion ($sin2\theta$ radiation pattern) is only slightly larger (by 10 percent) than that of an explosion. In this case one could still infer the source type from the moment estimate. For such strike-slip earthquakes, observations from all azimuthal quadrants (the four lobes of the $sin2\theta$ radiation pattern) will result in better constrained moment determinations.

The difficulty occurs in modeling the Rayleigh waves assuming a shallow source with a dip-slip orientation for which there is a singularity in the Green's function solutions. In this special case we would obtain a larger moment and the event's M_L - M_0 ratio would decrease towards the earthquake population. However, one can generally model and invert for earthquake sources that occur deeper than 3 km. When an event does not fit our regional Green's functions to some specified degree, we would assume it is shallow and model it as a vertical strike-slip earthquake. Thus, explosions would still discriminate as displayed above and shallow strike-slip earthquakes would still lie within in the earthquake population. M_0 for a shallow dip-slip earthquake, however, may be underestimated and could potentially fall within the explosion population. In a monitoring environment we would have a problematic event, to which other discrimination criterion would need to be applied in order to identify it correctly.

Applying the M_L:M_0 ratio in conjunction with other discriminants would yield a more effective source identification scheme. Phase information (*i.e.*, Rayleigh wave polarity) and Love wave data would be helpful in such cases, since reversed polarity Rayleigh waves and/or large Love wave amplitudes are diagnostic of a double couple source. A depth discriminant, based on the complexity and amplitude of the Rayleigh wave tail (coda), for example, would be useful for depth constraints to be placed on the moment tensor inversion of a source. In a related study Woods *et al.* (1992) found that the ratio of short-period energy in the vertical component *Pnl* wave train

to that in the long-period surface wave train (summed over all three components) of regional seismograms also separates source populations, although it, too, suffers similar magnitude threshold limitations.

For very small events information from high-frequency (f > 1 Hz) phases may be needed to compliment the M_L:M_0 discriminant. Comparisons of L_g spectral amplitude levels for different bandwidths (in the 0.5 to 8 HZ range) have been shown to effectively discriminate events with magnitudes down to $m_{b(Pn)} = 3.3$ (Murphy and Bennett, 1982; Taylor *et al.*, 1988). Although the M_L:M_0 discrimination threshold is slightly higher than this, the regional body wave phases and Rayleigh waves used in this method are not as susceptible to path "blockage" effects as is the L_g phase. Also, using relatively close-in stations for surface wave measurements, as it is possible to do with this method, path attenuation effects are minimized. The M_L:M_0 ratio discriminant would work well as a companion test, or check, for other high-frequency discrimination methods, particularly for events in the $3.5 < m_b < 4.5$ range for which teleseismic methods no longer work.

Because both source parameters used in this discrimination method can be obtained from a sparse broadband network, this discriminant can be applied throughout the world as more broadband stations similar to those of the IRIS network come on line. For an active tectonic region, the threshold for this discriminant is $M_L = 3.1$ for earthquakes and $M_L = 3.6$ for explosions for epicentral distances up to 600 km.

Bibliography

Aki, K., 1967. Scaling Law of Seismic Spectrum, *J. Geophys. Res.*, **72**, 1217-1231.

Aki, K., and Tsai, Y.-B., 1972. Mechanism of Love-Wave Excitation by Explosive Sources, *J. Geophys. Res.*, **77**, 1452-1475.

Aki, K., Bouchon, M., and Reasenberg, P., 1974. Sesimic Source Function for an Undrground Nuclear Explosion, *Bull. Seism. Soc. Am.*, **64**, 131-148.

Alewine, R. W., 1972. Theorectical and observed distance corrections for Rayleigh-wave magnitude, *Bull. Seism. Soc. Am.*, **62**, 6133-6142.

Archambeau, C. and Sammis, C., 1970. Seismic Radiation from Explosions in Pre-stressed Media and the Measuremnt of Tectonic Stress in the Earth, *Rev. Geophs. and Space Phys.*, **8**, 473-499.

Babich, V. M., Chikhachev, B. A. and Yanovskaya, T. B., 1976. Surface waves in a vertically inhomogeneous halfspace with a weak lateral inhomogeneity. *Izv. AN SSSR, Fizika Zemli*, **4**, 24-31.

Bache, T. C., Rodi, W. L., and Harkrider, D. G., 1978. Crustal structures inferred from Rayleigh-wave signatures of NTS explosions, *Bull. Seism. Soc. Am.*, **68**, 1399-1413.

Bache, T. C., Day, S. M., and Swanger, H. J., 1982. Rayleigh wave synthetic seismograms from multidimensional simulations of underground explosions. *Bull. Seism. Soc. Am.*, **72**, 15-28.

Bache, T. C., 1982. Estimating the yield of underground nuclear explosions, *Bull. Seism. Soc. Am.*, **72**, s131-s168.

Basham, P.W., 1969. Canadian magnitudes of earthquakes and nuclear explosions in South-Western North America, *Geophys. J. R. astr. Soc.*, **17**, 1-13.

Basham, P.W., 1971. A New Magnitude Formula for Short Period Continental Rayleigh Waves, *Geophys. J. R. astr. Soc.*, **23**, 255-260.

Basham, P. W. and Horner, R. B., 1973. Seismic magnitudes of underground nuclear explsoions, *Bull. Seism. Soc. Am.*, **63**, 105-131.

Båth, M., 1967. Recommendations of the IASPEI committee on magnitudes, *Seismological Bull.*, May, Seismological Institute, Uppsala.

Bent, A. L. and Helmberger, D. V., 1991. A Re-examination of Historic Earthquakes in the San Jacinto Fault Zone, California. *Bull. Seism. Soc. Am.*, **81**, 2289-2309.

Bolt, B. A., 1976. Nuclear Explosions and Earthquakes: The parted Veil, W. H. Freeman, San Francisco.

Brune, J. N. and Pomeroy, P. W., 1963. Surface Wave Radiation Patterns for Underground Nuclear Explosion and Small-Magnitude Earthquakes, *J. Geophys. Res.*, **68**, 5005-5028.

Brune, J. N., 1970. Tectonic Stress and the Spectra of Seismic Shear Waves from Earthquakes, *J. Geophys. Res.*, **75**, 4997-5009.

Burridge, R. and Weinberg, H., 1977. Horizontal rays and vertical modes, *Wave Propagation and underwater acoustics*, Springer-Verlag, Berlin, Heidelberg, New York.

Cohn, S. N., Hong T.-L., and Helmberger, D. V., 1982. The Oroville Earthquakes: A Study of Source Characteristics and Site Effects, *J. Geophys. Res.*, **87**, 4585-4594.

Dahlman, O. and Israelson, H., 1977. Monitoring Underground Explosions, Elsevier, Amsterdam.

Day S. M., and McLaughlin, K. L., 1991. Seismic Source Representation for Spall, *Bull. Seism. Soc. Am.*, **81**, 191-201.

Day S. M., Rimer, N., and Cherry, J. T., 1983. Surface Waves from Underground Explosions with Spall: Analysis of Elastic and Nonlinear Source Models, *Bull. Seism. Soc. Am.*, **73**, 247-264.

Der, Z. A., 1986. Comments on the Paper "Estimation of Scalar Moments from Explosion-Generated Surface Waves" by J. L. Stevens., *Bull. Seism. Soc. Am.*, **76**, 1822-1824.

Dobrin, M. B., 1976. *Introduction to Geophysical Prospecting*, McGraw-Hill, New York.

Doser, D. I. and Smith, R. B., 1989. An Assessment of Source Parameters of Earthquakes in the Cordillera of the Western United States, *Bull. Seism. Soc. Am.*, **79**, 1389-1409.

Doser, D. I., 1990. A Re-examination of the 1947 Manix, California, Earthquake Sequence and Comparison to Other Sequences of the Mojave Block, *Bull. Seism. Soc. Am.*, **80**, 267-277.

Douglas, A., 1966. Redetermination of earthquake body-wave magnitudes using ISC Bulletin data, United Kingdom Atomic Energy Authority, *AWRE Rept. No. O54-66.*, H.M.S.O. London.

Dreger, D. S. and Helmberger, D. V., 1990. Broadband Modeling of Local Earthquakes, *Bull. Seism. Soc. Am.*, **80**, 1162-1179.

Dreger, D. S. and Helmberger, D. V., 1991a. Complex Faulting Deduced from Broadband Modeling of the February 28, 1990 Upland Earthquake (M_L =5.2), *Bull. Seism. Soc. Am.*, **81**, 1129-1144.

Dreger, D. S. and Helmberger, D. V., 1991b. Source Parameters of the Sierra Madre Earthquake from Regional and Local Body Waves, *Geophys. Res. Lett.*, **18**, 2015-2018.

Dreger, D. S. and Helmberger, D. V., 1992. Determination of Source Parameters at Regional Distances with Three-Component Sparse Network Data, *J. Geophys. Res.* (in press).

Dziewonski, A. M., Bloch, S., and Landisman, M., 1969. A New technique for the analysis of transcient seismic signals, *Bull. Seism. Soc. Am.*, **59**, 427-444.

Dziewonksi, A. M., Chouw, T.-A., and Woodhouse, J. H., 1981. Determination of Earthquake Soure Parameters from Waveform Data for Studies of Global and Regional Seismicity, *J. Geophys. Res.*, **86**, 2825-2852.

Ekström, G. and Richards, P. G., 1993. Empirical Measurements of Tectonic Moment Release in Nuclear Explosions from Teleseismic Surface Waves and Body Waves, submitted to *Geophys. J. Int.*.

Evernden, J. F., 1971. Variation of Rayleigh-wave amplitude with distance, *Bull. Seism. Soc. Am.*, **67**, 405-411.

Evernden, J. F., Best, W. J., Pomeroy, P. W., McEvilly, T. V., Savino, J. M., and Sykes, L. R., 1971. Discrimination between Small-Magnitude Earthquakes and Explosions, *J. Geophys. Res.*, **76**, 8042-8055.

Evernden, J. F. and Filson, J., 1971. Regional depedence of surface-waves versus body-wave magnitudes, *J. Geophys. Res.*, **76**, 3303-3308.

Fletcher, J., Boatwright, J., Haar, L., Hanks, T., and McGarr, A., 1984. Source Parameters for Aftershocks of the Oroville, California Earthquake, *Bull. Seism. Soc. Am.*, **74**, 1101-1123.

Frankel, A., 1984. Source Parameters of Two $M_L \sim 5$ Earthquakes Near Anza, California and a Comparison with an Imperial Valley Aftershock, *Bull. Seism. Soc. Am.*, **74**, 1509-1527.

Given, J. W. and Mellman, G. R., 1986. Estimating explosion and tectonic release source parameters of underground nuclear explosions from Rayleigh and Love wave observations, *DARPA Report AFGL-TR-86-0171*, Sierra Geohysics Inc., Kirkland, WA.

Glover, P. and Harkrider, D. G., 1986. Numerical tests of surface wave path corrections, *Science Applications International Corp. Rept. No. C86-05*, MDA903-84-C-0020, McLean, VA.

Gupta, I. N., Lynnes, C. S., Chan, W. W., and Wagner, R. A., 1989. A Comparison of the Spectral Characteristics of Nuclear Explosions Detonated Below and Above the Water Table, *Teledyne Geotech Rept. No, TGAL-89-04*, GL-TR-89-0151, Alexandria, VA.

Hadley, D. and Kanamori, H., 1977. Seismic Structure of the transverse Ranges, California, *Geo. Soc. Am. Bull.*, **88**, 1469-1478.

Hadley, D. and Kanamori, H., 1979. Regional S-wave Structure for Southern California from the Analysis of Teleseismic ayleigh Waves, *J. Geophys. Res.*, **58**, 655-666.

Hannon, W. J., 1985. Seismic Verification of a Comprehensive Test Ban, *Science*, **227**, 251-257.

Hansen, R. A., Ringdal, F., and Richards, P. G., 1990. The Stability of RMS L_g Measurements and Their Potential for Accurate Estimation of the Yields of Soviet Underground Nuclear Explosions, *Bull. Seism. Soc. Am.*, **80**, 2106-2126.

Harkrider, D. G., 1964. Surface waves in multilayered media I. Rayleigh and Love waves from buried sources in a multilayered elastic half-space, *Bull. Seism. Soc. Am.*, **54**, 627-679.

Harkrider, D. G. and Anderson, D. L., 1966. Surface wave energy from point sources in plane layered earth models. *J. Geophys. Res.*, **71**, 2967-2980.

Harkrider, D. G., 1970. Surface Waves in Multilayered Elastic Media. Part II. Higher Mode Spectra and Spectral Ratios from Point Sources in Plane Layered Earth Models. *Bull. Seism. Soc. Am.*, **60**, 1937-1987.

Harkrider, D. G., 1981. Coupling near source phenomena into surface wave generation, *Identification of Seismic Sources - Earthquake or Underground Explosion*, editors: Husebye and Mykkeltveit, D. Reidel, Dordrecht, Boston, London. 277-326.

Haskell, N. A., 1967. Analytic Approximation for the Elastic Radiation from a Contained Underground Explosion, *J. Geophys. Res.*, **72**, 2583-2586.

Helle, H. and Rygg, E., 1984. Determination of Tectonic Release from Surface Waves Generated by Nuclear Explosions in Eastern Kazakhstan, *Bull. Seism. Soc. Am.*, **74**, 1883-1898.

Helmberger, D. V. and Hadley, D. M., 1981. Seismic Source Functions and Attenuation from Local and Teleseismic Observations of the NTS Events JORUM and HANDLEY, *Bull. Seism. Soc. Am.*, **71**, 51-67.

Helmberger, D. V. and Johnson, L. R., 1977. Source Parameters of Moderate Size Earthquakes and the Importance of Receiver Crustal Structure in Observations of Local Earthquakes. *Bull. Seism. Soc. Am.*, **67**, 301-314.

Herrin, E. and Goforth, T., 1977. Phase Matched Filtering: Applications to the Study of Rayleigh Waves, *Bull. Seism. Soc. Am.*, **76**, 1259-1275.

Herrmann, R. B., 1988. Computer Programs in Seismology, *Proceedings of the 10th Annual DARPA/AFGL Seismic Research Symposium*, 126.

Johnson, L. R. and McEvilly, T. V., 1974. Near-field Observations and Source Parameters of Central California Earthquakes, *Bull. Seism. Soc. Am.*, **64**, 1855-1886.

Johnson, L. R., 1988. Source Characteristics of Two Underground Nuclear Explosions, *Geophys. J.*, **95**, 15-30.

Kafka, A. L., 1990. R_g as a Depth Discriminant for Earthquakes and Explosions: A Case Study in New England, *Bull. Seism. Soc. Am.*, **80**, 373-394.

Kanamori, H. and Given, J. W., 1981. Source Parameters Determined from Long Period Surface Waves, *Phys. Earth Planet. Inter.*, **11**, 312-332.

Kanamori, H., Mori, J., Hauksson, E., Heaton, T. H., Hutton, L. K., and Jones, L. M., 1992. Determination of Earthquake Energy Release and M_L Using TERRAscope, *Bull. Seism. Soc. Am.*, **83**, 330-346.

Lambert, D. G. and Alexander, S. S., 1971. Relationship of Body and Surface Wave Magnitudes for Small Earthquakes and Explosions, *Final AFTAC Report VELA T/2706*, Teledyne Geotech, Alexandria, VA.

Langston, C. A. and Helmberger, D. V., 1974. Interpretation of Body and Rayleigh Waves from NTS to Tucson, *Bull. Seism. Soc. Am.*, **64**, 1919-1929.

Lapin, L. L., 1983. *Probability and Statistics for Modern Engineering*, Brooks/Cole, Monterey, CA.

Larson, D. B., 1981. Explosive energy coupling in geologic materials, *Lawrence Livermore National Laboratory*, Report UCID-85662.

Lay, T., Wallace, T. C., and Helmberger, D. V., 1984. The Effects of Tectonic Release on Short-Period *P* Waves from NTS Explosions, *Bull. Seism. Soc. Am.*, **74**, 819-842.

Levshin, A. L., 1985. Effects of lateral inhomogeneities on surface wave amplitude measurements, *Annales Geophysicae*, **3**, 511-518.

Liebermann, C. R. and Pomeroy, P. W., 1969. Relative Excitation of Surface Waves by Earthquakes and Underground Explosions, *J. Geophys. Res.*, **74**, 1575-1590.

Lilwall, R. C. and Neary, J. M., 1985. Redetermination of earthquake body-wave magnitudes using ISC Bulletin data, United Kingdom Atomic Energy Authority, *AWRE Rept. No. O 21/85*, H.M.S.O. London.

Ma, K. F. and Kanamori, H., 1991. Aftershock sequence of the 3 December 1988 Pasadena Earthquake, *Bull. Seism. Soc. Am.*, **81**, 2310-2319.

Marshall, P. D., 1970. Aspects of the Spectral Differences Between Earthquakes and Underground Explosions, *Geophys. J. R. astr. Soc.*, **20**, 397-416.

Marshall, P. D., Douglas, A., and Hudson, J. A., 1971. Surface waves from underground nuclear explosions, *Nature*, **234**, 8-9.

Marshall, P. D. and Basham, P. W., 1972. Discrimination between earthquakes and underground explosions employing an improved Ms scale, *Geophys. J. R. astr. Soc.*, **28**, 431-458.

Marshall, P. D., Springer, D. L., and Rodean, H. C., 1979. Magnitude corrections for attenuation in the upper mantle, *Geophys. J. R. astr. Soc.*, **57**, 609-638.

Mendiguren, J. A., 1977. Inversion of Surface Wave Data in Source Mechanism Studies, *J. Geophys. Res.*, **82**, 889-894.

Mitchell, B. J., 1975. Regional Rayleigh Wave Attenuation in North America, *Geophys. J. R. astr. Soc.*, **80**, 4904-4916.

Mooney, W. D. and Braile, L. W., 1989. The Seismic Structure of the Continental Crust and Upper Mantle of North America, *eds., Bally, A. W. and Palmer, A. R., The Geology of North America v. A: An overview*, ch. 4; Geological Society of Anerica, Boulder, Colorado.

Mori, J. and Frankel, A., 1990. Source Parameters for Small Events Associated with the 1986 North Palm Springs, California Earthquake Determined Using Empirical Green Functions, *Bull. Seism. Soc. Am.*, **80**, 278-295.

Müller, R. A. and Murphy, J. R., 1971. Seismic Characteristics of Underground Nuclear Detonations, *Bull. Seism. Soc. Am.*, **61**, 1675-1692.

Müller, R. A., 1973. Seismic Moment and Long-period Radiation of Underground Nuclear Explosions, *Bull. Seism. Soc. Am.*, **63**, 847-857.

Murphy, J. R., 1977. Seismic source functions and magnitude determinations for underground nuclear detonations, *Bull. Seism. Soc. Am.*, **67**, 135-158.

Murphy, J. R. and Bennett, T. J., 1982. A Discrimination Analysis of Short-Period Data Recorded at Tonto Forest Observatory, *Bull. Seism. Soc. Am.*, **72**, 1351-1366.

Nuttli, O.W., 1986. Yield Estimates of Nevada Test Site Explosions Obtained from Seismic Lg Waves, *J. Geophys. Res.*, **78**, 2137-2151.

Oliver, J., 1962. A Summary of Observed Surface Wave Dispersion, *Bull. Seism. Soc. Am.*, **52**, 81-86.

Patton, H. J., 1982. Measurements of Rayleigh-Wave Phase Velocities in Nevada: Implications for Explosion Sources and the Massachusetts Mountain Earthquake, *Bull. Seism. Soc. Am.*, **72**, 1329-1349.

Patton, H. J. and Taylor, S. R., 1984. Q Structure of the Basin and Range from Surface Waves, *J. Geophys. Res.*, **89**, 6929-6940.

Patton, H. J., 1988a. Source Models of the HARZER Explosion from Regional Observations of Fundamental-mode and Higher-Mode Surface Waves, *Bull. Seism. Soc. Am.*, **78**, 1133-1157.

Patton, H. J., 1988b. Application of Nuttli's method to estimate yield of Nevada Test Site explosions recorded on Lawrence Livermore National Laboratory's Digital Seismic System, *Bull. Seism. Soc. Am.*, **78**, 1759-1772.

Patton, H. J., 1991. Seismic moement estimation and the scaling of the explosion source, *Geophysical Monograph 65: Explosion Source Phenomenology*, editors: S. R. Taylor, H. J. Patton and P. G. Richards; AGU, Washington, D. C., 171-183.

Patton, H. J. and Zandt, G., 1991. Seismic Moment Tensors of Western U. S. Earthquakes and Implications for Tectonic Stress Field, *J. Geophys. Res.*, **96**, 18,245-18,259.

Peppin, W. A. and McEvilly, T. V., 1974. Discrimination Among Small Magnitude Events on Nevada Test Site, *Geophys. J. R. astr. Soc.*, **37**, 227-243.

Pomeroy, W. P., Best, W. J., and McEvilly, T. V., 1982. Test Ban Verification with Regional Data - A Review, *Bull. Seism. Soc. Am.*, **72**, s89-s129.

Press, F. and Archambeau, C., 1962. Release of Tectonic Strain by Underground Nuclear Explosions, *J. Geophys. Res.*, **67**, 337-343.

Priestly, K. and Brune, J., 1978. Surface Waves and the Structure of the Great Basin of Nevada and Western Utah. *J. Geophys. Res.*, **83**, 2265-2272.

Richards, P. G. and Zavales, J., 1990. Seismic Discrimination of Nuclear Explosions, *Annu. Rev. Earth. Sci.*, **18**, 257-286.

Richter, C. F., 1935. An Instrumental Magnitude Scale, *Bull. Seism. Soc. Am.*, **25**, 1-32.

Richter, C. F., 1958. *Elementary Seismology*, W.H. Freeman, San Francisco.

Romanowicz, B. A., 1982. Moment Tensor Inversion of Long Period Rayleigh Waves: A New Approach, *J. Geophys. Res.*, **87**, 5395-5407.

Russel, D. R. 1986. Mutli-channel Processing of Dispersed Surface Waves, *Ph.D. Dissertation*, Saint Louis University, St. Louis, MO.

Saikia, K. C., Kafka, A. L., Gnewuch, S. C., and McTigue, J. W., 1990. Shear Velocity and Intrinsic Q Structure of the Shallow Crust in Southeastern New England from R_g Wave Dispersion, *J. Geophys. Res.*, **95**, 8527-8541.

Saikia, C. K. and Burdick, L. J., 1991. Fine Structure of P_{nl} Waves from Explosions, *J. Geophys. Res.*, **96**, 14,383-14,401.

Saito, M., 1967. Excitation of free oscillations and surface waves by point sources in a vertically heterogeneous earth. *J. Geophys. Res.*, **72**, 3689-3699.

Savino, J. L., Sykes, L. R., Lieberman, R. C., and Mollnar, P., 1971. Excitation of Seismic Surface Waves with Periods of 15 to 70 Seconds for Earthquakes and Underground Explosions, *J. Geophys. Res.*, **76**, 8003-8020.

Schlittenhardt, J., 1988. Seismic Yield Estiamtion Using Teleseismic P- and PKP-waves Recorded at the GRF-(Gräfenberg) array, *Geophys. J.*, **95**, 163-179.

Springer, D. L., 1966. P-wave coupling of underground explosions, *Bull. Seism. Soc. Am.*, **56**, 861-876.

Springer, D. L. and Kinnaman, R. L., 1971. Seismic source summary for U. S. underground nuclear explosions, 1961-1970, *Bull. Seism. Soc. Am.*, **61**, 1073-1098.

Stevens, J. L., 1986a. Estimation of scalar moments from explosion-generated surface waves, *Bull. Seism. Soc. Am.*, **76**, 123-151.

Stevens, J. L., 1986b. Reply to Z. Der's "Comments on the Paper 'Estimation of Scalar Moments from Explosion-Generated Surface Waves,'" *Bull. Seism. Soc. Am.*, **76**, 1825-1829.

Stevens, J. L., 1991. Seismic source characteristics of cavity decoupled explosions in salt and tuff, *Bull. Seism. Soc. Am.*, **81**, 1272-1291.

Stump, B. W. and Johnson, L. R., 1984. Near-field Source Characteristics of Contained Nuclear Explosions in Tuff, *Bull. Seism. Soc. Am.*, **74**, 1-26.

Stump, B. W., 1985. Constraints on Explosive Sources with Spall from Near-source Waveforms, *Bull. Seism. Soc. Am.*, **75**, 1312-1325.

Sykes, L. R. and Cifuentes I. L., 1984. Yields of Soviet underground nuclear explosions from seismic surface waves: compliance with the Threshold Test Ban Treaty, *Proc. natl. Acad. Sci.*, U.S.A., 1922-1925.

Taylor, S. R. and Toksöz, M. N., 1982. Measurement of Interstation Phase and Group Velocities and Q Using Wiener Filtering, *Bull. Seism. Soc. Am.*, **72**, 73-91.

Taylor, S. R., 1983. Three-dimensional crust and upper mantle structure at the Nevada Test Site, *J. Geophys. Res.*, **88**, 2220-2232.

Taylor, S. R. and Patton, H. J., 1986. Shear-Velocity Structure from Regionalized Surface-Wave Dispersion, *Geophys. Res. Lett.*, **16**, 211-214.

Taylor, S. R. and Randall, G. E., 1989. The Effects of Spall on Regional Seismograms, *Geophys. Res. Lett.*, **16**, 211-221.

Thio, H. K. and Kanamori, H., 1991. A Surface Wave Study on the Structure of the Crust and Upper Mantle Under Southern California, (abstract) *Eos Trans AGU*, **72**, No. 44, 324.

Thio, H. K. and Kanamori, H., 1992. Moment Tensor Inversions in Southern California Using Surface Waves Recorded by TERRAscope, *Eos Trans AGU*, **73**, No. 43, 376.

Toksöz, M. N., Harkrider, D. G., and Ben-Menahem, A., 1965. Determination of Source Parameters by Amplitude Equalization of Seismic Surface Waves, *J. Geophys. Res.*, 907-922.

Toksöz, M. N., Thomson, K. C., and Ahrens, T. J., 1972. Generation of Seismic Waves by Explosions in Prestressed Media, *Bull. Seism. Soc. Am.*, **61**, 1589-1623.

Toksöz, M. N. and Kehrer, H. H., 1972. Tectonic Strain Release by Underground Nuclear Explosions and its Effect on Sesimic Discrimination, *Geophys. J. R. astr. Soc.*, **31**, 141-161.

U.S. Congress, 1988. *Seismic Verification of Nuclear Testing Treaties*, Office of Technology Assessment, OTA-ISC-361, U.S. Goverment Printing Office, Washington, D.C.

Vergino, E. S. and Mensing, R. W., 1989, Yield estimation using regional mb(Pn), *Lawrence Livermore National Laboratory* Report UCID-101600.

Viecelli, J. A., 1973. Spallation and the Generation of Surface Waves by an Underground Nuclear Explosion, *J. Geophys. Res.*, **78**, 2475-2487.

Vidal, A. and Munguia, L., 1991. Local Magnitude and Source Parameters for Earthquakes in the Peninsular Ranges of Baja California, Mexico, *Bull. Seism. Soc. Am.*, **81**, 2254-2267.

Von Seggern, D., 1973. Joint magnitude determination and analysis of variance for explosion magnitude estimates, *Bull. Seism. Soc. Am.*, **63**, 827-845.

Von Seggern, D., 1977. Amplitude distance relation for 20-Second Rayleigh waves, *Bull. Seism. Soc. Am.*, **67**, 405-511.

Wallace, T. C., Helmberger, D. V., and Engen, G. R., 1983. Evidence of Tectonic Release from Underground Nuclear Explosions in Long-Period *P* Waves, *Bull. Seism. Soc. Am.*, **73**, 593-613.

Wallace, T. C., Helmberger, D. V., and Engen, G. R., 1985. Evidence of Tectonic Release from Underground Nuclear Explosions in Long-Period S Waves, *Bull. Seism. Soc. Am.*, **75**, 157-174.

Werth, G. C. and Herbst, R. F., 1963. Comparison of amplitudes of seismic waves from nuclear explosions in four mediums, *J. Geophys. Res.*, **68**, 1463-1475.

Woodhouse, J. H., 1974. Surface waves in a laterally varying layered structure. *Geophys. J. R. astr. Soc.*, **37**, 461-490.

Woods, B. B., Kedar, S., and Helmberger, D. V., 1993. M_L:M_0 as a Regional Seismic Disriminant, *Bull. Seism. Soc. Am.*, **83**, 11677-1183.

Woods, B. B. and Harkrider, D. G., 1993. Determining Surface Wave Magnitudes from Regional NTS Data, *submitted to Geophys. J. Int.*

Woods, B. B., Saikia, C. K., and Helmberger, D. V., 1992. An Energy Discriminant for Regional Seismic Events, *Eos Trans AGU*, **73**, No. 43, 359.

Wyss, M. and Brune, J. N., 1968. Seismic Moment, Stress, and Source Dimensions for Earthquakes in the California-Nevada Region, *J. Geophys. Res.*, **73**, 4681-4694.

Yacoub, N. K., 1983. "Instantaneous amplitudes": A new method to measure seismic magnitude, *Bull. Seism. Soc. Am.*, **73**, 1345-1355.

Yelin, T. S. and Patton, H. J., 1991. Seismotectonics of the Portland, Oregon Region, *Bull. Seism. Soc. Am.*, **81**, 109-130.

Yomogida, K., 1985. Surface waves in a laterally slowly-varying media. *Geophys. J. R. astr. Soc.*, **82**, 511-533.

Zhao, L. S. and Helmberger, D. V., 1991. Broadband Modelling Along a Regional Shield Path, Harvard Recording of the Saguenay Earthquake, *Geophys. J. Int.*, **105**, 301-312.

Zhao, L. S. and Harkrider, D. G., 1992. Wavefields from an off-center explosion in an imbedded solid sphere, *Bull. Seism. Soc. Am.*, **82**, 1927-1955.

Zhao, L. S. and Helmberger, D. V., 1993. Source Estimation from Broadband Regional Seismograms, *submitted to Bull. Seism. Soc. Am.*